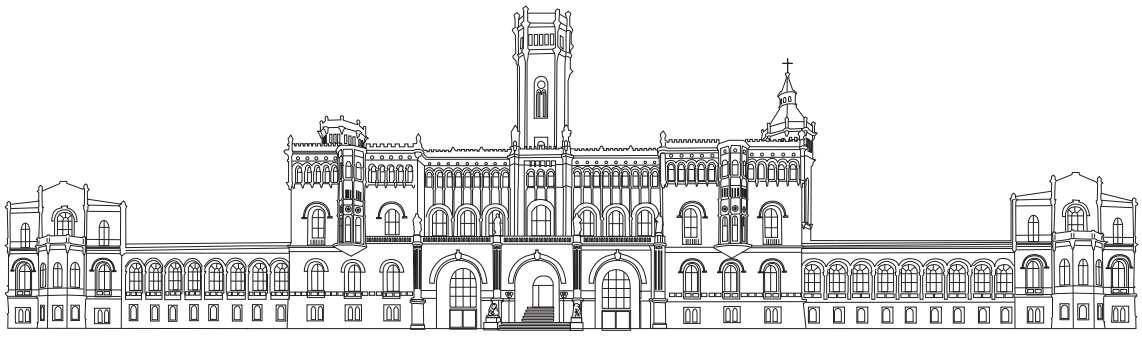

Analytical Investigations of Understudied Nuclides in Modern Environmental Nuclear Forensics

Der Fakultät für Mathematik und Physik
der Gottfried Wilhelm Leibniz Universität Hannover
zur Erlangung des akademischen Grades

Doktor der Naturwissenschaften
Dr. rer. nat.

genehmigte Dissertation von

Dorian Zok, M. Sc.

2021

Referent:	Prof. Dr. Georg Steinhauser Institut für Radioökologie und Strahlenschutz Fakultät für Mathematik und Physik Gottfried Wilhelm Leibniz Universität Hannover
1. Korreferent:	Prof. Dr. Clemens Walther Institut für Radioökologie und Strahlenschutz Fakultät für Mathematik und Physik Gottfried Wilhelm Leibniz Universität Hannover
2. Korreferent:	Prof. Dr. Thorsten Kleine Institut für Planetologie Fachbereich Geowissenschaften Westfälische Wilhelms-Universität Münster
Tag der Promotion:	25.06.2021

"A scientist in his laboratory is not only a technician: he is also a child placed before natural phenomena which impress him like a fairy tale."

— Marie Skłodowska-Curie

E. Curie, *Madame Curie: A Biography*, New York: Doubleday, Doran & Company Inc., 1937

Table of Contents

Abstract

Continuous improvement of modern analytical chemistry techniques has increased the possibilities of measurements in the field of nuclear forensics. Once successful, they can be expanded to more isotopic systems with increasing sensitivity. The examples in nuclear forensics considered in this thesis are investigations of the undeclared radioactive ruthenium release in 2017 and the source identification of cesium isotope ratios.

Air filter stations from the informal monitoring network "Ring of Five" permanently monitor and collect airborne particle samples. In October 2017, this network detected radioruthenium in its samples.

Radioruthenium was trapped in the filters, suggesting that only the radionuclides ^{103}Ru and ^{106}Ru were released in this undeclared event. Since no other elements were observed, a pure ruthenium release must have occurred. "Ring of Five" stations exchanged data and suggestions of the origin and background. The combination of airborne concentration data and air dispersion modeling allowed the network to trace its origin back to the Southern Urals (Russia), where the nuclear facility complex "Majak Production Association" is located.

Additional information such as age estimation was obtained by very accurate radioruthenium isotope measurements to reprocessed fuel of a likely age of less than two years. The reprocessing background and purity of the released ruthenium were determined by the complex chemistry of the behavior of different oxidation state compounds. It could be concluded that the release likely occurred in the form of $RuCl_3$ and RuO_2. These indicated a release during RuO_4 trapping with HCl, which is a part of nuclear reprocessing.

Going deeper in the area of isotope ratios, the stable ruthenium isotopes showed a strong contribution of non-natural ruthenium isotopes. A considerable shift from natural ratios was measured and could be linked to spent fuel from Russian reactor type VVER.

So far, no organization, facility or state has assumed responsibility for this release.

Isotopic ratio determination can strongly increase the knowledge about materials, age, origin, or processing. Advances in mass spectrometric techniques such as ICP-QQQ-MS enables the determination of previously difficult-to-measure isotopes or ratios due to interference, e.g. ^{135}Cs/^{137}Cs.

For this ratio determination, interfering isobars were reduced by a three step chemical protocol. Barium interferences are reduced up to several orders of magnitude, while the average cesium recovery rate yielded 78 %.

Abstract

Typical isotopic ratios were found for biological samples with known Chernobyl, Fukushima and global weapon fallout signatures of $^{135}Cs/^{137}Cs$. More importantly, an anomalous ratio was found for trinitite. This inconsistency was explained by different decay chain half-lifes, whereby the ^{135}Xe mother nuclide is predominantly blown away.
In conclusion, isotope ratios are an even more powerful tool to answer analytical questions than simple concentrations and activities due to the increased gain of information depth.

Keywords: Nuclear Forensics, ^{106}Ru, ^{135}Cs, Isotope Ratios, Mass Spectrometry

List of Publications

This cumulative dissertation consists of the following five peer-reviewed publications:

I Publication

Airborne Concentrations and Chemical Considerations of Radioactive Ruthenium from an Undeclared Major Nuclear Release in 2017

O. Masson, G. Steinhauser, D. Zok, O. Saunier, H. Angelov, D. Babić, V. Bečková, J. Bieringer, M. Bruggeman, C. I. Burbidge, S. Conil, A. Dalheimer, L.-E. De Geer, A. de Vismes Ott, K. Eleftheriadis, S. Estier, H. Fischer, M. G. Garavaglia, C. Gasco Leonarte, K. Gorzkiewicz, D. Hainz, I. Hoffman, M. Hýža, K. Isajenko, T. Karhunen, J. Kastlander, C. Katzlberger, R. Kierepko, G.-J. Knetsch, J. Kövendiné Kónyi, M. Lecomte, J. W. Mietelski, P. Min, B. Møller, S. P. Nielsen, J. Nikolic, L. Nikolovska, I. Penev, B. Petrinec, P. P. Povinec, R. Querfeld, O. Raimondi, D. Ransby, W. Ringer, O. Romanenko, R. Rusconi, P. R. J. Saey, V. Samsonov, B. Šilobritienė, E. Simion, C. Söderström, M. Šoštarić, T. Steinkopff, P. Steinmann, I. Sýkora, L. Tabachnyi, D. Todorovic, E. Tomankiewicz, J. Tschiersch, R. Tsibranski, M. Tzortzis, K. Ungar, A. Vidic, A. Weller, H. Wershofen, P. Zagyvai, T. Zalewska, D. Zapata García, B. Zorko

Proceedings of the National Academy of Sciences of the United States of America, vol. 116, no. 34, pp. 16750-16759, 2019. DOI: 10.1073/pnas.1907571116

II Publication

Identification of a Chemical Fingerprint Linking the Undeclared 2017 Release of ^{106}Ru to Advanced Nuclear Fuel Reprocessing

M. W. Cooke, A. Botti, D. Zok, G. Steinhauser, K. Ungar

Proceedings of the National Academy of Sciences of the United States of America, vol. 117, no. 26, pp. 14703-14711, 2020. DOI: 10.1073/pnas.2001914117

III Publication

Chemical and Radioanalytical Investigations of ^{106}Ru-containing Air Filters from Vienna in Fall 2017: Searching for Stable Element Anomalies

D. Zok, J. H. Sterba, G. Steinhauser

Journal of Radioanalytical and Nuclear Chemistry, vol. 318, pp. 415-421, 2018. DOI: 10.1007/s10967-018-6132-6

IV Publication

Non-Natural Ruthenium Isotope Ratios of the Undeclared 2017 Atmospheric Release Consistent with Civilian Nuclear Activities

T. Hopp*, D. Zok*, T. Kleine, G. Steinhauser

Nature Communications, vol. 11, no. 1, pp. 1-7, 2020. DOI: 10.1038/s41467-020-16316-3

V Publication

Determination of Characteristic vs Anomalous $^{135}Cs/^{137}Cs$ Isotopic Ratios in Radioactively Contaminated Environmental Samples

D. Zok, T. Blenke, S. Reinhard, S. Sprott, F. Kegler, L. Syrbe, R. Querfeld, Y. Takagai, V. Drozdov, I. Chyzhevskyi, S. Kirieiev, B. Schmidt, W. Adlassnig, G. Wallner, S. Dubchak, G. Steinhauser

Environmental Science & Technology, vol. 55, no. 8, pp. 4984-4991, 2021.

DOI: 10.1021/acs.est.1c00180

* T. Hopp and D. Zok contributed equally to this work

Chapter 1

Introduction

1.1 Modern Nuclear Forensics

The field of nuclear forensics is characterized by the analysis of radioactive materials and isotopes with the aim to answer questions of interest about the age, source, origin or even authenticity or legality of the material.[1,2] The focus is the determination of specific isotopes and elements, especially their isotopic ratios, amounts, or activities. Various analytical techniques in the area of spectroscopy and spectrometry can lead to improvements in the understanding of the above questions.[3]

These techniques are predominantly applied to natural or fissile isotopes of uranium and plutonium. Examples are the identification of $^{235}U/^{238}U$, or $^{240}Pu/^{239}Pu$, e.g. in the Chernobyl exclusion zone in particles.[4,5] These ratios indicate information such as the levels of enrichment, or the used fuel type. Age dating of Pu reference materials can be established by $^{234}U/^{238}Pu$ or $^{235}U/^{239}Pu$ or for U with $^{231}Pa/^{235}U$.[6–10] Information about the ratios can contribute to the knowledge of anthropogenic processes of these radionuclides.

Recently, there have been developments in the study of other isotope ratio systems, rather than exclusively looking at the pure natural and anthropogenic U and Pu chains. Mostly, radionuclides are underrepresented because of interfering, dominant radionuclides such as ^{137}Cs. An example is the $^{108m}Ag/^{110m}Ag$ ratio, which can be found in sea foods, because silver was released in the nuclear accident of Fukushima into the Pacific Ocean.[11,12] Furthermore, the $^{103}Ru/^{106}Ru$ ratio of the undeclared radioruthenium release in 2017 was used to identify the cooling time of the spent and reprocessed fuel.[13] Lately, the importance of the $^{135}Cs/^{137}Cs$ ratio is increasing. This allows an even more detailed source determination, especially the distinction between each reactor unit in Fukushima.[14–16]

Radiometric methods such as the gamma or alpha spectrometry are usually suitable for measuring many radionuclides and isotopes.[3,11] The powerful, but decreasing in popularity Instrumental Neutron Activation Analysis (INAA) can also be used to investigate long-lived radionuclides and stable isotopes. Not every radionuclide is radiometrically easily measurable due to its long half-life, possible interference from other nuclides, low activity or pure beta-emission. Today, various mass spectrometrical techniques such as the Thermal Ionisation Mass Spectrometry (TIMS),[6,16] Secondary Ionization Mass Spectrometry (SIMS),[4,5] Multicollector Inductively Coupled Plasma Mass Spectrometry (MC-ICP-MS),[7,9,10] Accelerator Mass Spectrometry (AMS),[15] or the upcoming Inductively Coupled Plasma Triple Quadrupole Mass Spectrometry (ICP-QQQ-MS) complement the analysis with radiometric techniques.[8,14,17]

In these cases, the further development of mass spectrometry have closed the gap and increased the sensitivity.

1.2 Nuclear Facilities and Industries

1.2.1 Power Plants

1.2.1.1 Nuclear Fission and Fission Fragments

The disintegration of a nucleus due to nuclear fission can occur in two different ways, namely as spontaneous fission (SF) or induced nuclear fission. The SF usually takes place at high mass nuclei such as the isotopes of uranium or plutonium, but is even more frequent for the heavier elements: americium, californium, curium, and beyond. With increasing number of protons, Z, in these super-heavy nuclides, the fission barrier is continuously decreased, resulting in a half-life shortened from the range of billions of years to nanoseconds. The general process of SF is shown in Figure 1.1. A nucleus changes its shape and finally deforms enough to pass the energetic barrier for a fission. The nucleus can split in three different scenarios: A (equal masses, different excitation) - B (different masses, equal excitation) - C (different masses, different excitation). The most probable scenario is the reaching of equal excitation energies, while masses are different. These is based on reaching low energetic states, e.g. shell closures. After the complete fission process, the excited products will release energy in different ways, e.g neutron emission or gamma-rays (γ). The newly created, lower-energy nuclei can decay by (several) beta-decays (β^-) to reach a stable nuclide of their isobar.[18–20]

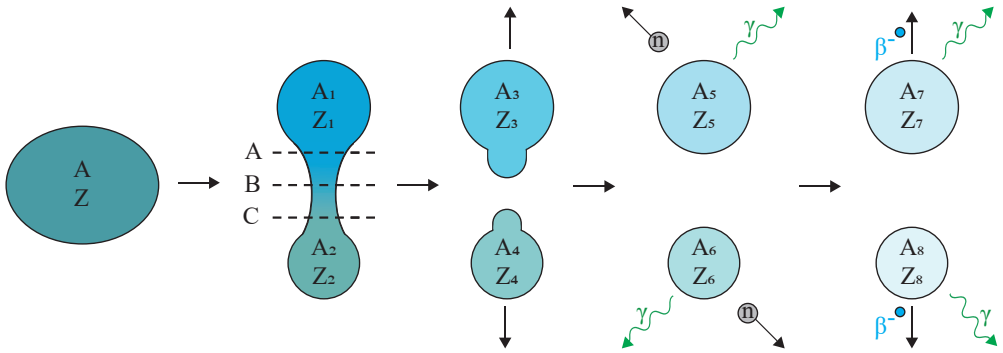

Figure 1.1: The steps of spontaneous fission. Adapted from *Nuclear and Radiochemistry: Fundamentals and Applications*.[18]

The induced nuclear fission (Figure 1.2) needs, in contrast to SF, an external particle. In the context of energy production, this is often a neutron, but deuterons, protons, or theoretically any other nucleus could be suitable. With moderated thermal neutrons (0.025 eV kinetic energy) in nuclear reactors, it is usually ^{235}U and ^{239}Pu that can be fissioned, while the most abundant ^{238}U will not undergo fission reactions with these thermal neutrons. The reason for this is the lower energetic state of the nucleus after capturing the external neutron. After the capture of the neutron, this energy gain allows fission of the nucleus, forming two or more products. Predominantly, two nuclei are formed with masses distributed around the magic numbers (50

and 82 neutrons), some residual neutrons and energy of around 200 MeV are released by a fission event. For 1 kg of fissioned ^{235}U a potential energy of $4 \cdot 10^{32}$ eV is released (explosion equivalent to 17 kt TNT).[21] The free, generated neutrons will have high energy and need to be moderated to maintain the chain reaction in a reactor in the region of thermal neutrons. Formed nuclei are neutron-rich radionuclides of various elements and vary in masses. If they are not stable, they will undergo a cascade of beta-decays, partly combined with gamma radiation until they reach a stable nuclide.[18,19,22]

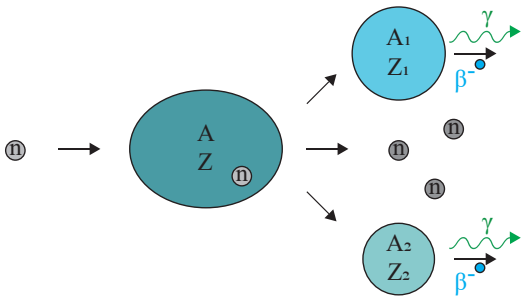

Figure 1.2: The steps of neutron-induced fission. Adapted from *Nuclear and Radiochemistry: Fundamentals and Applications*.[18]

The process of nuclear fission and the resulting fragments are strongly dependent on the present conditions. Enriched uranium is typically used in energy production. The distribution of fission products is a characteristic double maxima pattern of different formation probabilities (Figure 1.3). The use of ^{239}Pu instead of ^{235}U will shift the typical pattern to slightly higher masses. The use of higher energetic neutrons of some eV or even MeV will change this shape to a flatter profile, resulting in the formation of nearly symmetric fragment distribution.[23]

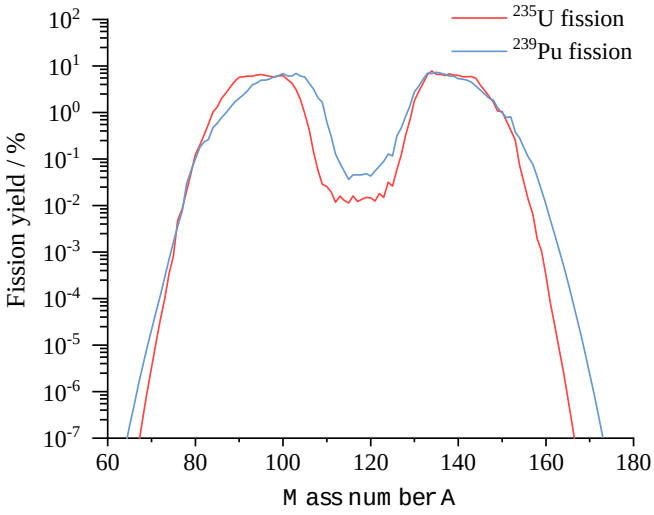

Figure 1.3: Fission yields of the thermal neutron-induced fission of ^{235}U and ^{239}Pu. Data from Nucleonica.[24]

1.2.1.2 Mining, Refining, and Enrichment

Uranium is a primordial and ubiquitous element in the Earth's upper crust and is obtained mostly by mining open-pit (13 %), underground mining (31 %) and *in-situ* leaching (50 %).[25] Leaching is performed by using acidic solutions pumped directly into the underground repository to dissolve uranium minerals. The largest producers with a total amount of around 60.000 tons of U are Kazakhstan, Canada, and Australia (2016).[25,26]

A wet refining routine is shown in Figure 1.4a. The essential steps are the dissolution in nitric acid, extractions for purification, conversion to the solid uranium oxides (UO_3, UO_2), and the transformation to uranium hexafluoride (UF_6) for the enrichment. The intermediate UO_2 can be used in heavy-water reactors, or the metal based U can be produced for Magnox fuels. A chemical transformation to U_3O_8 can be used as a safe state for storage.

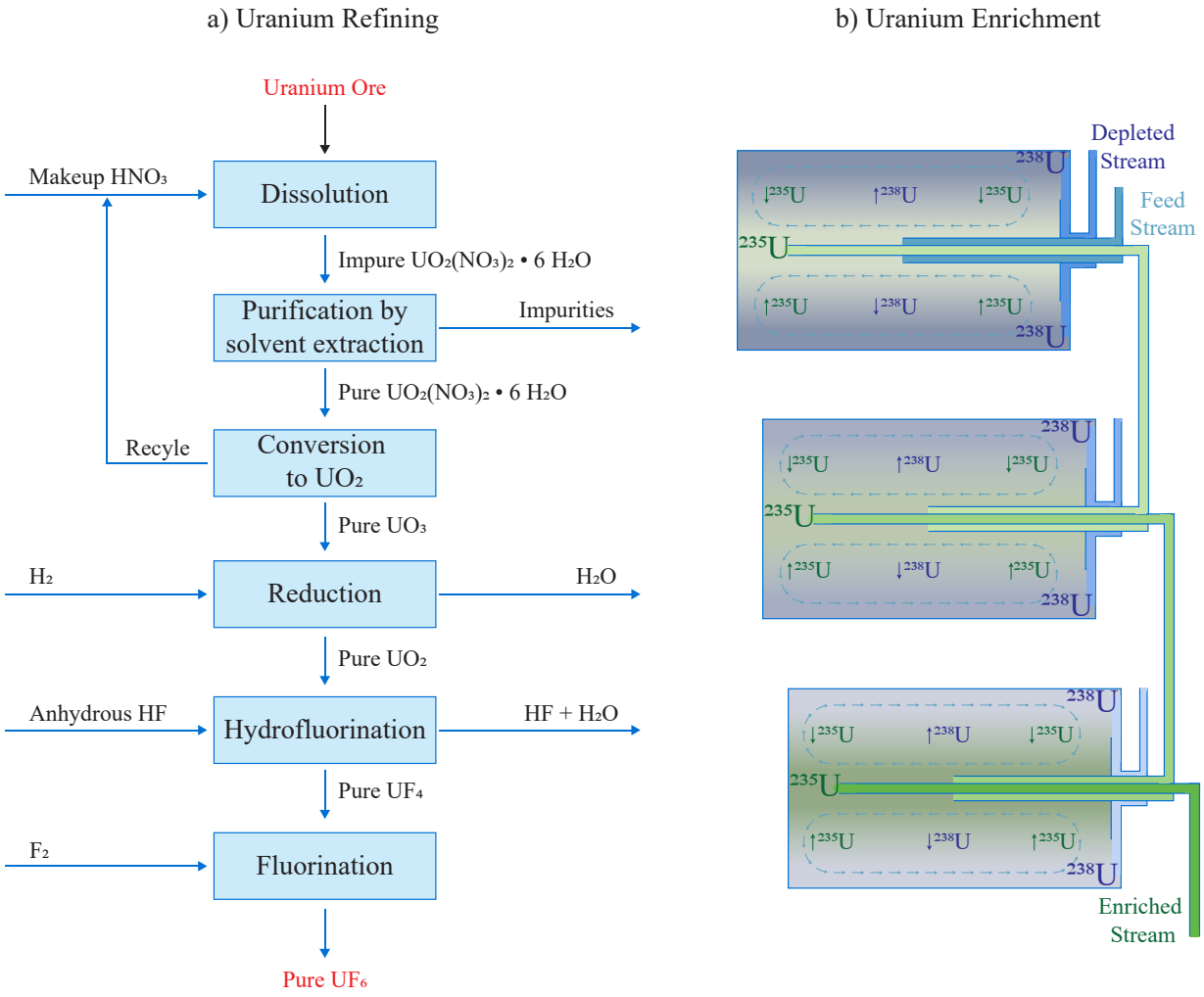

Figure 1.4: Stages in conventional, wet-route UF_6 refining-conversion process (a) and enrichment of produced UF_6 in a gas centrifuge cascade (b). Adapted from IAEA and USNRC.[27,28]

Uranium hexafluoride is the starting point for the gas centrifuge to enrich the uranium for the required ^{235}U isotope (Figure 1.4b). The natural U abundances of the three main isotopes are around 99.28 % ^{238}U, 0.711 % ^{235}U, and 0.0054 % ^{234}U.[27] For the enrichment of the UF_6, feed stream with natural isotopic ratios is fed into the gas centrifuge. There, it is accelerated to very high rotation speeds. Because of the higher centrifugal force of the heavier ^{238}U, it is pushed to the outer parts of the cylinder, while the lighter ^{235}U is slightly enriched in the center part of the centrifuge. This stream will be transported to the next centrifuge, while the depleted stream is feeding the previous centrifuge. These are the first steps in a long cascade of separations.[25]
Today, there are enrichment plants located in Russia, USA, Germany, and France.[26,29] The degree of enrichment for ^{235}U is often around 3-5 %, which varies for reactor type. For each kg of enriched U, over 9 kg of natural U is required.[23]

1.2.1.3 Reactor Types and Power Plants

The fission of uranium releases an energy of around 200 MeV per fission.[21,22] This energy can be harnessed in various reactor types which exist around the world. A general overview of the reactor types and their parameters is shown in Table 1.1. The four listed reactor types are the western Pressurized Water Reactor (PWR)/ Russian Water-Water-Energetic-Reactor (VVER), Boiling Water Reactor (BWR), Pressurized Heavy Water Reactor (PHWR), and High-Power Channel-Type Reactor (RBMK).
A significant difference between reactor types is the choice of the moderator and cooling water type. The fast neutrons at high energy in reactors need to be moderated to thermal energy of 0.025 eV. This can be done by light element moderator such as H, D or even C (as graphite). The number of necessary elastic scatters for lowering the kinetic energy rises with an increasing atomic number. Another difference is the used fuel. Enriched UO_2 can be directly generated from UF_6 and fabricated to fuel rods, or already spent nuclear fuel can be reprocessed to obtain a mixture out of plutonium and uranium oxide as mixed oxide (MOX).[18]

Table 1.1: General information of operating reactor types (01.2021). Data from IAEA.[27,30]

Reactor type	PWR/VVER	BWR	PHWR	RBMK
Moderator	H_2O	H_2O	D_2O	Graphite
Coolant				
Type	Pressurized H_2O	Boiling H_2O	Pressurized D_2O	Boiling H_2O
Pressure (bar)	155	70	110	70
Temp. outlet (°C)	320	286	310	284
Fuel				
Type	UO_2/MOX	UO_2/MOX	UO_2	UO_2
Enrichment	Up to 5 %	Up to 5 %	Natural U	Up to 3 %
Burn-up GWd/t_{HM}	Up to 60	Up to 55	Up to 7	Up to 25
Operating units (2021)	302	64	49	12
Total power (GW)	287.0	65.0	24.5	8.4

PWR/VVER The western Pressurized Water Reactor (PWR) or the Russian Water-Water-Energetic-Reactor (VVER) are the most common reactor types worldwide. They are operated with 200-300 rods of enriched UO_2 (equal to 80 - 100 t U) or MOX elements. Their advantage is the operation in two different water cooling cycles. One water cycle is passing the reactor vessel and is therefore contaminated with radionuclides. The second, not contaminated cycle is driving the turbine outside of the containment. The negative void coefficient is an additional safety aspect. A scheme of the reactor type is shown in Figure 1.5a.
The primary water cycle inside the containment is pumped through the reactor vessel, moderates the fast neutrons, and gets heated up to 320 °C. The hot water kept in liquid state by a pressure of 155 bar inside the system and flows thereafter to the heat exchanger. Within this less pressurized secondary cooling cycle, the hot water evaporates inside the steam generator. The water steam is directly introduced to a turbine for the generation of electric energy. Afterwards, the water is cooled down and pumped again to the heat exchanger for cooling the primary water cycle.[23,31]

BWR The Boiling Water Reactor (BWR) is also widely used, with over 60 reactors (operating as of 2021).[30] In comparison to the previous PWR, it contains one water cooling system with lower temperature and pressure, but uses the same enrichment, fuel, and moderator (Figure 1.5b). A reactor contains up to 750 rods, with a content of 140 t U. Beside the advantage of a simpler design, the biggest disadvantage of this reactor type is that the water is contaminated with radionuclides, whereby the turbine needs a shielding too.
The cooling water is pumped into the reactor vessel, heated up to over 280 °C and evaporated. The resulting steam is then pumped outside the reactor containment into the shielded turbine for electric energy generation and is later cooled down for re-use in the cooling system.[23,31]

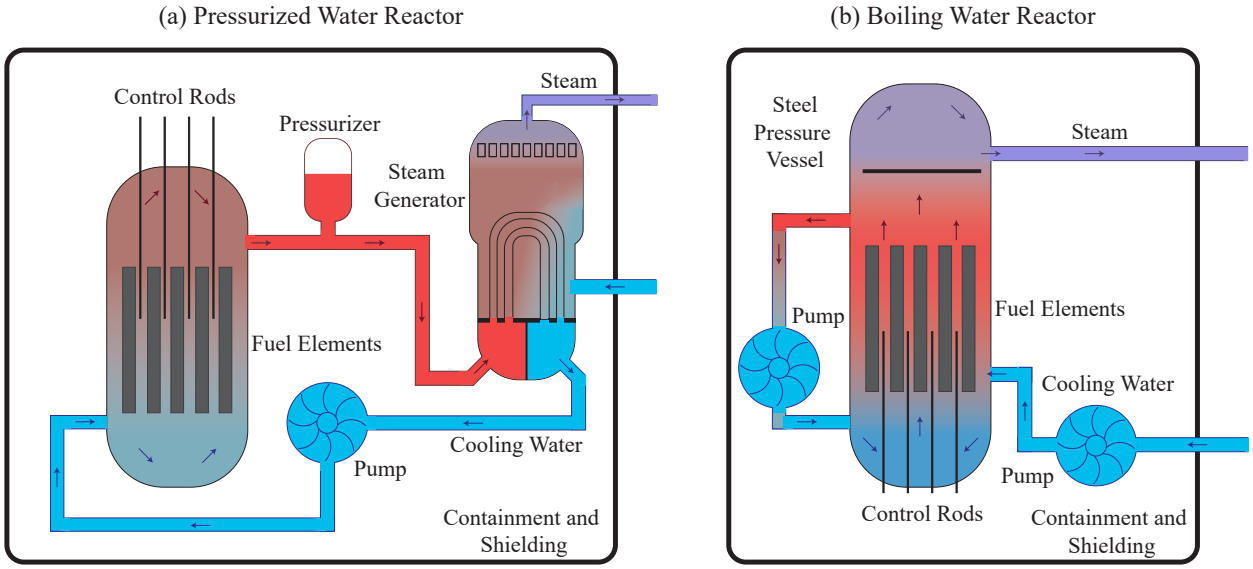

Figure 1.5: Schematic drawing of a PWR (a) and BWR (b), including water cycle and temperature profile. Adapted from World Nuclear Association.[31]

PHWR The Pressurized Heavy Water Reactor (PHWR) - also known as Canada Deuterium Uranium (CANDU) - is a natural uranium fuel and heavy water (D_2O) moderated reactor. A scheme is shown in Figure 1.6a. The huge advantage is the use of natural U fuel assemblies and the online replacement of the fuel. However, the significant expense of D_2O is a disadvantage. Cooling water is pumped into the fuel elements assembly, heated up to 310 °C and introduced into a heat exchanger. There, the secondary water cycle is evaporated and used to drive the turbine. After cooling down it can be re-used in the cycle.[23,31]

RBMK The High-Power Channel-Type Reactor (RBMK) is a Russian designed boiling water reactor type. The RBMK is special because fuel rods can be replaced while the reactor is in operation. This feature makes the RBMK suitable for energy as well as weapons-grade Pu production (Figure 1.6b).
Each fuel rod is placed in one separate channel (of around 1,900), surrounded by the graphite moderator. Cooling water passes through the channel and is heated up to 280 °C. The low pressure of 70 bars allows it to evaporate and generate steam. The formed steam is fed into a turbine for electrical energy production.[23,31]

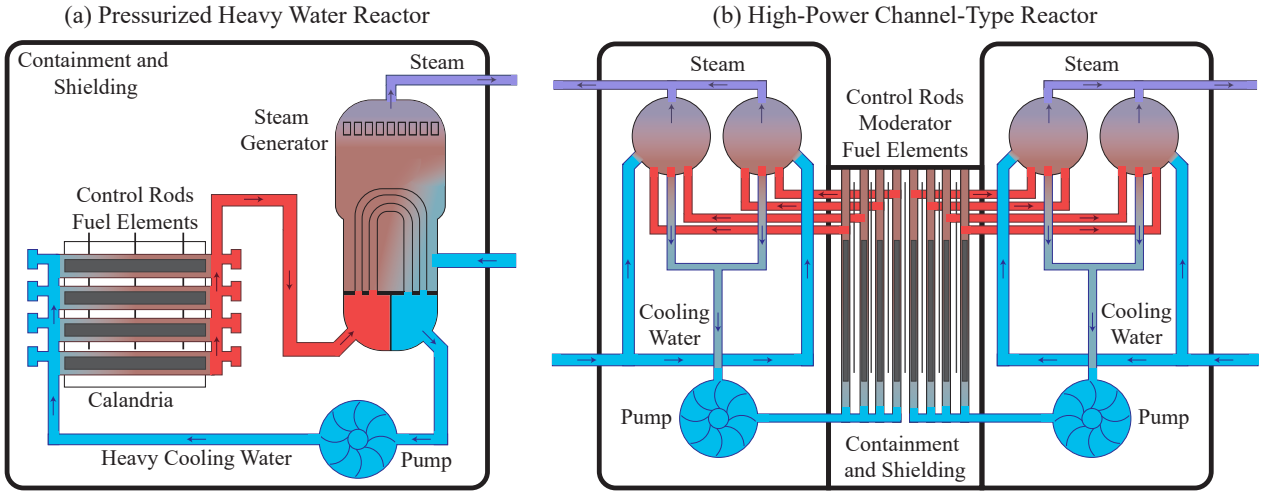

Figure 1.6: Schematic drawing of a PHWR (a) and RBMK (b), including water cycle and temperature profile. Adapted from World Nuclear Association.[31]

1.2.2 Reprocessing Plants

1.2.2.1 Overview

The amount of nuclear reactors all over the world is producing continuously more spent nuclear fuel and hence more radioactive waste. However, the waste is still full of usable material. Table 1.2 shows the composition of spent nuclear fuel compared to fresh fuel. After the regular burn-up time, the fuel element still contains almost the initial natural amount of ^{235}U and additionally fissionable Pu isotopes (^{238}Pu, ^{239}Pu, ^{241}Pu), minor actinides (Np, Am, Cm) and

fission products. The uranium and plutonium remaining in spent fuel can therefore been seen as valuable resource for a closed fuel cycle instead of the storage into a nuclear repository. Unfortunately, due to the short-lived radionuclides, spent fuel needs to be stored for some years to minimize radioactivity before being reprocessed.
Reprocessing for light water reactors is currently performed by different countries, such as "Mayak Production Association" in Russia, "La Hague Site" in France and "Sellafield Site" in the United Kingdom. Additionally, Japan is building a new facility in Rokkasho.[27,32]

Table 1.2: Comparison of fuel before and after irradiation in a PWR. Data from IAEA.[27]

Nuclide group	Fresh fuel (%)	Spent fuel (%)
^{235}U	4.00	0.67
^{236}U		0.50
^{238}U	96.00	93.06
U total	100.00	94.23
Pu fissile		0.67
Pu total		1.01
Minor actinides		0.10
Fission products		4.00
PWR with 4 % initial enrichment and 45 GWd/t burn-up		

1.2.2.2 PUREX Process

The plutonium and uranium extraction (PUREX) process is the commercially used method for the reprocessing of nuclear fuels and applied by all plants for the purification of plutonium and uranium (Figure 1.7). Other radionuclides (of e.g. Mo, Tc, Cs, Ba) or minor actinides (Np, Am, Cm) can be separated in more advantageous steps. Additionally, stable valuable platinum group elements (Ru, Pd, Rh) or rare earth elements (Nd, Ce, Sm) can be obtained.[33]
The spent fuel initially is chopped and dissolved in concentrated HNO_3. Some gaseous and volatile elements from the dissolved fuel such as krypton and iodine nuclides are removed. Present ruthenium will react into challenging chemical compound of ruthenium tetroxide (RuO_4) and has to be removed at the very beginning. The solution will be diluted and treated with the oxidizer sodium nitrate ($NaNO_2$) to gain the Pu^{IV} and U^{VI} oxidation state. By adding the tri-*n*-butyl phosphate (TBP) in kerosene as the first extraction medium, the Pu and U is transferred into the organic phase and separated from most of the other fission products.
At this point, the specific separation of Pu and U is performed. The addition of a reductant such as Fe^{II} or U^{IV} will reduce the Pu^{IV} to Pu^{III} and remove it from the organic to the aqueous phase, while U stays in the organic phase. The aqueous solution containing Pu will be extracted again with TBP for the purification of the fraction. Due to the high radiation levels, the TBP will be partly radiolyzed to dibutyl phospharic acid (DBP), which forms strong Pu complexes. The addition of aqueous sodium carbonate (Na_2CO_3) solution will suppress this. The refining of a washing step of the organic phase was an improvement.

At the same starting point, the uranium separation begins with a re-extraction into an aqueous phase with 0.01 M HNO_3 solution. By adding TBP, U will again be extracted into a purer organic phase. As with the washing step for the Pu, the DBP interference will be suppressed by adding Na_2CO_3. After the separation, Pu and U have to be transferred into the desired chemical form such as oxides or nitrates.[18,32]

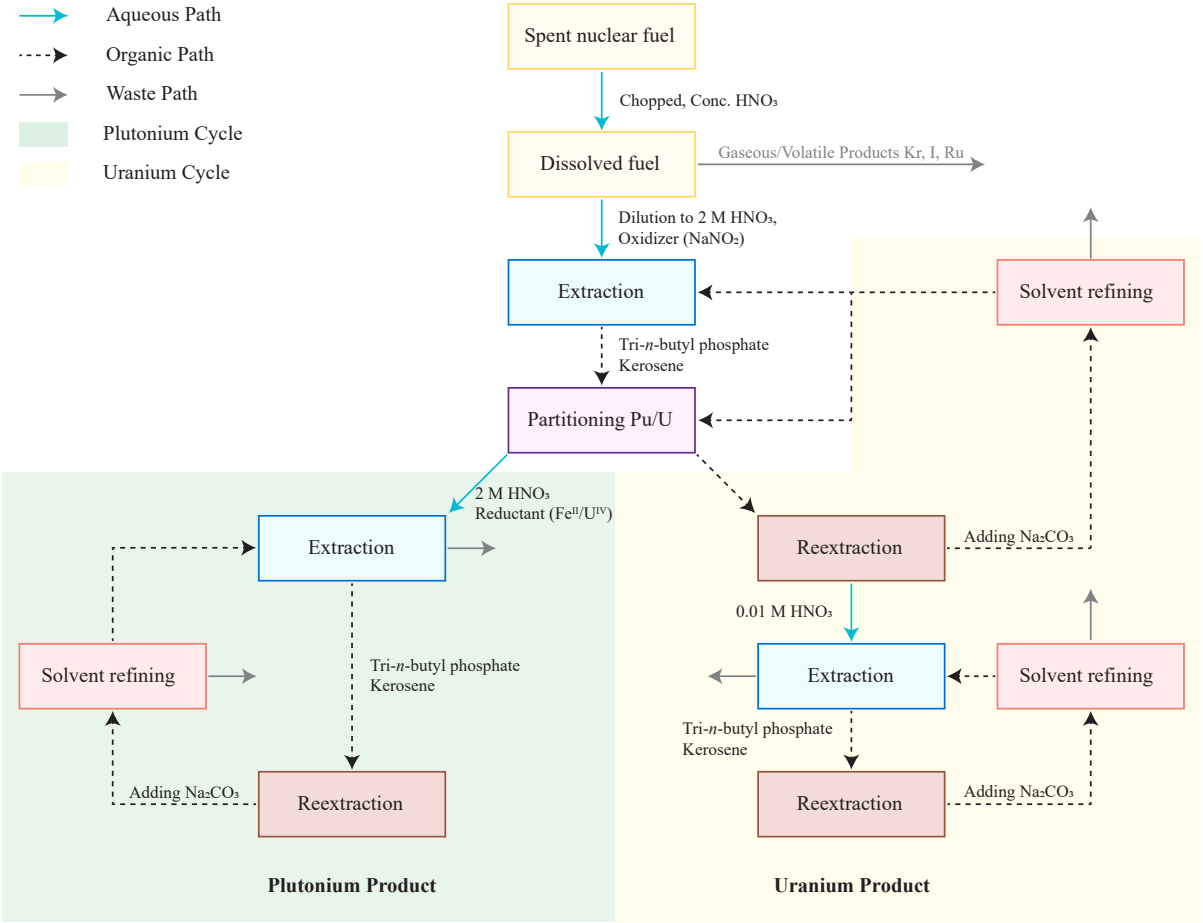

Figure 1.7: Scheme of the separation steps in PUREX process for Pu (green area) and U (yellow area). Adapted from World Nuclear Association and *Nuclear and Radiochemistry: Fundamentals and Applications*.[18,32]

1.2.2.3 Ruthenium in Reprocessing

A very problematic element in the nuclear fuel reprocessing is ruthenium, specifically the isotopes ^{106}Ru ($T_{1/2}$ = 373.6 days) and ^{103}Ru ($T_{1/2}$ = 39.2 days).[34] In fission, these isobars are quite probable to be formed, and is even higher for the fission of ^{239}Pu than for ^{235}U.[35] With the general cool down time for spent fuel of at least five to ten years, less activity is present, but stable ruthenium is still present and problematic.

In reprocessing, the ruthenium from dissolved fuel fractions, is oxidized by the concentrated HNO_3 to the ruthenium tetroxide (RuO_4) in two mechanisms (1.1 - 1.3). Additionally, a certain amount of ruthenium will not be oxidized and will form various, very stable ruthenium nitro-

syl nitrate compounds $[RuNO(NO_3)_x(NO_2)_y(OH)_z(H_2O)_{5\text{-}x\text{-}y\text{-}z}]^{3-x-y-z}$ with the nitrates (NO_3), nitrogen dioxide (NO_2), nitric oxide (NO) present in the aqueous solution.[35]

$$4\ HNO_3 \rightarrow 2\ H_2O + 4\ NO_2 + 2\ O_2 \tag{1.1}$$

$$Ru^{4+} + 2\ H_2O + O_2 \rightarrow RuO_4 + 4\ H^+ \tag{1.2}$$

$$Ru^{4+} + 2\ NO_2 + 2\ H_2O \rightarrow RuO_4 + 2\ NO + 4\ H^+ \tag{1.3}$$

In RuO_4, Ru is present in the high oxidation state of +VIII. Consequently, RuO_4 is a extremely aggressive, corrosive, reactive chemical and a very volatile substance (S_{bp} = 40 °C)[36]. Due to its β^- decay, the formed $^{106}RuO_4$ is challenging in reprocessing. Volatile RuO_4 will react with almost all compounds found in the reprocessing plant. This includes not only the vessel and tubing of the solution, but is also capable of radiolytically destroying TBP to DBP in the later separation steps due to the electrons produced in the β^- decay. Formed DBP is disadvantageous in reprocessing, because it will extract the ruthenium nitrosyl nitrates into further steps. Another problem is the decomposition of RuO_4 to elemental oxygen (O_2) and ruthenium dioxide (RuO_2) at high temperatures.[35]
To avoid any additional issues with Ru in its volatile form, it will be captured chemically in acidic (1.4)[37] or alkaline (1.5)[35,36] solutions to form less reactive species with lower oxidation states. Several reaction products are possible depending on different parameters.[35,38]

$$RuO_4 \xrightarrow[-4\ H_2O,-2\ Cl_2]{+10\ HCl} H_2[RuCl_6] \tag{1.4}$$

$$4\ RuO_4 \xrightarrow[-2\ H_2O,-O_2]{+4\ OH^-} 4\ RuO_4^- \xrightarrow[-2\ H_2O,-O_2]{+4\ OH^-} 4\ RuO_4^{2-} \tag{1.5}$$

1.3 Nuclear Accidents and Environmental Releases

1.3.1 International Organizations and Monitoring

Two big international organizations play a role in the field of the nuclear industries and facilities. These are the International Atomic Energy Agency (IAEA) and Comprehensive Nuclear-Test-Ban Treaty Organization (CTBTO). Both are today located in Vienna, Austria.

1.3.1.1 IAEA and INES

The IAEA was already approved in 1957. The IAEA operates worldwide in the field of nuclear technologies and sciences. It covers the peaceful and conventional use of nuclear energy, while the military use is tried to be prevented. Also they publish general information in the field of nuclear sciences and safeguards.[39–41]
The IAEA provides an overview of currently running reactor systems,[30] and introduced in 1990 the International Nuclear and Radiological Event Scale (INES) for describing a nuclear event.[42] This scale is shown in Figure 1.8 and is generally divided into seven logarithmic levels dependent on the impact and hazard of the event. Relevant factors are the impact on the safety of human beings and environment as well as the event's spreading and controllability.
For every level at least one nuclear event has already been assigned, most prominently the accidents of Chernobyl 1986 and Fukushima Daiichi 2011 with 7, the Kyshtym accident 1957 with 6 and the Windscale Pile 1957 and Three-Mile-Island 1979 accidents with 5.[43–45]

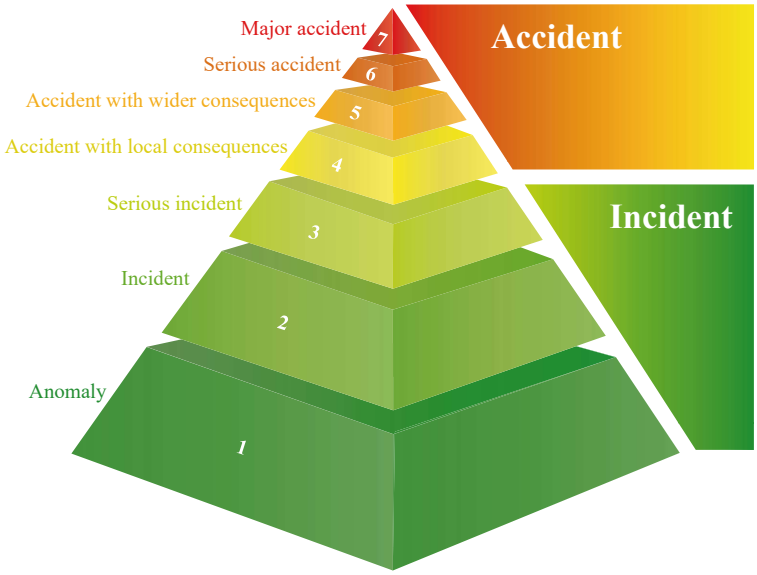

Figure 1.8: INES with levels and definitions. Adapted from IAEA.[42]

1.3.1.2 CTBTO and IMS

The CTBTO is the organization which supervises the Comprehensive Nuclear-Test-Ban Treaty (CTBT) and was founded in 1996, when the treaty was opened for signature. The treaty will ban every nuclear explosion for every state in any location (atmospheric, underwater, underground). It is therefore the next level of the previously signed Partial Test Ban Treaty (PTBT) to stop atmospheric explosions. To the date of this thesis it is not in force due to eight missing signatures and ratification into national law.[46,47]
Once completed, CTBTO will have a monitoring network - International Monitoring System (IMS) - with different methods for controlling compliance. These are distributed all over the world and have different tasks listed in Table 1.3.

Table 1.3: Monitoring Stations of the IMS. Data from CTBTO and Avenhaus *et al.*[40,46]

Method	Surveillance	Number of stations
Seismic:	Underground explosion	50 primary + 120 auxiliary
Hydroacoustic:	Underwater explosion	11
Infrasound:	Atmospheric explosion	60
Radionuclide:	Airborne radionuclides	80 + 16 laboratories
Total:		337

Although the treaty is not yet in force, many stations are already in operation and have detected the latest nuclear weapon tests of the Democratic People's Republic of Korea.[46]

1.3.2 Nuclear Weapons Testing

1.3.2.1 Development of Nuclear Warheads

The main research for the development of nuclear weapons and the chemistry of U and Pu was done in the United States "Manhattan Project" that started in 1942. Nuclear research and production facilities were constructed in several locations. The three main pillars were the Pu production in today's "Hanford Site"(Washington State), the U enrichment in "Oak Ridge" (Tennessee), and the research laboratory in "Los Alamos" (New Mexico).[45] On the 16th July 1945, the first human-made nuclear weapon was tested at the "Trinity Test Site" in the United States.[21,45,48]
Three different types of nuclear weapon assembly methods are shown in Figure 1.9. The main objective is to reach criticality of the fissile material that is initially present in a sub-critical state. At the critical point, there are enough free neutrons to maintain the fission chain reaction and to increase it exponentially. The uncontrolled fission release a huge amount of energy and will result in a giant nuclear explosion. Inside the gun-type assembly, the enriched ^{235}U becomes critical by combining two sub-critical masses by firing a conventional chemical explosive. This technique was originally used in the bombing of Hiroshima, Japan, on 6th August 1945 (*Little Boy*, 65 kg ^{235}U, 13 kt TNT eq.).[21,49] Implosion-type assembly weapons have explosive lenses

to compress a hollow sphere of Pu to make it critical. A prominent example of this is the bomb that destroyed Nagasaki, Japan, on 8th August 1945 (*Fat Man*, 6 kg ^{239}Pu, 21 kt TNT eq.).[21,49] A nuclear weapon with much more destructive potential is the thermonuclear bomb. This has a primary fission bomb inside, similar to the implosion type. The initial explosion will generate heat and x-rays to ignite the secondary fusion of deuterium and tritium. The fusion will release additional fast neutrons, which are energetically high enough to now fission the ^{238}U temper.

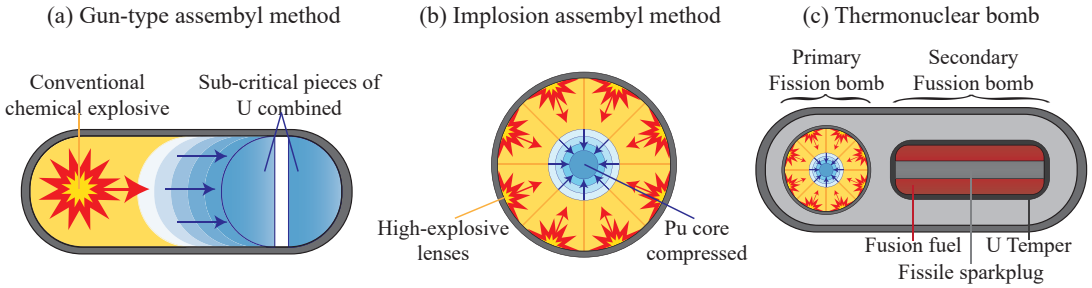

Figure 1.9: Three different types of nuclear warheads, including gun-type method (a), implosion type method (b), and thermonuclear (c) weapons. Adapted from CTBTO.[50]

1.3.2.2 Atmospheric Testing Phase

The main nuclear weapons testing countries were the United States, the former Soviet Union, France, the United Kingdom and China who have completed more than 2,000 tests overall. Their main testing sites are shown on the world map in Figure 1.10, though more than 60 sites are known to exist globally.

Figure 1.10: Main nuclear weapon test sites with number of performed tests. Data from CTBTO.[48]

Before the PTBT was signed by the United States and Soviet Union in 1963, most tests were done atmospherically (~25 % of total)[51] and released large amounts of radionuclides into the air. Airborne radionuclides were distributed worldwide as a result. This includes the fuel-components (U, Pu),[52–55] fission products (e.g. ^{89}Sr, ^{106}Ru, ^{137}Cs, ^{141}Ce),[20,56,57] as well as

material parts from the warhead itself. Afterwards, the testing with even more warheads continued in underground testing. Since 1996, nearly all states stopped testing nuclear warheads, excluding the underground testing of the Democratic People's Republic of Korea.

1.3.3 The Chernobyl Nuclear Accident in 1986

1.3.3.1 History and Accident Circumstances

On 26th April 1986 the worst nuclear accident in history occurred at the Chernobyl Nuclear Power Plant (ChNPP) in the former Ukrainian Soviet Socialist Republic. In this accident, a RBMK-1000 reactor, namely unit 4, was completely destroyed and opened to the environment. It was rated at 7 on the INES.[43] The accident considered to be the result of a failed experiment to simulate an independent power supply in an event of the loss of any external power source.[58,59] On the 25th of April 1986, the power of the reactor should have been lowered to 25 % (equal to 700-1,000 MW) of its maximum level. However, due to electric power requirements, the test was postponed to the night. At 23:10 the preparations for the test were re-started. After midnight on 26th April, energy suddenly decreased to just 30 MW. After some adjustments, mainly removing more control rods than permissible, the reactor power was more or less stable at 200 MW. In addition, variation of the cooling water flow at this time caused a different temperature distribution in the reactor. A disadvantageous low power output increased the poisoning of the reactor with the highly neutron capturing ^{135}Xe. In this state, the reactor was completely unstable and should have been shut down. Safety features had been disabled as they interfered with the parameters of the test. At 01:23 the experiments started. Just 30 s later, the power of the reactor increased rapidly, after the complete burn-up of the neutron capturing ^{135}Xe. As a consequence, more control rods were re-inserted to achieve a shutdown of the reactor. At this point, the big disadvantage of the RBMK played a major role in the accident. Due to the instability and different temperature distribution in the reactor, the water started to boil locally. This formed steam bubbles which reduced neutron absorption, and hence more neutrons remained for the fission (positive void coefficient). A similar effect was achieved by the graphite tips of the control rods which replaced liquid water when they were re-inserted into the reactor. Finally, the reactor reached prompt criticality, which resulted in a thermal destruction of the containment, leaving the reactor core exposed to the environment. Additionally, the graphite moderator started to burn and could not be extinguished for 10 days.[58–60]

1.3.3.2 Contamination and Long-Term Consequences

In total around 5,300 PBq (10^{15} Bq, excluding noble gases) of activity was released during the 10 days that the graphite was burning.[61] The open reactor core and the graphite fire did not just release short-lived volatile or intermediate volatile radionuclides (e.g. ^{106}Ru, ^{131}I, ^{132}Te, ^{133}Xe,

^{134}Cs ,^{137}Cs), but also smaller amounts of refractory long-lived radionuclides (e.g. ^{95}Zr, ^{141}Ce) as well as various isotopes of U, Np, Pu, Am, and Cm.[61–63] Workers at the plant, firefighters, and emergency workers around the plant received high dose rates and more than 100 people died due to acute radiation exposure.[58] Additionally, there was no official warning from the government, but in the following days many people were evacuated from the area. Nearly every country in Europe was affected by the accident and its contamination. Monitoring systems for the environment and food chain were established to achieve the best protection for the citizens of each state.[57] A contamination map with ^{137}Cs due to relevance and easy measurement is shown for Europe in Figure 1.11. The highest levels of contamination occurred in Ukraine, Belarus and Russia, but were measurable in each European country.

Figure 1.11: Surface contamination in kBq/m^2 for ^{137}Cs of Europe due to the Chernobyl accident in 1986. Adapted from UNSCEAR.[63]

1.3.4 The Fukushima Nuclear Accident in 2011

1.3.4.1 Causes of the Accident Series

The second INES case of 7 was the nuclear accident of Fukushima Daiichi in 2011.[44] The chain of accidents started with the Great East Japan Earthquake on 11$^{\text{th}}$ March 2011 with a high value of 9 on the magnitude scale. This initial natural disaster formed a huge tsunami near the Japanese coast with waves of more than 10 m in height. Thousands of people died or were injured, as entire towns were destroyed in the wake of these natural disasters. Infamously, to add to these disasters, the Fukushima Daiichi Nuclear Power Plant (FDNPP) operated by Tokyo Electric Power Company (TEPCO) lost the internal and external electrical power supply for the cooling and safety systems.[61,64]

The Japanese reactors were all shut down after registration of the occurring earthquake. Be-

cause of the still present decay heat inside the reactors, they had to be continuously cooled with water. Unfortunately, the natural disasters caused massive destruction of the infrastructure of north-eastern Japan, including the facilities of the FDNPP. In case of an emergency, every Nuclear Power Plant (NPP) has several diesel generators for an independent, internal power supply. However, they were damaged by the tsunami wave with run-up heights of 14-15 m and ceased operation.[64] The increasing temperature and pressure finally led to a hydrogen producing reaction between water and the cladding of the fuel. To avoid excessively high pressurization, the reactor pressure vessels were vented. Following the release of hydrogen into the service areas of the reactors, the hydrogen exploded inside the reactor buildings. This happened in Units 1 (12$^{\text{th}}$ March), 3 (14$^{\text{th}}$ March) and 4 (15$^{\text{th}}$ March). Unit 2 suffered an explosion inside its condensation chamber.[12,61]

1.3.4.2 Environmental Releases and Impact

The release of radionuclides from the FDNPP occurred from the venting operations, hydrogen explosions, and leakage of contaminated water. The releases were mostly limited to gaseous and volatile radionuclides. The total estimated activity of 520 PBq is largely based on ^{132}Te, ^{131}I, ^{133}I, ^{134}Cs, ^{137}Cs (excluding noble gases). The radionuclides ^{90}Sr and actinides such as U, Pu, and Am were only released in small amounts, especially for higher distances.[61]
The venting of the reactor pressure vessels was attempted whilst western winds prevailed to minimize an onshore contamination.[64] Evacuation zones were established in various parts of the affected areas around the NPP and districts in the Fukushima prefecture. A monitoring overview of the air dose rate in 2011 is shown in Figure 1.12.[65]

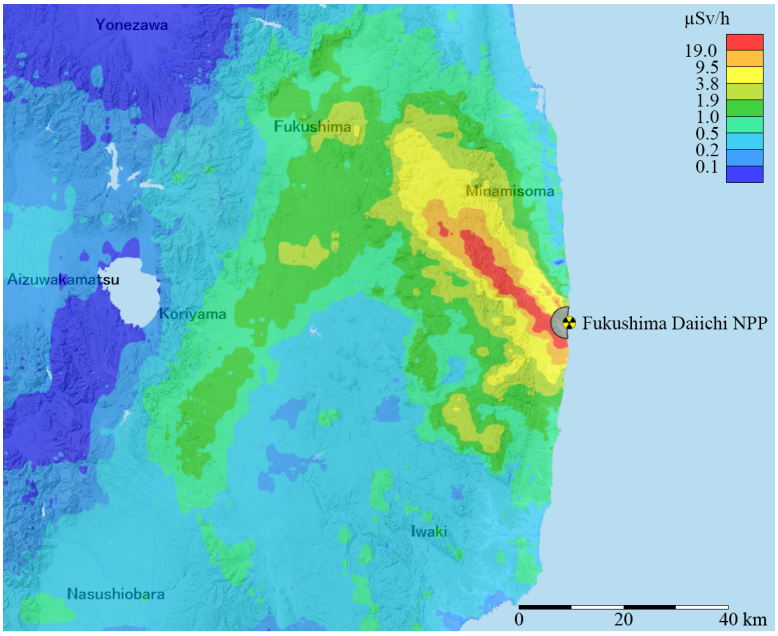

Figure 1.12: Air dose rate 1 m above ground level in µSv/h in 2011 in Fukushima and neighboring prefectures. Adapted from Extension Site of Distribution Map of Radiation Dose, etc.[65]

1.4 Examples of Environmental Nuclear Forensics

1.4.1 Undeclared Ruthenium Release in 2017

An overview of relevant stable and radioactive ruthenium isotopes is shown in Figure 1.13. The relevant mother nuclides of technetium and molybdenum for the forming of ruthenium isotopes in nuclear fission are also added in the figure.

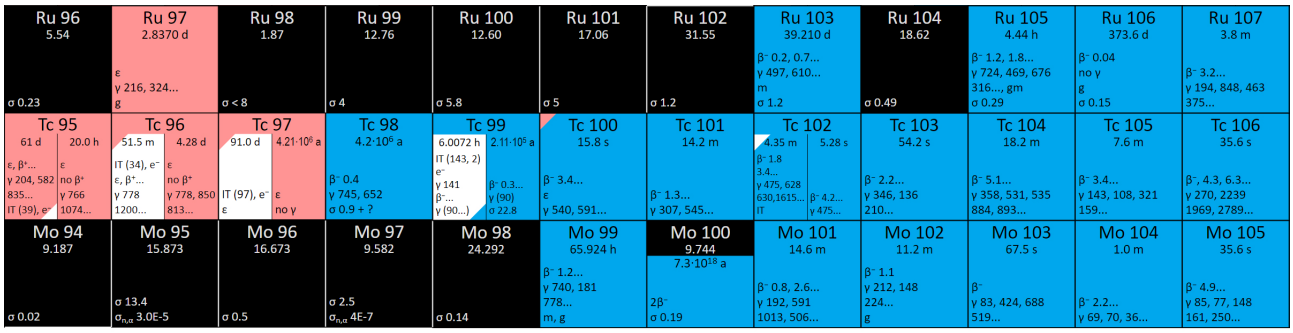

Figure 1.13: Section of the Karlsruhe Nuclide Chart for stable and radioactive ruthenium (^{96}Ru - ^{107}Ru), technetium (^{95}Tc - ^{106}Tc), and molybdenum (^{94}Mo - ^{105}Mo) isotopes. Adapted from Nucleonica.[24]

In early October 2017, an Italian laboratory first registered the unusual airborne activity of ^{106}Ru ($T_{1/2}$ = 373.6 days) on air filters collecting air from September 29th to October 2nd. The measured activity concentration was in the range of some lower mBq/m^3. Following this, new reports were subsequently added by laboratories in the Czech Republic, Austria, and Norway. Finally, almost every European country except the western-most countries reported ^{106}Ru in their air filters.[13] Some countries could also quantify much lower ^{103}Ru ($T_{1/2}$ = 39.21 days) activity concentrations in the air.

On October 7th, the IAEA requested data from all 43 Eurasian states and asked for the origin of release. Preliminary atmospheric transport models suggested a location of the release in the Southern Urals. However, the Russian Federation denied any release on their territory. November 21st, Russian Federal Service for Hydrometeorology and Environmental Monitoring (Roshydromet) announced to have measured high ^{106}Ru values in Southern Ural, while the reprocessing plant "Production Association Mayak", which is located there, denied any connection to these findings.[66] A press conference of the IAEA on November 23rd declared the completion of data collecting, but the responsibility was not assumed by any state.[67]

Based on monitoring results from the "Ring of Five" network, the airborne 2017 release of ^{106}Ru was surveilled across Europe. Huge data sets of activity concentrations and depositions over Europe were published in Masson and Steinhauser *et. al*[13] (Publication I, Chapter 3). In addition, arising hypotheses about the origin were examined. Most common hypothesis was the re-entry of a ^{106}Ru containing radioisotope thermoelectric generator satellite as origin. This has subsequently been proven to be incorrect, based on declarations of space agencies and different

attitude monitoring twin-stations. A re-entering satellite would cause a vertical distribution of the activity concentrations, which was not observed by four independent stations. It was further proposed to be of medical origin, since ^{106}Ru has some medicinal applications. But the total estimated released activity of 250 TBq would need improbable combination of several ophthalmic sources.

Thanks to modern meteorological techniques, the preliminary atmospheric models as well as more advanced ones in Saunier *et. al*[68] located the release within the Southern Urals. An additional linkage between already named facility in Mayak and the release may be a high-activity ^{144}Ce source order of the Italian Gran Sasso National Laboratory (GSNL). The requirements for the ordered radiocerium source is usually not achievable with the routine reprocessing protocol of spent nuclear fuel due to the required geometric and activity conditions. A process change such as decreasing the cool-down time of spent nuclear fuel to less than three years, would be enough to fulfill the requirements. A shortened cool-down time to produce this ^{144}Ce source may be observed in the measured ^{103}Ru/^{106}Ru ratio. The ratio was unexpectedly high in comparison to the short half-lived ^{103}Ru. This indicates a cool-down time of less than two years according to analysis of spent nuclear fuel after irradiation in a nuclear reactor. The needed shortened cool-down time for the ^{144}Ce therefore may agree with the estimated time from the measured high ruthenium ratio. A following unsubstantiated cancellation of the order shortly after this release was announced from Mayak.[69,70]

A very high purity of the released ^{106}Ru suggested again a nuclear reprocessing facility as origin. Chemical speciation may offer clues, as was investigated in Cooke *et al.*[71] (Publication II, Chapter 4). The speciation was done by specific polypyridyl chemistry and dissolution experiments. A different behavior of the ^{106}Ru on air filters in case of different chemical species was observed. Namely, a mixture of a small percentage of reacting $RuCl_3$ and inert RuO_2 is present. Both give an indication of a possible chemical trapping of volatile and very reactive RuO_4 out of the nuclear fuel reprocessing in liquid HCl.

The absence of radionuclides other than ^{106}Ru, and in some cases ^{103}Ru, are also very unlikely for releases. Therefore, stable element analyses were done by INAA to find some anomalies in the environmental composition of elements. The neutron activation of the filters in Zok *et al.*[72] (Publication III, Chapter 5) showed no significant evidence for unusual elements or concentrations compared to continental crust element distribution. The purity of radioactivity and natural stable element composition was unique and specific in this release.

The ruthenium purity was further investigated in Hopp and Zok *et al.*[73] (Publication IV, Chapter 6). Performing precise measurements of stable Ru isotope ratios was possible by chemical separations and subsequent MC-ICP-MS analysis. Various ratios showed a giant shift from the natural occurring Ru abundances in the range of several percentages, which could not be generated by natural phenomena. Mixing graphs of the Ru isotopes allowed a determination of 80 % reactor-based Ru on the air filter. Most notably, the different isotope ratios fit to the reprocessed fuel of the civilian VVER reactor type and not to the plutonium production.

On January 22nd 2018, a meeting of the Nuclear Safety Institute of the Russian Academy of Sciences was held with an invitation to protection experts from Germany, France, Finland, Sweden, the United Kingdom, and Russia itself.[74] Later, on April 11th 2018 a second meeting was organized. Some results of the meetings were communicated, but the main question about the origin and background of the ^{106}Ru release could not be completely answered.[75,76]
This is still the official position of Rosatom until today.[77]

1.4.2 Application of Radiocesium Isotope Ratios

Stable cesium is a rare monoisotopic element (^{133}Cs), that occurs only in the +I oxidation state.[78] There are three important radioisotopes of cesium in the field of radioecology. Namely, the short-lived activation product ^{134}Cs ($T_{1/2}$ = 2.07 a) and the two long-lived fission products ^{135}Cs ($T_{1/2} = 2.3 \cdot 10^6$ a) and ^{137}Cs ($T_{1/2}$ = 30.04 a).[24]

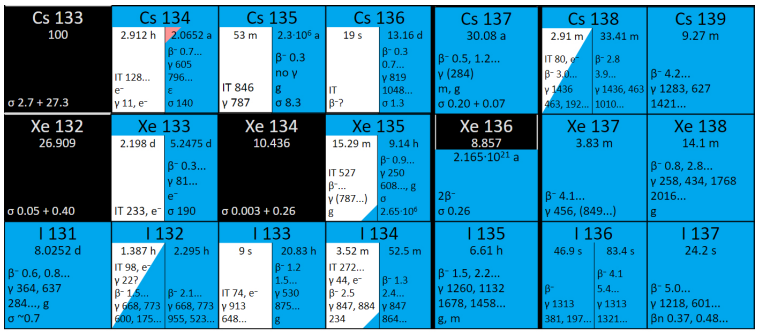

Figure 1.14: Section of the Karlsruhe Nuclide Chart for stable and radioactive cesium (^{133}Cs - ^{139}Cs), xenon (^{132}Xe - ^{138}Xe), and iodine (^{131}I - ^{137}I) isotopes. Adapted from Nucleonica.[24]

Widespread environmental contaminations with radioactive cesium isotopes were caused by the release of atmospheric weapons testing (545-765 PBq ^{137}Cs), major nuclear accidents (59-122.5 PBq ^{137}Cs) and, nuclear reprocessing sites (42.3 PBq ^{137}Cs).[17] The high yield of the 137 isobar in nuclear fission and the straight forward measurability of ^{137}Cs by gamma-spectrometry make it a radionuclide of interest for human or environmental considerations after releases (e.g. Figure 1.11). Additionally, ^{134}Cs can be quantified simultaneously by gamma-spectrometry and used for a ^{134}Cs/^{137}Cs ratio determination. Not as much forensic insight can be gained due to similar production mechanism of both isotopes inside reactor fuel and the short half-life of the ^{134}Cs. By increasing the burn-up time, the production of ^{137}Cs will increase as well as the activation of stable ^{133}Cs to ^{134}Cs. A more robust ratio is the ^{135}Cs/^{137}Cs ratio as forensic fingerprint to identify a source, due to different production mechanisms. The ^{135}Cs production is dependent on the prevailing neutron flux density, because of the immense neutron capture cross section of $2 \cdot 10^6$ b of its mother nuclide ^{135}Xe ($T_{1/2}$= 9.14 h). A high

neutron flux density will result in a neutron capture to the ^{136}Xe nuclide, while a low neutron flux densities will result in a radioactive decay to ^{135}Cs.
The measurement of the pure beta-emitter ^{135}Cs without any gamma emission is challenging. Radiometric techniques are not satisfactory to determinate this activity. Alternatives are modern mass spectrometry, such as TIMS, AMS, or ICP-QQQ-MS, which was also primary used in this thesis.[79] Critical in mass spectrometric measurement of ^{135}Cs and ^{137}Cs are the isobaric interferences of the more abundant stable barium isotopes ^{135}Ba and ^{137}Ba. Prior to measurement, barium has to be removed chemically, while the ICP-QQQ-MS also provides a reaction cell to additionally decrease the barium content by reaction with nitrous oxide. Additionally, polyatomic interferences of antimony, tin, xenon, and barium may interfere. An overview of possible interferences is shown in Table 1.4.

Table 1.4: Possible interference for the mass spectrometric measurement of ^{135}Cs/^{137}Cs ratio. Data from Bu *et al.*[80]

Interference	^{135}Cs Isobar	^{137}Cs Isobar
Isobaric:	$^{135}Ba^{+}$	$^{137}Ba^{+}$
Polyatomic:	$^{134}Ba^{1}H^{+}$	$^{136}Ba^{1}H^{+}$
	$^{134}Xe^{1}H^{+}$	$^{136}Xe^{1}H^{+}$
	$^{119}Sn^{16}O^{+}$	$^{121}Sb^{16}O^{+}$
	$^{95}Mo^{40}Ar^{+}$	$^{97}Mo^{40}Ar^{+}$

Nevertheless, ratios of ^{135}Cs/^{137}Cs are useful to establish a unique fingerprint and can be used in the identification of the source of contamination. For comparing the results, an accepted and available reference material is needed. Currently, the IAEA reference materials from Chernobyl are quite suitable for this purpose. Unfortunately, the IAEA-375 soil material is no longer in stock, but widely used.[14,81–85] Newer publications rely on the Chernobyl contaminated IAEA-330 Spinach and IAEA-372 Grass for comparison with previous references.[16,84] However, the ratio for ^{135}Cs/^{137}Cs in these materials is not certified. Also, no reference data has been established as a standard for decay correction. In most cases, the Chernobyl accident (1986) or the Fukushima accident (2011) are used as reference dates. An example of the values is given in Table 1.5

Table 1.5: ^{135}Cs/^{137}Cs ratio values for 1986, 2011 and 2020.

Location	^{135}Cs/^{137}Cs	Year	^{135}Cs/^{137}Cs	Year	^{135}Cs/^{137}Cs	Year
Fukushima[82]			0.33 - 0.34	2011	0.41 - 0.42	2020
Chernobyl[81]	0.28 - 0.32	1986	0.50 - 0.57	2011	0.61 - 0.70	2020
Global fallout[86,87]	1.29 - 1.88	1986	2.30 - 3.35	2011	2.83 - 4.12	2020
IAEA-375[14,81–85]	0.28 - 0.31	1986	0.48 - 0.55	2011	0.62 - 0.68	2020
IAEA-330[16,83,88–90]	0.28 - 0.30	1986	0.50 - 0.58	2011	0.61 - 0.70	2020
IAEA-372[16]	0.30	1986	0.57	2011	0.64	2020

More comparable data for the $^{135}Cs/^{137}Cs$ ratio was published in Zok *et al.*[79] (Publication V, Chapter 7). More data was generated for the internationally used IAEA reference materials for the isotope ratios as well as internal control samples for the method evaluation. Characteristic Chernobyl (0.5) and Fukushima (0.35) ratios were reproducible by usage of biological samples from both accident sites, including fish and moss. Also, a global fallout signature could be measured by the usage of historical, ashed lung samples from the early 1960s from Vienna with 1.9 (all decay corrected to 11th March 2011). An anomaly from the common, nuclear weapon signature for the $^{135}Cs/^{137}Cs$ was observed in trinitite minerals with lower than 0.4 on 11th March 2011. The different half-lives and conditions during as well as shortly after explosion led to a high, previously unknown fractionation between both isotopes.

Chapter 2

Analytical Techniques and Methods

2.1 Radiometric Methods

2.1.1 Gamma Spectrometry

Compared with alpha and beta radiation, gamma rays are more straight forward to measure and quantify with semiconductor detectors. Three main interactions of gamma photons with matter are useful to explain this technique: photoelectric effect, Compton effect, and pair production (Figure 2.1). Gamma rays from radioactive decays have various discrete energies due to the energetic scheme of excitation potentials. The gamma ray may transfer its entire energy by interacting with one electron. Due to the high energetic increase the inner electron is removed from the atom and outer electrons will drop down into lower energy levels by the emission of discrete fluorescence photons (x-rays) in case of the photoelectric effect (2.1a). A partial angle-depending energy transfer on an electron is called the Compton effect (2.1b). The maximum energy is hereby transferred to the electron of the atom with an angle of 180°. Gamma rays with energies higher than 1.022 MeV may undergo an interaction with the nuclei field by producing an electron and positron (2.1c). The positron will annihilate quickly with electrons, forming two annihilation photons with an energy of 511 keV each. The probabilities for these three interactions are energy dependent. The photoelectric effect predominantly occurs for low energies up to 1 MeV, after which the Compton effect becomes dominant. With energies higher than 3 MeV, pair production is the most important.[20,22]

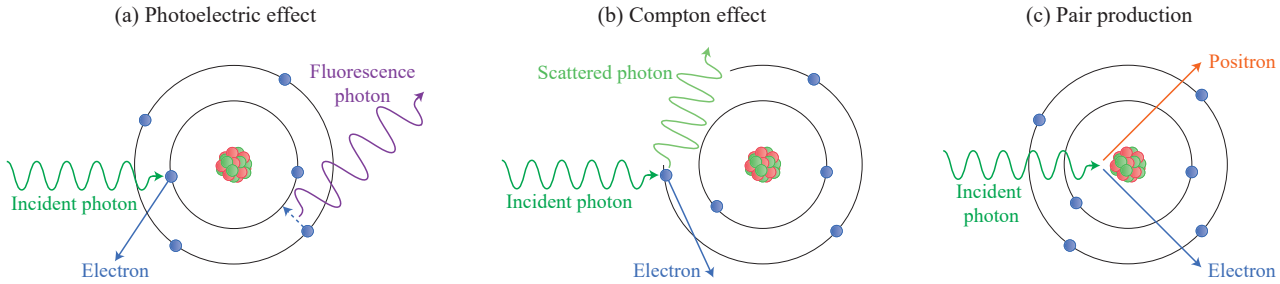

Figure 2.1: Interaction of gamma-rays with matter. Adapted from *Grundzüge des praktischen Strahlenschutzes*.[22]

The interaction of gamma rays with matter is therefore strongly dependent on the energies as well as on the material (average atomic number). For the present work the detection was performed by semiconducting High-Purity Germanium (HPGe) detectors. Despite the high purity, the Ge crystal is not perfect and contains foreign atoms (1 foreign atom per 10^{10} Ge atoms). Crystallographic defects of the crystal lead to a dark current increasing background and decreasing sensitivity of the measurement. Therefore, the crystals are usually cooled down with liquid nitrogen (77 K) to minimize the thermal effect.
Some parts of the crystal are specially doped with foreign atoms, resulting in n-, and p-conducting zones. By placing electron-donating atoms such as P or As into a Ge crystal, a n-conducting zone is generated. They can now contribute an electron to the crystal. In case

of p-conducting zones, elements with lower valencies are used, e.g. B or Ga, which can accept electrons. The combination of both p-, and n-conducting zones will create a p-n-diode (Figure 2.2). Applying a voltage at the p-n-diode will lead to a separation of the acceptor holes at the n-conducting zone (p-zone) and of the donor electrons at the p-conducting (n zone) in case of reverse biasing. Between both areas, a depletion zone is formed, which is nearly free from donor and acceptor components.
Ionizing photon radiation such as gamma rays interacts with this depletion zone of semiconductors. From these interactions a large amount of free charge carrier (holes and electrons) are formed depending on the energy of radiation. In this moment, the crystal will become conductive, because electrons are lifted from the valence band to an energetically higher conductive band. The resulting pulse-height signals are sorted by a multichannel analyzer into different channels. After a calibration with known radionuclides and energies, each of these channels has an assigned energy level, and therefore gamma ray energies and the pulse peak areas are correlated. The measured area can be used to calculate the efficiency of the detector crystal at a given energy. This describes the ratio between actually emitted gamma rays with a defined emission probability by the reference and the ones detected by the detector. It strongly depends on energy, sample geometry and density. Energies not covered by the reference were fitted with the Jäckel-Westmeier function.[91] This ensures that at least the activity of the radionuclide can be calculated by net counting rate (background corrected) divided by the gamma emission probability and previously calculated efficiency.[18,22]

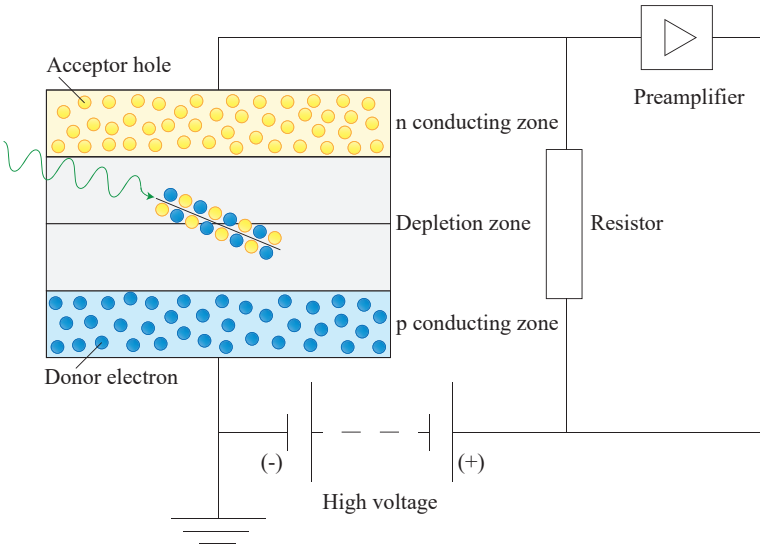

Figure 2.2: Function of a semiconductor detector with p-n junction. Adapted from *Grundzüge des praktischen Strahlenschutzes*.[22]

Due to the already named three main interactions of gamma-rays with matter, some additional peaks can be found in gamma spectra. If one or both annihilation photons of the pair production process leave the detector volume, the photo peak or full energy peak will be decreased by

511 and 1022 eV, respectively. These are referred to single-escape and double-escape peaks. Some gamma rays are also back-scattered into the germanium crystal, which results in a back-scattering peak with less energy due to external losses. Two simultaneously detected rays will be considered as one. This will lead to a sum peak at the sum of both independent photon energies. Because of the voltage, all generated electrons and holes will be separated to the p- and n-zone, respectively. The crystal will again become non-conductive, awaiting the next ray to be detected.

The biggest advantage of HPGe is the high resolution of the measured peaks. This is because of the low energy required for the ionization of Ge (3 eV). By interaction with the Ge, many more electrons per gamma-ray can be released and the signal intensity increases. Measurable ray energies in this technique usually range from some keV up to several MeV, however with different detector response. Depending on the energy type, the material through which the energy enters the semiconductor may need to be adapted. Beryllium is suitable for low energy rays, while aluminum windows shield low energy gamma- and x-rays. A crystal then has a volume of approx. 450 cm^3 with doped zones of µm up to the lower mm range.[18,22]

2.1.2 Instrumental Neutron Activation Analysis

The basic principle of Instrumental Neutron Activation Analysis (INAA) is the production of (short-lived), gamma-emitting radionuclides by nuclear reactions in the course of neutron capture. Such nuclear reactions may be a (n,γ) reaction, in which a thermal neutron is captured by the target (Figure 2.3). The various reaction paths such as (n,p), (n,α), etc. are possible and dependent on the target nucleus. The formed compound nucleus of the mostly dominating (n,γ) reaction will release energy by emission of prompt gamma-rays and particles to lose energy. The remaining radioactive nucleus will continue to decay by (several) slower beta- and gamma-decays. These characteristic emission energies of the radioactive nucleus are measured to identify elements, or even quantify them with gamma-spectrometry.

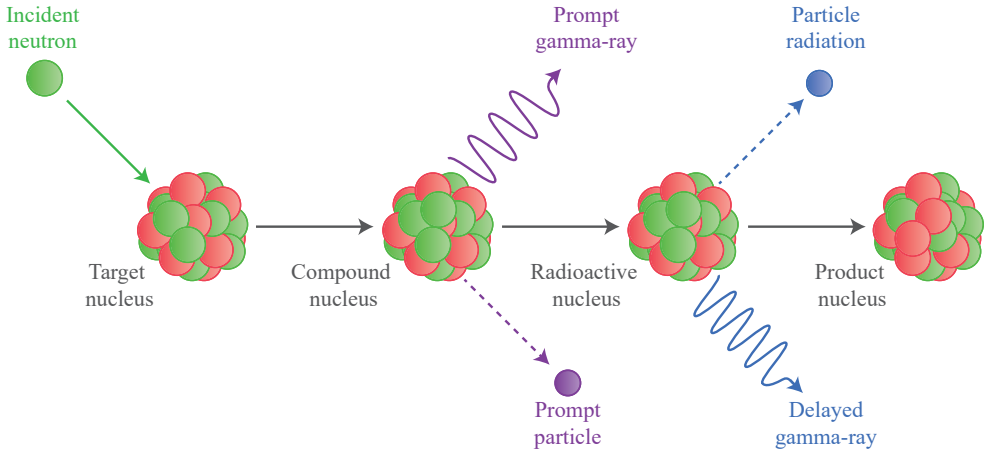

Figure 2.3: Schematic activation process and decay of a nucleus in the Instrumental Neutron Activation Analysis (INAA). Adapted from *Encyclopedia of Global Archaeology*.[92]

The activity A_s of the radionuclide at the end of the irradiation is described by equation (2.1). A required reactor operating parameter is the neutron flux density Φ in $cm^{-2}s^{-1}$ and the irradiation duration inside the neutron flux of the reactor t_{irr}. Values for the cross section σ in cm^2 for the neutron capture, Avogadro constant N_A, atomic element mass M in u, and relative isotope abundance H can be taken from the literature. For each radioactive produced nucleus the decay constant λ, with $\lambda = \ln(2)/T_{1/2}$, have to be taken into account.
A simplification can be achieved by using σ_b values form the Karlsruhe Nuclide Chart in the unit of barn (1 b = 10^{-24} cm^2) and $N_A = 6.022 \cdot 10^{23}$ atoms.[18]

$$A_s = \sigma \cdot \Phi \cdot \frac{N_A}{M} \cdot H \cdot \left(1 - e^{-\lambda \cdot t_{irr}}\right) \quad \Rightarrow \quad A_s = 0.602 \cdot \sigma_b \cdot \Phi \cdot \frac{H}{M} \cdot \left(1 - e^{-\lambda \cdot t_{irr}}\right) \tag{2.1}$$

Efficiency of activation is not identical for all elements and isotopes, whereby different amounts can be quantified. The most relevant, customizable parameter is the irradiation time $t_{irr.}$, which can be between seconds and even some weeks. This results in detectable mass ratios of up to sub picogram levels (10^{-14} g) of analyte per gram sample. With INAA more than 30 elements can be easily and matrix-independently analyzed with one gamma measurement. Depending on the half-life of the produced radionuclide, measurement of the target can be performed directly after irradiation or after a defined time to minimize interferences from short-lived, but high-activity radionuclides.
INAA can be an absolute method or a relative one with external calibration standard. Also it is used as one major technique for the calibration and certification of reference materials, especially in trace level analysis. Long-lived radionuclides can be transformed to short-lived activation products to make them measurable.[18]

2.2 Mass Spectrometry of Inorganic Analytes

2.2.1 General Aspects

Modern mass spectrometry (MS) has various different approaches suitable for a large quantity of chemical and analytical questions. It can generate qualitative or quantitative data about atoms, elements, or even whole molecules. The fundamental principle of MS is the separation of charged ion mass ratios (m/z). Generally, a mass spectrometer is always built up of three parts: ionization source, mass analyzer, and detection system, combined with a sample introduction and a data handling system. All three main parts have to be adapted for the required usage. Main advantages of MS are the high sensitivity and resolution, while the vacuum system makes it relatively expensive.[93,94]

2.2.2 Inductively Coupled Plasma

An established ionization source for the quantification of elements or determination of isotope ratios is the Inductively Coupled Plasma (ICP). The source is generated as argon gas plasma in a torch (Figure 2.4).
An electrical spark is formed via a Tesla generator, which introduces some initial electrons into the systems. These are accelerated by the fluctuating magnetic field generated by the radio-frequency of the coil. The Ar will be ionized by the electrons and form a plasma, which is a mixture of charged (Ar^+, e^-) and neutral atoms at high temperatures (6,000 - 10,000 K). The Ar plasma is stabilized by the inductive heating. High energy is used to evaporate the sample stream from the sample introduction system, destroy the chemical bonds, atomize molecules, and ionize atoms.
After the ionization inside the plasma, the charged analytes are transferred to the high vacuum parts of the MS by passing the sampler and skimmer cone interface. Afterwards, it is focused by different ion lenses in the mass analyze.

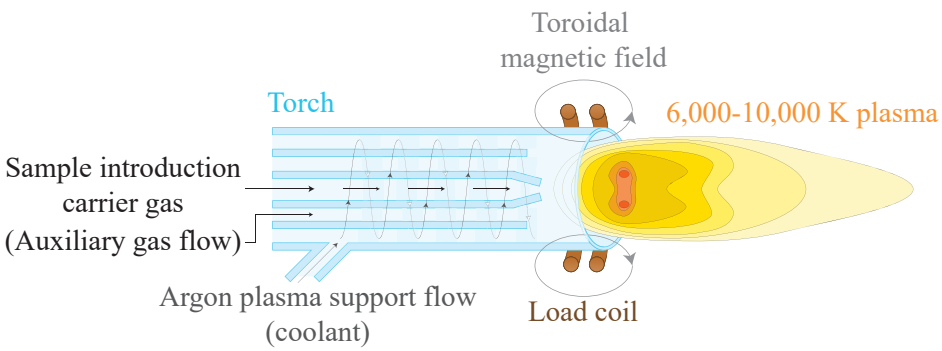

Figure 2.4: Schematic plasma torch with gas flows and temperature distribution inside the plasma. Adapted from *Massenspektrometrie - Ein Lehrbuch*.[93]

2.2.3 Mass Bias and Mass Discrimination

An Inductively Coupled Plasma Mass Spectrometry (ICP-MS) faces challenges from an isotope mass-dependent discrimination (mass bias effect) during the analysis. The effect is mostly based on the mutual repulsion of positively charged ions in the plasma and the fast expansion between the cones due to the high pressure change. This results in a preferential transmission of the heavier isotope into the MS compared to the lighter one. Generally, the mass bias is more pronounced for lighter element isotopes than for heavier ones due to the smaller relative mass difference. A matrix and time dependence of this effect can also be observed.[94,95]
In the case of isotope ratio measurements, the mass bias plays a significant role in the potential error of the measurement. However, in MS it can be corrected to gain the real isotopic composition of a sample. Internally, the sample can be spiked with two enriched isotopes of the same element with a known isotope ratio or with a foreign, similarly behaving element, with known abundances. An external measurement order such as reference-sample-reference bracketing with known isotopic signature of the reference can also be used. Usually, these references can be used for quality control and comparability with other methods.
After the data acquisition, the exponential law (2.2)[96] is used to correct the measured sample isotope ratios with the known spike or reference ratio. Additionally, the masses M of the targeted isotopes have to be taken into account and is also used for the estimation of the fractionation factor β in (2.3). The example in (2.2) is shown for the correction of ruthenium isotopes.

$$\left(\frac{^{99}\mathrm{Ru}}{^{101}\mathrm{Ru}}\right)_{\mathrm{corrected}} = \left(\frac{^{99}\mathrm{Ru}}{^{101}\mathrm{Ru}}\right)_{\mathrm{measured}} \cdot \left[\frac{M(^{99}\mathrm{Ru})}{M(^{101}\mathrm{Ru})}\right]^{\beta} \tag{2.2}$$

$$\beta = \frac{\ln\left[(^{99}\mathrm{Ru}/^{101}\mathrm{Ru})_{\mathrm{reference}}/(^{99}\mathrm{Ru}/^{101}\mathrm{Ru})_{\mathrm{measured}}\right]}{\ln\left[M(^{99}\mathrm{Ru})/M(^{101}\mathrm{Ru})\right]} \tag{2.3}$$

2.2.4 Quadrupole and Triple Quadrupole MS

Commercial MS to determinate elemental concentrations often relies on quadrupoles as mass analyzers. They are arranged as by four quadratically assembled cylindrical electrodes, in which the opposite ones have the same potential. One potential is on direct current, while the other is on alternating current and both are in a periodic switch of the poles. The incoming ion from the cone interface will be passing through the quadrupole in a spiral path. This path is caused by the changes of attraction and repulsion due to the pole switch of the electrodes. The overall stability of a path will be given by the ratio of both currents, and is not stable for each m/z (Figure 2.5). By changing the conditions of the different currents, specific m/z ratios or just one will pass the analyzer and reach the detector. Ions on unstable paths will hit an electrode, become neutralized to neutral atoms and are no longer measurable in the MS technique. However, the resolution of a quadrupole is relatively low and separation beyond nominal masses is tricky. Other elements can also have a stable, interfering isotope on the

same nominal mass. The quadrupole cannot resolve these differences, which may lead to a misassesment of concentration, if the interference is not accounted for properly. This is the biggest disadvantage of as quadrupole mass analyzer.[93,94]

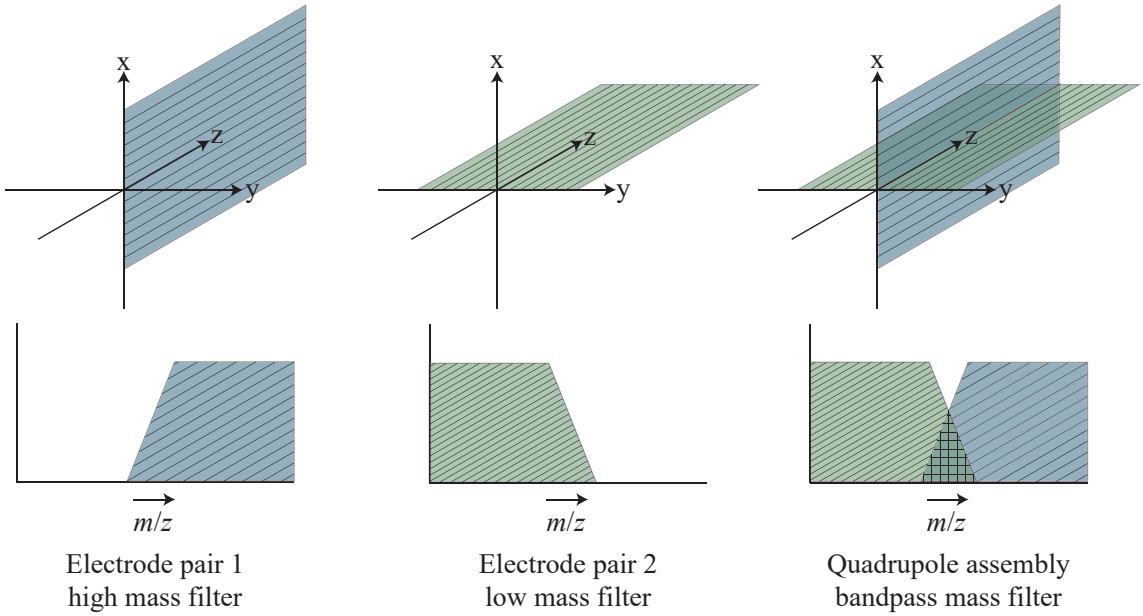

Figure 2.5: Combination of electrode pairs in a quadrupole to achieve a m/z band-pass filter. Adapted from *Isotopic Analysis: Fundamentals and Applications Using ICP-MS*.[94]

A recent development in the field of the quadrupole MS is the arrangement of three multipoles in form of a Inductively Coupled Plasma Triple Quadrupole Mass Spectrometry (ICP-QQQ-MS) (Figure 2.6). In this set-up, a first quadrupole will filter all non relevant m/z. Other ones enter the second multipole - here an octupole - which is not used as filter, but rather as reaction cell. Inside the cell, collision (He, Ar, N_2) or reaction gases (O_2, H_2, NH_3) may be introduced to induce a chemical reaction or bond breaking.[14,97–100] Based on the conditions, the interfering or the targeted isotope will be shifted to another mass, whilst the other isotope remains in its current mass. The octupole has a higher transmission for m/z ratios if the direct current is zero. This will lead the multipole to become a wide band pass filter. After the reaction cell, a second quadrupole can be operated as second analyzer for a measurement of the m/z ratios, while interferences are shifted to different masses.

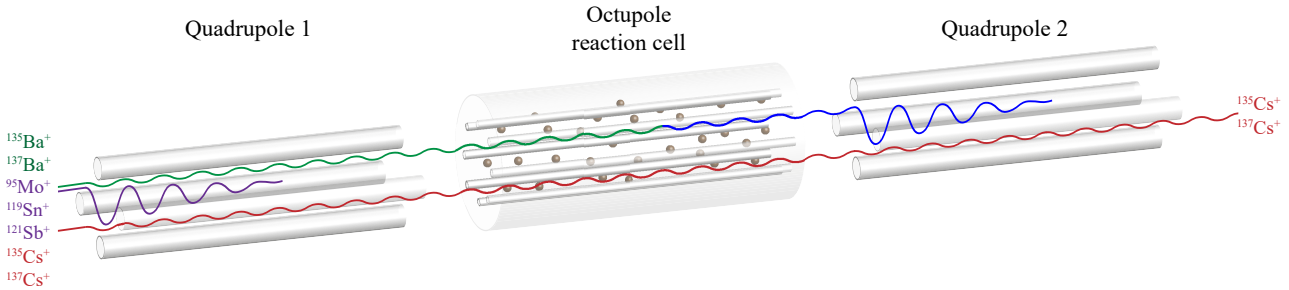

Figure 2.6: Schematic separation of barium and cesium by ICP-QQQ-MS.

A detailed example for the separation of $^{135}Cs/^{137}Cs$ from barium and other elements is given in equations (2.4) and (2.5), as well as in Figure 2.6. Interfering molybdenum, tin, and antimony will not pass the first quadrupole and therefore cannot form interferences on the interested isobars in the reaction cell (oxides, argon-cluster). In the reaction cell, more abundant Ba^+ will react with the nitrous oxide (N_2O) to form barium oxide (BaO^+) due to the negative reaction enthalpy of -236.8 kJ/mol.[101] The Cs^+ will react substantially less with the N_2O compared to than the Ba^+ because of the positive reaction enthalpy of +106.3 kJ/mol.[101] Thereby, the N_2O is the softer oxygen donor than pure oxygen gas. Upon entering the second quadrupole, the mass-shifted Ba^+ is removed from the targeted m/z ratio and does not cause interference in the measurement. The different reactivity and affinity of elements and reaction gas is a successful separation method in the ICP-QQQ-MS technique.[101]

$$^{135}Ba^+ \xrightarrow{N_2O} {}^{135}Ba^{16}O^+ \qquad ^{137}Ba^+ \xrightarrow{N_2O} {}^{137}Ba^{16}O^+ \qquad \Delta H_r = -236.8 \text{ kJ/mol} \tag{2.4}$$

$$^{135}Cs^+ \xrightarrow{N_2O} {}^{135}Cs^+ \qquad ^{137}Cs^+ \xrightarrow{N_2O} {}^{137}Cs^+ \qquad \Delta H_r = +106.3 \text{ kJ/mol} \tag{2.5}$$

2.2.5 Sector Field Mass Spectrometry

Sector field mass spectrometers are used for high-precision measurements of isotopic signatures. They consist of combined, double-focusing magnetic and electrostatic sector field analyzers, which are built in the so called Nier-Johnson geometry (Figure 2.7) for scanning of m/z ratios in the magnetic sector. Depending on the scanning speed of the m/z ratios, the resolution can be higher than 10,000.[93]

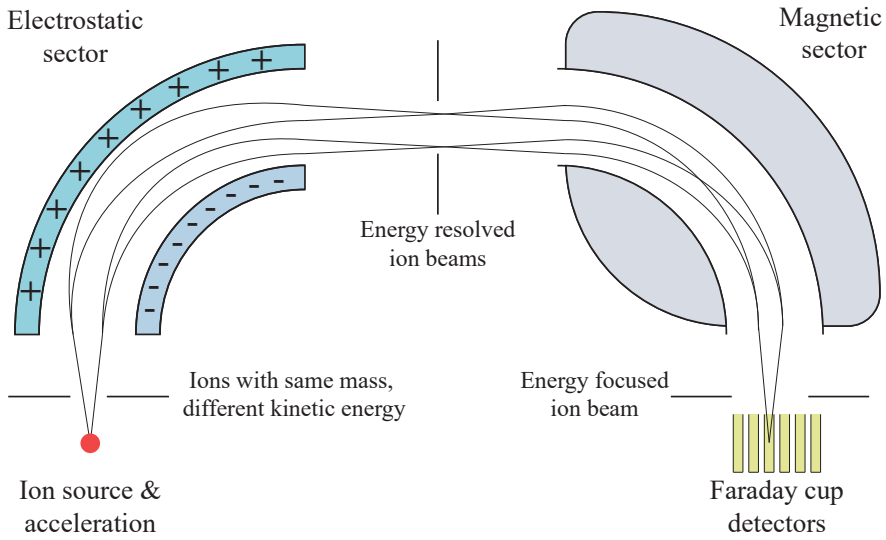

Figure 2.7: Nier-Johnson double focusing geometry of a MC-ICP-MS for ions with same mass, but different kinetic energy. Adapted from *Massenspektrometrie - Ein Lehrbuch*.[93]

The ICP ion source will produce ions with different m/z ratios and kinetic energies. E.g. one m/z ratio ion beam with different kinetic energies will enter the electrostatics analyzer field. Between the charged plates, the ion beam with different kinetic energy will be separated along various circular paths. Physically, the process is driven by the centripetal force F_{C} and each circular path can be predicted by equation (2.6).

$$F_{\mathrm{C}} = \frac{mv^2}{r_{\mathrm{e}}} = qE \qquad \Leftrightarrow \qquad r_{\mathrm{e}} = \frac{mv^2}{qE} = \frac{2E_{\mathrm{kin}}}{qE} \tag{2.6}$$

For the calculation of the radius of the path r_{e}, ion mass m, velocity v, and charge q as well as the strength of electric field E are required. Simplification can be achieved by using the kinetic energy of ions E_{kin}.[94] Therefore, an energy resolved beam will be acquired after the first sector. After passing several lenses, the beam will be introduced into the second, magnetic sector of the double-focusing system. This one is not a mass analyzer, but rather a momentum p separator. Based on the relation of momentum with mass m and velocity v ($p = mv$) the energy resolved ions are focused into a single m/z ratio beam for detection. The radius of the path r_{m} can be calculated by the physical quantity of the Lorentz force F_{L} (equation (2.7), $E = 0$). Here the velocity needs to be perpendicular to the magnetic field $v \perp B$.[94]

$$F_{\mathrm{L}} = \frac{mv^2}{r} = qvB \qquad \Leftrightarrow \qquad r_{\mathrm{m}} = \frac{mv}{qB} \tag{2.7}$$

After both focusing sectors, detection will be performed in a Faraday cup array for MC-ICP-MS. This grounded metal cup has a high electrical resistance (~10^{11} Ω). Entering ions are neutralized by electrons from the cup and induce a potential change. The difference is a measure for the final ion signal intensity.[94]

2.3 Chromatographic Methods

2.3.1 Classification

The basic principle of chromatography is the separation of one or more analytes in a mobile phase from unwanted components due to interactions with a stationary phase. In case of liquid chromatography (LC), a liquid mobile phase is used. Generally, the LC can be performed by different separation mechanisms shown in Table 2.1.
The chromatographic process can be executed easily on silica surfaces, and improved by chemical modification of the surface. In this case, organic species are bound to the surface to make it either more non-polar or specific to the requested analyte. Separation is achieved by different distribution between both phases due to different molecular interactions. A stronger interaction with the surface is found in the liquid-solid chromatography. Here, an adsorption mechanism of the analyte into the solid is used. Gel permeation chromatography performs the separation without any direct interactions. Molecules passing the resin are separated according to their size. Larger molecules pass the resin rapidly, while smaller ones are trapped inside the pores of the phase. Ionic interactions are used in the ion exchange chromatography, which uses modified ion exchanging surfaces. The mechanism may further be categorized into cationic and anionic resins.[102–104]

Table 2.1: Classification of liquid chromatographic methods. Data from *Instrumentelle Analytik*.[103]

Method	Stationary phase	Mechanism
LC with chemically modified phases	Surface bounded organic species	Distribution
Liquid-solid chromatography	Solids	Adsorption
Gel permeation chromatography	Porous solids	Size exclusion
Ion exchange chromatography	Ion exchanger	Ion exchange

2.3.2 Adsorption Chromatography of Cesium

The enrichment and separation of cesium from the matrix can be performed with the polyoxometalate derivate ammonium molybdophosphate (AMP) hydrate ($(NH_4)_3PO_4Mo_{12}O_{36} \cdot x\,H_2O$; Figure 2.8). The structural molybdate chains form twelve MoO_6 octahedrons as Keggin structure type. Inside the structure, a central tetrahedric coordinated phosphorus atom (purple) is placed. The octahedral interstitial positions are occupied by water and ammonium molecules, while these can easily and very effectively be replaced with cesium ions (2.8).[17,105]

$$[\text{AMP}]\text{-}NH_4^+ \quad + \quad Cs^+ \quad \rightleftharpoons \quad NH_4^+ \quad + \quad [\text{AMP}]\text{-}Cs^+ \tag{2.8}$$

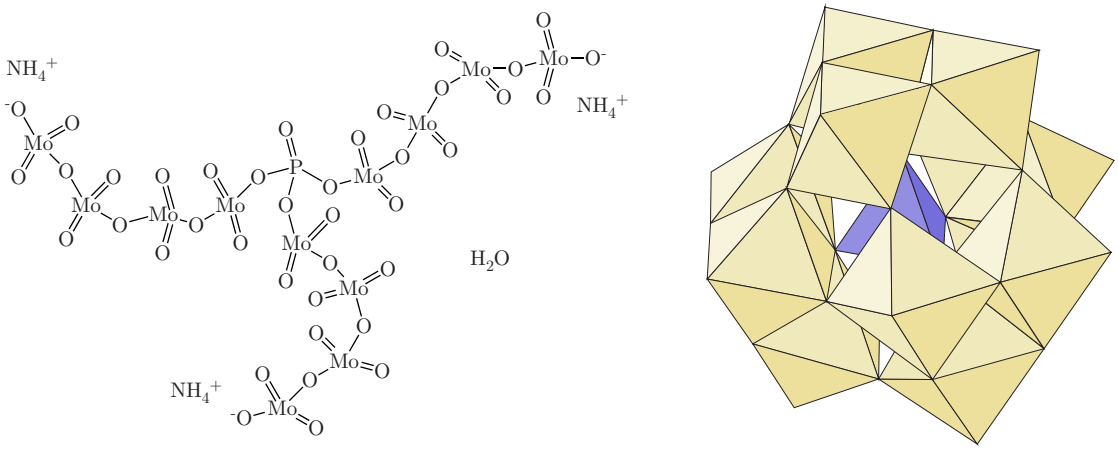

Figure 2.8: Ammonium molybophosphate hydrate $(NH_4)_3PO_4Mo_{12}O_{36} \cdot x\ H_2O$ as structural formula (left) and as Keggin crystal structure type $[PO_4Mo_{12}O_{36}]^{3-}$ (right). Adapted from *Anorganische Strukturchemie*.[105]

The AMP can be put directly into the solution, stirred for some minutes up to 1 h and filtered afterwards. Alternatively, it can be immobilized on a inert carrier for the use as a column.[17] The incorporation rate of the cesium into the lattice is very high and even more selective in acidic solutions. AMP loaded with Cs can than be directly measured by gamma spectrometry or dissolved in alkaline solutions to release Cs for further purposes such as the ion exchange chromatography.[17]

2.3.3 Ionic Exchange Chromatography

In case of the ion exchange chromatography, an inert carrier polymer [P] is functionalized chemically with charged, chemical groups. It has to be distinguished between cationic and anionic prior separations. The strength of ionic binding can be adjusted, depending on the chemical species on the surface (Table 2.2). Common exchangers for cations are carboxylic acids ($-COO^-$) or sulfonic acid ($-SO_3^-$) groups. In case of anionic separations, various alkaline amines ($-NH_xR_{3-x}^+$) are used. Corresponding ions are typically protons or sodium and hydroxides and chloride ions, respectively.[102]

Table 2.2: Overview of functional groups for the ion exchange. Data from *Instrumentelle Analytik und Bioanalytik*.[104]

Resin Type	Weak exchanger	Strong exchanger
Cationic	[P]-COO^- H^+	[P]-SO_3^- H^+
	Carboxylic acids	Sulfonic acids
Anionic	[P]-N-R_3^+ Cl^-	[P]-NH-R_2^+ Cl^-
	Quaternary amine	Secondary amine

[P] is the polymeric resin carrier

For successful separation, first, the suitable resin has to be preconditioned. The active sites for the ion exchange resin will be all the same and occupied by these conditioning ions (1 in Figure 2.9). After the conditioning, the sample solution is loaded, including the targeted analyte ions and the dissolved matrix (2). The conditioning ions are removed by the analyte and some matrix ions due to stronger affinity. The column is washed to remove unbound material from the mobile phase (3). Finally, an elution solution will remove the analyte from the active sites, release it from the column, and will be collected in the eluate (4). The process is completed when every analyte ion is removed from the column (5).

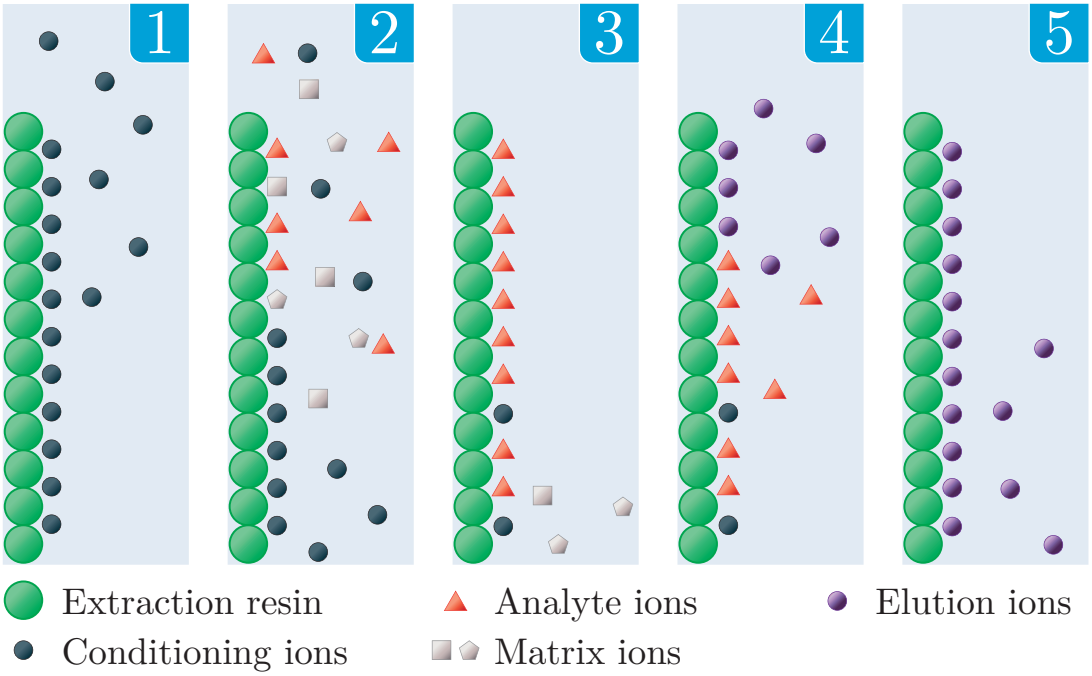

Figure 2.9: Schematic process of ion extraction by a chromatographic resin.

For the strong cationic (2.9) and anionic (2.10) exchange resin, exchange can be performed with any cation M^{x+} or anion N^{y-}, respectively. The capacity of possible ion exchange reactions, the used solutions in each step and their concentrations are important characteristics.[103]

$$x \cdot \text{[P]-SO}_3^- \ \text{H}^+ + \text{M}^{x+} \rightleftharpoons (\text{[P]-SO}_3^-)_x \ \text{M}^{x+} + x \cdot \text{H}^+ \tag{2.9}$$

$$y \cdot \text{[P]-NR}_3^+ \ \text{Cl}^- + \text{N}^{y-} \rightleftharpoons (\text{[P]-NR}_3^+)_y \ \text{N}^{y-} + y \cdot \text{Cl}^- \tag{2.10}$$

As an example, a cesium scheme after an AMP separation is shown in Figure 2.10. After the AMP dissolution, the concentration of molybdenum is high. For removal of Mo as well as Sn and Sb, an anionic exchange resin is used in the first step. Cesium will not be retained by such a resin and will just pass through, while molybdates, antimonates, and stannates will be retained.

In the subsequent cation resin, Cs and Ba will be retained on the resin. After washing the resin, Cs will be eluted by strong acids with high concentrations. This works ideally with hydrochloric acid.[14,106] After separation, the solution can be used for ICP-QQQ-MS measurements.

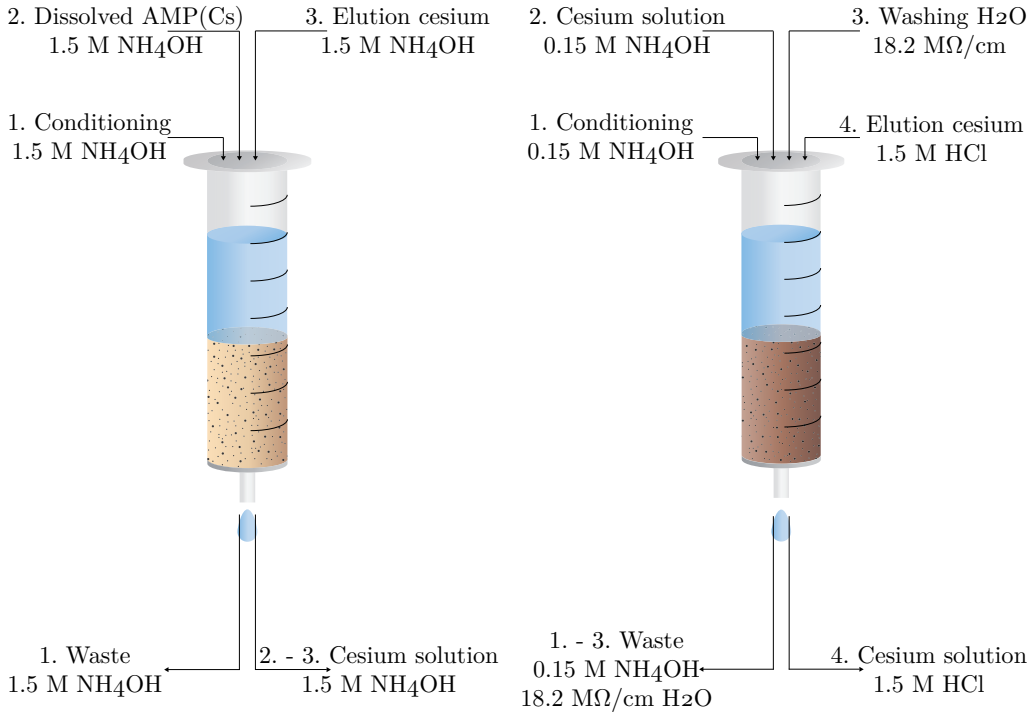

Figure 2.10: Preparation steps for the anion (left) and cation (right) exchange resin for the separation of cesium.

Chapter 3

Airborne Concentrations and Chemical Considerations of Radioactive Ruthenium from an Undeclared Major Nuclear Release in 2017

O. Masson*†, G. Steinhauser*†, D. Zok, O. Saunier, H. Angelov, D. Babić, V. Bečková, J. Bieringer, M. Bruggeman, C. I. Burbidge, S. Conil, A. Dalheimer, L.-E. De Geer, A. de Vismes Ott, K. Eleftheriadis, S. Estier, H. Fischer, M. G. Garavaglia, C. Gasco Leonarte, K. Gorzkiewicz, D. Hainz, I. Hoffman, M. Hýža, K. Isajenko, T. Karhunen, J. Kastlander, C. Katzlberger, R. Kierepko, G.-J. Knetsch, J. Kövendiné Kónyi, M. Lecomte, J. W. Mietelski, P. Min, B. Møller, S. P. Nielsen, J. Nikolic, L. Nikolovska, I Penev, B. Petrinec, P. P. Povinec, R. Querfeld, O. Raimondi, D. Ransby, W. Ringer, O. Romanenko, R. Rusconi, P. R. J. Saey, V. Samsonov, B. Šilobritienė, E. Simion, C. Söderström, M. Šoštarić, T. Steinkopff, P. Steinmann, I. Sýkora, L. Tabachnyi, D. Todorovic, E. Tomankiewicz, J. Tschiersch, R. Tsibranski, M. Tzortzis, K. Ungar, A. Vidic, A. Weller, H. Wershofen, P. Zagyvai, T. Zalewska, D. Zapata García, B. Zorko

Proceedings of the National Academy of Sciences of the United States of America, vol. 116, no. 34, pp. 16750-16759, 2019. DOI: 10.1073/pnas.1907571116

Author contributions:
O.M. and G.S. designed research
O.M., G.S., D.Z., O.S., [...] performed research
O.M., G.S., O.S., L.E.D.G., H.F., I.H., J.W.M., P.P.P., P.R.J.S., K.U., and H.W. analyzed data
O.M., G.S., and D.Z. wrote the paper

* O. Masson and G. Steinhauser contributed equally to this work
† To whom correspondence may be addressed.
Email: olivier.masson@irsn.fr or steinhauser@irs.uni-hannover.de

Airborne concentrations and chemical considerations of radioactive ruthenium from an undeclared major nuclear release in 2017

O. Masson[a,1,2], G. Steinhauser[b,1,2], D. Zok[b], O. Saunier[c], H. Angelov[d], D. Babić[e], V. Bečková[f], J. Bieringer[g], M. Bruggeman[h], C. I. Burbidge[i], S. Conil[j], A. Dalheimer[k], L.-E. De Geer[l,3], A. de Vismes Ott[m], K. Eleftheriadis[n], S. Estier[o], H. Fischer[p], M. G. Garavaglia[q], C. Gasco Leonarte[r], K. Gorzkiewicz[s], D. Hainz[t], I. Hoffman[u], M. Hýža[f], K. Isajenko[v], T. Karhunen[w], J. Kastlander[l], C. Katzlberger[x], R. Kierepko[s], G.-J. Knetsch[y], J. Kövendiné Kónyi[z], M. Lecomte[aa], J. W. Mietelski[s], P. Min[bb], B. Møller[cc], S. P. Nielsen[dd], J. Nikolic[ee], L. Nikolovska[ff], I. Penev[d], B. Petrinec[e], P. P. Povinec[gg], R. Querfeld[b], O. Raimondi[hh], D. Ransby[ii], W. Ringer[jj], O. Romanenko[kk], R. Rusconi[ll], P. R. J. Saey[t], V. Samsonov[mm], B. Šilobritienė[nn], E. Simion[oo], C. Söderström[l], M. Šoštarić[e], T. Steinkopff[k], P. Steinmann[o], I. Sýkora[gg], L. Tabachnyi[pp], D. Todorovic[ee], E. Tomankiewicz[s], J. Tschiersch[qq], R. Tsibranski[rr], M. Tzortzis[ss], K. Ungar[u], A. Vidic[tt], A. Weller[b], H. Wershofen[uu], P. Zagyvai[vv], T. Zalewska[ww], D. Zapata García[uu], and B. Zorko[xx]

[a]Direction de l'Environnement, Institut de Radioprotection et de Sûreté Nucléaire, 13115 St Paul lez Durance, France; [b]Institute of Radioecology and Radiation Protection, Leibniz Universität Hannover, 30419 Hannover, Germany; [c]Service des Situations d'Urgence et d'Organisation de Crise, Institut de Radioprotection et de Sûreté Nucléaire, 92260 Fontenay-Aux-Roses, France; [d]Basic Environmental Observatory Moussala, Institute for Nuclear Research and Nuclear Energy, BG-1784 Sofia, Bulgaria; [e]Institute for Medical Research and Occupational Health, 10001 Zagreb, Croatia; [f]Section of Monitoring, National Radiation Protection Institute, 140 00 Prague 4, Czech Republic; [g]Atmosphärische Radioaktivität und Spurenanalyse, Bundesamt für Strahlenschutz, 79098 Freiburg im Breisgau, Germany; [h]StudieCentrum voor Kernenergie-Centre d'Etude de l'Energie Nucléaire, 2400 Mol, Belgium; [i]Office of Radiation Protection and Environmental Monitoring, Environmental Protection Agency, Dublin, D14 H424, Ireland; [j]Observatoire Pérenne de l'Environnement, Agence Nationale des Déchets Radioactifs, 55290 Bure, France; [k]Deutscher Wetterdienst, 63067 Offenbach, Germany; [l]Chemical, Biological, Radiological and Nuclear Defence and Security Division, Swedish Defence Research Agency, 16490 Stockholm, Sweden; [m]Laboratoire de Mesure de la Radioactivité dans l'Environnement, Institut de Radioprotection et de Sûreté, 91400 Orsay, France; [n]Institute of Nuclear and Radiological Sciences & Technology, Energy & Safety, National Centre for Scientific Research "Demokritos", 15310 Athens, Greece; [o]Environmental Radioactivity Section, Federal Office of Public Health, CH-3097 Liebefeld, Switzerland; [p]Radioactivity Measurements Laboratory, University of Bremen, 28359 Bremen, Germany; [q]Dipartimento Prevenzione, Agenzia Regionale per la Protezione dell'Ambiente del Friuli Venezia Giulia, 33100 Udine, Italy; [r]Unidad de Radiactividad Ambiental y Vigilancia Radiológica, Centro de Investigaciones Energéticas, Medioambientales y Tecnológicas, 28040 Madrid, Spain; [s]Department of Nuclear Physical Chemistry, The Henryk Niewodniczanski Institute of Nuclear Physics, 31-342 Kraków, Poland; [t]Atominstitut, Vienna University of Technology, 1020 Vienna, Austria; [u]Health Canada, Ottawa, K1A 1C1 ON, Canada; [v]Central Laboratory for Radiological Protection, PL 03-134 Warsaw, Poland; [w]Environmental Monitoring, Radiation and Nuclear Safety Authority, FI-00881 Helsinki, Finland; [x]Department of Radiation Protection and Technical Quality Assurance, Austrian Agency for Health and Food Safety, 1220 Vienna, Austria; [y]Centre for Environmental Safety and Security, National Institute for Public Health and the Environment, NL-3720 BA Bilthoven, The Netherlands; [z]Division of Environmental and Public Radiohygiene, National Research Institute for Radiobiology and Radiohygiene, H-1221 Budapest, Hungary; [aa]Division de la Radioprotection, Ministère de la Santé, L-2120 Luxembourg, Luxembourg; [bb]National Commission for Nuclear Activities Control, District 5, 050706 Bucharest, Romania; [cc]Emergency Preparedness and Response, Norwegian Radiation and Nuclear Safety Authority, NO-9925 Svanvik, Norway; [dd]Center for Nuclear Technologies, Technical University of Denmark (DTU) Risø, DK-4000 Roskilde, Denmark; [ee]Department of Radiation and Environmental Protection, Institute for Nuclear Sciences, University of Belgrade, 11351 Belgrade, Serbia; [ff]Radiology Laboratories, Institute of Public Health, 1000 Skopje, North Macedonia; [gg]Department of Nuclear Physics and Biophysics, Comenius University, 84248 Bratislava, Slovakia; [hh]Tutela dell'Ambiente Naturale e Costruito, Dipartimento Prevenzione, 47893 Borgo Maggiore, Republic of San Marino; [ii]Computing Centre, Alfred Wegener Institute, Helmholtz Centre for Polar and Marine Research, 27570 Bremerhaven, Germany; [jj]Department of Radon and Radioecology, Austrian Agency for Health and Food Safety, 4020 Linz, Austria; [kk]Rivne Nuclear Power Plant, National Nuclear Energy Generating Company "Energoatom", 34400 Rivne Oblast, Ukraine; [ll]Centro Regionale Radioprotezione, Agenzia Regionale per la Protezione dell'Ambiente della Lombardia, 20124 Milan, Italy; [mm]Republican Center of Hydrometeorology, Radioactive Contamination Control and Environmental Monitoring, 220114 Minsk, Belarus; [nn]Environmental Protection Agency, 09311 Vilnius, Lithuania; [oo]National Reference Laboratory, National Environmental Protection Agency, 060031 Bucharest, Romania; [pp]Ukrainian Hydrometeorological Center, 01601 Kyiv, Ukraine; [qq]Institute of Radiation Medicine, Helmholtz Zentrum München, 85764 Neuherberg, Germany; [rr]Safety Department, Kozloduy Nuclear Power Plant, 3321 Kozloduy, Bulgaria; [ss]Radiation Inspection and Control Services, Department of Labour Inspection, CY-1080 Nicosia, Cyprus; [tt]Radiation Protection Center, Institute for Public Health, 71000 Sarajevo, Federation of Bosnia and Herzegovina; [uu]Environmental Radioactivity Laboratory, Physikalisch-Technische Bundesanstalt, 38116 Braunschweig, Germany; [vv]Centre for Energy Research, Hungarian Academy of Sciences, 1121 Budapest, Hungary; [ww]Institute of Meteorology and Water Management, National Research Institute, 01673 Warsaw, Poland; and [xx]Infrastructural Group for Ionizing Radiation Measurements, Institut "Jožef Stefan", 1000 Ljubljana, Slovenia

Edited by John H. Seinfeld, California Institute of Technology, Pasadena, CA, and approved June 21, 2019 (received for review May 2, 2019)

In October 2017, most European countries reported unique atmospheric detections of aerosol-bound radioruthenium (^{106}Ru). The range of concentrations varied from some tenths of μBq·m^{-3} to more than 150 mBq·m^{-3}. The widespread detection at such considerable (yet innocuous) levels suggested a considerable release. To compare activity reports of airborne ^{106}Ru with different sampling periods, concentrations were reconstructed based on the most probable plume presence duration at each location. Based on airborne concentration spreading and chemical considerations, it is possible to assume that the release occurred in the Southern Urals region (Russian Federation). The ^{106}Ru age was estimated to be about 2 years. It exhibited highly soluble and less soluble fractions in aqueous media, high radiopurity (lack of concomitant radionuclides), and volatility between 700 and 1,000 °C, thus suggesting a release at an advanced stage in the reprocessing of nuclear fuel. The amount and isotopic characteristics of the radioruthenium release may indicate a context with the production of a large ^{144}Ce source for a neutrino experiment.

Author contributions: O.M. and G.S. designed research; O.M., G.S., D.Z., O.S., H.A., D.B., V.B., J.B., M.B., C.I.B., S.C., A.D., L.-E.D.G., A.d.V.O., K.E., S.E., H.F., M.G.G., C.G.L., K.G., D.H., I.H., M.H., K.I., T.K., J.K., C.K., R.K., G.-J.K., J.K.K., M.L., J.W.M., P.M., B.M., S.P.N., J.N., L.N., I.P., B.P., P.P.P., R.Q., O. Raimondi, D.R., W.R., O. Romanenko, R.R., P.R.J.S., V.S., B.Š., E.S., C.S., M.Š., T.S., P.S., I.S., L.T., D.T., E.T., J.T., R.T., M.T., K.U., A.V., A.W., H.W., P.Z., T.Z., D.Z.G., and B.Z. performed research; O.M., G.S., O.S., L.-E.D.G., H.F., I.H., J.W.M., P.P.P., P.R.J.S., K.U., and H.W. analyzed data; O.M., G.S., and D.Z. wrote the paper; and G.S. and A.W. acquired funding.

The authors declare no conflict of interest.

This article is a PNAS Direct Submission.

[1]O.M. and G.S. contributed equally to this work.

[2]To whom correspondence may be addressed. Email: olivier.masson@irsn.fr or steinhauser@irs.uni-hannover.de.

[3]Retired.

This article contains supporting information online at www.pnas.org/lookup/suppl/doi:10.1073/pnas.1907571116/-/DCSupplemental.

Published online July 26, 2019.

Significance

A massive atmospheric release of radioactive ^{106}Ru occurred in Eurasia in 2017, which must have been caused by a sizeable, yet undeclared nuclear accident. This work presents the most compelling monitoring dataset of this release, comprising 1,100 atmospheric and 200 deposition data points from the Eurasian region. The data suggest a release from a nuclear reprocessing facility located in the Southern Urals, possibly from the Mayak nuclear complex. A release from a crashed satellite as well as a release on Romanian territory (despite high activity concentrations) can be excluded. The model age of the radioruthenium supports the hypothesis that fuel was reprocessed ≤2 years after discharge, possibly for the production of a high-specific activity ^{144}Ce source for a neutrino experiment in Italy.

environmental radioactivity | ruthenium | nuclear forensics | environmental release | accidental release

Nuclear accidents are serious threats due to their immediate and perceived consequence for both health and environment. The lay public thus relies on the responsibility of their leaders to provide information on radioactive releases and their impact on human and environment health. Early in the 1960s, and even more after the Chernobyl accident, European radioprotection authorities established or strengthened radionuclide monitoring networks on a national scale. Today most of these European networks are connected to each other via the informal "Ring of Five" (Ro5) platform for the purpose of rapid exchange of expert information on a laboratory level about airborne radionuclides detected at trace levels. The Ro5 was founded in the mid-1980s by 5 member countries: Sweden, Federal Republic of Germany, Finland, Norway, and Denmark. Today, the memberships have grown to laboratories in 22 countries (while the name was kept), and the Ro5 is still an informal arrangement on a laboratory level and between scientists. In January 2017, the Ro5 alerted its members regarding the widespread detection of airborne ^{131}I in Europe (1). In October 2017, an unprecedented release of ruthenium-106 (^{106}Ru; $T_{1/2}$ = 371.8 d) into the atmosphere was the subject of numerous detections and exchanges within the Ro5. The goal of this report is to give an overview of the global spreading of this fission product through airborne concentrations observed in Europe and beyond, its forensic history, and chemistry.

Chronology of the Event

On October 2, 2017, an informal alert by an Italian laboratory was issued to the Ro5 network, reporting the detection of airborne ^{106}Ru in the millibecquerel per cubic meter (mBq·m^{-3}) range in Milan, Italy. Limits of detection (LOD) in laboratories connected to the Ro5 are typically in the range of 0.1 to 10 microbecquerels per cubic meter (μBq·m^{-3}). This first report occurred on a Monday, when most European laboratories usually exchange their aerosol filters, which are operated on a weekly basis. Later that day, ^{106}Ru detections were reported from Czech Republic, Austria, and Norway in the 1- to 10-mBq·m^{-3} range. This widespread detection in such range immediately suggested a considerable release.

After 2 d (and further detection reports from Poland, Austria, Switzerland, Sweden, and Greece), official information notes were published by national radioprotection authorities, for example, in Switzerland, Austria, and Norway. On October 7, 2017, the International Atomic Energy Agency (IAEA) requested data and possible known sources of radioruthenium from all 43 European member states. On October 9, 2017, Chelyabinsk and Sverdlovsk regional authorities ruled out any possible ^{106}Ru release from their region (Russian Federation). On November 21, 2017, the Russian Federal Service for Hydrometeorology and Environmental Monitoring (Roshydromet) declared to have measured ^{106}Ru in the southern Urals in the late September (2). However, one possible source in the region, the Federal State Unitary Enterprise "Production Association Mayak" in Ozersk, immediately declared that it was not the source of increased ^{106}Ru (3). On November 23, 2017, the IAEA addressed the release of ^{106}Ru in a press conference. All members submitted the requested data, but none declared an accident and none declared being aware of any source. On December 8, 2017, Russian officials once again claimed that Mayak could not be the source because of the lack of any radioruthenium traces in the soil around the facility (4). Instead, the officials pointed at the possibility of a radionuclide battery of a satellite that had burned during its reentry into the atmosphere. On January 22, 2018, the Nuclear Safety Institute of the Russian Academy of Sciences invited radiation protection experts from Germany, France, Finland, Sweden, the United Kingdom, and Russia to aid in the elucidation of the release. Two commissions of inquiry were held: on January 31, 2018 and on April 11, 2018. The second meeting concluded by emphasizing that not enough data were yet available to point out any verified hypothesis of the origin of the ^{106}Ru (5). The present article aims at closing this gap.

Results and Discussion

Monitoring Results. Information sources: The entire airborne concentration dataset and deposition dataset are available as *SI Appendix*, Tables S1–S4 and were mainly compiled through Ro5 exchanges, personal exchange, and data already published. Valuable information are also available on the Roshydromet website (6, 7), on the Typhoon Association website (6), and on the website of the Unified State Automated Monitoring System of the Radiation Situation in the Russian Federation (8). Data from the Comprehensive Nuclear-Test-Ban Treaty Organization (CTBTO) (9) are not part of the dataset except for those already published (10). The International Monitoring System (IMS) data supporting the CTBTO (9) are available directly from the CTBTO upon request and signing a confidentiality agreement to access the virtual Data Exploitation Platform. This study provides ^{106}Ru observations (>1,120 data points related to airborne activity and about 200 data points for deposited contamination, from about 330 sampling locations) that can be used for the purpose of atmospheric dispersion and deposition model validation.

With the exception of the westernmost parts of Europe, most monitoring stations reported detections of ^{106}Ru in the range between some tenths μBq·m^{-3} meter and more than a 100 mBq·m^{-3}. Fig. 1 illustrates the maximum activity levels per country. Activity concentrations in the millibecquerel per cubic meter range were reported between September 29, 2017 and October 7, 2017, exhibiting a short build-up and rapid decline behavior. The last traces of the plume (microbecquerel per cubic meter range) were measured in sampling periods ending between October 12, 2017 and the end of October by laboratories equipped with high-volume samplers and low-level γ-ray spectrometry. The eastern and southeastern parts of Europe, including western Russia, exhibited the highest reported levels. The maximum level in Europe was reported from Romania (176 ± 18 mBq·m^{-3}). Even at this level, the plume did not represent any threat for human and environmental health.

However, it is important to note that these compiled data were obtained with different sampling durations, which limits their comparability without further correction.

Outside Europe, ^{106}Ru was also detected east of the geographical border between Europe and Asia in the Urals region (Russian Federation) with activity levels of some tens mBq·m^{-3}. Tiny amounts of ^{106}Ru were also pointed out elsewhere in the northern hemisphere by aerosol stations belonging to the IMS supporting the CTBTO: in Guadeloupe, Kuwait, Florida (United States), Russia (central and eastern parts), and Mongolia. ^{106}Ru is a

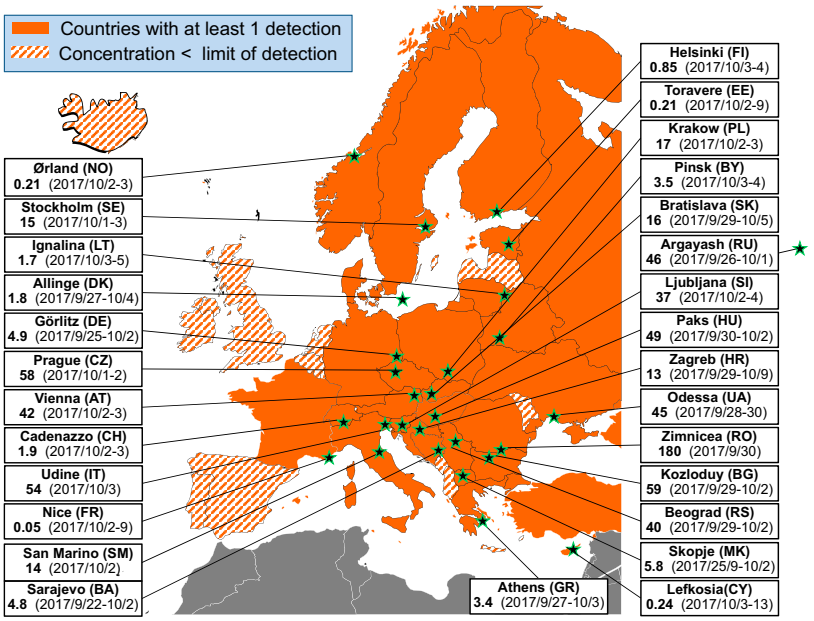

Fig. 1. Compiled maximum ^{106}Ru airborne "uncorrected" activity concentrations (in mBq·m^{-3}; sampling period in parentheses) in Europe.

nuclide that may be released upon detonation of a nuclear weapon, and is therefore a "CTBT-relevant radionuclide."

^{106}Ru had not been detected in the global atmosphere since the Chernobyl accident (11) [estimated release <73 PBq (12)], not even after the Fukushima accident on the Japanese territory (13, 14), because of the different accident and release characteristics. As a result, there is no usual background or reference level, which could be used to define an increasing factor. As a matter of fact, this radionuclide is usually not detected in the atmosphere. Besides aerosol filtration, gaseous sampling was conducted at some locations (Austria, Sweden, Italy, and Poland), thus allowing checking for the presence of gaseous Ru species. Ruthenium may be present in volatile forms, especially in the form of ruthenium tetroxide, RuO_4 (15). Since gaseous RuO_4 is a highly reactive and strong oxidizer, it is expected to rapidly nucleate into particulate and low volatile RuO_2. No ^{106}Ru was detected in gaseous form.

In addition to ^{106}Ru, the anthropogenic ruthenium isotope ^{103}Ru ($T_{1/2}$ = 39.3 d) was detected at a limited number of high-performing stations (*SI Appendix*, Table S2): Austria, Czech Republic, Poland, and Sweden (10) with activity levels ranging from 0.04 to 7.3 μBq·m^{-3} (average 2.6 ± 0.1 μBq·m^{-3}). The average ratio ^{103}Ru/^{106}Ru was about (2.7 ± 0.9)·10^{-4}, and the minimum ^{106}Ru activity concentration associated with a ^{103}Ru detection was about 4 mBq·m^{-3} (*SI Appendix*, Table S4). Several organizations in Europe analyzed the filters for the occurrence of other γ-emitters, as well as difficult-to-measure radionuclides, such as Pu, Am, Cm, or ^{90}Sr by low-level radiochemical analyses. No unusual traces were found that would have been indicative of a release of any of these radionuclides concurrently with the ^{103,106}Ru. This excludes an accidental release from a nuclear reactor as the source, as this would have resulted in an emission of a great multitude of fission products. Instead, the origin of ^{103,106}Ru is rather associated with nuclear fuel reprocessing or with (medical or technical) radioactive sources. In addition, no unusual (stable) element contamination was found on a ^{106}Ru-containing filter from Vienna (Austria) (16).

Discussion of a Possible Source Melting. Melting of radioactive sources already occurred in the past, leading to detection of radionuclides in several European countries. Indeed, at the end of May 1998, a ^{137}Cs source estimated 0.3 to 3 TBq was incidentally melted in a steelworks near Algeciras (Spain) and led to detections in several European countries (17). ^{106}Ru in ophthalmic radiotherapy sources have typical activities less than 10 MBq, which is clearly insufficient to explain the observed concentrations on a wide scale, as emphasized by the IAEA (18), as it would have required the melting of numerous ophthalmic sources at once.

Discussion of a Possible Satellite Reentry. The possibility of the disintegration of a satellite equipped with a radioisotope thermoelectric generator (RTG) operated with a ^{106}Ru source during its reentry into the atmosphere, as vaguely indicated previously (19), warrants investigation. Generally, such a source appears rather

Table 1. Comparison of airborne ^{106}Ru at high-altitude and at closest low-altitude sampling locations (with similar time stamps)

Country	High-altitude location (meters above sealevel)	Date (2017)	^{106}Ru (mBq·m^{-3})	Nearest low-altitude location	Date (2017)	^{106}Ru (mBq·m^{-3})
Austria	Sonnblick (3,105)	October 2	0.17 ± 0.11	Klagenfurt	October 2	4.90 ± 0.34
Bulgaria	Moussala peak (2,925)	October 3	1.8 ± 0.54	Yana	September 29 to October 4	17.6 ± 1.6
Greece	Helmos Mountain peak (2,314)	September 27 to September 29	0.99 ± 0.19	Athens	September 27 to October 3	2.64 ± 0.63
Germany	Zugspitze (2,964)	September 25 to October 2	<0.026	Garmisch-Partenkirchen	September 25 to October 2	<0.023

unlikely because of the rather short half-life of ^{106}Ru compared with the expected or desired satellite life span and the low power level (~33 W·g^{-1}) generated by a ^{106}Ru-powered RTG and radiation protection issues during its manufacture and handling. In addition, several space organizations concluded that no satellite went missing during the ^{106}Ru episode (*SI Appendix*). Other arguments are also not in favor of the satellite disintegration hypothesis. If a satellite had burned during its reentry into the atmosphere, it would have caused a vertical distribution of ^{106}Ru in the air: the higher the altitude, the higher the concentration. However, ^{106}Ru at high-altitude locations was either below LOD or significantly lower than ^{106}Ru registered above LOD at low altitude (Table 1). The very low level (below LOD) at the station on Zugspitze mountain (Germany) is also very indicative of low concentrations at high altitude. In addition, the levels of ^{7}Be (a cosmogenic radionuclide produced in the upper troposphere/lower stratosphere and used as a tracer of atmospheric movement) remained close to usual range, thus indicating that no downdraft from the lower stratosphere or upper troposphere occurred at that time. Therefore, the ^{106}Ru release has likely happened in the lower tropospheric layers and cannot be linked to a satellite disintegration. Moreover, the concomitant detections of infinitesimal traces of ^{103}Ru and traces of ^{106}Ru at some locations definitely outmoded the satellite reentry hypothesis due to the short ^{103}Ru half-life ($T_{1/2}$ = 39.3 d).

Sequence of Airborne ^{106}Ru Detections in Europe. Most early ^{106}Ru detections occurred on the aerosol filters sampled during week 39 (September 25 to October 2, 2017), regardless of the location in Europe, including Russia (September 26 to October 1, 2017). In Ukraine, ^{106}Ru was first detected in the sampling period from September 22 to September 29, 2017. Within the framework of national monitoring programs of airborne radionuclides, most aerosol samplings in Europe are performed either on a weekly basis for γ-counting or on a daily basis (in the vicinity of nuclear facilities), first for the purpose of gross β-counting by plant operators, or for γ-counting, for example, within the IMS network. Aerosol filters sampled in Romania were acquired with the highest temporal resolution (down to 5 h plus 1-h shutdown intervals). After sampling, filters of 2 or 4 sequences were compiled before measurement, thus reflecting 10-h sampling of 12 to 20 h of 24 for each composite sample. In addition, the Romanian network consists of several tens of aerosol sampling stations, which made it possible to reconstruct the pattern of the ^{106}Ru plume. The duration of the episode proved to be rather short: at more than 30 Romanian sampling locations that detected ^{106}Ru, this radionuclide was detectable on exclusively 1 d (30% of sampling locations), on 2 consecutive days (45%) and on 3 consecutive days (25%). Detections over 2 or 3 consecutive days indicate that the plume presence in Romania was rather short and characterized by a narrow peak (Fig. 2).

The shapes of the Romanian time series match with a short release (i.e., typically less than 1 d), subject to the wind direction did not vary a lot during transport and that the plume border did not undulate while passing at the sampling locations. The detection pattern also provides vague distance-related information on the release point of ^{106}Ru, as multiple Romanian stations detected the plume simultaneously. This is only possible if the plume originated at a sufficiently remote release point to have time to widen to the width of Romania (approximately 600 km) (Fig. 3). Although highest activity concentrations of this ^{106}Ru episode (>100 mBq·m^{-3}) have been reported for Romania, the width of the plume supports excluding a release point on the Romanian territory.

All eastern Romanian stations reported airborne ^{106}Ru on September 29, 2017. From September 30, 2017, the general trend indicated a ^{106}Ru front traveling westwards. Peak values were noticed between September 29 and October 1, 2017, depending on the location. On October 1, 2017, eastern stations ceased their detections. From October 4, 2017, no more detection was reported from Romania. In Bulgaria, the ^{106}Ru plume was also assumed to be present only 3 to 4 d (mostly from October 2 to October 4, 2017) (20), about 3 d in Austria and Czech Republic, and over 4 d in Hungary (21). These observations clearly confirm both the shortness of the plume length and the eastern origin of the plume. The discussion of the plume duration exemplifies that in many cases, the sampling duration was longer than the plume duration (21). As a result, a significant fraction of uncontaminated air was pumped through the filter, thus "diluting" the ^{106}Ru activity concentration in most cases. To encompass the entire plume duration regardless of the location, we chose a 7-d integration period. In practice, this decreases the average airborne ^{106}Ru concentration for locations where the ^{106}Ru plume was detected over a period

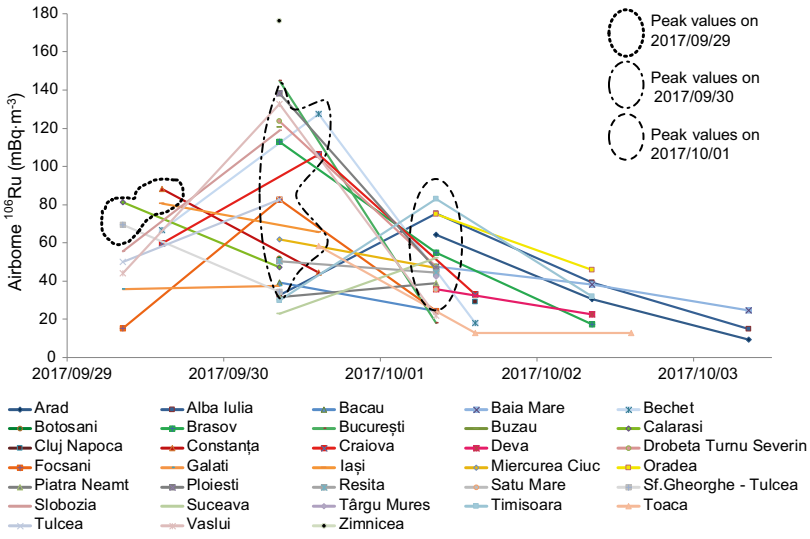

Fig. 2. Airborne ^{106}Ru concentrations (mBq·m^{-3}) at Romanian locations (values have been attributed to the midsampling date of the composite samples). The connecting lines between data points are only meant to guide the eye.

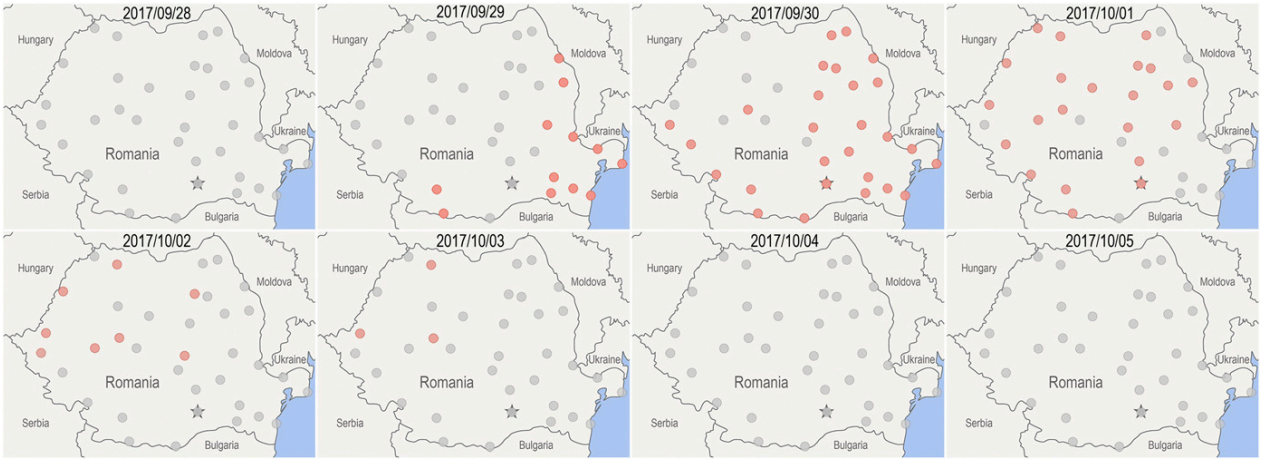

Fig. 3. Daily maps of above-LOD airborne ^{106}Ru (red dots) in Romania from September 28 to October 5, 2017. Gray dots indicate sampling locations with ^{106}Ru levels below the respective limits of detection at the given time.

of <7 d (because the absolute amount of ^{106}Ru was mathematically "diluted" with more clean air), while it consequently increases the ^{106}Ru concentration for sampling periods >7 d (as the plume is mathematically "concentrated" with a smaller amount of air) (Fig. 4). This mathematical unification of the sampling periods lets that the corrected values obtained in Romania no longer stand out as the highest, while it can be observed that they are in the same range from the Urals to southern-central Europe as a result of the conservation of the absolute amount of ^{106}Ru transported along the route of the air masses.

At the Romanian laboratory of Zimnicea—that is, the location with the highest uncorrected value (176 ± 18 mBq·m^{-3}, detected on September 30, 2017 between 3 AM and 2 PM local time)—a Hybrid Single Particle Lagrangian Integrated Trajectory Model (HYSPLIT) back-trajectory analysis shows that air masses came from Russia and then traveled across Ukraine (Fig. 5).

The trajectory model suggests that air masses arriving at Zimnicea on September 30, 2017 had previously traveled close to the Mayak industrial complex around September 25, 2017 at an altitude of at most about 500 m. According to Roshydromet (2), the meteorological situation in the Southern Urals and central part of European Russia during the period of September 25 to October 6, 2017 was due to a vast anticyclone centered around the White Sea (south of the Kola Peninsula) practically merging with an anticyclone in the central part of Western Siberia. Their report (2) reads, "As a result, conditions for an active transfer of air masses and pollutants from the territory of the Southern Urals and southern Siberia to the Mediterranean region and, then, to the north of Europe, arose in the southern part of Western Siberia, in the Southern Urals, in the Caspian lowland and Ciscaucasia." Among the different every 3-h back-trajectories, only 2 passed very close to the Mayak industrial complex. The detection of the ^{106}Ru plume at Zimnicea on September 30, 2017 hence indicates a release from Mayak would have occurred between September 25, 2017, around 6 PM coordinated universal time (UTC) and September 26, 2017, around noon (UTC) (Fig. 5).

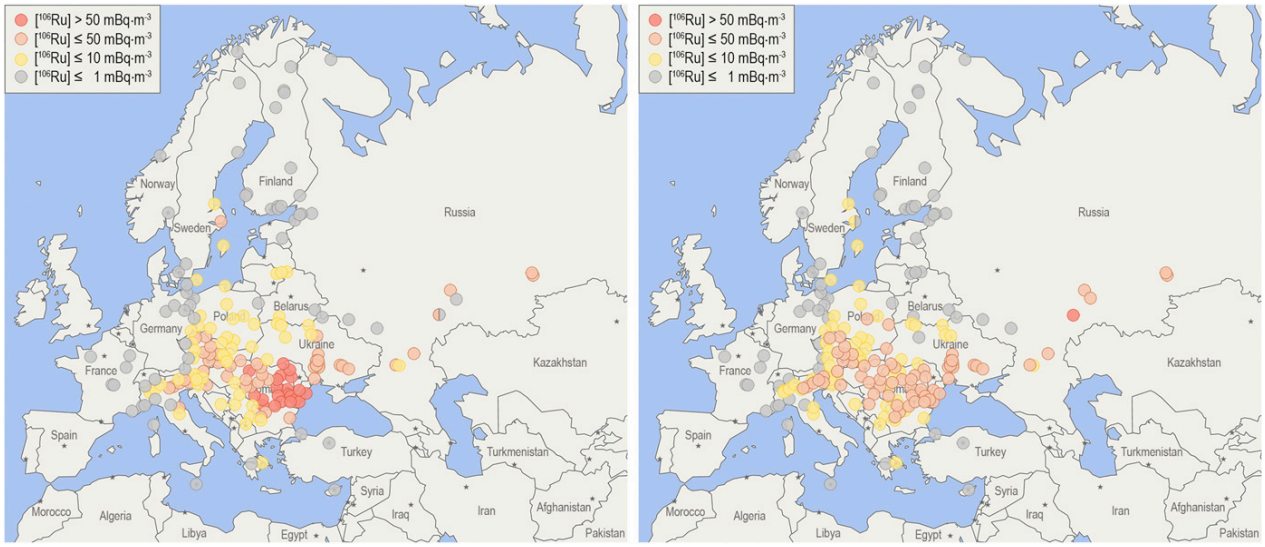

Fig. 4. (*Left*) Map of uncorrected average concentrations at European stations, and (*Right*) map of 7-d corrected average concentrations (based on average plume duration of 7 d at each location).

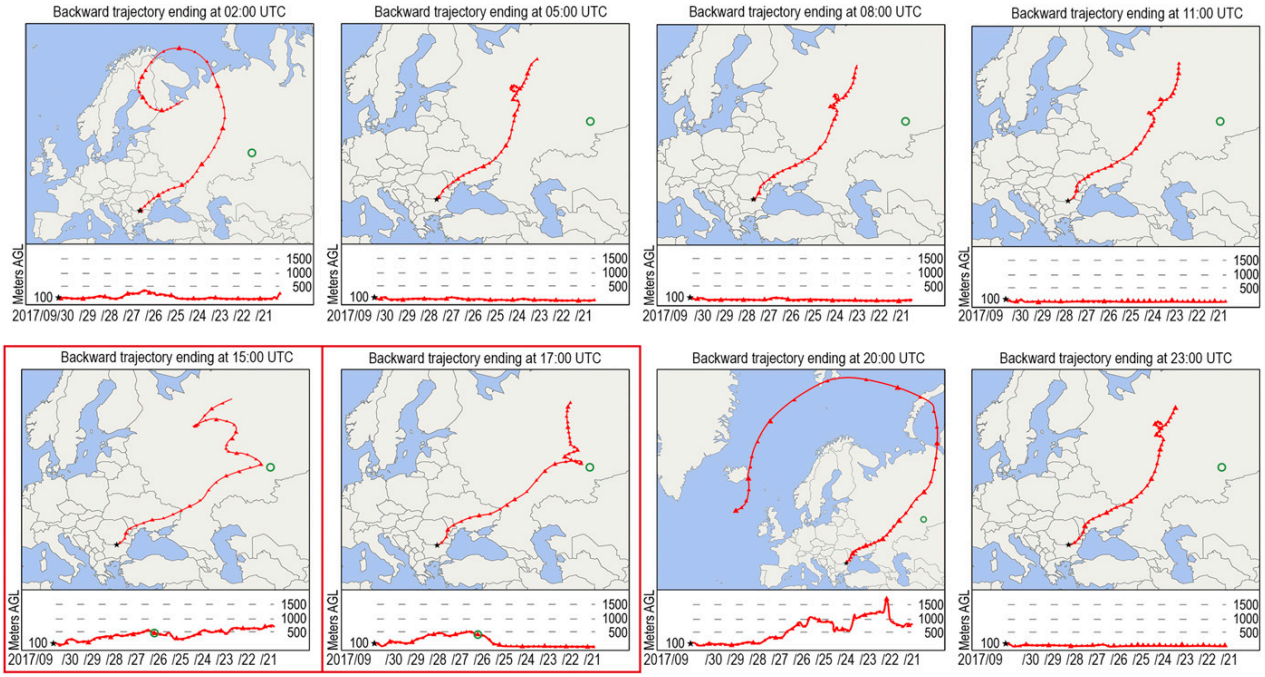

Fig. 5. HYSPLIT-based 240-h backward trajectories ending at the Romanian monitoring station in Zimnicea (black star) (43.666 N, 25.666 E), every 3 h on September 30, 2017, from 2 AM to 11 PM UTC. The National Oceanic and Atmospheric Administration (NOAA) HYSPLIT model uses Global Data Assimilation System (GDAS) meteorological data. The Model Vertical Velocity was used as vertical motion calculation method. The green circle indicates the position of the Mayak industrial complex. The altitude of the air parcels is given in meters above ground level (AGL). The green circle in the altitude sections of the trajectories ending at 3 PM and 5 PM UTC (maps surrounded by red frames), respectively, indicates the time and altitude (approximately 500 m) the air parcels were in closest proximity to the Mayak area.

The Mayak Production Association was one of the first and largest nuclear facilities of the former Soviet Union and spearheaded the Soviet nuclear weapons program. In the Cold War era, it hosted a total of 10 nuclear reactors, mainly for the production of weapons-grade plutonium. In 2014, the Mayak complex employed ∼12,000 people and hosted 2 reactors for isotope production, storage facilities for nuclear materials, and a nuclear fuel reprocessing facility (22). On September 29, 1957, a chemical explosion took place in a radioactive waste storage tank at the Mayak nuclear complex, causing a massive release of radionuclides. The accident became known as the "Kyshtym accident." In the course of this accident, about 2,700 TBq of ^{106}Ru (together with various other radionuclides) were released into the environment, causing a significant contamination in a more than 100-km-long strip that has been termed the East Urals Radioactive Trace (23). More than 10,000 residents had to be evacuated (24). The Kyshtym accident was retrospectively rated at level 6 on the International Nuclear and Radiological Event Scale.

Although such incidents have become rare events in recent years, ^{106}Ru was released from nuclear reprocessing facilities in the past on multiple occasions. On September 26, 1973, following an exothermic reaction at the Windscale reprocessing plant (United Kingdom), 35 workers were contaminated through an atmospheric release of ^{106}Ru estimated at 0.37 TBq (25). On April 6, 1993, an explosion at the reprocessing plant of the Tomsk-7 nuclear complex (Siberia, Russian Federation) led to the release of approximately 0.52 TBq of ^{106}Ru among other fission products and actinides (26, 27). About 200 km^2 were contaminated. On May 18, 2001 and October 31, 2001, a failure in the vitrification shops at the La Hague reprocessing plant (France) led to an atmospheric release of ^{106}Ru. Based on aerosols sampled at 200 km downwind from the stack and grass sampled in the vicinity, the first release was estimated between 0.005 and 0.05 TBq, while the second was estimated to range between 0.0005 and 0.02 TBq (28). Significant atmospheric releases also occurred from the early Hanford operations that were linked to United States nuclear weapons production, with ^{106}Ru (14 TBq from 1944 to 1972) being a relatively minor constituent (compared with 2.7 EBq ^{131}I in the same time span) (29). For comparison, the present, undeclared accident released an estimated activity of 250 TBq at once.

Ruthenium Deposition across Europe. Besides airborne activity determinations, several rainwater, plant, and soil samples attested the deposition of ^{106}Ru across Europe (*SI Appendix*, Tables S3 and S4). Most deposition arose from rain events that occurred between the last week of September 2017 and the first week of October, as for example at several Scandinavian sampling locations (up to about 50 Bq·m^{-2} in Sweden and about 50–90 Bq·m^{-2} in Finland) or, for example, in Greece in the second week of October (30). In Poland (up to about 80 Bq·m^{-2}), a washout ratio ([^{106}Ru$_{rain}$]/[^{106}Ru$_{air}$]) of at least 4,900 was found. In central Europe, fallout deposition reached 5 Bq·m^{-2} in Vienna (Austria) between October 3 and October 5, 2017; 40 Bq·m^{-2} in Ostrava (Czech Republic) from October 2 to October 3, 2017; and 8 Bq·m^{-2} in Udine (northeastern Italy) the last week of September 2017 and the first week of October (*SI Appendix*, Tables S3 and S4). The majority of the highest surface-deposition records have been reported from locations within 20 km from the Mayak complex: Khudaiberdinskiy, Argayash, Novogorny, and Metlino (31, 32), where the surface deposition reached up to 343 Bq·m^{-2}. However, the sole accumulation of positive reports from the vicinity of the Mayak facilities, by itself, is not a conclusive indication of the source, as a nuclear facility naturally is more densely monitored than nonnuclear areas. Depending on the official Russian source, levels are highly variable: up to a factor of 10 that can arise from the deposition pattern.

For the purpose of clarifying the situation, a soil-sampling campaign was conducted by the French Commission for Independent Research and Information on Radioactivity (CRIIRAD) nongovernmental organization (33) around the Mayak facilities in December 2017 at a closest authorized distance of about 16 km. Among the 8 soils sampled in various directions, only the 1 sampled west-southwest from Mayak indicated a ^{106}Ru deposited activity estimated between 580 and 1,200 Bq·m^{-2}. Inasmuch as abnormal, again, this sole result is not sufficient to clearly demonstrate whether or not the ^{106}Ru originated from Mayak, as deposition levels are not as high as one might expect from a major release. However, the weak soil-sampling density may also be a good reason for the plume deposition to escape from the investigation grid. Moreover, the atmospheric behavior (e.g., the transfer kinetics from volatile RuO_4 into particulate RuO_2) and deposition of ^{106}Ru are not well understood, especially when released in its volatile form of RuO_4. At a longer distance (530 km in Bugulma, Russian Federation) in the same direction, deposition of ^{106}Ru (noticed only on samples collected on September 26 to September 27, 2017 [11.3 Bq·m^{-2}] and September 27 to September 28, 2017 [30 Bq·m^{-2}]) matches with the hypothesis of a release from the Mayak industrial complex on September 25, 2017, which, therefore, has to be considered as a possible candidate for the source of the release of ^{106}Ru. A detailed dispersion analysis using inverse dispersion modeling techniques and field observations using the data from the present study (airborne concentration and deposition) was conducted to assess both the source location and the source term. This modeling work also suggests that a hot-spot of ^{106}Ru deposition occurred in southeastern Bulgaria. Accordingly, pine needles, oak leaves, forest litter, grass, and soil samples from this area confirm that ^{106}Ru deposition originating from a release on September 26, 2017 from the Mayak area was prone to produce these depositions in combination with rain events.* The ^{106}Ru-deposited activity in plants sampled in the southeast area of Bulgaria was up to several tens Bq·kg^{-1}, whereas they remained in the millibecquerel per kilogram (mBq·kg^{-1}) range in the western part of the country where no rain occurred, while the variability of ^{106}Ru volume activity in the atmosphere remained somewhat limited across the country. Other ^{106}Ru detections occurred in early 2018 (until March) in fallout and rainwater samples (in Norway, Poland, Slovenia), and even in March 2019 (Poland), but they were assumed to be induced by the resuspension of previously contaminated soil particles, indicating that ^{106}Ru had not yet completely migrated from the topsoil layer.

Radioruthenium Forensics: Age Estimate, Chemistry, and Volatility.

Model age. Concomitant presence of minute amounts of shorter-lived ^{103}Ru together with ^{106}Ru at about 15 locations allowed estimating the model age of fission-derived radioruthenium (Fig. 6). We define the model age as the time elapsed after the end of neutron irradiation of the nuclear fuel. In a simplified approach, this roughly coincides with the discharge (unloading) of the spent nuclear fuel from the reactor. The average ^{103}Ru/^{106}Ru activity ratio was found to be in the range of (2.7 ± 0.9)·10^{-4}, suggesting an age of the released radioruthenium between 530 and 590 d after the end of irradiation in a power reactor [assuming spent nuclear fuel at the end of its fuel lifetime, stemming from a standard power reactor, depending on reactor type and fuel (34) and calculating decay according to the nuclides' half-lives].

There have been speculations in a *Science* commentary (35) that the release of ^{106}Ru may have been associated with the production of a powerful cerium-144 (^{144}Ce; $T_{1/2}$ = 285 d) source at Mayak for a neutrino experiment in the Gran Sasso National

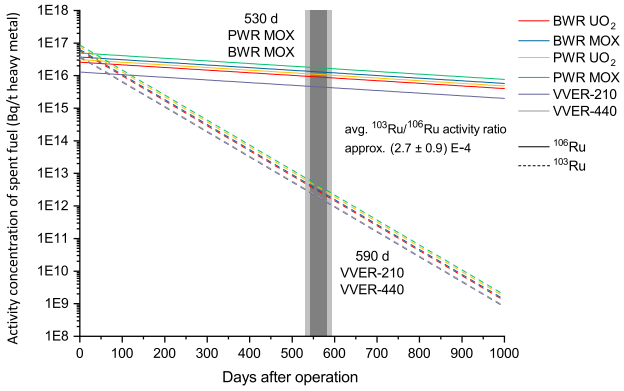

Fig. 6. Age estimation of radioruthenium from various power reactor types (boiling water reactor, BWR; pressurized water reactor, PWR; Russian Water-Water-Energetic-Reactor, VVER) based on ^{103}Ru/^{106}Ru activity ratios of regular spent nuclear fuels (UO_2 and mixed oxide fuel, MOX) at the end of their fuel lifetimes. The light gray area represents the uncertainty of the ratio.

Laboratory (Italy). The experiment is set up around the liquid scintillator "Borexino" (Italian diminutive of BOREX, Boron Solar Neutrino Experiment). In an experiment called Short Baseline Neutrino Oscillations with Borexino (SOX-Borexino), the existence of a hypothetical fourth (sterile) should be tested by positioning a powerful, yet compact ^{144}Ce-^{144}Pr source in the vicinity of the Borexino detector to induce nuclear reactions of the inverse β-decay type (36). According to Vivier et al. (37), the Mayak reprocessing facility has been identified as the only potential supplier to have the chemical capabilities to produce a ^{144}Ce antineutrino source with sufficient activity (approximately 3.5 to 5 PBq ^{144}Ce) and purity (38, 39). In this facility, sources are produced using fission product solutions from spent fuel reprocessing. Reprocessing of spent nuclear fuel from VVER-440 reactors for the purpose of production of petabecquerel sources of ^{144}Ce for sterile neutrino experiments is discussed in Gerasimov et al. (40). The authors suggest reprocessing spent fuel with a cooling period of 3 y after irradiation. Apparently, "fresher" fuel with less cooling is not being considered, as the extremely high activity levels in such fuel may cause problems in the reprocessing and handling. For example, western reprocessing facilities, such as La Hague (France), do not consider reprocessing of spent fuel until at least 4 (or even 10) y after irradiation (34, 41). However, shorter irradiation duration of the nuclear fuel (1 or 2 y instead of 3 y) is being discussed as a potential way to yield higher specific activities of ^{144}Ce in the entire (mainly stable) fission-derived cerium fraction. Indeed, the onset of stable Ce in the fuel becomes a crucial factor for the production of such source. While the activity of 3.5 to 5 PBq ^{144}Ce corresponds to 30 to 43 g of this radionuclide only, this amount makes up less than 1% of the total mass of Ce that is being isolated from the spent fuel (40). The SOX experiment required a source of ideally at least 3.7 PBq ^{144}Ce with a total mass of 2.5 kg of ultrapure Ce (including both stable and radioactive nuclides) (42), which is challenging to produce. Previously, other radionuclides (including ^{106}Ru) were considered for the SOX-Borexino experiment (36), but ^{144}Ce was found to be easier to extract from spent nuclear fuel. Spent nuclear fuel reprocessing is usually based on the PUREX method (Plutonium Uranium Recovery by Extraction), in which the UO_2 fuel is chopped into smaller fragments and dissolved in 7 to 7.5 M HNO_3. Most fission products (including Ce) are dissolved in the aqueous raffinate; however, a part of the Ru is oxidized to highly volatile RuO_4 and found in the off-gas, where it has to be captured and treated. Fuel components (U and Pu) are recovered by extraction into a kerosene/tri*n*-butyl phosphate phase

*O. Saunier, A. Mathieu, D. Didier, O. Masson, J. Dumont le Brazidec, Atmospheric modeling and source reconstruction of radioactive ruthenium from an undeclared major nuclear release. *Proc. Natl. Acad. Sci. U.S.A.*, in review.

before they are further processed and recycled. For the isolation of the cerium fraction in the aqueous phase, complexing displacement chromatography techniques were identified, which would yield a cerium fraction with sufficient purity, which would then be converted to CeO_2 and sintered (43). The final product should have fit into a capsule of <15 cm diameter, compact enough to be considered as a point-like source (43).

A critical factor of the attempted ^{144}Ce source is its required extraordinarily high specific activity. While the specific activity of ^{144}Ce per gram of fission-derived Ce can be increased by 28%, when the VVER-440 fuel is irradiated for 2 y instead of 3 y (and by 76% when irradiated for 1 instead of 3 y) (40), the reduction of the cooling time from 3 to 2 y causes a gain in specific activity by more than 140% (based on data from ref. 34). In fact, the aspired specific activity of at least 3.7 PBq of ^{144}Ce in 2.5 kg of ultrapure Ce can hardly be achieved only by reducing the irradiation duration of the fuel (in theory, this goal is only barely reachable when using 1-y-irradiated fuel), but can easily be achieved by reducing the cooling period from 3 y down to ∼2 y (even for 5 PBq sources and even from regular spent fuel at the end of its fuel lifetime). The reduction of the cooling period of the spent fuel may have been regarded as the only feasible way to yield a sufficient activity of ^{144}Ce in a yet reasonably small-sized source volume that was needed for the SOX experiments. If the ^{106}Ru release was indeed linked to the production of the SOX source, these considerations concerning the specific activity of the ^{144}Ce source would explain the young age of the Ru fission products at the time of the release. According to the source term estimates, the estimated release of 250 TBq of ^{106}Ru would correspond to an accidental loss of about 7 to 10% of the ^{106}Ru contained in the amount of VVER-440 fuel (700 to 1,000 kg, corresponding to 2 fuel assemblies) that would be necessary for the production of a 3.5 to 5 PBq ^{144}Ce source (assuming regular spent VVER-440 fuel at the end of its lifetime, based on data from ref. 34 and 2 y of cooling). In any case, the unusually young age of the ^{103,106}Ru of about 2 y after the end of irradiation in a power reactor would match the hypothesis of a release of ^{106}Ru during the production of the ^{144}Ce SOX source. Regarding this production, the fact that the order of the ^{144}Ce source was canceled by the Mayak facility shortly after the ^{103,106}Ru release attracted the attention of the nuclear community and initiated speculations whether both events (the release of ^{103,106}Ru and the cancelation of the ^{144}Ce order) may be linked (35). No finding of our research refuted or disproved the hypothesis of a linkage between the radioruthenium detection episode and the production of a ^{144}Ce source.

If the radioruthenium came from the production of the ^{144}Ce source, and if spent fuel has been reprocessed before reaching the end of its fuel lifetime in reactor, the above age estimate would represent a slight underestimate, as the "youth-indicator" ^{103}Ru would be present in "fresher" fuel in disproportionally higher concentrations compared with ^{106}Ru. The nonetheless young age of the ^{103,106}Ru also speaks against the "satellite hypothesis" as such young radionuclide batteries would not typically be available, because of a lack of facilities that can routinely handle such young fuel (possibly with the exception of the Mayak industrial complex).

Particle size and solubility. The released ^{103,106}Ru was found to be evenly distributed on air filters and no larger ^{103,106}Ru-rich particles were found in autoradiographic imaging (*SI Appendix*, Fig. S4) and scanning-electron microscopic investigations (*SI Appendix*, Fig. S5). Therefore, it may be concluded that the radioruthenium was released in a gaseous or extremely finely dispersed particulate form (particle sizes <1 μm). At room temperature, RuO_4 is an easily melting solid (melting point 25 °C), but due its high vapor pressure and low boiling point (40 °C), it is notorious for being a highly reactive and volatile substance (44), even from solutions (45). It is a highly unstable compound and decomposes to chemically inert RuO_2 (and O_2) in an explosive reaction when heated above 100 °C. The explosive properties may also be accident-relevant for the present release. Given its high reactivity, a release of highly oxidizing, gaseous RuO_4 would be followed by subsequent reduction or decomposition to RuO_2 on [organic or inorganic (46)] atmospheric dust particles and trapping on their surface. The lack of any traces of concomitant radionuclides in the Ro5 aerosol filters suggests a high degree of fractionation of the ^{103,106}Ru from other radionuclides, which would be achievable by a separation of highly volatile RuO_4 from other, less volatile radionuclides via the gas phase. Knowledge on the ^{106}Ru fractionation (gas/particle) would also have direct consequences on deposition in the environment close to the emission point. This is especially the case for the particulate fraction in case of rain or for species that remain in gaseous form. Various investigations at participating research institutions suggest a radiopurity of the ^{103,106}Ru of up to a factor of 10^4 over concomitant radionuclides. Thus, we conclude that the release most likely involved RuO_4, which either was released directly or possibly underwent chemical processing for its stabilization (e.g., trapping in NaOH or HCl) before its release into the environment. The fact that no apparent stable element anomalies were found in addition to the release supports the assumption that the release was limited to the isotopes of Ru (16).

In chemical investigations, several research laboratories have found that at least one of the ^{106}Ru species on the filters was highly soluble (about 50% within 10 min) when the filter was immersed in pH neutral water. The insoluble fraction remained insoluble even if the immersion duration was extended to 24 h. The solubility was marginally greater in when a filter fragment was immersed into 1 M HCl solution (24 h), namely to about 60%. The filtrate was filtered through syringe filters with pore sizes of 470 nm and 20 nm, respectively, which reduced the activity in the aqueous phase only marginally, thus excluding the breakthrough of suspended ^{106}Ru-containing particles in the water, which might have pretended dissolution. Assuming that the ^{106}Ru was trapped on air filters in the form of RuO_2 (reduction product of RuO_4), this high degree of solubility comes unexpectedly, at least when the macroscopic chemical behavior of RuO_2 is extrapolated to the submacroscopic scale of ultratrace levels of ^{106}Ru. Hence, the results may suggest that at least 2 species are present on the filter materials and that half of the total amount of ^{106}Ru is present in highly water-soluble form. Solubility experiments in serum ultrafiltrate fluid (SUF), however, reveal very high and rapid solubility (>90%) of the ^{106}Ru on air filters, which were brought in contact with SUF to simulate dissolution in the lungs. Two different kinetics were found

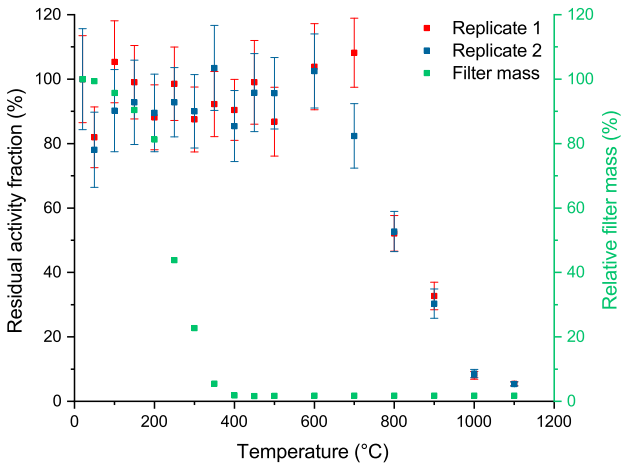

Fig. 7. Volatility tests of ^{106}Ru trapped on an air filter from Vienna (2 replicates with 30 Bq ^{106}Ru pieces). The loss of mass is shown in green for comparison.

to underlie the dissolution (*SI Appendix*, Fig. S2). The latter results may indicate that the Ru is associated with 2 different types of aerosol particles or particle surfaces, 1 of which may be binding ^{106}Ru more strongly than the other. In contrast to H_2O, SUF contains ligands that may out-compete surface binding sites for Ru.

Volatility. In heating experiments, the volatility of the Ru species from the filter was investigated. We found that the ^{106}Ru activities remained quite constant (with some fluctuations due to the thermal deformation of the filter fragments causing geometrical issues during the γ-measurement) (*SI Appendix*, Fig. S3) for the temperature range between room temperature and 600 °C. From 700 °C to 1,000 °C, the activity levels in the filter fragments' ashes decrease rapidly, suggesting almost complete volatilization of the Ru species in this temperature range (Fig. 7). In macroscopic amounts, highly refractory RuO_2 does not exhibit comparable volatilization in this temperature range (47). In combination with the solubility tests, this result suggests that the released Ru species has not been (or not exclusively) RuO_4, because one would expect low volatility and solubility from its reaction product RuO_2. Instead, a mixture of several chemical species of ruthenium may have been released.

Summary

Almost exactly 60 y after the Kyshtym and Windscale nuclear accidents in 1957, both substantial sources of ^{106}Ru in the environment (23), a significant release of ^{106}Ru occurred in the southern Eurasian border region in September 2017. It led to detectable yet innocuous levels of this airborne fission product in the rest of Europe. Based on times series of detections at various locations in Central Europe, the event was characterized as a short release. The plume duration lasted about 1 to 3 d on average, depending on the location, with the exception of a few areas (e.g., in Italy where the labeled air mass, once arrived, stayed longer than elsewhere). The release was too substantial to be associated with the incineration of a medical radionuclide source. A satellite crash can also be excluded as the source of the ^{106}Ru. It is much more likely that the ^{106}Ru escaped during reprocessing of spent nuclear fuel, possibly in the course of the miscarried production of a highly radioactive ^{144}Ce source for research applications in the Gran Sasso Laboratory in Italy. This study confirms high radiopurity of the radioruthenium, an age of about 2 y or less, as well as both relatively high solubility and volatility of the Ru species on the air filters. According to detection time series, a back-trajectory analysis, and chemical considerations, the Mayak nuclear complex in southern Urals should be considered as a likely candidate for the release.

Materials and Methods

Aerosol sampling is performed on a routine basis using medium- to high-flow rate pumps (60 to more than 1,000 $m^3 \cdot h^{-1}$). Airborne radionuclide monitoring on a nation-wide scale is usually based on weekly sampling, but the frequency may be increased by certain stations in unusual events, like the present one. Depending on the network and organization, different kinds of filter media are being used in Europe (glass fibers, glass plus cellulose, polyvinyl chloride, or polypropylene), all having a high (>90%) collection efficiency. After sampling, filters are typically pressed into pellets of various diameters depending both on filter and detector sizes.

^{106}Ru is a pure β-emitter and thus not directly measurable by γ-ray spectrometry. However, its detection can be achieved via decay of its daughter rhodium-106 (^{106}Rh), which reaches secular equilibrium within a few minutes with its parent due to its short half-life ($T_{1/2}$ = 30.1 s) and which is detectable by de-excitation γ-photons of the excited state of its decay product: palladium-106 (^{106}Pd, stable). The radionuclide is first identified by its 621.9-keV photopeak (emission intensity 9.87%) in a γ-ray spectrum and, once identified, the presence of ^{106}Ru can be confirmed by characteristic peaks at 1050.4 keV and 616.2 keV. All measurements were thus obtained by γ-ray spectrometry using coaxial or well-type, high-purity germanium detectors. Proper quantification should comply with recommendations in the Joint Research Centre technical report provided by the European Commission (48) regarding interferences and coincidence summing corrections. Indeed, these corrections can be significant, reaching up to deviations of up to 25%, depending on the detector and the counting geometry. For maximum activity concentrations, uncertainties were typically ranging from 5 to ~30% depending on detector and sample features. An example of a γ-ray spectrum exhibiting detectable activities of both ^{103}Ru and ^{106}Ru is shown in *SI Appendix*, Fig. S6. It exemplifies that, thanks to excellent energy resolution in modern γ-ray detectors, the unique γ-ray peaks of ^{106}Rh (^{106}Ru) at 621.9 keV and 616.2 keV are not disturbed by the presence of natural ^{214}Bi (609.3 keV).

Data Materials and Availability. We thank the CTBTO for providing analysis results in the framework of a Virtual Data Exploration Centre agreement (https://www.ctbto.org/specials/vdec/). IMS raw data collected by the CTBTO are confidential and may not be shared.

ACKNOWLEDGMENTS. We thank all data providers, among them the Environmental Protection Agency (Lithuania) and the Ignalina Nuclear Power Plant Laboratory (Lithuania); the National Oceanic and Atmospheric Administration Air Resources Laboratory, for the provision of the HYSPLIT model for back-trajectory calculations; and the Comprehensive Nuclear-Test-Ban Treaty Organization for providing analysis results in the framework of a virtual Data Exploration Centre agreement (https://www.ctbto.org/specials/vdec/). We acknowledge financial support by the VolkswagenStiftung (Az. 94403). A.W. acknowledges funding by the Deutschen Bundesstiftung Umwelt. The views expressed in this study are those of the authors and do not necessarily reflect the views of the Preparatory Commission for the Comprehensive Nuclear-Test-Ban Treaty Organization.

1. O. Masson *et al.*, Potential source apportionment and meteorological conditions involved in airborne ^{131}I detections in January/February 2017 in Europe. *Environ. Sci. Technol.* **52**, 8488–8500 (2018).
2. Roshydromet, On emergency, extremely high and high pollution of the environment in the territory of the Russian Federation in the period from 6 to 13 October 2017 (Об аварийном, экстремально высоком и высоком загрязнении окружающей среды на территории Российской Федерации в период с 6 по 13 октября 2017 года) [in Russian] (2017). http://www.meteorf.ru/product/infomaterials/91/15078/?sphrase_id=134576. Accessed 1 March 2018.
3. Production Association Mayak (2017). https://po-mayak.ru/wps/wcm/connect/mayak/site/info/news_main/094f7100436c8c33a8eca8e03176b6c3. Accessed 1 March 2018 (site discontinued).
4. Nuclear Engineering International, Russian commission says Mayak not the source of Ru-106 (2017). https://www.neimagazine.com/news/newsrussian-commission-says-mayak-not-the-source-of-ru-106-6000301/. Accessed 12 March 2018.
5. IBRAE, 2nd meeting of the international independent scientific commission for investigation of Ru-106 case in Europe in September–October 2017 (2018). http://en.ibrae.ac.ru/newstext/911/. Accessed 27 July 2018.
6. Federal Service for Hydrometeorology and Environmental Monitoring, Typhoon Association (2018). www.rpatyphoon.ru. Accessed 5 March 2018.
7. Roshydromet, Report on the causes and source of ruthenium-106 on the territory of Russia in September-October 2017 (Отчет по определению причин и источника рутения-106 на территории России в сентябре-октябре 2017 года) [in Russian] (2017). http://egasmro.ru/files/documents/reports/report_28_12_2017.pdfs. Accessed 15 May 2018.
8. EGASMRO, Radiation situation on the territory of the Russian Federation (Радиационная обстановка на территории РФ) [in Russian] (2018). http://egasmro.ru/ru. Accessed 1 March 2018.
9. CTBTO, Verification regime (2018). https://www.ctbto.org/verification-regime/. Accessed 5 March 2018.
10. H. Ramebäck *et al.*, Measurements of ^{106}Ru in Sweden during the autumn 2017: Gamma-ray spectrometric measurements of air filters, precipitation and soil samples, and in situ gamma-ray spectrometry measurement. *Appl. Radiat. Isot.* **140**, 179–184 (2018).
11. J. Paatero, S. Kulmala, T. Jaakkola, R. Saxén, M. Buyukay, Deposition of ^{125}Sb, ^{106}Ru, ^{144}Ce, ^{134}Cs and ^{137}Cs in Finland after the Chernobyl accident. *Boreal Environ. Res.* **12**, 43–54 (2007).
12. UNSCEAR, *Exposures and Effects of the Chernobyl Accident (Annex J)* (United Nations, New York, 2000).
13. T. Yamamoto, Radioactivity of fission product and heavy nuclides deposited on soil in Fukushima Dai-Ichi Nuclear Power Plant accident. *J. Nucl. Sci. Technol.* **49**, 1116–1133 (2012).
14. G. Steinhauser, Fukushima's forgotten radionuclides: A review of the understudied radioactive emissions. *Environ. Sci. Technol.* **48**, 4649–4663 (2014).
15. Z. Hölgye, M. Křivánek, On the volatility of ruthenium. *J. Radioanal. Chem.* **42**, 133–141 (1978).
16. D. Zok, J. H. Sterba, G. Steinhauser, Chemical and radioanalytical investigations of ^{106}Ru-containing air filters from Vienna in fall 2017: Searching for stable element anomalies. *J. Radioanal. Nucl. Chem.* **318**, 415–421 (2018).
17. D. Quélo *et al.*, Validation of the polyphemus platform on the ETEX, Chernobyl and Algeciras cases. *Atmos. Environ.* **41**, 5300–5315 (2007).

18. IAEA, *Status of Measurements of Ru-106 in Europe* (IAEA, Vienna, 2017), p. 19.
19. Rosatom, The comment of The State Atomic Energy Corporation ROSATOM for the Media, 22 November 2017 (2017). https://rosatom.ru/en/press-centre/news/the-comment-of-the-state-atomic-energy-corporation-rosatom-for-the-media/. Accessed 4 June 2018.
20. I. Penev, H. Angelov, T. Arsov, S. Georgiev, N. Uzunov, ^{106}Ru aerosol activity observation above southeast Europe in October 2017. *Dokl. Bulg. Akad. Nauk.* **71**, 613–618 (2018).
21. D. Jakab *et al*., Methods, results and dose consequences of ^{106}Ru detection in the environment in Budapest, Hungary. *J. Environ. Radioact.* **192**, 543–550 (2018).
22. NTI, Mayak Production Association (2014). https://www.nti.org/learn/facilities/894/. Accessed 12 June 2019.
23. S. Jones, Windscale and Kyshtym: A double anniversary. *J. Environ. Radioact.* **99**, 1–6 (2008).
24. B. V. Nikipelov *et al*., Accident in the southern Urals on 29 September 1957 (International Atomic Energy Agency Report INFCIRC-368, International Atomic Energy Agency, Vienna, 1989).
25. IAEA, "Significant incident in nuclear fuel cycle facilities" (IAEA-TECDOC-867, IAEA, Vienna, 1996).
26. IAEA, *The Radiological Accident at the Reprocessing Plant at Tomsk* (IAEA, Vienna, 1998).
27. E. S. Husebye, A. M. Dainty, *Monitoring a Comprehensive Test Ban Treaty* (NATO Science Series E, NATO Advanced Study Institute, Springer, Alvor, 1996).
28. G. Nord-Cotentin, Analyse de 2 incidents de rejet atmosphérique de ruthénium 106 en 2001 [in French] (2002). http://www.gep-nucleaire.org/. Accessed 12 June 2019.
29. C. M. Heeb, "Radionuclide releases to the Atmosphere from Hanford operations, 1944-1972" (PNWD-2222 HEDR, Pacific Northwest Laboratories, Richland, WA, 1994).
30. S. Padovani, I. Mitsios, M. Anagnostakis, D. Mostacci, Analysis of the vertical distribution and size fractionation of natural and artificial radionuclides in soils in the vicinity of hot springs. *Radiat. Eff. Defects Solids* **173**, 794–806 (2018).
31. EGASMRO, Bulletin on the radiation situation in Russia in October 2017 (БЮЛЛЕТЕНЬ о радиационной обстановке на территории России в октябре 2017 г) [in Russian] (2017). http://egasmro.ru/files/documents/ro_bulletins/byulleten_rorf_10_2017.pdf. Accessed 4 March 2019.
32. EGASMRO, Bulletin on the radiation situation in Russia in October 2017 (БЮЛЛЕТЕНЬ о радиационной обстановке на территории России в сентябре 2017 г) [in Russian] (2017). http://egasmro.ru/files/documents/ro_bulletins/byulleten_rorf_09_2017.pdf. Accessed 4 March 2019.
33. CRIIRAD, Ruthenium-106 contamination (Contamination par le ruthénium 106) [in French] (2018). http://www.criirad.org/accident-et-pollutions/Note_CRIIRAD_N_18-21_Ru_106_Mayak.pdf. Accessed 4 March 2019.
34. F. Pfeiffer *et al*., Waste specification and quantity structure (Abfallspezifikation und Mengengerüst, GRS-278) [in German] (2011). https://www.grs.de/publication/grs-278-abfallspezifikation-und-mengengeruest-basis-ausstieg-kernenergienutzung. Accessed 4 March 2019.
35. E. Cartlidge, Isotope cloud linked to failed neutrino source. *Science* **359**, 729 (2018).
36. M. Cribier *et al*., Proposed search for a fourth neutrino with a PBq antineutrino source. *Phys. Rev. Lett.* **107**, 201801 (2011).
37. M. Vivier *et al*., SOX: Search for short baseline neutrino oscillations with Borexino. *J. Phys. Conf. Ser.* **718**, 062066 (2016).
38. Irfu, Institut de recherche sur les lois fondamentales de l'Univers (2018). http://irfu.cea.fr/Phocea/Vie_des_labos/Ast/. Accessed 1 March 2018.
39. M. Meyer, "SOX–Towards the detection of sterile neutrinos in Borexino: Beta spectrum modeling, Monte Carlo development and sensitivity studies for the sterile neutrino search in Borexino," PhD thesis, Universität Hamburg, Germany (2016).
40. A. S. Gerasimov, V. N. Kornoukhov, I. S. Sald'ikov, G. V. Tikhomirov, Production of high specific activity ^{144}Ce for artificial sources of antineutrinos. *At. Energy* **116**, 54–59 (2014).
41. Compagnie Générale des Matières Nucléaires (COGEMA), *Specifications of Vitrified Residues Produced from Reprocessing at UP-2 or UP-3 La Hague Plants* (COGEMA, Second Series, 1986).
42. K. Altenmüller *et al*., The search for sterile neutrinos with SOX-Borexino. *Phys. At. Nucl.* **79**, 1481–1484 (2016).
43. T. Lasserre *et al*., Radioactive source experiments in Borexino. *Proceedings of Science* **244**, 025 (2015).
44. C. Mun, L. Cantrel, C. Madic, A literature review on ruthenium behavious in nuclear power plant severe accidents (2007). https://hal-irsn.archives-ouvertes.fr/irsn-00177621/document. Accessed 12 June 2019.
45. S. Sato, N. Endo, K. Fukuda, Y. Morita, Optimization for removal of ruthenium from nitric acid solution by volatilizing with electrochemical oxidation. *J. Nucl. Sci. Technol.* **49**, 182–188 (2012).
46. E. T. Maas , Jr, J. M. Longo, Confinement of ruthenium oxides volatilized during nuclear fuels reprocessing. *Nucl. Technol.* **47**, 451–456 (1980).
47. J.-Y. Kim *et al*., Template-free synthesis of ruthenium oxide nanotubes for high-performance electrochemical capacitors. *ACS Appl. Mater. Interfaces* **7**, 16686–16693 (2015).
48. M. Hult, G. Lutter, *Detection of ^{106}Ru, via the Decay of Its Daughter ^{106}Rh, in Gamma-Ray Spectra* (Joint Research Centre, Geel, 2017).

Chapter 4

Identification of a Chemical Fingerprint Linking the Undeclared 2017 Release of ^{106}Ru to Advanced Nuclear Fuel Reprocessing

M. W. Cooke†, A. Botti, D. Zok, G. Steinhauser, K. Ungar

Proceedings of the National Academy of Sciences of the United States of America, vol. 117, no. 26, pp. 14703-14711, 2020. DOI: 10.1073/pnas.2001914117

Author contributions:
M.W.C. designed research
M.W.C., A.B. and D.Z. performed research
G.S. and K.R.U. contributed new reagents/analytic tools
M.W.C. analyzed data and wrote the paper
G.S. and K.U. provided sample, personnel, and technical support

† Correspondence to: michaelw.cooke@canada.ca

Identification of a chemical fingerprint linking the undeclared 2017 release of ^{106}Ru to advanced nuclear fuel reprocessing

Michael W. Cooke[a,1], Adrian Botti[a], Dorian Zok[b], Georg Steinhauser[b], and Kurt R. Ungar[a]

[a]Radiation Protection Bureau, Health Canada, Ottawa, ON K1A 1C1, Canada; and [b]Institute of Radioecology and Radiation Protection, Leibniz Universität Hannover, 30419 Hannover, Germany

Edited by Kristin Bowman-James, University of Kansas, Lawrence, KS, and accepted by Editorial Board Member Marcetta Y. Darensbourg May 1, 2020 (received for review February 7, 2020)

The undeclared release and subsequent detection of ruthenium-106 (^{106}Ru) across Europe from late September to early October of 2017 prompted an international effort to ascertain the circumstances of the event. While dispersion modeling, corroborated by ground deposition measurements, has narrowed possible locations of origin, there has been a lack of direct empirical evidence to address the nature of the release. This is due to the absence of radiological and chemical signatures in the sample matrices, considering that such signatures encode the history and circumstances of the radioactive contaminant. In limiting cases such as this, we herein introduce the use of selected chemical transformations to elucidate the chemical nature of a radioactive contaminant as part of a nuclear forensic investigation. Using established ruthenium polypyridyl chemistry, we have shown that a small percentage (1.2 ± 0.4%) of the radioactive ^{106}Ru contaminant exists in a polychlorinated Ru(III) form, partly or entirely as β-^{106}RuCl$_3$, while 20% is both insoluble and chemically inert, consistent with the occurrence of RuO$_2$, the thermodynamic endpoint of the volatile RuO$_4$. Together, these findings present a clear signature for nuclear fuel reprocessing activity, specifically the reductive trapping of the volatile and highly reactive RuO$_4$, as the origin of the release. Considering that the previously established ^{103}Ru:^{106}Ru ratio indicates that the spent fuel was unusually young with respect to typical reprocessing protocol, it is likely that this exothermic trapping process proved to be a tipping point for an already turbulent mixture, leading to an abrupt and uncontrolled release.

ruthenium | polypyridyl complex | radiochemistry | nuclear forensics

In the fall of 2017, the man-made, high-yield fission product ^{106}Ru (half-life, $t_{1/2}$ = 373.6 d) was detected by monitoring networks across Europe (1–4), along with sporadic detections of minute amounts of the relatively short-lived ^{103}Ru ($t_{1/2}$ = 39.2 d) in select locations. Although unprecedented in scale (250 TBq) (5), airborne and surface measurements substantiated a timely assessment that there was no detrimental impact to human health (6). Nevertheless, the undeclared intrusion of such radioactivity into the air space and soil of sovereign nations demands investigation, in support of national and coordinated global security.

To address the location of the ^{106}Ru source, recent reports have used dispersion modeling and field measurements of ^{106}Ru concentration (airborne and ground deposition) to demonstrate an origin in the Southern Urals of Russia, in the area of the Mayak industrial complex (1, 5–9). A long history of nuclear-related activities in this area, combined with the radiopurity of the field observations and the detection of the short-lived ^{103}Ru, lends credence to the scenario of an accidental release during nuclear fuel reprocessing and serves to dispel some persistent theories on the origin of the release (e.g., nuclear reactor accident, downed radioisotope thermoelectric generator satellite, volatilized medical sources, etc.) (1). However, to make a direct link to fuel reprocessing activity on this basis alone is circumstantial and as such provides room for plausible deniability. Direct evidence to this end constitutes the identification of unique signatures. From a radiological perspective, there is none. Samples have been shown to be radiopure and to carry the stable ruthenium isotopic signature of civilian spent nuclear fuel (10), while stable elemental analysis by scanning electron microscopy and neutron activation has revealed no detectable anomalies compared to aerosol filter media sampled prior to the advent of the ^{106}Ru contaminant (1, 11). We are, then, left with the definition of a limiting case for a nuclear forensic investigation.

Fortunately, we are concerned with an element that has significant covalent character to its bonding interactions (12). This affords the opportunity to perform chemical transformations, with and without the presence of a stable form of the same element. By selecting reactions that are well understood and/or by varying reaction conditions, we can compare the distribution of the radioactive element to the stable form in the reaction product(s) (Scheme 1). In this way, it is possible to deduce both general and highly specific information about the atomic connectivity, that is, the chemical context, of the radioactive contaminant, given that the rules for reactivity are well understood.

Results and Discussion

To help refine synthetic targets amenable to the strategy proposed in Scheme 1, we subscribe to the hypothesis that the

Significance

In the fall of 2017, a massive, undeclared release of ^{106}Ru occurred that was detected across Eurasia. To conclusively address the nature of the release, we have used carefully selected and established chemical transformations to reveal a chemical fingerprint for the ^{106}Ru contaminant that is uniquely consistent with specific methodology employed in the reprocessing of spent nuclear fuel. In view of international attention and investigation to date, this chemical fingerprint is the first direct evidence to this effect. This work serves, by example, as a potentially valuable addition to the field of nuclear forensics, considering that it is the only means to extract historical information from a radiopure contaminant in the absence of stable elemental anomalies.

Author contributions: M.W.C. designed research; M.W.C., A.B., and D.Z. performed research; G.S. and K.R.U. contributed new reagents/analytic tools; M.W.C. analyzed data; M.W.C. wrote the paper; and G.S. and K.R.U. provided samples, personnel, and technical support.

The authors declare no competing interest.

This article is a PNAS Direct Submission. K.B.-J. is a guest editor invited by the Editorial Board.

[1]To whom correspondence may be addressed. Email: michaelw.cooke@canada.ca.

This article contains supporting information online at https://www.pnas.org/lookup/suppl/doi:10.1073/pnas.2001914117/-/DCSupplemental.

First published June 15, 2020.

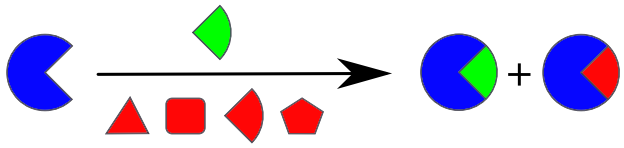

Scheme 1. High-level concept depicting the reactive incorporation of both stable (green) and radioactive (red) chemical species of an element into isostructural end products.

release of ^{106}Ru into the environment is associated with fuel reprocessing activity. Owing to its complex chemistry and high specific activity (typically 6 to 9% of fission products) in spent nuclear fuel (12–16), the removal of radio-ruthenium from waste streams poses a significant challenge. While a myriad of approaches has been proposed, the vast majority center about the PUREX (plutonium–uranium extraction) process where the recovery of uranium and plutonium is accomplished by liquid extraction with an organophosphate from fuel that is digested in nitric acid (16–18). To amplify the oxidative power of the mixture, oxidants such as ceric ammonium nitrate can be added to encourage the evolution of the volatile and highly reactive RuO_4, which can then be driven off with carrier gas and subsequently trapped or passivated. At this early dissolution stage, and later during the vitrification of raffinates, the condensation and decomposition of RuO_4 to relatively inert oxides inside the containment vessels can lead to problems of accumulated dose and accelerated corrosion (14, 15, 19, 20). To address this, considerable investigative effort has been made to remove ruthenium at the fuel dissolution phase (17, 21, 22). Nevertheless, the formation of RuO_4 is still a very appealing option with respect to simplicity, cost, and scalability, as evidenced by recent investigations into ruthenium volatilization through RuO_4 generation (23–26). Subsequent chemical reduction of RuO_4 to more passive forms is also appealing with respect to such considerations, despite introducing additional waste material for management. Some of the more notable options in this regard are the efficient formation of RuO_4^{-2} and RuO_4^{-} salts under alkaline conditions (21, 27), the formation of RuO_2 on contact with reducing media (26, 28), and the generation of Ru(III) and Ru(IV) polychlorinated complexes in hydrochloric acid (29–31).

Treatment of filter pieces from both German and Swedish radionuclide surveillance networks with solvent gave highly reproducible results for partitioning of the ^{106}Ru contaminant. Good partitioning reproducibility, in conjunction with autoradiographic imaging (*SI Appendix*, Fig. S21), supports a homogenously distributed contaminant. We have found that 51.3 ± 2.4% of the ^{106}Ru contaminant was associated with the aqueous extract. This result is in very good agreement with that determined by other laboratories (1) and clearly indicates that the ^{106}Ru is composed of more than one chemical form. Partitioning experiments similarly performed with carbon tetrachloride showed no discernable association with the ^{106}Ru contaminant. This indicates an absence of adsorbed RuO_4, which is typically soluble in carbon tetrachloride, one of the few solvents that does not succumb to attack by this powerful oxidizing agent (13). This is not surprising, since RuO_4 decomposes to RuO_2 (hydrated) in water under ambient conditions and further upon exposure to light (15, 32), while reoxidation of RuO_2 back to RuO_4 is very slight and reserved for atmospheric oxidants such as ozone (32). Interestingly, we found that a small but highly reproducible fraction (7.35 ± 0.70%) of the ^{106}Ru contaminant was partitioned into ethanol. This result further supports a multicomponent composition for the ^{106}Ru contaminant. In light of the aforementioned discussion regarding the pragmatic treatment of RuO_4 in nuclear fuel reprocessing, β-$RuCl_3$ is expected to be formed from the passivation of RuO_4 in HCl to an extent that depends directly upon time and temperature (30, 31). Among inorganic ruthenium compositions, it is noteworthy that β-$RuCl_3$ possesses the rare quality of being highly soluble in dative solvents. Thus, we have chosen to explore the hypothesis that the passivation of RuO_4 in HCl was implicated in the environmental release.

This hypothesis informs an appropriate selection of chemical reactions and synthetic targets toward revealing a unique signature, and other meaningful chemical information, about the ^{106}Ru contaminant. To this end, polypyridyl chemistry is appealing as a reactive vehicle to incorporate ^{106}Ru, since such ruthenium complexes are exceptionally robust and formed in high yield under ambient conditions. Also, characteristic charge-transfer electronic transitions that lie in the visible region of the spectrum make these complexes intensely colored, facilitating chromatographic separation (33, 34). Of the polypyridyl ligands available, those derived from the tridentate 2,2′:6′,2″-terpyridine ligand are particularly well-suited as they offer achiral products and superior kinetic stability (33). Considering the ease of synthesis afforded by one-pot procedures to form 4′-substituted analogs of 2,2′:6′,2″-terpyridine, we have elected to synthesize 4′-p-tolyl-2,2′:6′,2″-terpyridine (ttpy; Fig. 1) according to reported procedures (35, 36), albeit with a notable exception regarding its purification (*Materials and Methods*). With this ligand in hand, we are supported by a plethora of established ruthenium coordination chemistry, the vast majority of which is derived from reaction with β-$RuCl_3$. In particular, we have identified the subsequent monoligated complex, ttpy$RuCl_3$ (37), and the reduced, bis-ligated complex, Ru(ttpy)$_2^{2+}$ (38), as targeted reaction products for isolation and radiometric measurement, in adherence to the general strategy presented in Scheme 1. Although the former has invariably served as a reaction intermediate to the formation of heteroleptic complexes (39, 40), it takes center stage in this work. This is due to the fact that the formation of ttpy$RuCl_3$ (or related complexes based upon 2,2′:6′,2″-terpyridine) is expected to be highly selective to β-$RuCl_3$ and related compounds, considering that there is no alteration in oxidation state or local coordination geometry about the ruthenium atom. In fact, to the best of our knowledge, the formation of ttpy$RuCl_3$ has only ever been performed from β-$RuCl_3$. Therefore, by investigating the formation of ttpy$^{106}RuCl_3$ from the relatively small proportion of the ^{106}Ru contaminant that is extractable in ethanol and by demonstrating the highly selective nature of the reaction, we can speak to the existence of β-$^{106}RuCl_3$. In this way, we may determine whether or not passivation of RuO_4 in hydrochloric acid was invoked.

Radiochemistry 1: Synthesis and Purification of ttpy$RuCl_3$ in the Presence of ^{106}Ru. With the tridentate ligand (ttpy) in hand, reaction of 1.1 equivalents with β-$RuCl_3$ proceeds in high yield (>80%) from ethanolic solution, provided that the reactant concentration is >0.01 M. The overall radiochemical reaction is presented in Scheme 2 (see also *SI Appendix*, Fig. S16), and experimental details are provided in *Materials and Methods*. Ethanol containing leached ^{106}Ru (74.5 ± 5.3 mBq ^{106}Ru) was used to synthesize ttpy$RuCl_3$ from stable β-$RuCl_3$ in 88% yield (0.12 g theoretical yield). The insoluble precipitate formed was isolated and counted using a high-purity germanium well detector, using the gamma photon emission at 622 keV (9.93% intensity) associated with the short-lived ^{106}Rh progeny as the analytical signal. Relative to the ethanol extract, 28.8 ± 3.5% of the ^{106}Ru activity was found to be localized in the initial precipitated material. The remaining ethanolic filtrate was chromatographed on silica gel using an eluent mixture of acetonitrile and saturated, aqueous potassium nitrate solution (7:1, respectively) to isolate the sole by-product, Ru(ttpy)$_2^{2+}$, after work-up with NH_4PF_6. This material was similarly gamma-counted and was found to contain 11.2 ± 2.0% (8.37 ± 1.41 mBq) of the ^{106}Ru activity from the ethanol extract. In contrast to the fate of the stable ruthenium, this is a sizeable proportion of ^{106}Ru. However,

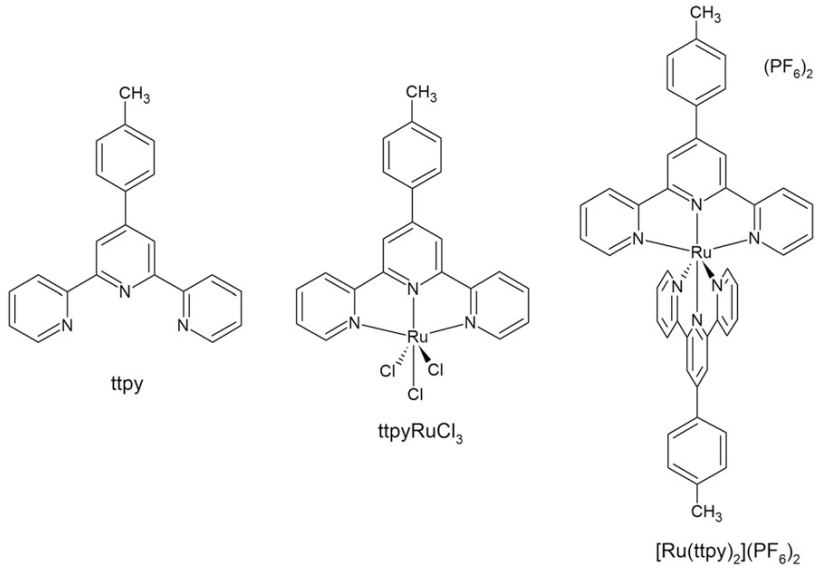

Fig. 1. Synthetic targets used to evaluate the reactivity and distribution of ^{106}Ru.

this is quite reasonable considering that the 0.1 equivalent excess of ttpy used in the reaction (i.e., 7.5 mg) constitutes an enormous molar excess over ^{106}Ru (4.03×10^{12}-fold), and that inorganic ruthenium species other than β-$RuCl_3$ will react to form $Ru(ttpy)_2^{2+}$ under these conditions. Again, we see evidence of a complex, multicomponent ^{106}Ru contaminant.

While 28.8 ± 3.5% of the ethanol-extracted ^{106}Ru was found to be isolated with the stable product, $ttpyRuCl_3$, consideration of potential flocculation effects precluded the conclusion that $ttpy^{106}RuCl_3$ was formed to any extent. To address this, a high-performance liquid chromatography (HPLC) method was developed to separate $ttpyRuCl_3$ from $Ru(ttpy)_2^{2+}$, and from other environmental contaminants associated with the filter material. This HPLC method was first developed on an analytical scale and later adapted to a semi-preparative one, using a C_{18} stationary phase and a mobile phase consisting of an isocratic mixture of *N,N′*-dimethylformamide (DMF) and methanol (90:10, respectively), optimized at 1.30 mM of tetrabutylammonium chloride (*SI Appendix*, Figs. S14 and S15). Note that method development was confined by the limited solubility of $ttpyRuCl_3$ (appreciably soluble in *N,N′*-DMF, tolerating no more than 30% methanol) and that effective separation of $ttpyRuCl_3$ and $Ru(ttpy)_2^{2+}$ was afforded mainly by the addition of the tetrabutylammonium chloride. The characteristic ligand-to-metal and metal-to-ligand charge-transfer bands that characterize $ttpyRuCl_3$ and $Ru(ttpy)_2^{2+}$, respectively, were used to arrive at a detection wavelength of 450 nm in the electronic spectrum.

The entirety of the crude $ttpyRuCl_3$ isolated in Scheme 2 (108 mg, 20.9 ± 2.5 mBq ^{106}Ru) was purified by HPLC (Fig. 2). Fractions collected at set times in the HPLC purification process were combined and concentrated for gamma counting. The very small amount of ^{106}Ru measured in these reaction components required long detection count times ranging from 1 to 2 Ms. For this range of count time, the concomitant span of detection capabilities, as defined by the critical limit (L_c) and detection limit (L_d) at 95% confidence, corresponded to L_c = 3.7 mBq and L_d = 7.5 mBq for 1 Ms and L_c = 2.9 mBq and L_d = 5.9 mBq for 2 Ms. Nevertheless, a very good account of the initial ^{106}Ru in the crude $ttpyRuCl_3$ was provided by the components of the HPLC purification process. The elution peak at retention time (R_t) = 2.96 min, corresponding to $ttpyRuCl_3$, was found to contain 10.2 ± 2.6 mBq of ^{106}Ru (Fig. 3), while the fraction collected from 0 to 2.0 min, representing unretained material from the column hold-up volume, was found to contain 12.7 ± 3.1 mBq of ^{106}Ru (*SI Appendix*, Figs. S19 and S20). These quantities represent 48.7 ± 13.2% ($ttpyRuCl_3$) and 60.9 ± 14.8% (unretained) of the

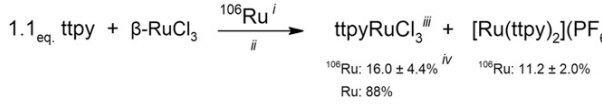

Scheme 2. Reaction targeting the formation of $ttpyRuCl_3$ in the presence of ^{106}Ru. *i*^{106}Ru obtained from ethanol extraction. *ii*Two hours at reflux temperature. *iii*Purified by reverse-phase HPLC. *iv*Adjusted for chemical recovery.

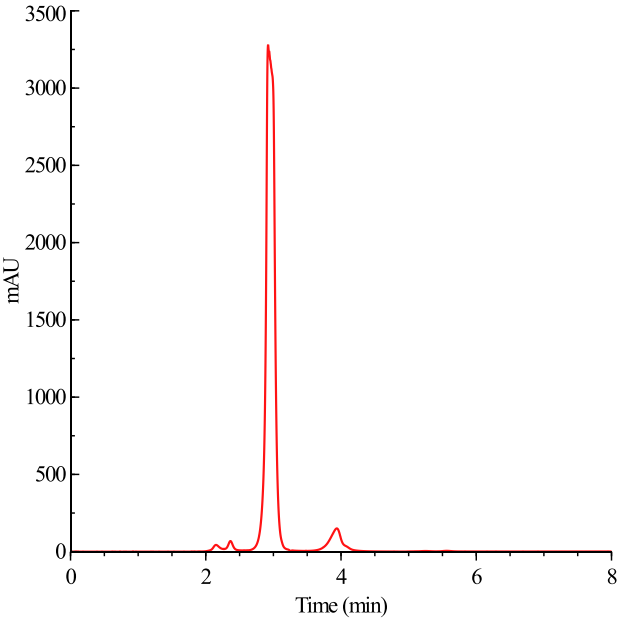

Fig. 2. HPLC purification of $ttpyRuCl_3$ (R_t = 2.96 min) that precipitated from the radiochemical reaction described in Scheme 2. Monitored at λ = 450 nm.

^{106}Ru measured in the crude ttpyRuCl$_3$ before purification. The unretained fraction of ^{106}Ru likely consists of unreactive species removed by flocculation as ttpyRuCl$_3$ precipitated from the reaction solution.

Radiochemistry 2: Reaction of ^{106}Ru without Stable Ru Precursor. To provide additional insight and validation, particularly in light of the relatively large counting uncertainty associated with the gamma measurements of the preceding radiochemical experiment (Scheme 2), an analogous experiment was performed without the use of stable ruthenium precursor. In this instance, the formation of the reduced, bis-ligated complex $[^{106}Ru(ttpy)_2]^{2+}$ was targeted (Scheme 3 and *SI Appendix*, Fig. S18). The reaction to form $[Ru(ttpy)_2]^{2+}$ from 2.1 equivalents of ttpy in ethanol alone was found to be more broadly applicable than previously believed, proceeding smoothly from both Ru(III) and Ru(IV) precursors containing suitable counter anions, as demonstrated by chemical recoveries obtained with β-RuCl$_3$ (89%), $(NH_4)_2RuCl_6$ (94%), and Ru(NO)(NO$_3$)$_3$ (90%). Thus, we can use an excess of ttpy to compare the reactive fractions of the ^{106}Ru contaminant (extractable in ethanol) obtained from both carrier and carrier-free approaches (Table 1).

Here, a mere 0.20 mg of ttpy amounted to an extraordinary molar excess (1.7×10^{10}-fold) relative to ^{106}Ru. Following termination of the reaction, stable $[Ru(ttpy)_2](PF_6)_2$ was added as a tracer to enable chromatographic purification. Gamma counting of the isolated fraction revealed that 28.6 ± 2.6% (0.137 ± 0.013 Bq) of the ^{106}Ru from the ethanol extract was colocated with the added $[Ru(ttpy)_2](PF_6)_2$. A spectral overlay of the gamma-counted reaction components is presented in Fig. 3. From Table 1, summing contributions of the isolated components from the β-RuCl$_3$ radiochemical reaction (Scheme 2, ttpyRuCl$_3$ and $Ru(ttpy)_2^{2+}$), we find a total reactive fraction of 27.2 ± 9.0%. This result is in excellent agreement with the reactive fraction found for the corresponding carrier-free reaction (Scheme 3). Such an intersection of results strengthens further the identification and contribution of ttpy^{106}RuCl$_3$ and additionally serves

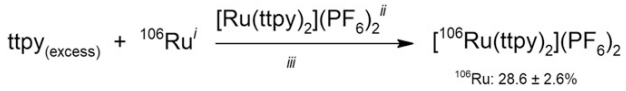

Scheme 3. Reaction to form $[^{106}Ru(ttpy)_2](PF_6)_2$. ^{i}^{106}Ru obtained from ethanol extraction. ^{ii}Stable complex added postreaction as a tracer for chromatographic isolation. ^{iii}Ethanol, 90 °C, 16 h.

to provide a more accurate uncertainty estimate considering the higher activity (i.e., lower counting uncertainty) afforded by the carrier-free reaction (Fig. 3).

Formation of ttpyRuCl$_3$: Reaction Selectivity. While the formation of ttpyRuCl$_3$ has only ever been performed from β-RuCl$_3$ (37, 40), we undoubtedly expect the reaction to proceed to an appreciable extent from higher-order polychlorinated Ru(III) compounds, given the favorable binding interaction afforded by the tridentate ligand, ttpy, and considering that their solution equilibria in dative solvent will include the formation of RuCl$_3$ (41, 42). Nevertheless, by defining the applicable scope of this reaction, we refine and gain confidence in the types of contaminant ruthenium species that could lead to the observed formation of ttpy^{106}RuCl$_3$. Instead of testing an exhaustive selection, several compounds were chosen that reflect a systematic variation from soluble polychlorinated Ru(III) species, namely, variation with respect to ruthenium valency, exchangeable supporting ligands, and physical format. To this end, we had selected the polychlorinated Ru(IV) salt, $(NH_4)_2RuCl_6$, the Ru(III) mixture, Ru(NO)(NO$_3$)$_3$ (in nitric acid), and the highly insoluble allotrope to β-RuCl$_3$, α-RuCl$_3$. In nitric acid solution, what is denoted commercially as Ru(NO)(NO$_3$)$_3$ is actually a mixture of ruthenium (III/IV) complexes varying in proportion of coordinated and exchangeable nitrate, nitrite, and water molecules, depending on solution conditions (16, 43); moreover, it is directly representative of the nitric acid-based oxidative mixtures

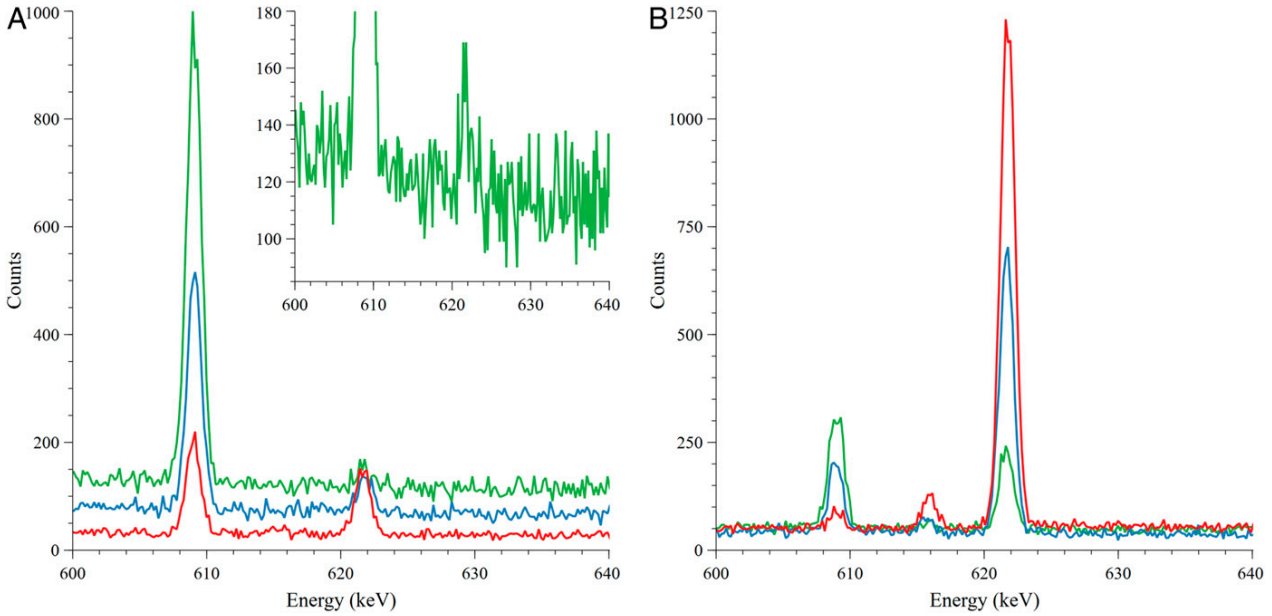

Fig. 3. Overlay of gamma spectra, in the analytical region of interest (600 to 640 keV) for ^{106}Ru measured in the reaction components leading to the formation and isolation of ttpyRuCl$_3$ (*A*) and $[^{106}Ru(ttpy)_2](PF_6)_2$ (*B*). Depicted are gamma emission peaks corresponding to ^{214}Bi (609 keV, naturally occurring) and ^{106}Ru (616 and 622 keV). (*A*) Ethanol extract (red); crude ttpyRuCl$_3$ (blue); purified ttpyRuCl$_3$ (green). (*B*) Filter piece (red); ethanol extract (blue); isolated fraction colocated with added $[Ru(ttpy)_2](PF_6)_2$ (green).

Table 1. Allocation of ^{106}Ru in the radiochemical reactions relative to the initial quantity measured in the ethanol extract

Reaction	ttpyRuCl$_3$ (% ^{106}Ru, k = 1)	[Ru(ttpy)$_2$](PF$_6$)$_2$ (% ^{106}Ru, k = 1)	Reactive fraction of ^{106}Ru, %
ttpy + β-RuCl$_3$ + ^{106}Ru	14.0 ± 3.9* (16.0 ± 4.4)†	11.2 ± 2.0	27.2 ± 9.0
ttpy + ^{106}Ru	—	28.6 ± 2.6	28.6 ± 2.6

*Isolated ttpyRuCl$_3$ fraction from HPLC (R_t = 2.96 min).
†Adjusted for chemical recovery.

used to dissolve spent fuel early in the PUREX process (16, 17). Subjecting these model compounds to the reaction conditions used to synthesize ttpyRuCl$_3$ (*Materials and Methods*), with the notable exception of using saturated ethanolic and aqueous ethanolic solutions of potassium chloride in the case of Ru(NO)(NO$_3$)$_3$, produced no discernable trace of ttpyRuCl$_3$ (Table 2). These tests demonstrate that the reactive tolerance is limited to polychlorinated ruthenium (III) compositions. Therefore, we can conclude that the isolated ttpy^{106}RuCl$_3$ in these experiments originated from ^{106}Ru filter contaminant that exists as β-^{106}RuCl$_3$ or, more generally, [^{106}RuCl$_n$(H$_2$O)$_{6-n}$]$^{3-n}$. Considering the sequential fractionation of ^{106}Ru in the described experiments, from filter material to ethanolic extract (7.35 ± 0.70%) to precipitated ttpyRuCl$_3$ (28.8 ± 3.5% with 88% chemical recovery) to HPLC isolated ttpyRuCl$_3$ (48.7 ± 13.2%), we determine that 1.17 ± 0.36% of the filter contaminant exists in this chemical form.

Assessment of the Bulk ^{106}Ru Contaminant. That a small proportion of the ^{106}Ru contaminant is composed of polychlorinated ^{106}Ru(III) species is direct evidence that fuel reprocessing was the origin of the 2017 environmental release. Plausible reprocessing activities that could lead to such compounds are limited to either the reductive trapping of oxidatively generated RuO$_4$ in hydrochloric acid (29–31) or the electrochemical reduction and metallization of uranium in spent fuel from molten alkali chloride mixtures (44–46). Fortunately, the compositions formed from both approaches differ substantially. An interrupted process involving the reductive trapping of RuO$_4$ in hydrochloric acid would reasonably be expected to contain some measure of the inert RuO$_2$, owing to the decomposition of RuO$_4$, along with a mixture of Ru(IV) and Ru(III) chloro complexes, the proportion of which will depend upon temperature, duration, and HCl concentration but should favor heavily the reduction to Ru(IV) (30, 31). Mixed nitrosyl–nitrate–nitrite Ru(III/IV) complexes derived from an oxidative nitric acid slurry used to generate the RuO$_4$ may also become entrained upon release, depending on the system engineered. In the case of the pyroprocessing of spent fuel from molten alkali chloride mixtures, chloro complexes are exclusively formed and, although dependent on melt temperature and duration, center upon the formation of Ru(III) chloro complexes with some disproportionation/decomposition to metallic ruthenium occurring very slowly at temperatures >550 °C (44).

By investigating the reactive nature of the bulk of the ^{106}Ru contaminant, we may reveal additional information to help discern between these scenarios. To do this, we have selected commercially available ruthenium compounds representative of the types encountered in such reprocessing activities (Table 2). These compounds comprise a diverse array, differentiated by ruthenium valency, supporting ligand, and physical format, and we can use them to characterize an appropriate reaction (i.e., establish the rules of reactivity). Then, by applying the reactive conditions to the ^{106}Ru contaminant and tracking its subsequent fate and distribution, we may make reasonable deductions about the bulk chemical composition of the ^{106}Ru contaminant and examine how these align with the two plausible scenarios.

Reaction to form the homoleptic complex [Ru(ttpy)$_2$](PF$_6$)$_2$ (Fig. 1) was used as the reactive vehicle. Forceful reaction conditions by way of elevated temperature (154 °C), extended duration (16 h), and provision of dechlorinating agent (AgNO$_3$) were selected to encourage reaction completion (*Materials and Methods*). Interestingly, to date, such reactions have only been performed using Ru (III) (typically β-RuCl$_3$) or specially prepared Ru (II) halogenated compounds (47, 48). Only one literature reference was found pertaining to solvent reduction of a Ru (IV) compound, and this was carried out under microwave irradiation, unrelated to polypyridyl complexation (49). It is therefore quite interesting that this reaction system was found to be very effective for both Ru(III) and Ru(IV) precursors, to the extent that a potent oxidizing agent used in organic synthesis, KRuO$_4$ (50, 51), reacted appreciably while the highly refractory allotrope of RuCl$_3$, α-RuCl$_3$, was found to react smoothly and in essentially quantitative yield (Table 2). Such marked general reactivity using these conditions underscores the complete absence of reactivity observed in the case of RuO$_2$.

Radiochemical details are provided in *Materials and Methods*. For all reactions, we have coupled chromatography and radiography to demonstrate that ^{106}Ru has been incorporated into the isolated complex (i.e., [Ru(ttpy)$_2$](PF$_6$)$_2$ + [^{106}Ru(ttpy)$_2$](PF$_6$)$_2$). Here, we have used thin-layer chromatography (TLC) (normal phase, preparative scale) to demonstrate the purity of the isolated [Ru(ttpy)$_2$](PF$_6$)$_2$ by elution with an aqueous acetonitrile solution of high ionic strength. The decay progeny, ^{106}Rh [$t_{1/2}$ = 30 s, $\beta_{(mean)}$ = 1,410 keV] is a hard beta-particle emitter, making it well-suited to autoradiographic imaging. Prolonged exposure of the phosphor imaging plate (6 wk) yields darkened areas that

Table 2. Chemical yields of [Ru(ttpy)$_2$](PF$_6$)$_2$ and ttpyRuCl$_3$ from representative inorganic ruthenium compounds

Reactant	Ru ox. state	Solid-state form	[Ru(ttpy)$_2$](PF$_6$)$_2$, % yield	ttpyRuCl$_3$, % yield
Ru(NO)(NO$_3$)$_3$*	3$^+$	Molecular	92	No reaction†
(NH$_4$)$_2$RuCl$_6$	4$^+$	Molecular	96	No reaction
β-RuCl$_3$	3$^+$	Polymeric	94	88
α-RuCl$_3$	3$^+$	Polymeric	95	No reaction
KRuO$_4$	7$^+$	Molecular	19	No reaction
RuO$_2$	4$^+$	Polymeric	No reaction	No reaction

*Mixture in nitric acid. ox., oxidation.
†Reacted in presence of large excess of potassium chloride.

correlate to the $[Ru(ttpy)_2](PF_6)_2$ isolated from reactions involving ^{106}Ru-contaminated filter pieces and their aqueous extracts (*SI Appendix*, Fig. S22). As with all radiochemical experiments described herein, every effort to provide a full account of the initially measured ^{106}Ru activity has been made by measuring all subsequently isolated reaction products, by-products, and other relevant materials. In this way, the reactive and unreactive portions of the ^{106}Ru contaminant can be independently determined, where ^{106}Ru localized with $[Ru(ttpy)_2](PF_6)_2$ constitutes the reactive portion and ^{106}Ru measured in other materials and by-products (AgCl) constitutes the unreactive portion. For all reactions, a reasonably full account has been provided in consideration of the respective measurement uncertainty carried by each experimental component (General) and of the potential loss of material given the considerable number of mass transfer steps involved (*Radiochemistry*).

Direct Reaction with a Contaminated Filter Piece. Direct reaction of a portion (0.144 g, 7.99 ± 0.53 Bq) of the ^{106}Ru-contaminated filter piece in the presence of β-$RuCl_3$ resulted in 79.6 ± 4.9% (6.36± 0.39 Bq) of the ^{106}Ru being localized with the isolated $[Ru(ttpy)_2](PF_6)_2$ after gamma counting. The balance of the activity (unreactive portion) was reasonably well accounted for, with 8.62 ± 0.68% (0.689 ± 0.054 Bq) and 7.77 ± 0.60% (0.460 ± 0.035 Bq) measured in the remaining filter piece and the insoluble AgCl by-product, respectively.

Reactions Subsequent to Aqueous Extraction of a Filter Piece. To gain a bit more resolution, a similar reaction was performed on the aqueous extract of another filter piece. The ^{106}Ru that partitioned into the water extract (51.3 ± 2.4%, 6.14 ± 0.46 Bq) was found to be almost completely localized in the isolated $[Ru(ttpy)_2](PF_6)_2$ (95.3 ± 6.0%, 5.85 ± 0.37 Bq) with the balance of activity reasonably accounted for in the AgCl precipitate (6.06 ± 0.41%, 0.372 ± 0.025 Bq).

The filter piece was found to retain 27.8 ± 1.9% (3.33 ± 0.22 Bq) of the ^{106}Ru contaminant after aqueous extraction. The balance of ^{106}Ru activity (~20.9%) was most likely lost in transfer to the submicron filtration material which could not be accommodated in the well-detector space for measurement (*Gamma Spectrometry*). Direct reaction of the water-washed filter piece resulted in 75.2 ± 4.9% (2.50 ± 0.16 Bq) of the activity being localized in the isolated $[Ru(ttpy)_2](PF_6)_2$, with the balance reasonably accounted for in the AgCl by-product (16.2 ± 1.1%, 0.540 ± 0.038 Bq) and the remaining filter piece (9.06 ± 0.71%, 0.302 ± 0.024 Bq). Assuming that the activity remaining on the filter piece is representative of the entirety of ^{106}Ru that did not partition into the aqueous phase (i.e., 48.7 ± 2.4%) and summing reactive and unreactive contributions, we find that 85.6 ± 8.1% and 15.2 ± 1.4% of the initial ^{106}Ru contaminant to be reactive and unreactive, respectively. These results are in reasonably good agreement with those obtained by direct reaction on a ^{106}Ru-contaminated filter piece. Clearly, one or more of the water-insoluble components is chemically inert to the reaction conditions employed. According to Table 2, chemical inertness and a high degree of water insolubility are certainly consistent with the occurrence of RuO_2. Against the previously mentioned compositional characteristics for both trapping and pyroprocessing scenarios, the delineation of a small Ru(III) polychlorinated component (1.17 ± 0.36%) and a substantial water-insoluble, reactively inert component (~20%) consistent with RuO_2 support an origin from the reductive trapping of RuO_4 in HCl. Such activity further explains the high radiopurity of radio-ruthenium observed in environmental samples (1), since volatilization of RuO_4 from waste streams stands alone as the means to provide optimal separation efficiency (14).

Concluding Remarks

We have revealed compositional markers for the ^{106}Ru contaminant that are uniquely consistent with nuclear waste reprocessing, namely the reductive trapping of RuO_4 in HCl. This finding aligns with other empirical evidence pertaining to radiopurity and age estimation (i.e., time since removal from irradiation) for spent nuclear fuel obtained from measurement of the ^{103}Ru:^{106}Ru ratio (1). An age estimate of ~2 y is considerably less than the usual time (≥3 y) allotted before reprocessing under typical reactor operating conditions (52). Therefore, a RuO_4 trapping process in HCl would undoubtedly be exothermic, exacerbating an already energetic mixture that, in light of the high volatility and potential explosive decomposition of RuO_4 (15), gives credence to the occurrence of an abrupt, uncontrolled release (i.e., explosion). Such conditions would certainly aid in the volatilization and dispersion of otherwise nonvolatile ruthenium species. For a facility undertaking the purification of fission products from spent nuclear fuel for commercial gain, it is hard to ignore the potential profit afforded by obtaining ^{106}Ru in high-specific activity, considering its long-standing medical use in the development of brachytherapy plaques for the treatment of eye cancer (53, 54). For this application, it is commonly electrodeposited from solution onto silver, along with the addition of carrier $RuCl_3$ (54, 55). Since this requires a highly soluble form of ^{106}Ru, it makes sense to invoke a reductive technique that generates polychlorinated Ru(III/IV) species with a high degree of radiopurity and aqueous solubility, rather than the vast majority of passivation techniques that ultimately produce the highly insoluble RuO_2.

In closing, the detection of ^{106}Ru in aerosol filters across European surveillance networks in 2017 represents a limiting case for forensic investigation, considering the high radiopurity of the contaminant and the absence of detectable signatures or anomalies from colocated stable elements. However, as this work has demonstrated, new opportunities arise when the radioisotope pertains to an element capable of covalent bond formation. By subjecting the radioactive contaminant to iterative, well-characterized chemical transformations and determining its subsequent fate and distribution, we create an inferential process from which we can gain both generalized and highly specific information about the chemical form(s) of the radioactive contaminant. This work constitutes direct evidence for specific nuclear fuel reprocessing activity and, coupled with other measurements and atmospheric dispersion modeling, provides irrefutable proof as to the origin of the 2017 environmental release of ^{106}Ru. Moreover, this work serves, by example, as a potentially valuable addition to the established suite of nuclear forensic capabilities.

Materials and Methods

General. Particulate filters containing ^{106}Ru from the radiological monitoring networks of Germany (German Meterological Services Deutscher Wetterdienst) and Sweden (Swedish Defense Research Agency Totalförsvarets forskninginstitut) were graciously donated. Chemical experimentation was conducted on portions of a particulate filter sample obtained from Vienna, Austria, and was composed of polypropylene (air collection from 2017-09-28 to 2017-10-04 at a rate of 675 m^3/h).

Chromatographic supports consisting of alumina (neutral, type WN-6, super grade, flash chromatography), silica (high-purity grade, 220 to 440 mesh, flash chromatography), and preparative TLC plates (glass-backed, 2.0-mm SiO_2 layer) were purchased from Sigma-Aldrich, Ltd. Columns (C_{18}, XBridge: 3.5 μm, 250 × 4.6 mm and 5 μm, 250 × 10 mm) were purchased from Waters, Ltd. for analytical and preparative-scale HPLC separations, respectively. All aqueous and ethanolic extracts of contaminated filter pieces were filtered through conditioned syringe filters (0.1-μm pore size; Fisher Scientific) prior to gamma counting and subsequent reaction.

Solvents and reagents were used as received. These include *N,N′*-dimethylformamide (Fisher Chemical, ACS grade), acetonitrile (Fisher Chemical, ACS grade), methanol (Fisher Chemical, Optima grade), dichloromethane (Fisher Chemical, ACS grade), diethyl ether (Fisher Chemical, ACS grade), potassium nitrate (Sigma-Aldrich, ≥ 99%), silver nitrate (Sigma-Aldrich, ≥ 99%), ammonium hexafluorophosphate (Acros Organics, 99%), 2-acetyl pyridine (Sigma-Aldrich, 99%), *p*-tolualdehyde (Sigma-Aldrich, 97%), β-ruthenium chloride hydrate (Sigma-Aldrich, reagent plus), ammonium hexachlororuthenate (Strem Chemicals, 99%), ruthenium (III) nitrosyl nitrate solution (Sigma-Aldrich, 1.5% Ru in 6.8 wt % nitric acid), ruthenium (IV)

oxide (Sigma-Aldrich, 99.9%), potassium perruthenate (Sigma-Aldrich), α-ruthenium chloride (Merck), and tetrabutylammonium chloride (Sigma-Aldrich, 98%).

Experimental uncertainty was derived by combining contributions from counting statistics, counting efficiency, and mass transfer (if applicable) in quadrature.

Synthesis and Characterization.

Synthesis of 4′-p-tolyl-2,2′; 6′,2″-terpyridine (ttpy). Synthesis of this ligand resembled previously reported procedures (35, 36); however, these procedures were found to yield unsatisfactory purity considering the application. In our hands, 2-acetylpyridine (7.83 g, 0.065 mol and KOH aqueous solution (5 mL, 15 wt %) were stirred briefly in methanol (60 mL) at room temperature (~5 min). *p*-tolualdehyde (3.56 g, 0.03 mol) and concentrated ammonium hydroxide (25 mL) were then added and the mixture heated to reflux with vigorous stirring for 48 h. After cooling, the reaction mixture was decanted into a large separatory funnel. To this was added 600 mL of water and 600 mL of dichloromethane. After agitation, the dichloromethane layer was removed, washed once more with 600 mL water, then separated and dried over sodium sulfate. The dichloromethane was removed by distillation and the remaining residue was recrystallized from 95:5 ethanol/water to yield 2.45 g of slightly impure material. High purity was achieved by flash chromatography using 688 g of alumina, previously deactivated by thorough mixing with water (5% by mass) and using toluene as the mobile phase. Yield = 1.91 g (20%); ^{1}H NMR (600 MHz, d_6-DMSO) δ ppm: 2.40 (s, 3H, H_{tolyl}), 7.40 (d, J = 8.0 Hz, 2H, $H_{tolyl\ 3,5}$), 7.53 (dd, J = 7.5 Hz, J = 5.0 Hz, 2H, $H_{5,5''}$), 7.83 (d, J =8.0 Hz, 2H, $H_{tolyl\ 2,6}$), 8.04 (t, J = 7.5 Hz, 2H, $H_{4,4''}$), 8.67 (d, J = 8.0 Hz, 2H, $H_{3,3''}$), 8.70 (s, 2H, $H_{3',5'}$), 8.76 (d, J = 5.0 Hz, 2H, $H_{6,6''}$). ESI(+)MS found (calcd) for $C_{22}H_{17}N_3H$: 324.1511 (324.1501).

Synthesis of ttpyRuCl$_3$. This compound was prepared according to literature procedure. Note that reactant concentration should be maintained ≥0.01 M to attain high yield. Note also that the ethanol extract from a filter piece contaminated with ^{106}Ru, after filtration through a submicron filter, would be used in place of ethanol alone, according to the following typical preparation. The ligand ttpy (0.0825 g, 2.55 × 10^{-4} mol) and $RuCl_3$ hydrate (0.0607 g, 2.32 × 10^{-4} mol) were combined in 20 mL of ethanol (95%) and heated to reflux with agitation for 2 h. After cooling, the insoluble solid was isolated by filtration over a glass filter frit then agitated 5 to 10 min in ethanol (40 mL) and filtered. The residue was then rinsed with an additional portion of ethanol (40 mL) and finally with diethyl ether (40 mL). The solid was dried under vacuum. Yield = 0.123 g (88%). ESI(+)MS found (cald) from DMF solution for $C_{44}H_{34}N_6RuCl_3Na$: 554.9445 (554.9416).

Synthesis of [Ru(ttpy)$_2$](PF$_6$)$_2$ from β-RuCl$_3$.

Procedure (A). This compound was prepared similarly to literature procedures. Typically, the ligand ttpy (0.111 g, 3.42 × 10^{-4} mol, 2.1 equivalents), $RuCl_3$ hydrate (0.0426 g, 1.63 × 10^{-4} mol), and $AgNO_3$ (4.89 × 10^{-4} mol) were combined in *N,N′*-DMF (reagent grade, 50 mL) and heated to reflux for 16 h. The reaction mixture was then cooled to room temperature, and the AgCl by-product was removed by vacuum filtration over a glass filter frit. The filtrate was then distilled to dryness and the residue chromatographed on silica using an acetonitrile/saturated, aqueous potassium nitrate (7:1) mixture as mobile phase. The isolated compound was transferred to a separatory funnel, followed by addition of water, NH_4PF_6, and enough dichloromethane to render a phase separation. After washing, the aqueous layer was removed and discarded. This process was repeated twice more, after which the organic phase was collected and distilled to dryness. The residue was then redissolved in acetonitrile and precipitated from water. This precipitate was collected by vacuum filtration, redissolved in acetonitrile, and precipitated from diethyl ether. This final precipitate was collected by filtration and dried under vacuum. Yield = 0.160 g (94%); ^{1}H NMR (600 MHz, CD_3CN) δ ppm: 2.54 (s, 3H, H_{tolyl}), 7.18 (dd, J = 8.0 Hz, J = 6.0 Hz, 2H, $H_{5,5''}$), 7.42 (d, J = 6.0 Hz, 2H, $H_{6,6''}$), 7.58 (d, J = 8.0 Hz, 2H, $H_{tolyl\ 3,5}$), 7.94 (t, J = 8.0 Hz, 2H, $H_{4,4''}$), 8.11 (d, J = 8.0 Hz, 2H, $H_{tolyl\ 2,6}$), 8.64 (d, J = 8.0 Hz, 2H, $H_{3,3''}$), 8.99 (s, 2H, $H_{3',5'}$). ESI(+)MS found (calcd) for $C_{44}H_{34}N_6Ru$ (M^{2+}): 373.9200 (374.0962).

Procedure (B). Alternatively, the ligand ttpy (0.111 g, 3.42 × 10^{-4} mol, 2.1 equivalents) and $RuCl_3$ hydrate (0.0426 g, 1.63 × 10^{-4} mol) were combined in ethanol (95%, 50 mL) and heated to reflux for 16 h. Distillation of the ethanol, followed by chromatographic isolation and work-up as outlined above in *Procedure (A)* gave the target complex in 89% yield (0.151 g). Notably, the same molar quantities and conditions applied to $(NH_4)_2RuCl_6$ and $Ru(NO)(NO_3)_3$ gave comparable yields (94 and 90%, respectively) for the formation of $[Ru(ttpy)_2](PF_6)_2$.

Synthesis of [Ru(ttpy)$_2$](PF$_6$)$_2$ from α-RuCl$_3$, (NH$_4$)$_2$RuCl$_6$, Ru(NO$_3$)$_3$(NO), KRuO$_4$, and RuO$_2$ in N,N′-DMF. These compounds were reacted, and subsequently isolated, according to the scale and conditions outlined in *Procedure (A)* for β-$RuCl_3$. Yield (α-$RuCl_3$) = 0.162 g (95%); yield ($(NH_4)_2RuCl_6$) = 0.163 g (96%); yield ($Ru(NO_3)_3(NO)$) = 0.156 g (92%); yield ($KRuO_4$) = 0.032 g (19%); yield (RuO_2) = no reaction.

Gamma Spectrometry. The gamma detection system used was a small anode germanium (SAGe) well detector (GSW275L; Mirion Technologies) outfitted with a cosmic veto (plastic scintillator) detector to reduce the background (CV System-LM; Mirion Technologies). The SAGe well detector has a diameter of 28.00 mm and a depth of 40.00 mm with an active volume for the germanium crystal of 65.50 mm (thickness) by 86.6 mm (diameter). The resolution of the detector (full width at half maximum) is 1.835 keV at 1,332.5 keV. The gamma acquisition software used was Genie 2000 v3.4.1 (Mirion Technologies), with the counting efficiencies of the samples in the well of the SAGe simulated using LabSOCS v4.4.1 (Mirion Technologies). The analysis software used in quantifying the activity of ^{106}Ru was a peak-fitting and peak identification program called UniSAMPO (v 2.67)-Shaman (v 1.2), developed by Baryon Oy of Finland. The HPGe well detector was calibrated for energy and shape resolution using a National Institute of Standards and Technology–traceable standard (SRS 112559; Eckert & Ziegler) prior to measurement. Data were collected from 0 to 2,800 keV for 16,384 channels. Samples were counted in 20-mL glass scintillation vials (61 × 28 mm, outer dimensions). Detector count times varied greatly depending on the amount of ^{106}Ru in the sample and ranged anywhere from several thousand to several million seconds, ideally until an acceptable counting uncertainty was attained (<10%). Analysis was based upon the 622-keV gamma emission (9.93% abundance) associated with the ^{106}Ru progeny, ^{106}Rh, while decay corrections were performed using $t_{1/2}$ = 371.8 d for ^{106}Ru. For the experiment incorporating ^{106}Ru into $ttpyRuCl_3$, the purified reaction components were gamma counted until the critical limit (L_c) was exceeded and the peak was automatically identified by the peak search algorithm of the analysis software (UniSAMPO-Shaman, Baryon Oy, Finland). For instance, detection count times ranging from 1 to 2 Ms corresponded to detection capabilities, as defined by the L_c and detection limit (L_d) at 95% confidence, of L_c = 3.7 mBq, L_d = 7.5 mBq and L_c = 2.9 mBq, L_d = 5.9 mBq, respectively.

NMR and Mass Spectrometry. The ^{1}H NMR spectra were acquired on a Bruker AVANCE III 600 MHz spectrometer by the University of Ottawa NMR Facility. Chemical shifts are reported relative to Me_4Si as an internal reference. Mass spectra were obtained using a Micromass Q-TOF II Electrospray Ionization Mass Spectrometer by the John L. Holmes mass spectrometry facility at the University of Ottawa.

HPLC. HPLC was performed using a Dionex ICS-6000 instrument equipped with photodiode array detector (PDA-1; Thermo Scientific), autosampler (AS-AP; Thermo Scientific), and fraction collector (ASX-280-FC; Thermo Scientific) and employing a C_{18} column (3.5 μm, 250 × 4.6 mm and 5 μm, 250 × 10 mm) from Waters, Ltd. Chromeleon 7 (Thermo Scientific) was the software package used for instrument control and analysis. All injections and subsequent runs were monitored at both 254- and 450-nm wavelength.

Radiochemistry. Transformation of β-$RuCl_3$ to form either $ttpyRuCl_3$ or $[Ru(ttpy)_2](PF_6)_2$ in the presence of ^{106}Ru adhered to the respective protocols outlined above in *Synthesis and Characterization*. Typically, a filter piece was shaved with a razor into many thin pieces, and these were placed inside a scintillation vial for gamma counting prior to reaction. Once transferred to the reaction vessel, the empty scintillation vial was gamma-counted once more to ensure the efficacy of transfer.

Reactions with β-RuCl$_3$. For reaction to form $ttpyRuCl_3$ (*SI Appendix*, Fig. S16), the shaved filter pieces (1.03 ± 0.08 Bq ^{106}Ru) were immersed in 5 mL of ethanol and agitated in an ultrasound bath for 10 to 20 min, after which the ethanol was removed via syringe and filtered. The process was repeated twice more, and the ethanol fractions were combined and gamma-counted (0.074 ± 0.005 Bq ^{106}Ru). The ethanol washings were then transferred to a reaction vessel, along with an additional 5 mL of ethanol (rinse). The reaction protocol described herein for $ttpyRuCl_3$ (*Synthesis and Characterization*) was carried out, giving the target complex in 88% yield. This material was then gamma-counted, as were the subsequent components from its HPLC purification.

For direct reaction of a filter piece to form $[Ru(ttpy)_2](PF_6)_2$ (*SI Appendix*, Fig. S17), the gamma-counted filter shavings (7.99 ± 0.53 Bq ^{106}Ru) were transferred to a reaction vessel followed by the addition of 10 mL of water. After brief agitation in an ultrasound bath, the reaction protocol outlined herein for $[Ru(ttpy)_2](PF_6)_2$ was carried out (*Synthesis and Characterization*), giving a comparable yield for the final product (93%). All components

(i.e., $[Ru(ttpy)_2](PF_6)_2$, AgCl by-product, and the remaining filter pieces) were subsequently gamma-counted.

For reaction to form $[Ru(ttpy)_2](PF_6)_2$ from the aqueous extract (*SI Appendix*, Fig. S17), the shaved filter pieces (11.97 ± 0.89 Bq ^{106}Ru) were immersed in 5 mL of water and agitated for 10 to 20 min in an ultrasound bath, after which the water was separated via syringe and filtered. The process was repeated twice more, and the aqueous fractions were combined and gamma-counted. The aqueous extract was then transferred to a reaction vessel, followed by an additional 5 mL of water (rinse). Complexation was carried out according to the procedure described herein for $[Ru(ttpy)_2](PF_6)_2$ (*Synthesis and Characterization*), with the exception that a higher-proportion of DMF was used (60 mL). The target complex, $[Ru(ttpy)_2](PF_6)_2$, was isolated in 95% yield. All components (i.e., $[Ru(ttpy)_2](PF_6)_2$, AgCl by-product, and the remaining filter pieces) were subsequently gamma-counted. The remaining, washed filter pieces were reacted separately in DMF to give the isolated $[Ru(ttpy)_2](PF_6)_2$ in 94% yield, which was then gamma-counted along with the other reaction components.

Carrier-free reaction. Shaved filter pieces (0.48 ± 0.03 Bq ^{106}Ru) were immersed in 5 mL of ethanol and agitated in an ultrasound bath for 10 to 20 min, after which the ethanol was removed via syringe and filtered. The process was repeated twice more, and the ethanol fractions were combined and gamma-counted. The ethanol washings were concentrated by vacuum distillation then transferred with rinse solutions to a 3-mL conical reaction vessel. The ligand (0.20 mg, 6.18×10^{-7} mol) was added from a stock solution in ethanol to give a final reaction volume of 0.5 mL. A stir bar was added and a Teflon screw cap was secured. The reaction solution was agitated while immersed in an oil bath set to 90 °C for 16 h (*SI Appendix*, Fig. S18). After cooling to room temperature, the stir bar was removed and the reaction solution transferred to a distillation flask, followed by 20 mg of $[Ru(ttpy)_2](PF_6)_2$ (stable Ru). The solvent was removed by distillation, and the mixture was chromatographed on silica gel and worked up as previously described above in *Synthesis and Characterization*. The isolated complex was quantitatively recovered and gamma-counted.

Autoradiography. Autoradiography of chromatographed reaction products (*SI Appendix*, Figs. S21 and S22), isolated in the presence of ^{106}Ru, was performed on a BAS-5000 Image Analysis System (Fujifilm). Imaging plates (BAS-SR2025; GE Healthcare) were developed in closed imaging cassettes (EXPSR CASS. 20 × 25 cm; GE Healthcare) and erased (zeroed) using an IP Eraser 3 (Fujufilm). Images were acquired using BASReader software (Fujifilm) and processed using Multi Gauge v.3.1 (Fujifilm).

Data Availability. All relevant data and protocols (synthetic and radiochemical) are provided in the paper and *SI Appendix*.

ACKNOWLEDGMENTS. M.W.C. and K.R.U. thank Dr. Andreas Bollhöfer (Bundesamt für Strahlenschutz) and Dr. Johan Kastlander (Totalförsvarets forskninginstitut) for provision of filter samples. D.Z. and G.S. acknowledge financial support from VolkswagenStiftung.

1. O. Masson *et al*., Airborne concentrations and chemical considerations of radioactive ruthenium from an undeclared major nuclear release in 2017. *Proc. Natl. Acad. Sci. U.S.A.* **116**, 16750–16759 (2019).
2. H. Ramebäck *et al*., Measurements of ^{106}Ru in Sweden during the autumn 2017: Gamma-ray spectrometric measurements of air filters, precipitation and soil samples, and in situ gamma-ray spectrometry measurement. *Appl. Radiat. Isot.* **140**, 179–184 (2018).
3. I. Penev, H. Angelov, T. Arsov, S. Georgiev, N. Uzunov, ^{106}Ru aerosol activity observation above Southeast Europe in october 2017. *Dokl. Bulg. Akad. Nauk.* **71**, 613–618 (2018).
4. D. Jakab *et al*., Methods, results and dose consequences of ^{106}Ru detection in the environment in Budapest, Hungary. *J. Environ. Radioact.* **192**, 543–550 (2018).
5. O. Saunier, D. Didier, A. Mathieu, O. Masson, J. Dumont Le Brazidec, Atmospheric modeling and source reconstruction of radioactive ruthenium from an undeclared major release in 2017. *Proc. Natl. Acad. Sci. U.S.A.* **116**, 24991–25000 (2019).
6. P. Bossew *et al*., An episode of Ru-106 in air over Europe, september-october 2017 - geographical distribution of inhalation dose over Europe. *J. Environ. Radioact.* **205–206**, 79–92 (2019).
7. J. H. Sørensen, Method for source localization proposed and applied to the October 2017 case of atmospheric dispersion of Ru-106. *J. Environ. Radioact.* **189**, 221–226 (2018).
8. V. Shershakov, R. Borodin, Some results of determining the source and reasons for the appearance of 106Ru in Russia in september – october 2017. *IOP Conf. Ser. Mater. Sci. Eng.* **487**, 012002 (2019).
9. V. Shershakov, R. Borodin, Y. S. Tsaturov, Assessment of possible location Ru-106 source in Russia in September–October 2017. *Russ. Meteorol. Hydrol.* **44**, 196–202 (2019).
10. T. Hopp, D. Zok, T. Kleine, G. Steinhauser, Non-natural ruthenium isotope ratios of the undeclared 2017 atmospheric release consistent with civilian nuclear activities. *Nat. Commun.*, 10.1038/s41467-020-16316-3.
11. D. Zok, J. H. Sterba, G. Steinhauser, Chemical and radioanalytical investigations of ^{106}Ru-containing air filters from Vienna in fall 2017: Searching for stable element anomalies. *J. Radioanal. Nucl. Chem.* **318**, 415–421 (2018).
12. F. A. Cotton, G. Wilkinson, C. A. Murillo, M. Bochmann, "Part 3: The chemistry of the transition elements" in *Advanced Inorganic Chemistry*, (Wiley-Interscience, ed. 6, 1999), pp. 877–1084.
13. J. A. Rard, Chemistry and thermodynamics of ruthenium and some of its inorganic compounds and aqueous species. *Chem. Rev.* **85**, 1–39 (1985).
14. I. Kajan, ""Transport and containment chemistry of ruthenium under severe accident conditions in a nuclear power plant," doctoral thesis" (Chalmers University of Technology, Gothenburg, Sweden, 2016).
15. C. Mun, L. Cantrel, C. Madic, A literature review on ruthenium behaviour in nuclear power plant severe accidents. (2007). https://hal-irsn.archives-ouvertes.fr/irsn-00177621. Accessed 10 April 2018.
16. C. Lefebvre, T. Dumas, M.-C. Charbonnel, P. L. Solari, Speciation of ruthenium in organic TBP/TPH organic phases: A study about acidity of nitric solutions. *Procedia Chem.* **21**, 54–60 (2016).
17. P. Swain, C. Mallika, R. Srinivasan, U. Kamachi Mudali, R. Natarajan, Separation and recovery of ruthenium: A review. *J. Radioanal. Nucl. Chem.* **298**, 781–796 (2013).
18. K. Motojima, Removal of ruthenium from PUREX process. *J. Nucl. Sci. Technol.* **26**, 358–364 (1989).
19. I. Kajan, T. Kärkelä, A. Auvinen, C. Ekberg, Effect of nitrogen compounds on transport of ruthenium through the RCS. *J. Radioanal. Nucl. Chem.* **311**, 2097–2109 (2017).
20. N. Yoshida, T. Ohno, Y. Amano, H. Abe, Migration behaviour of gaseous ruthenium tetroxide under boiling and drying accident condition in a reprocessing plant. *J. Nucl. Sci. Technol.* **55**, 599–604 (2018).
21. M. A. El-Absy, M. A. El-Amir, M. Mostafa, A. A. Abdel Fattah, H. M. Aly, Separation of fission produced ^{106}Ru and ^{137}Cs from aged uranium targets by sequential distillation and precipitation in nitrate media. *J. Radioanal. Nucl. Chem.* **266**, 295–305 (2005).
22. N. L. Sonar *et al*., Use of nickel sulfide-PMMA composite beads for removal of ^{106}Ru from alkaline radioactive liquid waste. *Sep. Sci. Technol.* **44**, 3753–3769 (2009).
23. S. Sato, N. Endo, K. Fukuda, Y. J. Morita, Optimization for removal of ruthenium from nitric acid solution by volatilizing with electrochemical oxidation. *Nucl. Sci. Tech.* **49**, 182–188 (2012).
24. P. Swain *et al*., Separation and recovery of ruthenium from nitric acid medium by electro-oxidation. *J. Radioanal. Nucl. Chem.* **303**, 1865–1875 (2015).
25. J. M. Richards, B. J. Mincher, Selective partitioning of ruthenium from nitric acid media. *Solvent Extr. Ion Exch.* **35**, 49–60 (2017).
26. P. Kumar Verma, R. Bhikaji Gujar, P. Kumar Mohapatra, An efficient method for radio-ruthenium separation from acidic feeds: Extraction, transport and spectroscopic studies. *J. Environ. Chem. Eng.* **6**, 5830–5836 (2018).
27. F. Mousset, F. Bedioui, C. Eysseric, Electroassisted elimination of ruthenium from dissolved RuO_2xH_2O in nitric acid by using Ag(II) redox mediator: Toward a new insight into nuclear fuel reprocessing. *Electrochem. Commun.* **6**, 351–356 (2004).
28. P. Swain *et al*., Separation of ruthenium from simulated nuclear waste in nitric acid medium using n-paraffin hydrocarbon. *Sep. Sci. Technol.* **49**, 112–120 (2014).
29. H. Meyer *et al*., "Processes and devices for removing ruthenium as RuO_4 from ruthenate-containing solutions by distillation." US Patent Application Pub. US20120058043A1 (2012).
30. M. Balcerzak, E. Swicicka, Determination of ruthenium and osmium in each other's presence in chloride solutions by direct and third-order derivative spectrophotometry. *Talanta* **43**, 471–478 (1996).
31. M. Balcerzak, Analytical methods for the determination of ruthenium: The state of the art. *Crit. Rev. Anal. Chem.* **32**, 181–226 (2002).
32. G. L. Zimmerman, S. J. Riviello, T. A. Glauser, J. G. Kay, Photochemical decomposition of RuO_4. *J. Phys. Chem.* **94**, 2399–2404 (1990).
33. J. P. Sauvage, J. P. Collin, J. C. Chambron, S. Guillerez, C. Coudret, Ruthenium (II) and osmium (II) bis(terpyridine) complexes in covalently-linked multicomponent systems: Synthesis, electrochemical behaviour, absorption spectra, and photochemical and photophysical properties. *Chem. Rev.* **94**, 993–1019 (1994).
34. D. W. Thompson, I. Akitaka, T. J. Meyer, $[Ru(bpy)_3]^{2+*}$ and other remarkable metal-to-ligand charge transfer (MLCT) excited states. *Pure Appl. Chem.* **85**, 1257–1305 (2013).
35. J. Wang, G. S. Hanan, A facile route to sterically hindered and non-hindered 4′-Aryl-2,2′′:6′,2′′-terpyridines. *Synlett* **8**, 1251–1254 (2005).
36. K. Ohr, R. L. McLaughlin, M. E. Williams, Redox behavior of phenyl-terpyridine-substituted artificial oligopeptides cross-linked by Co and Fe. *Inorg. Chem.* **46**, 965–974 (2007).
37. B. P. Sullivan, J. M. Calvert, T. J. Meyer, Cis-trans isomerism in $(trpy)(PPh_3)RuCl_2$: Comparisons between the chemical and physical properties of a cis-trans isomeric pair. *Inorg. Chem.* **19**, 1404–1407 (1980).
38. J.-P. Collin *et al*., Photoinduced processes in dyads and triads containing a ruthenium(II)-bis(terpyridine) photosensitizer covalently linked to electron donor and acceptor groups. *Inorg. Chem.* **30**, 4230–4238 (1991).
39. M. Rupp *et al*., Photocatalytic hydrogen evolution driven by a heteroleptic ruthenium(II) bis-(terpyridine) complex. *Inorg. Chem.* **58**, 9127–9134 (2019).

40. P. A. Benavides, T. A. Matias, K. Araki, Unexpected lability of the [Ru^{III}(phtpy)Cl_3] complex. *Dalton Trans.* **46**, 15567–15572 (2017).
41. M. M. Taqui Khan, G. Ramachandraiah, R. S. Shukla, Ruthenium (III) chloride in aqueous solution: Kinetics of the aquation and anation reactions of the chloro complexes. *Inorg. Chem.* **27**, 3274–3278 (1988).
42. T. Suzuki *et al*., Speciation of ruthenium (III) chloro complexes in hydrochloric acid solutions and their extraction characteristics with an amide-containing amine compound. *Metals* **8**, 558–568 (2018).
43. F. Mousset, C. Eysseric, F. Bediour, "Studies of dissolution solutions of ruthenium metal, oxide and mixed compounds in nitric acid." https://inis.iaea.org/collection/NCLCollectionStore/_Public/36/013/36013944.pdf?r=1. Accessed 5 December 2019.
44. A. A. Osipenko, V. A. Volkovich, Study of ruthenium behavior in alkali chloride melts using electronic absorption spectroscopy. *AIP Conf. Proc.* **2174**, 20045 (2019).
45. A. Merwin, M. A. Williamson, J. L. Willit, D. Chidambaram, Review – metallic lithium and the reduction of actinide oxides. *J. Electrochem. Soc.* **164**, H5236–H5246 (2017).
46. E.-Y. Choi, S. M. Jeong, Electrochemical processing of spent nuclear fuels: An overview of oxide reduction in pyroprocessing technology. *Pro. Nat. Sci. Mater.* **25**, 572–582 (2015).
47. R. Ziessel, V. Grosshenny, M. Hissler, C. Stroh, cis-[Ru(2,2′:6′,2′ ′-terpyridine)(DMSO) Cl(2)]: Useful precursor for the synthesis of heteroleptic terpyridine complexes under mild conditions. *Inorg. Chem.* **43**, 4262–4271 (2004).
48. I. P. Evans, A. Spencer, G. Wilkinson, Dichlorotetrakis (dimethyl sulphoxide) ruthenium(II) and its use as a source material for some new ruthenium (II) complexes. *J. Chem. Soc. Dalton Trans.* **2**, 204–209 (1973).
49. A. V. Bashilov, A. A. Fedorova, V. K. Runov, Reduction of ruthenium (IV) to ruthenium (III) in aqueous alcohol solutions of hydrochloric acid under microwave radiation. **Ж. анал. химии 55**, 1250–1255 (2000).
50. R. Ciriminna *et al*., Aerobic oxidation of alcohols in carbon dioxide with silica-supported ionic liquids doped with perruthenate. *Chemistry* **12**, 5220–5224 (2006).
51. A. J. Bailey, W. P. Griffith, S. I. Mostafa, P. A. Sherwood, Studies on transition-metal oxo and nitrido complexes: Perruthenate and ruthenate anions as catalytic organic oxidants. *Inorg. Chem.* **32**, 268–271 (1993).
52. A. S. Gerasimov, V. N. Kornoukhov, I. S. Sal'dikov, G. V. Tikhomirov, Production of high specific activity ^{144}Ce for artificial sources of antineutrinos. *At. Energy* **116**, 54–59 (2014).
53. B. Damato, I. Patel, I. R. Campbell, H. M. Mayles, R. D. Errington, Local tumor control after 106Ru brachytherapy of choroidal melanoma. *Int. J. Radiat. Oncol. Biol. Phys.* **63**, 385–391 (2005).
54. M. Hermida-López, L. Brualla, Technical note: Monte Carlo study of ^{106} Ru/^{106} Rh ophthalmic plaques including the ^{106} Rh gamma spectrum. *Med. Phys.* **44**, 2581–2585 (2017).
55. R. B. Manolkar *et al*., The treatment of eye cancer. *Bhabha Atomic Research Centre Newsletter* **309**, 397–403 (2009).

Chapter 5

Chemical and Radioanalytical Investigations of ^{106}Ru-containing Air Filters from Vienna in Fall 2017: Searching for Stable Element Anomalies

D. Zok, J.H. Sterba, G. Steinhauser†

Journal of Radioanalytical and Nuclear Chemistry, vol. 318, pp. 415-421, 2018.
DOI: g/10.1007/s10967-018-6132-6

Authors contributions:
D.Z. and G.S. designed research
D.Z., J.H.S. and G.S. performed research
D.Z. and G.S. wrote the paper

† Correspondence to steinhauser@irs.uni-hannover.de

Journal of Radioanalytical and Nuclear Chemistry (2018) 318:415–421
https://doi.org/10.1007/s10967-018-6132-6

Chemical and radioanalytical investigations of ^{106}Ru-containing air filters from Vienna in fall 2017: searching for stable element anomalies

Dorian Zok[1] · Johannes H. Sterba[2] · Georg Steinhauser[1]

Received: 19 April 2018 / Published online: 1 September 2018

Abstract
Related to the recent nuclear release of radioactive ruthenium isotopes in fall 2017, we analyzed air filters from Vienna for irregularities in the (stable) elemental composition of particulate matter from this period. Methods were SEM/EDXS and INAA. For comparison, a reference filter from 2007 and blank filters were used. The chemical fingerprint encompassed 28 elements. The results show no indication for a considerable change in the elemental composition of the suspended matter. For example, no anomalies in the abundance of platinum group elements were found. The results suggest that the release of ^{106}Ru had not been accompanied by a release of detectable amounts of (activatable) stable elements.

Keywords Neutron activation analysis · Radioruthenium · ^{106}Ru · Environmental air filter · Stable element anomalies

Introduction

The release of radioactive materials into the environment is inherently associated with great public concern. The radioactive fallout from atmospheric nuclear explosions in the 20th century has been largest contributor to anthropogenic radionuclides in the environment. At the height of the cold war in the early 1960s, global fallout reached a magnitude that was no longer irrelevant for the public health. These concerns ultimately triggered diplomatic attempts to ban atmospheric nuclear tests by establishing the Partial Test Ban Treaty (PTBT; sometimes also referred to as Limited Test Ban Treaty, LTBT), which was opened for signature in 1963. In 1996, the Comprehensive Nuclear-Test-Ban Treaty (CTBT) opened for signature [1], aiming to terminate nuclear testing in any environment. For the verification of the CTBT, the international monitoring system (IMS) was installed, designed to detect any violations of the CTBT by geophysical and radionuclide monitoring of the globe. The establishment of the IMS coincided with increased attempts of national governmental efforts to set up monitoring networks that would allow the detection and public risk assessment of undeclared nuclear releases such as the Windscale or Kyshtym accidents in 1957 [2] or the Chernobyl accident in 1986.

Two unusual incidents of radionuclide releases occurred in 2017. In January/February of that year, an unusually long episode of ^{131}I was observed [3]. In fall 2017, European monitoring stations reported an unusual and unprecedented detection of radioruthenium in air [4]. Rapid gamma measurements revealed the presence of radioactive ^{106}Ru ($T_{½}$ = 373.6 days), and in some stations also ^{103}Ru ($T_{½}$ = 39.2 days) in air. Relatively little is known about the release at this point. However, several monitoring stations reported of futile attempts to detect other radionuclides in addition with the radioruthenium. This indicates that the source of the radioruthenium was probably not an accident of a nuclear reactor. Until today, the source remains uncertain and intensely debated [4]. Although ^{103}Ru may be produced by neutron activation of stable ^{102}Ru, both radioruthenium nuclides are prominent fission products. The fission yield, however, largely depends on the type of fissile material, as ^{239}Pu based nuclear fuel produces ^{106}Ru at a higher yield than ^{235}U. For ^{103}Ru, this difference in the yield is not so pronounced. More on the nuclear background of the production can be found elsewhere [5].

✉ Georg Steinhauser
steinhauser@irs.uni-hannover.de

[1] Institute of Radioecology and Radiation Protection, Leibniz Universität Hannover, Herrenhäuser Str. 2, 30419 Hannover, Germany

[2] Atominstitut, TU Wien, Stadionallee 2, 1020 Vienna, Austria

Table 1 Elements, activation products, half-lives, gamma energies, and reference materials used for quantitative analysis

Element	Activation product	Half-life	Gamma energy (keV)	CFA	IMS	TIA	GBW	LSS
Short time activation analysis								
Al	^{28}Al	2.25 min	1778	x	x	x	x	x
Ca	^{49}Ca	8.72 min	3084	x			x	x
Ti	^{51}Ti	5.8 min	320	x	x	x		x
V	^{52}V	3.75 min	1434	x	x	x	x	x
Mn	^{56}Mn	2.58 h	1810	x	x	x	x	x
Dy	^{165}Dy	2.35 h	95	x			x	x
Middle time activation analysis (5 days decay)								
Na	^{24}Na	15.0 h	2754	x	x		x	x
K	^{42}K	12.4 h	1525	x	x		x	x
As	^{76}As	26.4 h	559	x	x		x	x
La	^{140}La	40.3 h	1596	x	x		x	x
Sm	^{153}Sm	46.3 h	103	x	x		x	x
Lu	^{177}Lu	6.7 days	208	x			x	x
U	^{239}Np*	56.6 h	278	x	x		x	x
Long time activation analysis (21 days decay time)								
Sc	^{46}Sc	83.8 days	1121	x	x		x	x
Cr	^{51}Cr	27.7 days	320	x	x	x	x	x
Fe	^{59}Fe	44.5 days	1099	x	x	x	x	x
Co	^{60}Co	5.27 days	1173	x	x	x	x	x
Zn	^{65}Zn	244.3 days	1116	x	x		x	x
Rb	^{86}Rb	18.6 days	1077	x	x		x	x
Zr	^{95}Zr	64.0 days	757	x		x	x	x
Ru	^{103}Ru	39.2 days	497			x		
Sb	^{124}Sb	60.2 days	1691	x	x		x	x
Ba	^{131}Ba	11.5 days	496	x	x		x	x
Cs	^{134}Cs	2.07 days	796	x	x		x	x
Ce	^{141}Ce	32.5 days	145	x	x		x	x
Nd	^{147}Nd	11.0 days	531	x	x		x	x
Eu	^{152}Eu	13.5 days	1408	x			x	x
Tb	^{160}Tb	72.3 days	879	x			x	x
Yb	^{169}Yb	32.0 days	177	x			x	x
Lu	^{177}Lu	6.7 days	208	x			x	x
Hf	^{181}Hf	42.4 days	482	x			x	x
Ta	^{182}Ta	114.4 days	1221	x			x	x
Th	^{233}Pa*	27.0 days	312	x	x		x	x

x certified reference value used for quantitative analysis

*^{233}Pa and ^{239}Np are produced by β-decay of the activation products of ^{232}Th and ^{238}U, respectively. Neutron capture forms short-lived ^{233}Th ($T_{1/2}$ = 22.3 min) and ^{239}U ($T_{1/2}$ = 23.5 min), respectively

In the present study, we aim at the analysis of stable element analysis in order to establish a chemical fingerprint of the airborne particulate matter at the time of the release. We are interested in the elemental composition of the particulate matter as the released radioruthenium may have been associated with some anomalous stable elements that went unnoticed so far. Such anomalies may be represented on the ^{106}Ru containing air filters. Therefore, we performed instrumental neutron activations analysis (INAA) in Vienna and electron microscopy to elucidate the chemical composition and morphology of the particulate matter contained within the filter materials.

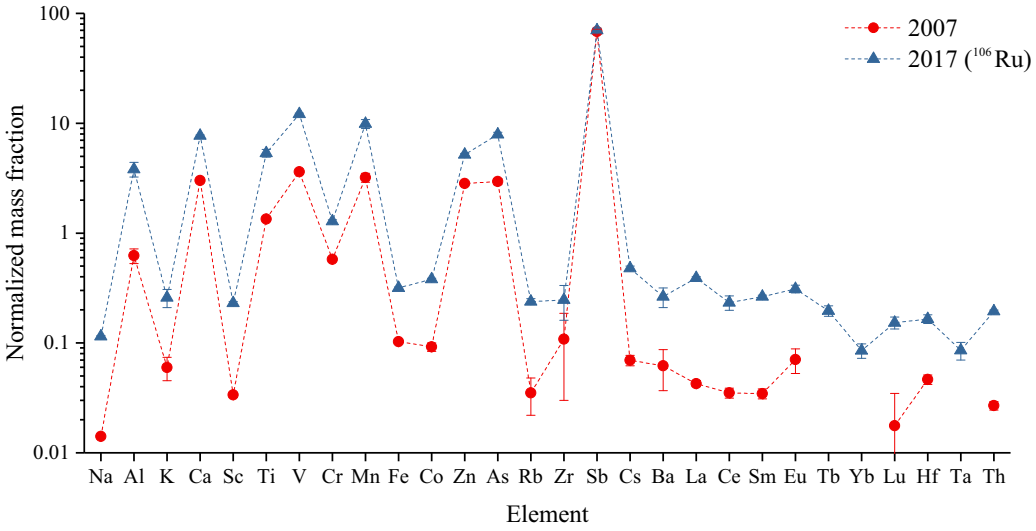

Fig. 1 Distribution pattern of elemental mass fractions of two PP filters from Vienna (2007 and 2017, respectively). All values are normalized to the average elemental abundance of the upper continental crust [13]

Experimental

Location and sampling

The high-volume air filter system used filters made of polypropylene (PP) and was stationed in Vienna, Austria during the ^{106}Ru episode. Collection time was nearly 140 h, namely from the 28 Sep. 2017 12:24 to 04 Oct. 2017 8:14. A total volume of 94,444 m^3 air passed through the PP filter during this time, during which the maximum of the ^{106}Ru plume passed Vienna. After collection, the filter was pressed to a round sample with 5.0 cm diameter, a height of 0.55 cm and a mass of 9.7 g. The round filter was measured by gamma spectrometry and then split in half (5.4 g). This segment was used in this study. The total activities collected on the filter were 546 Bq ^{7}Be, 461 Bq ^{212}Pb, 0.66 Bq ^{103}Ru, and 2030 Bq ^{106}Ru, respectively. Activities are decay-corrected to 04.10.2017, 08:30. Radioberyllium (^{7}Be) and radiolead (^{212}Pb) are typical naturally occurring radionuclides, which are continuously produced in the earth's higher atmosphere (^{7}Be) or by decay of primordial ^{232}Th, respectively. Their presence in the air filter hence comes expectedly [6, 7].

Instrumental neutron activation analysis

For INAA, pellets were punched from the PP filter using a punch press with 0.5 cm diameter. Each pellet has a mass of around 80 mg. Three unused PP filter pellets (filter background), two reference PP filter pellets from 2007 (air particulate matter background) and three ^{106}Ru-containing PP filter pellets were put in polyethylene (PE) vials. In addition, approx. 35 mg of five certified reference materials were used for a quantitative analysis of the elemental composition. The following reference materials were used: NIST SRM 1633b/Coal Fly Ash (CFA), NIST SRM 2702/Inorganics in Marine Sediment (IMS), NIST SRM 173c/Titanium Alloy (TIA), MC Rhyolite GBW 07113 (GBW) and BCR No. 142/Light Sandy Soil (LSS). An overview of the activation products and the reference materials used for quantification is given in Table 1. This table also outlines, which reference materials have been used for quantification (partly, mean values of various reference materials were used.

A short-time (2 min) and a long-time irradiation (32 h) was performed at the 250 kW TRIGA Mark II research reactor of the Atominstitut in Vienna, Austria. The short-time irradiation was performed with the pneumatic sample transfer system into the F-ring of the reactor (thermal neutron flux density 2×10^{12} cm^{-2} s^{-1}). The long term irradiation took place in a dry irradiation tube in the graphite reflector, with a neutron flux density of about 1×10^{12} cm^{-2} s^{-1}.

For the analysis of short-lived, activatable radionuclides such as ^{28}Al, ^{49}Ca, ^{51}Ti, ^{52}V, ^{56}Mn, and ^{156}Dy, the sample vials were transferred into the irradiation position by means of a pneumatic transfer system (neutron flux density of approx. 3×10^{12} cm^{-2} s^{-1}). After 2 min irradiation, sample vials were cleaned on the outside (adding up to 5 min cooling time) and measured immediately by gamma spectrometry with a measurement time of 5 min, yielding the activities of ^{28}Al, ^{49}Ca, ^{51}Ti, and ^{52}V. Following a 3 h decay, another measurement was performed with a measurement time of 12 min, yielding the activities of ^{56}Mn and ^{156}Dy. Gamma spectrometry was performed with a 151 cm^3 HPGe-detector (1.8 keV resolution at the

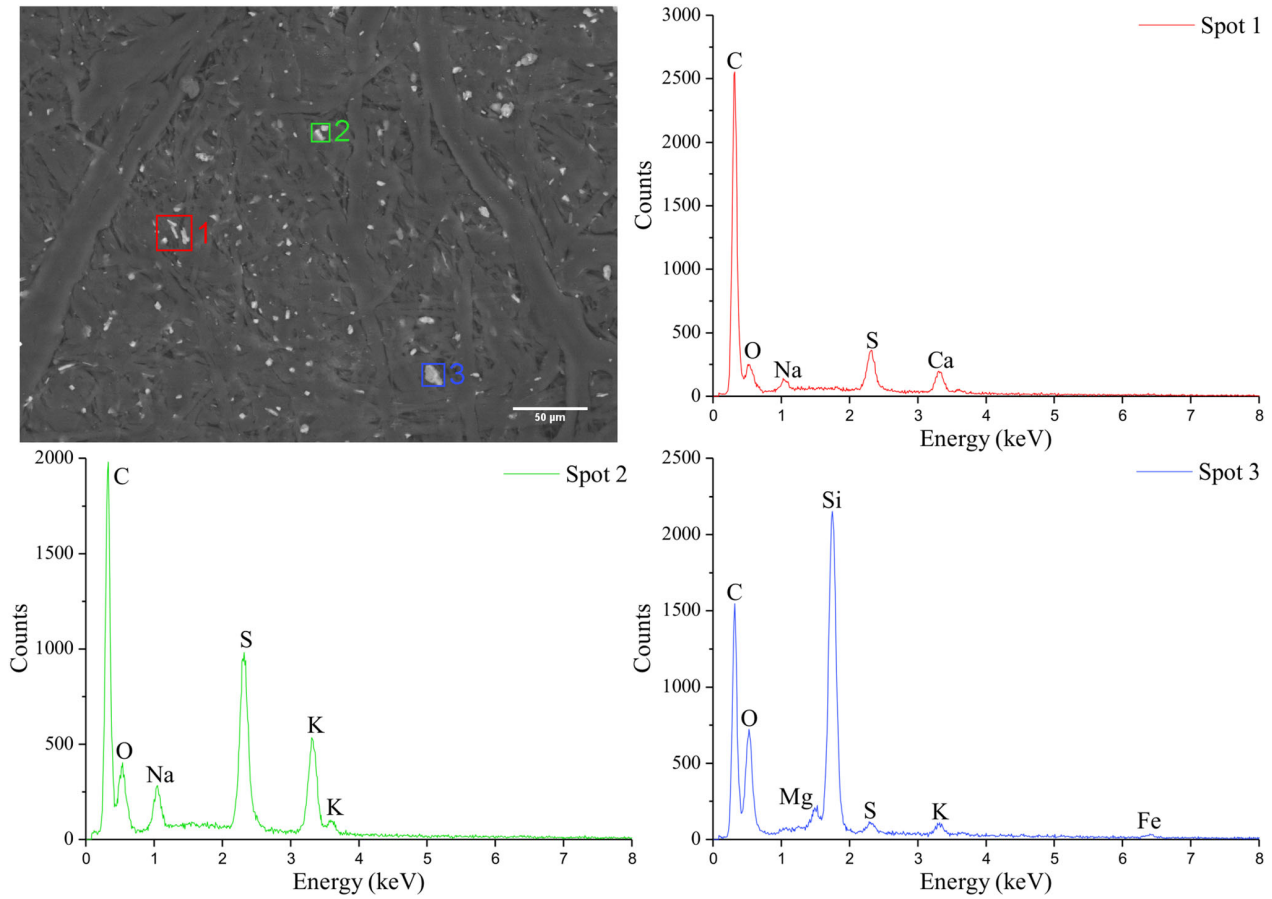

Fig. 2 SEM pictures and EDXS spectra of three different spots found on the filter material

1332 keV ^{60}Co peak, 50.1% relative efficiency), and a multi-channel analyzer with a preloaded digital filter and loss-free counting system [8, 9].

After the short-time irradiation, samples were irradiated for 32 h in the dry irradiation tube of the TRIGA Mk II in Vienna. After a decay time of 5 days, the medium-lived activation products ^{24}Na, ^{42}K, ^{76}As, ^{140}La, and ^{239}Np (U) were measured. After 21 days of cooling, the long-lived activation products ^{46}Sc, ^{51}Cr, ^{59}Fe, ^{60}Co, ^{65}Zn, ^{86}Rb, ^{95}Zr, ^{124}Sb, ^{131}Ba, ^{134}Cs, ^{141}Ce, ^{147}Nd, ^{152}Eu, ^{160}Tb, ^{169}Yb, ^{177}Lu, ^{181}Hf, ^{182}Ta, and ^{233}Pa (Th) were measured. The measurement time was 1800 s and 10,000 s, respectively. All quantifiable elements, including their neutron activation products, their half-life and gamma energy is listed in Table 1. Additionally, it is noted which reference material has a certified value for which element. Further information on the measurement can be found elsewhere [10–12].

Particle size and main elemental composition

For a microscopic inspection of the particles collected on the filter surface, scanning electron microscopy (SEM) was used. Without further preparation, the surface of the pressed PP filter samples was imaged with the Philips SEM XL30 ESEM, which is coupled with an energy dispersive X-ray spectroscopy (EDXS) system by EDAX. SEM pictures were taken in back-scattered electron mode and a voltage of 20 kV. With this method, an overview of existing particles and their general size was obtained to check for any apparent anomalies. Furthermore, it allows the investigation of the elemental distribution of the particles by using the EDXS.

Results and discussion

INAA

The results of the INAA are shown in Fig. 1, whereby the mass fractions of the elements are normalized to the content of the upper continental crust [13, 10]. The data points in blue represent the normalized concentrations of the radioactive filter that was in operation during the ^{106}Ru episode in 2017. The red data points represent the

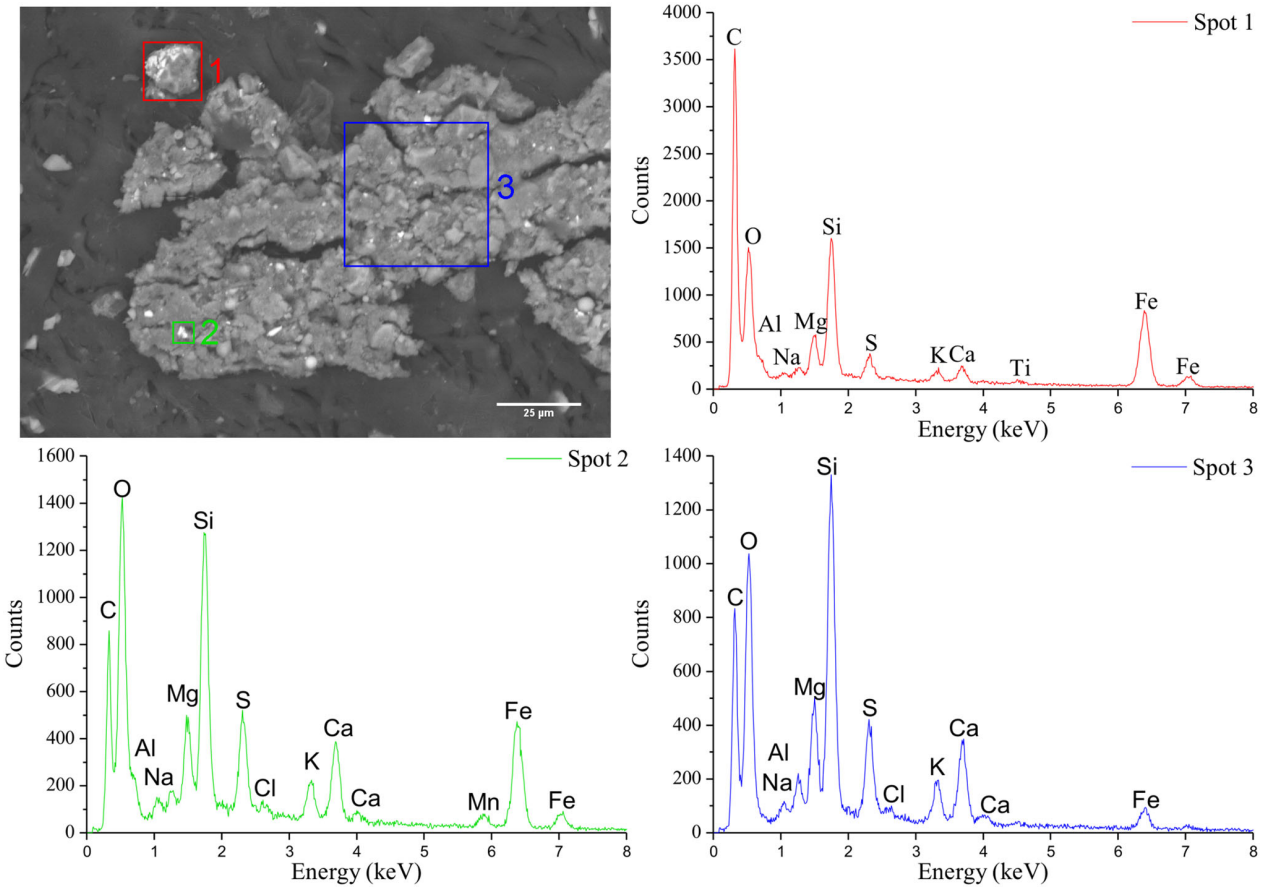

Fig. 3 SEM pictures and EDXS spectra of three different spots on a larger agglomerate

normalized concentrations of the "reference filter" from 2007, which allows comparison of the typical elemental patterns before and during the ^{106}Ru episode. Generally, the elemental concentrations vary considerably when compared to the upper continental crust, spanning around two orders of magnitude. Some of these "outliers", such as Sb, are generally associated with emissions caused by modern traffic (emission of abraded particles from brake pads) and urban environment in a large European city such as Vienna. This is not uncommon, as it has to be emphasized that only airborne particles have been sampled, which do not represent the bulk composition of the Earth's crust.

For comparison of the determined elemental concentrations to other urban areas, the elemental mass fraction values from reference materials NIST SRM 1648a Urban Particulate Matter can be used. The comparison shows that there are no anomalies or uncommon occurrences of certain elements in unusual concentrations or ratios in urban living areas.

Please note that the the mass fractions of the reference filter from 2007 are constantly lower than from the ^{106}Ru containing filter sample from 2017. It is apparent that the amount of filtered air has been much lower in 2007, although the actual amount remains unknown. This clearly indicates that a lower amount of particulate matter had been sampled in 2007 compared with 2017. The differences in the mass fraction range are mainly shifted to lower amounts with a factor of less than 10. In addition to the elements that have been displayed in Fig. 1, the following elements have been detected, but could not be quantified (due to a lack of certification values in the reference materials we used): gold, chlorine, bromine, osmium, and magnesium. No stable ruthenium isotopes were detected, because ruthenium is determined with low sensitivity in INAA. In addition, a spectral interference with activation products of barium raised the detection limit. With the exception of osmium, INAA did not reveal detectable amounts of other platinum group elements (Rh, Pd, Ir, and Pt), which are characterized by a similar chemical behavior like ruthenium. Although uranium is a common finding in INAA of geological materials [7–9], no traces have been detected in the filter.

SEM and EDXS

Figures 2 and 3 show two SEM images of the ^{106}Ru containing filter as well as three EDXS spectra of potentially interesting spots. The SEM images show the distribution of particles of various sizes that one would expect from an air filter in an urban area: the size distribution of dust particles ranges from a few µm up to a small amount of agglomerates with some hundreds µm in diameter. EDXS revealed that the majority of particles were made of light naturally abundant elements such as potassium, sodium, sulfur, oxygen, and silicon. Also, bigger agglomerates with heavier metals and elements such as manganese, iron, titanium, and chlorine were found. In summary, the patterns of particle sizes and elements within the particles reveal no uncommon characteristics. No abnormal particulate matter that could be indicative of an unusual phase carrying the ^{106}Ru have been detected. This is in agreement with the observation that the ^{106}Ru activities are evenly distributed on the filter surface, indicating a high degree of homogeneity.

Conclusions

In this study, attempts have been undertaken to reveal possible anomalies in the chemical (including trace element) composition and the morphology of particles contained in an air filter that previously collected radioactive ^{106}Ru in Vienna in fall 2017. By using the SEM/EDXS a general overview concerning the particle shape and major element composition was obtained. Neither particle shape nor composition revealed uncommon or unusual characteristics that may be indicative of an unusual carrier phase of the anthropogenic radionuclide ^{106}Ru. No unusual heavy metal spots were found in the SEM imaging.

Instrumental neutron activation analysis was used to provide more comprehensive and thus more reliable chemical information on the stable element composition of the ^{106}Ru-containing filter. By INAA, the chemical fingerprints of activatable major and trace elements of the ^{106}Ru filter (2017) have been determined and compared to a filter that had been in operation 10 years ago in the same urban environment. This method generated values for 28 elements, however no uncommon element appearance or scale of mass fraction was determined. All values for 2017 are comparable with 2007. So no hint was found for a chemical/stable element irregularity or anomaly in the filtered, radioruthenium containing air from 2017 compared to 2007.

Acknowledgements We gratefully acknowledge the financial support by the VolkswagenStiftung (Grant 94403). We would like to thank Michaela Foster and Jan M. Welch from the Atominstitut as well as Martin Weiss from the IRS for their assistance in the lab.

References

1. Preparatory Commission CTBTO (2017) CTBT: ending nuclear explosions. https://www.ctbto.org/fileadmin/user_upload/public_information/2017/CTBT_Ending_Nuclear_Explosions_07Sep_2017.pdf. Accessed April 2018
2. Jones S (2008) Windscale and Kyshtym: a double anniversary. J Environ Radioact 99:1–6
3. Masson O, Steinhauser G, Wershofen H, Mietelski JW, Fischer HW, Pourcelot L, Saunier O, Bieringer J, Steinkopff T, Hýža M, Møller B, Bowyer TW, Dalaka E, Dalheimer A, de Vismes-Ott A, Eleftheriadis K, Forte M, Gasco Leonarte C, Gorzkiewicz K, Homoki Z, Isajenko K, Karhunen T, Katzlberger C, Kierepko R, Kövendiné Kónyi J, Malá H, Nikolic J, Povinec PP, Rajacic M, Ringer W, Rulík P, Rusconi R, Sáfrány G, Sykora I, Todorović D, Tschiersch J, Ungar K, Zorko B (2018) Potential source apportionment and meteorological vonditions involved in airborne ^{131}I detections in January/February 2017 in Europe. Environ Sci Technol 52(15):8488–8500. https://doi.org/10.1021/acs.est.8b01810
4. IRSN (2017) Information report: detection of ruthenium-106 in France and in Europe. http://www.irsn.fr/EN/newsroom/News/Documents/IRSN_Information-Report_Ruthenium-106-in-europe_20171109.pdf. Accessed April 2018
5. Byerly B, Tandon L, Hayes-Sterbenz A, Martinez P, Keller R, Stanley F, Spencer K, Thomas M, Xu N, Schappert M, Fulwyler J (2016) Determination of initial fuel state and number of reactor shutdowns in archived low-burnup uranium targets. J Radioanal Nucl Chem 307(3):1871–1876. https://doi.org/10.1007/s10967-015-4538-y
6. Querfeld R, Merchel S, Steinhauser G (2017) Low-cost production of a ^{7}Be tracer from rainwater and purification: preliminary results. J Radioanal Nucl Chem 314(1):521–527. https://doi.org/10.1007/s10967-017-5433-5
7. Kuśmierczyk-Michulec J, Bourgouin P (2018) Influence of mineral dust on changes of ^{7}Be concentrations in air as measured by CTBTO global monitoring system. J Environ Radioact 192:454–466. https://doi.org/10.1016/j.jenvrad.2018.07.015
8. Westphal GP (1982) Real-time correction of counting losses in nuclear pulse spectroscopy. J Radioanal Chem 70(1):387–410. https://doi.org/10.1007/bf02516125
9. Westphal GP, Cadek GR, Kero N, Sauter T, Thorwartl PC (1995) Digital implementation of the preloaded filter pulse processor. J Radioanal Nucl Chem 193:81–88
10. Steinhauser G, Sterba JH, Bichler M (2007) "Chemical fingerprints" of pumice from Cappadocia (Turkey) and Kos (Greece) for archaeological applications. Appl Radiat Isot 65(5):488–503. https://doi.org/10.1016/j.apradiso.2006.12.004

11. Sterba JH, Mommsen H, Steinhauser G, Bichler M (2009) The influence of different tempers on the composition of pottery. J Arch Sci 36(7):1582–1589
12. Sterba JH (2018) A workflow for neutron activation analysis of archaeological ceramics at the Atominstitut in Vienna. Austria. J Radioanal Nucl Chem 316(2):753–759. https://doi.org/10.1007/s10967-018-5803-7
13. Taylor SR, McLennan SM (1985) The continental crust: its composition and evolution. Geoscience texts. Blackwell Scientific Publications, Oxford

Chapter 6

Non-Natural Ruthenium Isotope Ratios of the Undeclared 2017 Atmospheric Release consistent with Civilian Nuclear Activities

T. Hopp*, D. Zok*, T. Kleine†, G. Steinhauser†

Nature Communications, vol. 11, no. 1, pp. 1-7, 2020. DOI: 10.1038/s41467-020-16316-3

Authors contribution:
T.H. and D.Z. contributed equally to the study
G.S. and D.Z. designed the study and D.Z. prepared and digested the samples
T.H. conducted the chemical separation and MC-ICP-MS measurements.
T.H. and T.K. evaluated the isotope measurement data
T.H., D.Z., T.K., and G.S. discussed the results and contributed to the writing of the manuscript

* T. Hopp and D. Zok contributed equally to this work
† Correspondence to: thorsten.kleine@uni-muenster.de or steinhauser@irs.uni-hannover.de

nature COMMUNICATIONS

ARTICLE

https://doi.org/10.1038/s41467-020-16316-3 OPEN

Non-natural ruthenium isotope ratios of the undeclared 2017 atmospheric release consistent with civilian nuclear activities

Timo Hopp [1,3,4], Dorian Zok [2,4], Thorsten Kleine [1✉] & Georg Steinhauser [2✉]

Understanding the circumstances of the undeclared 2017 nuclear release of ruthenium that led to widespread detections of the radioisotope ^{106}Ru in the Eurasian region, and whether it derives from a civilian or military source, is of major importance for society and future improvements in nuclear safety. Until now, the released nuclear material has merely been studied by analyzing short-lived radioisotopes. Here, we report precise measurements of the stable isotopic composition of ruthenium captured in air filters before, during, and after the nuclear release, and find that the ruthenium collected during the period of the 2017 nuclear release has a non-natural isotopic composition. By comparing our results with ruthenium isotopic compositions of spent nuclear fuels, we show that the release is consistent with the isotopic fingerprints of a civilian Russian water-water energetic reactor (VVER) fuel at the end of its lifetime, and is not related to the production of plutonium for nuclear weapons.

[1] Institut für Planetologie, University of Münster, Wilhelm-Klemm-Str. 10, 48149 Münster, Germany. [2] Institute of Radioecology and Radiation Protection, Leibniz Universität Hannover, Herrenhäuser Str. 2, 30419 Hannover, Germany. [3] Present address: Origins Laboratory, Department of the Geophysical Sciences and Enrico Fermi Institute, The University of Chicago, Chicago, IL 60637, USA. [4] These authors contributed equally: Timo Hopp, Dorian Zok. ✉email: thorsten.kleine@uni-muenster.de; steinhauser@irs.uni-hannover.de

A nuclear accident may become a serious hazard for humankind and exhibit long-lasting consequences for the environment. Decades ago, and especially in the aftermath of the Chernobyl nuclear accident, global networks of monitoring stations were established for atmospheric radioactivity surveillance. They now have the sensitivity and precision to identify atmospheric releases of even small amounts of anthropogenic radionuclides[1]. In September and October 2017, these monitoring stations detected a radioactive cloud over a wide swath of Europe containing the fission products ^{106}Ru ($T_{1/2} = 371.8$ d) and traces of ^{103}Ru ($T_{1/2} = 39.2$ d)[2]. The characteristics of the release (e.g., lack of concomitant radionuclides) suggested that the source was a spent nuclear fuel reprocessing facility. The source term of the release was estimated at 250 TBq ^{106}Ru, and atmospheric modeling indicated that the cloud originated in the southern Urals in the Russian Federation[2,3]. This area hosts one of the largest nuclear facilities in the world, the Federal State Unitary Enterprise (FSUE) Production Association Mayak in Ozersk, Russia.

Currently, no country has assumed responsibility for this considerable release, which is likely the single-largest accidental release from civilian nuclear reprocessing[4]. Despite a large number of meteorological indications[3,5–8], Russian authorities and institutions have repeatedly denied any involvement of the Mayak facility in the release[9–11]. In their official statement[9], the Rosatom State Nuclear Energy Corporation emphasized that there were not any incidents at any of the Rosatom sites during the period of September–October 2017. The FSUE Production Association Mayak is a subsidiary of Rosatom. The Russian authority also referred to this statement in response to a query concerning the release of ^{106}Ru from the International Atomic Energy Agency (IAEA) to its 43 member states in the region[12]. According to IAEA, none of the countries reported an event that could be the cause of the release of ^{106}Ru in the fall of 2017[12]. In an interview with Nuclear Engineering International Magazine, the deputy director of the Nuclear Safety Institute of the Russian Academy of Sciences (IBRAE) argued that "if the Mayak facility [were] the source, then we would have found concentrations hundreds of thousands of times the norm around it and in the soil[10]." The IBRAE also set up an International Independent Scientific Commission for the investigation of the release of ^{106}Ru. The Commission gathered two times, in January and April 2018[13,14]. The Commission agreed on an estimated release source term of the event of ~100 TBq[13]. Science reported that a representative of the Russian nuclear regulator Rostechnadzor who inspected Mayak in November 2017 told the Commission that he saw no anomalies in the Mayak facility from a month earlier[11]. Early alternative attempts at explanation of the release, such as a release on Romanian territory[9] or the burning of a satellite's radionuclide battery containing ^{106}Ru[10] had been addressed previously[2] and were essentially dispelled. While it is difficult to imagine that a private facility could routinely handle such considerable activities, it is clear that nuclear facilities (both private and state-run), including reprocessing facilities, must be operated under strict governmental regulatory control[15] and report any events to the regulator.

Previous studies have focused on tracking the cloud across Europe and have provided chemical insights, suggesting that the release occurred at an advanced stage of the reprocessing, when the Ru species had been transformed from initially produced gaseous RuO_4, at least in part, into one or more soluble compounds with medium volatility[2]. One of the released chemical species was identified as a polychlorinated Ru(III) form[16]. The release carried a ^{103}Ru/^{106}Ru signature of very young spent fuel (i.e., only 1.5 or 2 years after the end of neutron irradiation, assuming regular high-burnup fuel)[2]. Together with other indications, this suggests that the ^{106}Ru release could have originated during the production of a highly radioactive ^{144}Ce source commissioned for the European sterile neutrino project SOX-Borexino in the Gran Sasso National Laboratory (GSNL)[2,11].

The degree of burnup of the reprocessed fuel is key for understanding the fuel's past use prior to the release. High burnup would imply a civilian purpose of the spent fuel. Low burnup, by contrast, may indicate a military purpose, such as production of weapons-grade Pu or even utilization of low-burnup fissile material in a nuclear-powered missile[17]. With increasing burnup, nuclear fuel will increasingly accumulate ^{240}Pu, which thwarts its applicability in nuclear warheads.

Any use of low-burnup fuel would also affect the model age of the released material. The above model age of 1.5–2 years after neutron irradiation applies only to high-burnup fuel. In particular, if low-burnup fuel had been used to produce the ^{144}Ce source above mentioned, the measured ratio of ^{103}Ru/^{106}Ru would make the released material appear younger than its actual age. In other words, low burnup could also mean that the fuel that was used for the ^{144}Ce source was in fact "older" than the suggested ≤2 years. This could mean that it underwent the established and safe reprocessing scheme with ~3 years of cooling. As outlined in ref. [18], the compact design of the ^{144}Ce source required exceptionally high specific activity, which is only achievable either by reducing the minimum cooling time from 3 to 2 years (high-burnup scenario) or by reprocessing fuel that has undergone only approximately one-third of its nominal burnup (i.e., prior to reaching the end of its lifetime), while allowing 3 years of cooling (low-burnup scenario). In any case, since Mayak not only hosts a reprocessing facility but also has an explicit military history, it has until now not been possible to rule out a military context or another low-burnup scenario of the release.

The circumstances of the incident cannot be assessed solely by analyzing the detected radioactive Ru isotopes, because the resulting ^{103}Ru/^{106}Ru ratio is a function of neutron flux, energy spectrum, fuel type that varies by reactor type and burnup, and decay time. Since none of these variables are known, the ^{103}Ru/^{106}Ru ratios do not allow the direct distinction of the provenance of the released material. The stable isotopic composition of fission-generated Ru also depends on the fuel type, hence, varies by reactor type and burnup, but not on radioactive decay. Therefore, precise measurements of the stable isotopic composition of fission-generated Ru can serve as an indicator of whether the released material was produced in a civilian reactor or during a low-burnup scenario, e.g., the production of weapons-grade Pu[19–21].

Here, we show that precise stable isotope analyses of Ru in environmental samples can be used to constrain the provenance of nuclear material released into the atmosphere. We present the first high-precision measurements of stable Ru isotopic compositions of particulate matter collected in air filters including one sample that contains material from the 2017 Ru release. We conclude that the stable isotopic composition of the 2017 nuclear release is consistent with fission-generated Ru produced in regular, high-burnup spent fuel; hence, the nuclear release was most likely related to an accident during reprocessing of spent fuel used in civilian nuclear activities.

Results

Ruthenium isotopic compositions of air filter samples. Isotopic anomalies caused by the decay of anthropogenic radioisotopes are extremely difficult to observe in regular environmental samples as the additional input of the decay products will be usually insignificant compared with the overwhelming abundance of natural occurring isotopes. Consequently, such anomalies have been reported only for environments with a high level of radioisotope

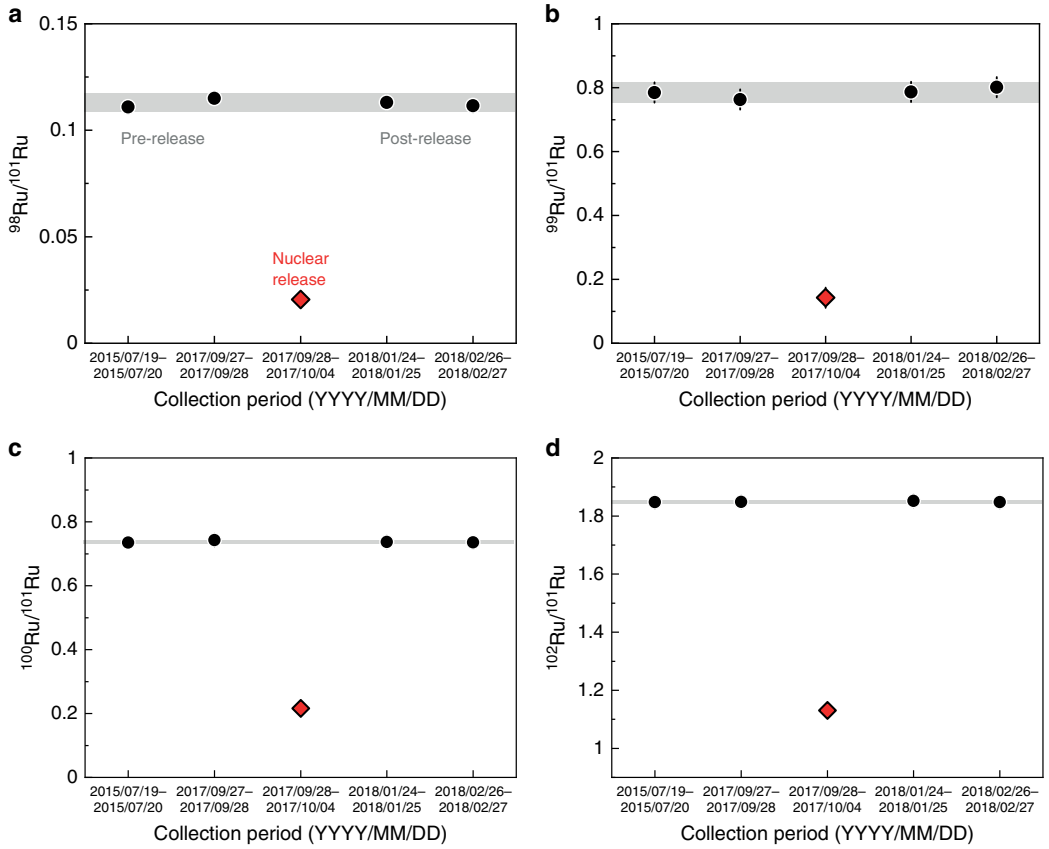

Fig. 1 Isotope ratios from a series of air filters from Vienna, Austria. Isotope ratios for **a** ^{98}Ru/^{101}Ru, **b** ^{99}Ru/^{101}Ru, **c** ^{100}Ru/^{101}Ru, and **d** ^{102}Ru/^{101}Ru. The ^{106}Ru containing sample air filter of the 2017 atmospheric release of nuclear Ru (red diamond) exhibits distinctly non-natural Ru isotope ratios. Four reference air filter samples (black circles) collected from 2015 to 2018 have similar Ru isotope ratios that agree with natural Ru and are indicative of the typical background Ru collected by air filters in Vienna. The gray bars represent the standard deviation (2 s.d.) on the average isotope ratios of the four reference filters and are treated as the external reproducibility of the measurements. Error bars on individual samples correspond to 2 s.e. ($n < 3$) or 2 s.d. ($n \geq 3$) of measurements and are, if not visible, smaller than the symbols.

contamination, i.e., those that were directly impacted by anthropogenic nuclear activities[22,23]. However, alongside the radioisotopes, almost any nuclear release also contains stable isotopes of the same element, but with anomalous, non-natural abundances that reflect production by nuclear fission and capture reactions. We investigated the stable isotopic compositions of a few nanograms of airborne Ru collected by a series of air filters from Vienna, Austria, including one sample that incorporated radioactive Ru from the atmospheric release in 2017[24] using multicollector inductively coupled plasma mass spectrometry (see Methods). Four other filters from air collections between 2015 and 2018 (Supplementary Table 1) are used to characterize the typical background Ru isotopic composition of particulate matter sampled at that specific air filter station (Fig. 1; Supplementary Notes 1 and 2; Supplementary Tables 2 and 3). Two of these filters were used to collect particulate matter prior to the 2017 nuclear release; the other two were in operation after the radioruthenium episode. Our results show that all four background air filters exhibit isotope ratios of ^{98}Ru/^{101}Ru, ^{99}Ru/^{101}Ru, ^{100}Ru/^{101}Ru, and ^{102}Ru/^{101}Ru in excellent agreement with one another and with natural Ru isotope abundances (Fig. 1). By contrast, the sample filter that collected air at the same station during the time of the radioruthenium episode over Europe in September/October 2017 (2017/09/28 to 2017/10/04) displays drastically different, non-natural Ru isotopic composition compared with the defined background of environmental (terrestrial and potentially anthropogenic) Ru (Fig. 1). The significant shift of the ^{i}Ru/^{101}Ru ratios is on the order of tens of percent. Natural processes cannot produce isotope fractionations of such magnitude for heavy elements[25–27].

Isotope abundances of natural and fission-derived ruthenium. A key observation from our data is that, compared with natural Ru[28], the Ru stable isotopic composition of the air filter from the radioruthenium episode is depleted in the lighter Ru isotopes (^{96}Ru, ^{98}Ru, ^{99}Ru, and ^{100}Ru), while the heavier Ru isotopes (^{101}Ru, ^{102}Ru, and ^{104}Ru) are enriched. This pattern is consistent with the expected composition of Ru produced during nuclear fission, because the formation of ^{96}Ru, ^{98}Ru, ^{99}Ru, and ^{100}Ru is suppressed by stable Mo and long-lived Tc nuclides along the beta-decay series of these isobars. By contrast, the formation of ^{101}Ru, ^{102}Ru, and ^{104}Ru is not inhibited by other isotopes, and they are the stable termini of their beta-decay series (Fig. 2). The non-natural Ru isotopic composition of Ru collected during the radioruthenium episode, therefore, indicates a significant contribution of fission-generated Ru to the particulate matter collected in the investigated air filter.

Discussion

Most importantly, our results can be used to assess the provenance of the non-natural Ru. This is because ^{235}U and ^{239}Pu

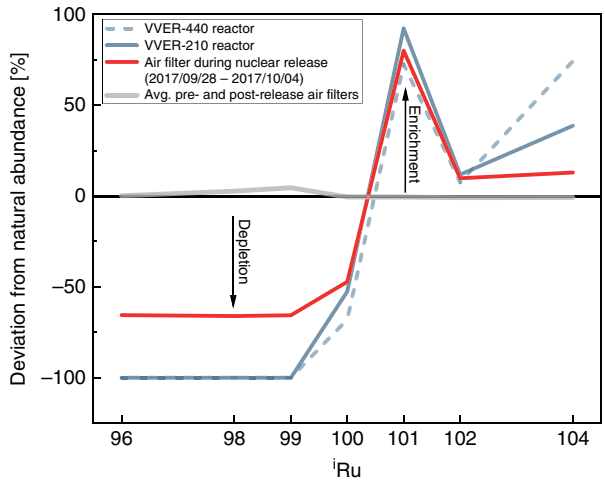

Fig. 2 Ruthenium isotope abundances of the radioactive air filter and Ru produced by nuclear reactors relative to natural Ru. Ruthenium produced by nuclear reactors, e.g., VVER-type reactors (blue lines), contain negligible amounts of ^{96}Ru, ^{98}Ru, and ^{99}Ru, whereas heavier Ru isotopes (^{101}Ru, ^{102}Ru, and ^{104}Ru) are enriched relative to natural Ru[27,28]. The gray line gives the abundances calculated for the reference filters from 2015 to 2018. The isotope abundances derived for the non-natural Ru in the air filter (red line) display the typical depletion of the lighter and enrichment of the heavier isotopes produced by mixing of nuclear reactor-derived Ru with natural Ru.

fission are characterized by distinct thermal fission yields of Ru isotopes, where ^{239}Pu fission favors heavier Ru isotopes compared with ^{235}U fission. Weapons-grade Pu is produced from low-burnup uranium fuel to minimize the ingrowth of ^{240}Pu during irradiation and contains a fission product signature consistent with ^{235}U fission. In contrast, civilian power production reactors use a very high-burnup fuel cycle that not only produces a much higher ^{240}Pu content, but also a significantly higher overall Pu content. As a result, at the end of the nuclear fuel's lifetime, over 50% of fissions in civilian reactors come from ^{239}Pu bred in during irradiation, producing a different fission product signature that is a mix of ^{235}U and ^{239}Pu fission yields. These differences explain why fission-generated Ru has distinct isotopic compositions when produced in civilian power reactors versus low-burnup operation for the production of weapons-grade Pu or other low-burnup scenarios (Fig. 3; Supplementary Note 3; Supplementary Table 4). Specifically, Ru produced in civilian power reactors has higher ^{100}Ru/^{101}Ru and ^{102}Ru/^{101}Ru ratios due to the increasing contribution of ^{239}Pu fission in the later lifetime of energy-producing nuclear fuel (Fig. 3)[29]. By contrast, the ^{100}Ru/^{101}Ru and ^{102}Ru/^{101}Ru ratios measured from the (military) Hanford Site groundwater are much lower, due to ^{235}U fission dominating the signal with only marginal input from ^{239}Pu fission (Fig. 3a, c).

Given that the air filters before and after the ^{106}Ru release already contained natural ruthenium, the Ru collected during the radioruthenium episode is expected to be a mixture between fission-generated Ru and natural ruthenium (Supplementary Note 4). Accordingly, the Ru isotope ratios of the air filter containing the fission-generated Ru should fall on a mixing array of natural Ru with the characteristic signatures of the source of the fission-generated Ru. Consistent with this, the Ru stable isotopic composition from the radioruthenium episode air filter falls on mixing arrays with civilian power reactors, but not on mixing arrays with Ru generated during low-burnup scenarios such as ^{239}Pu production (Fig. 3a, c). Hence, the atmospheric release of fission-generated Ru was most likely related to spent nuclear fuel used in civilian power reactors, whereas an origin related to weapons-related Pu production or other low-burnup scenarios is less likely. Nuclear fuel used in different types of civilian nuclear reactors has varying contents of ^{235}U and ^{239}Pu. For instance, mixed oxide fuel (MOX) uses both ^{235}U and ^{239}Pu, typically from spent fuel reprocessing, whereas most other reactor fuel is based on low enriched ^{235}U (Supplementary Tables 5 and 6). Therefore, MOX carries a distinct Ru isotopic signature compared with other fuel types with lower ^{239}Pu contents (Fig. 3b). This means that Ru isotopic signatures can help not only distinguishing a civilian from a military origin of anthropogenic Ru, but also to differentiate between different types of the civilian power reactors. For instance, the isotopic characteristics of various common civilian power reactor types, in particular Western pressurized water reactors (PWR), boiling water reactors (BWR), and water–water energetic reactor types (VVER) (a Russian version of PWR) are distinct[29] (Fig. 3b, c). The VVER-210 is the discontinued lower-power version of the VVER family, whereas the VVER-440 is still frequently used (Supplementary Note 5). The Ru isotopic signature of the sample filter is distinct from the expected composition of Ru from nuclear power reactors using MOX or uranium oxide fuel mixed with natural Ru (Fig. 3b, d). In contrast, the sample filter Ru falls on a mixing line of natural Ru and anthropogenic Ru produced in VVER reactors for both ^{102}Ru/^{101}Ru and ^{100}Ru/^{101}Ru, respectively (Fig. 3b, d; Supplementary Note 4; Supplementary Table 7). Mass balance calculations predict that around 65–90% of the total Ru found in the sample filter in question is attributable to a reactor (Fig. 3b, d). Furthermore, the isotope abundances of the VVER reactor types and the air filter compared with the natural Ru isotope abundances confirm that the Ru in the air filter is a mixture of natural Ru with fission-generated Ru most likely produced in a VVER reactor. Such a mixture has the typical depletion in ^{96}Ru, ^{98}Ru, ^{99}Ru, and ^{100}Ru and enrichment in ^{101}Ru, ^{102}Ru, and ^{104}Ru (Fig. 2). Thus, our data are best explained by a scenario in which the undeclared radioactive Ru release of September 2017 carried stable isotope ratios that match the signature of spent VVER reactor-type nuclear fuel at the end of its lifetime, mixed with a minor component of natural Ru.

The Russian Federation operates five reactors of the VVER-440 type, one of which is located at Novovoronezh NPP and four at Kola NPP (Supplementary Note 5; Supplementary Table 8). Kola NPP was en route of a railway transportation (Supplementary Fig. 1) of naval spent nuclear fuel from Andreeva Bay[30] via Murmansk that arrived in Mayak 6 weeks prior to the estimated release date[31]. Since there is both a temporal and spatial coincidence, this fuel shipment may potentially be relevant to the release. In any case, while pressurized water reactors of the VVER type are commonly used in many countries, there are comparatively very few operating reprocessing plants. Consistent with the recent reconstruction and air modeling of the origin of the radioruthenium cloud,[2,3,5] the Ru stable isotope signature points to the involvement of a reprocessing facility. Furthermore, the fission-generated Ru component in the air filter displays the signature of spent VVER nuclear fuel. This result is important in the context of a possible connection between the nuclear release and the production of a compact ^{144}Ce source for the Borexino antineutrino detector at the GSNL. While it would have been possible to meet the specifications of the ^{144}Ce source by using spent fuel with low burnup[2], the Ru stable isotope signature confirms that spent fuel at the end of its lifetime was reprocessed[32–34]. In this case, the cooling time of the nuclear fuel must have been decreased to ≤2 years to achieve the required high specific activity of ^{144}Ce in the compact CeO_2 source[18,33]. Hence,

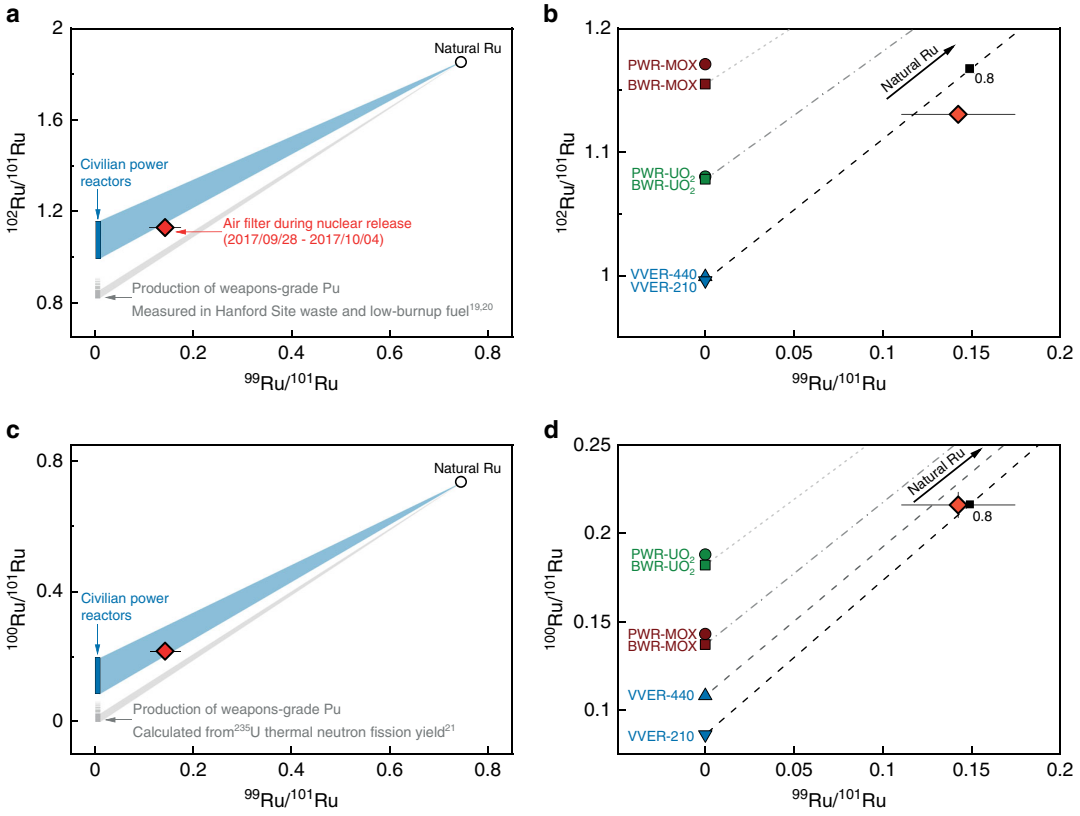

Fig. 3 Source identification of the nuclear Ru released into the atmosphere based on Ru isotope ratio plots. Subplots (**a**) and (**b**) show ratios of $^{102}Ru/^{101}Ru$ versus $^{99}Ru/^{101}Ru$ and (**c**) and (**d**) show $^{100}Ru/^{101}Ru$ versus $^{99}Ru/^{101}Ru$. Ruthenium produced in civilian power reactors (blue rectangle)[29] has distinctive isotope compositions compared with Ru produced during the production of weapons-grade Pu (gray rectangles) (**a**, **c**) (e.g., Hanford Site[19], low-burnup fuels[20], or ^{235}U thermal neutron fission yield[21]). A higher contribution of ^{239}Pu fission may increase the $^{102}Ru/^{101}Ru$ and $^{100}Ru/^{101}Ru$ ratios. The Ru isotopic composition of the sample air filter falls within mixing arrays of Ru produced in civilian power reactors and natural Ru (blue fields) (**a**, **c**). Different types of power reactor and nuclear fuels have distinctive Ru isotope compositions: Pressurized water reactor (PWR)—circle; boiling water reactor (BWR)—square; mixed oxide fuel (MOX)—brown; uranium oxide fuel (UO_2)—green; water-water energetic reactor (VVER-210 or VVER-440)—blue (**b**, **d**)[29]. Less common reactor types such as pressurized heavy-water reactors or low-power reactors such as research reactors were not considered here. The atmospheric Ru released in 2017 falls on mixing lines with VVER-type nuclear fuel and natural Ru with ~65–90% of the total Ru derived from nuclear fuel (**b**, **d**). Error bars correspond to the external reproducibility (2 s.d.) of the four reference filters (Supplementary Table 3).

the combination of atmospheric observations of the undeclared nuclear release and the Ru stable isotope signature of the released Ru suggests that the release may have occurred during reprocessing of regular spent VVER-type fuel after a shorter than typical cooling time, most likely at the Mayak reprocessing plant. This is the first observation of nuclear-related Ru stable isotope signatures in air particulate samples and a demonstration of its forensic value for assessing the provenance of the release. The correlation of the air filter's isotopic signature with spent VVER-440 fuel is consistent with the fact that spent VVER-440 fuel is routinely reprocessed at the Mayak facility, whereas fuel from VVER-1000 or from RBMK power reactors is not[35] (Supplementary Note 5).

Methods

Air filter samples. The air filters used in this study are square polypropylene (PP) filters with rectangular shape (size 46 × 57 cm). They are employed in a high-volume air filter station (675 $m^3 \cdot h^{-1}$) on the rooftop (~100 m above ground) of a building in Vienna, Austria (48.23 N; 16.42 E)[24]. Air sampling is performed at this station with an air collection time of usually 1 day or up to 1 week. After sampling, the filter is removed from the sampler and pressed into a round shape with a diameter of 5 cm. This geometry is preferred for routine gamma measurements. Five air filters from the years 2015 to 2018 were investigated in this study (Supplementary Table 1). Within this sample set, two filters prior and two after the incident (Supplementary Table 1) bracket the air filter that collected radioruthenium during the week from 2017/09/28 to 2017/10/04. Note that one sample was taken the day before the radioruthenium episode over Austria (2017/09/27). Hence, the set of samples allows comparing the isotopic composition of the regular, environmental Ru background at the air filter station with the isotopic composition of the fission-generated (and radioactive) Ru-impregnated air filter. In addition, a pristine (blank) filter that was doped with ~20 ng Ru from an Alfa Aesar™ standard solution was used to test the sample preparation and chemical separation, as well as to estimate the reproducibility of the MC-ICPMS measurements (Supplementary Table 1).

Chemicals and standard solution. The sample preparation was performed at the Institute of Radioecology and Radiation Protection at the Leibniz University Hannover. For digestion, nitric acid with Millipore Emsure™ grade and hydrochloric acid with Millipore Suprapur™ grade from Merck were used. Dilutions with water were done with Merck Millipore Milli-Q™ water (18.2 MΩ cm). The ashing was performed in porcelain crucibles from Morgan Advanced Materials Haldenwanger. Cellulose filter with particle retention of lower than 2 µm were purchased from GE Healthcare - Whatman™. The chemical purification of Ru was performed in a class-10,000 clean room environment using class-10 laminar flow hoods in the Institut für Planetologie at the University of Münster. We used pre-cleaned Savillex Teflon perfluoralkoxy (PFA) vials and bottles. Acids (HNO_3 and HCl) of Millipore Emsure™ grade were double distilled in Savillex™ DST-1000 Acid Purification Systems. Dilution of chemicals was conducted with Merck Millipore Milli-Q™ water (18.2 MΩ cm). In the absence of a certified standard reference solution for Ru, we used an in-house Ru standard solution purchased from Alfa Aesar.

Sample preparation for MC-ICPMS analyses. The filters were cut in ~2.5 g pieces and ashed in an oven over night at 450 °C. The ashed samples were transferred four times with 2.5 ml of 69% nitric acid into a 110 mL polytetrafluoroethylene (PTFE) vessel. The sealed vessels were put into a MARS 6 microwave digestion system from CEM Corporation™ for a more efficient digestion. These were heated 20 min to a temperature of 160 °C and held at this temperature for 30 min. After cooling, the solutions were filtered through a cellulose filter with a particle retention of 2 µm. The filtrates were evaporated to dryness and dissolved in 5 ml of 6 M hydrochloric acid. Due to the matrix change, a second filtration step was performed to yield a particle-free solution.

The chemical separation of Ru followed a modified two-stage ion exchange chromatography procedure based on the method outlined in ref. [36]. After filtration, the sample solutions were transferred into 15 ml Savillex PFA beakers and then dried down at 100 °C on a hot plate. Cations were converted into their chloride form using multiple dry-downs in 6 M HCl and re-dissolved in 5 ml of 0.2 M HCl. In the first step, the sample solutions were loaded onto cation exchange columns filled with 10 mL pre-cleaned BioRad AG 50W-X8 (100–200 mesh) resin. On these columns, the bulk of the Ru was eluted in a total volume of 14 mL 0.2 M HCl, while the major elements (i.e., Fe and Ni) remain adsorbed on the resin. Then the Ru fractions were dried down on a hot plate and re-dissolved three times using 5 mL of 1 M HF. To remove remaining interfering elements (Zr, Mo, Pd), the Ru fractions were dissolved in 7 mL 1 M HF and were loaded onto anion exchange columns filled with 2 ml of pre-cleaned BioRad AG 1-X8 (100–200 mesh) resin. Ruthenium was eluted in 14 mL 1 M HF, whereas Zr, Mo, and Pd remain adsorbed onto the resin. The final Ru fractions were dried and re-dissolved in 0.5 mL 0.28 M HNO_3.

This procedure led to Ru fractions of the air filter samples with Mo/Ru < 0.03 and Pd/Ru < 0.009 (for the non-natural Ru filter <0.003 and <0.001, respectively) that allow for precise interference correction on ^{96}Ru, ^{98}Ru, ^{100}Ru, ^{102}Ru, and ^{104}Ru within the precision given on the Ru isotope data. The total amount of Ru available for isotope ratio measurements by MC-ICPMS were determined by comparing the intensity of a ~10% aliquot of each sample solution to a standard. The amounts of Ru available ranged between 0.4 to 3.4 ng.

Mass spectrometry and data reduction. The Ru isotope measurements were conducted using a Thermo Scientific Neptune Plus MC-ICPMS at the Institut für Planetologie in Münster, Germany. Prior to the measurements, samples were dissolved in 0.28 M HNO_3 and were introduced into the mass spectrometer using a CETAC Aridus II desolvating system combined with an 80 µL·min^{-1} ESI PFA nebulizer. The formation of oxides was monitored as CeO/Ce and reduced to <1% by the addition of N_2 to the sample gas. Sample and standard solutions were measured at concentrations of ~10 and ~1 ppb using conventional Ni H cones. Ion beams were simultaneously collected in static mode for all seven stable Ru isotopes (^{96}Ru, ^{98}Ru, ^{99}Ru, ^{100}Ru, ^{101}Ru, ^{102}Ru, ^{104}Ru) together with ^{97}Mo and ^{105}Pd as interference monitors. Ion beams were measured using Faraday cups connected to 10^{11} Ω feedback resistors, except the ion beams of ^{99}Ru and ^{101}Ru that were collected using 10^{12} Ω feedback resistors. Total ion-beam intensities corresponded to ~110 V·ppm^{-1}. Sample measurements comprised 30 × 4.2 s integrations of the ion beams and consumed ~2 ng Ru for 10 ppb and ~0.2 ppb Ru for 1 ppb solutions, respectively. The baselines were measured on peak with 40 × 8.4 s integrations on a solution blank prior each measurement. Each sample measurement was bracketed by measurements of an Alfa Aesar Ru standard solution with matching concentration (±10%). After each sample or standard measurement, the system was rinsed for 4 min (1 ppb Ru solution) or 8 min (10 ppb Ru solution), respectively.

Accuracy and reproducibility. The measured Ru isotope ratios of the air filter samples were corrected for instrumental mass bias by normalizing the bracketing standards to ^{99}Ru/^{101}Ru of 0.745 following the exponential law and using the average isotope fractionation factor (β) calculated from the two bracketing standards. Interferences of Mo and Pd on ^{96}Ru, ^{98}Ru, ^{100}Ru, ^{102}Ru, and ^{104}Ru were corrected with the mass bias corrected ^{97}Mo and ^{105}Pd monitors.

Supplementary Table 2 shows the long-term reproducibility of 10 and 1 ppb standard solution measurements (including all bracketing standard measurements). In addition, a Ru-doped (~20 ng) blank filter was processed through the complete chemical purification procedure to determine the external reproducibility. The 10 and 1 ppb measurements of this Ru-doped blank filter show a standard deviation of ~0.002 (2 s.d.) on all Ru isotope ratios (Supplementary Table 2). Of note, the deviation on ^{102}Ru/^{101}Ru of the 10 ppb Ru-doped blank filter solution relative to the standard (i.e., natural ^{102}Ru/^{101}Ru) can be explained by a higher Pd/Ru ratio (>0.01) possibly due to contamination of the 10 ppb solution prior measurements. The Ru isotope ratios determined from the 1 ppb Ru-doped filter measurements (Pd/Ru < 0.008) agree within uncertainty with standard solution measurements (Supplementary Table 2; Supplementary Fig. 2). All other air filter samples analyzed in this study have Pd/Ru < 0.008 and Mo/Ru < 0.03. The air filter containing the fission-generated and radioactive Ru has Pd/Ru < 0.001 and Mo/Ru < 0.003.

Code availability

No custom code or mathematical algorithm was used in this study.

Data availability

All data are available in the main text or in the Supplementary Materials.

Received: 25 October 2019; Accepted: 27 April 2020;
Published online: 09 June 2020

References

1. Masson, O. et al. Potential source apportionment and meteorological vonditions involved in airborne ^{131}I detections in January/February 2017 in Europe. *Environ. Sci. Technol.* **52**, 8488–8500 (2018).
2. Masson, O. et al. Airborne concentrations and chemical considerations of radioactive ruthenium from an undeclared major nuclear release in 2017. *Proc. Natl Acad. Sci. USA* **116**, 16750–16759 (2019).
3. Saunier, O., Mathieu, A., Didier, D., Masson, O. & Dumont le Brazidec, J. Atmospheric modelling and source reconstruction of radioactive ruthenium from an undeclared major nuclear release in 2017. *Proc. Natl Acad. Sci. USA* **116**, 24991–25000 (2019).
4. IAEA. *Significant Incidents in Nuclear Fuel Cycle Facilities*. IAEA-TECDOC-867 (IAEA, 1996).
5. Sørensen, J. H. Method for source localization proposed and applied to the October 2017 case of atmospheric dispersion of Ru-106. *J. Environ. Radioact.* **189**, 221–226 (2018).
6. Shershakov, V. & Borodin, R. Some results of determining the source and reasons for the appearance of ^{106}Ru in Russia in September–October 2017. *IOP Conf. Ser.: Mater. Sci. Eng.* **487**, 012002 (2019).
7. Shershakov, V. M., Borodin, R. V. & Tsaturov, Y. S. Assessment of possible location Ru-106 source in Russia in September–October 2017. *Russ. Meteorol. Hydrol.* **44**, 196–202 (2019).
8. Bossew, P. et al. An episode of Ru-106 in air over Europe, September–October 2017—Geographical distribution of inhalation dose over Europe. *J. Environ. Radioact.* **205-206**, 79–92 (2019).
9. Rosatom. *Rosatom Official Statement Ru-106*, http://www.rosatominternational.com/en/news/2017/11/23-11-2 (2017).
10. Nuclear Engineering International. *Russian Commission Says Mayak not the Source of Ru-106*, http://www.neimagazine.com/news/newsrussian-commission-says-mayak-not-the-source-of-ru-106-6000301/ (2017).
11. Cartlidge, E. Isotope cloud linked to failed neutrino source. *Science* **359**, 729 (2018).
12. IAEA. *Press Conference, IAEA Board of Governors*, http://iaea.streaming.at/20171123 (from minute 12:00) (2017).
13. Nuclear Safety Institute of the Russian Academy of Sciences. *Meeting of the International Independent Scientific Commission for Investigation of Ru-106 Case*, http://en.ibrae.ac.ru/newstext/915/ (2018).
14. Nuclear Safety Institute of the Russian Academy of Sciences. *2nd Meeting of the International Independent Scientific Commission for Investigation of Ru-106 Case in Europe in September—October 2017*, http://en.ibrae.ac.ru/newstext/911/ (2018).
15. IAEA. *Specific Safety Guide No. SSG-42: Safety of Nuclear Fuel Reprocessing Facilities*, https://www-pub.iaea.org/MTCD/Publications/PDF/P1744_web.pdf (2017).
16. Cooke, M. W., Botti, A., Zok, D., Steinhauser, G. & Ungar, K. R. Identification of a chemical fingerprint linking the undeclared 2017 release of ^{106}Ru to advanced nuclear fuel reprocessing. *Proc. Natl. Acad. Sci. USA*, https://doi.org/10.1073/pnas.2001914117 (2020).
17. Landay, J. *U.S.-based Experts Suspect Russia Blast Involved Nuclear-powered Missile*, https://www.reuters.com/article/us-russia-blast-usa-idUSKCN1UZ2H5 (2019).
18. Gerasimov, A. S., Kornoukhov, V. N., Sald'ikov, I. S. & Tikhomirov, G. V. Production of high specific activity ^{144}Ce for artificial sources of antineutrinos. *At. Energy* **116**, 54–59 (2014).
19. Dresel, P. E., Evans, J. C. & Farmer, O. T. *Investigation of Isotopic Signatures for Sources of Groundwater Contamination at the Hanford Site*, https://www.pnnl.gov/main/publications/external/technical_reports/pnnl-13763.pdf (2002).
20. Byerly, B. et al. Determination of initial fuel state and number of reactor shutdowns in archived low-burnup uranium targets. *J. Radioanal. Nucl. Chem.* **307**, 1871–1876 (2016).
21. Shima, M., Thode, H. G. & Tomlinson, R. H. Cumulative yields of stable and long-lived isotopes of ruthenium and palladium in neutron-induced fission. *Can. J. Phys.* **56**, 1340–1352 (1978).
22. Hanson, S. K. et al. Measurements of extinct fission products in nuclear bomb debris: Determination of the yield of the Trinity nuclear test 70 y later. *Proc. Natl Acad. Sci. USA* **113**, 8104–8108 (2016).
23. Loss, R. D. et al. The Oklo natural reactors: cumulative fission yields and nuclear characteristics of Reactor Zone 9. *Earth Planet. Sci. Lett.* **89**, 193–206 (1988).

24. Zok, D., Sterba, J. H. & Steinhauser, G. Chemical and radioanalytical investigations of ^{106}Ru-containing air filters from Vienna in fall 2017: searching for stable element anomalies. *J. Radioanal. Nucl. Chem.* **318**, 415–421 (2018).
25. Hoefs, J. *Stable Isotope Geochemistry* 8th edn (Springer, 2018).
26. Johnson, C. M., Beard, B. L. & Albarède, F. Overview and General Concepts. *Rev. Mineral. Geochem.* **55**, 1–24 (2004).
27. Hopp, T., Fischer-Gödde, M. & Kleine, T. Ruthenium stable isotope measurements by double spike MC-ICPMS. *J. Anal. At. Spectrom.* **31**, 1515–1526 (2016).
28. Berglund, M. & Wieser, M. E. Isotopic compositions of the elements 2009 (IUPAC technical report). *Pure Appl. Chem.* **83**, 397–410 (2011).
29. Pfeiffer, F. et al. *Abfallspezifikation und Mengengerüst, GRS-278 (in German)*, https://www.grs.de/en/node/1749 (2011).
30. Nilsen, T. *Nucelar Waste Removal Starts in Andreeva Bay*, https://thebarentsobserver.com/en/ecology/2017/05/nuclear-waste-removal-starts-andreeva-bay (2017).
31. *Nilsen, T. First Load of Nuclear Waste from Andreeva Bay Arrives in Mayak*, https://thebarentsobserver.com/en/security/2017/08/first-load-nuclear-waste-andreeva-bay-arrives-mayak (2017).
32. Cribier, M. et al. Proposed search for a fourth neutrino with a PBq antineutrino source. *Phys. Rev. Lett.* **107**, 201801 (2011).
33. Vivier, M. et al. SOX: search for short baseline neutrino oscillations with Borexino. *J. Phys. Conf. Ser.* **718**, 062066 (2016).
34. Meyer, M. *SOX—Towards the Detection of Sterile Neutrinos in Borexino: Beta Spectrum Modeling, Monte Carlo Development and Sensitivity Studies for the Sterile Neutrino Search in Borexino*. PhD thesis, Universität Hamburg (2016).
35. Bolshov, L. *Safety for Nuclear Fuel Cycle in the Russian Federation*, http://www.oecd-nea.org/nsd/workshops/fcsafety/proceedings/documents/Session_3_2_Presentation_4.pdf (2007).
36. Hopp, T. & Kleine, T. Nature of late accretion to Earth inferred from mass-dependent Ru isotopic compositions of chondrites and mantle peridotites. *Earth Planet. Sci. Lett.* **494**, 50–59 (2018).

Acknowledgements

We acknowledge financial support by the VolkswagenStiftung (Az. 94403). This research received funding to T.K. from the European Research Council under the European Community's Seventh Framework Program (FP7/2007–2013 Grant Agreement 616564 'ISOCORE'). The authors benefited greatly from constructive comments on an earlier draft of the paper by G. A. and C. R. Brennecka.

Author contributions

T.H. and D.Z. contributed equally to the study. G.S. and D.Z. designed the study and D.Z. prepared and digested the samples. T.H. conducted the chemical separation and MC-ICPMS measurements. T.H. and T.K. evaluated the isotope measurement data. All authors discussed the results and contributed to the writing of the manuscript.

Competing interests

The authors declare no competing interests.

Additional information

Supplementary information is available for this paper at https://doi.org/10.1038/s41467-020-16316-3.

Correspondence and requests for materials should be addressed to T.K. or G.S.

Peer review information *Nature Communications* thanks Stephen Lamont, Camille Palmer, and the other, anonymous, reviewer(s) for their contribution to the peer review of this work.

Reprints and permission information is available at http://www.nature.com/reprints

Publisher's note Springer Nature remains neutral with regard to jurisdictional claims in published maps and institutional affiliations.

Chapter 7

Determination of Characteristic vs Anomalous $^{135}Cs/^{137}Cs$ Isotopic Ratios in Radioactively Contaminated Environmental Samples

D. Zok, T. Blenke, S. Reinhard, S. Sprott, F. Kegler, L. Syrbe, R. Querfeld, Y. Takagai, V. Drozkov, I. Chyzhevskyi, S. Kirieiev, B. Schmidt, W. Adlassnig, G. Wallner, S. Dubchak, G. Steinhauser†

Environmental Science & Technology, vol. 55, no. 8, pp. 4984-4991, 2021.
DOI: 10.1021/acs.est.1c00180

Author contributions:
D.Z. and G.S. designed the study
D.Z., T.B., S.R., S.S., F.K., L.S., R.Q., Y.T. V.D., I.C., S.K., G.W. and S.D.performed sample collecting and/or preparation as well as gamma spectrometry and evaluation
B.S. and W.A. performed mosses species classification
D.Z. performed elemental separations, ICP-QQQ-MS measurements and evaluations
D.Z. and G.S contributed to the writing of the paper

† Correspondence to: steinhauser@irs.uni-hannover.de

Environmental Science & Technology

pubs.acs.org/est

Article

Determination of Characteristic vs Anomalous $^{135}Cs/^{137}Cs$ Isotopic Ratios in Radioactively Contaminated Environmental Samples

Dorian Zok, Tobias Blenke, Sandra Reinhard, Sascha Sprott, Felix Kegler, Luisa Syrbe, Rebecca Querfeld, Yoshitaka Takagai, Vladyslav Drozdov, Ihor Chyzhevskyi, Serhii Kirieiev, Brigitte Schmidt, Wolfram Adlassnig, Gabriele Wallner, Sergiy Dubchak, and Georg Steinhauser*

Cite This: *Environ. Sci. Technol.* 2021, 55, 4984−4991

Read Online

ACCESS | Metrics & More | Article Recommendations | Supporting Information

ABSTRACT: A contamination with the ubiquitous radioactive fission product ^{137}Cs cannot be assigned *per se* to its source. We used environmental samples with varying contamination levels from various parts of the world to establish their characteristic $^{135}Cs/^{137}Cs$ isotope ratios and thereby allow their distinction. The samples included biological materials from Chernobyl and Fukushima, historic ashed human lung tissue from the 1960s from Austria, and trinitite from the Trinity Test Site, USA. After chemical separation and gas reaction shifts inside a triple quadrupole ICP mass spectrometer, characteristic $^{135}Cs/^{137}Cs$ isotope signatures (all as per March 11, 2011) were obtained for Fukushima- (∼0.35) and Chernobyl-derived (∼0.50) contaminations, in agreement with the literature for these contamination sources. Both signatures clearly distinguish from the characteristic high ratio (1.9 ± 0.2) for nuclear-weapon-produced radiocesium found in human lung tissue. Trinitite samples exhibited an unexpected, anomalous pattern by displaying a low (<0.4) and nonuniform $^{135}Cs/^{137}Cs$ ratio. This exemplifies a ^{137}Cs-rich fractionation of the plume in a nuclear explosion, where ^{137}Cs is a predominant species in the fireball. The onset of ^{135}Cs was delayed because of the longer half-life of its parent nuclide ^{135}Xe, causing a spatial separation of gaseous ^{135}Xe from condensed ^{137}Cs, which is the reason for the atypical $^{135}Cs/^{137}Cs$ fractionation in the fallout at the test site.

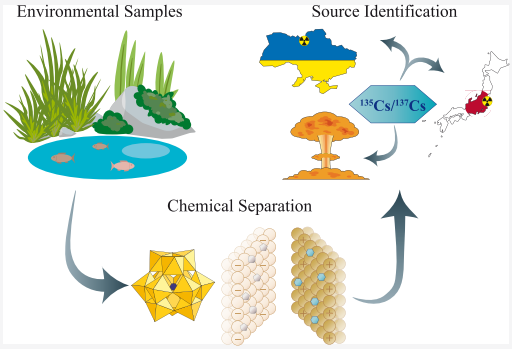

INTRODUCTION

Cesium-137 ($T_{1/2}$ = 30.1 y) is a high-yield product of nuclear fission and one of the most notorious radioactive contaminants globally. It has been released in great amounts in the course of nuclear testing as well as all the major nuclear accidents in Fukushima (2011),[1,2] Chernobyl (1986),[3] Windscale (1957), and Kyshtym (1957),[4] thus making it a ubiquitous environmental contaminant. Due to its many sources, ^{137}Cs alone cannot be assigned to its source(s) but requires the use of sophisticated analytical techniques to include difficult-to-measure, long-lived ^{135}Cs ($T_{1/2}$ = 2.3 × 10^6 y) to establish a characteristic $^{135}Cs/^{137}Cs$ isotopic ratio. This ratio is becoming a powerful tool for the assignment of an environmental radiocesium contamination to its source and thereby may help reveal crucial forensic information such as the legal background or age of said contamination.[5] Even migration pathways or mixing of sources could be resolved by application of $^{135}Cs/^{137}Cs$ ratios as isotopic fingerprints. While the use of ratios of typical actinide isotopes of plutonium or uranium is well established in nuclear forensics, the use of the radiocesium system $^{135}Cs/^{137}Cs$ is fairly novel, rapidly expanding, and not yet fully explored.[6−10] In the first years after a nuclear accident, some forensic insight can be derived from establishing the ratio of shorter-lived ^{134}Cs ($T_{1/2}$ = 2.1 y) to ^{137}Cs. However, the applicability of this ratio is not only limited by the short half-life of ^{134}Cs but also by the nuclear production routes of the radiocesium isotopes. ^{134}Cs is produced by neutron capture of the stable fission product ^{133}Cs, which is the end-point of the 133 isobar. In contrast, ^{137}Cs is a fission product cumulating any parent nuclides on the 137 isobar. Last, ^{135}Cs is a direct fission product, but its onset is greatly suppressed by its parent nuclide ^{135}Xe that has a giant cross section (2.6 × 10^6 b) for thermal neutron capture.[11] Depending on the neutron flux density inside the reactor, ^{135}Xe will be burnt off to a significant degree and thus prevent the onset of ^{135}Cs. This scenario refers to operating nuclear reactors in particular. However, whenever the reactor is shut down, ^{135}Xe will be produced by its parent ^{135}I ($T_{1/2}$ = 6.6 h) after the neutron flux has stopped, and ^{135}Xe ($T_{1/2}$ = 9.1 h) will be allowed to decay into its daughter ^{135}Cs. The same scenario applies to the explosion of a nuclear warhead, with its very short duration and intense as well as high-energy neutron flux that allows for the

Received: January 8, 2021
Revised: February 12, 2021
Accepted: February 17, 2021
Published: March 12, 2021

formation of ^{135}Cs. In contrast to ^{134}Cs and ^{137}Cs, both of which are produced as a function of burnup, the onset of ^{135}Cs mainly depends on the (lack of) neutron action on its parent. This adds much more distinct features to the $^{135}Cs/^{137}Cs$ fingerprint as compared to the easy-to-measure $^{134}Cs/^{137}Cs$ ratio, which is fairly similar for fuel with similar burnup and cooling times.[12]

The distinct nuclear production routes of ^{135}Cs and ^{137}Cs allow for a characteristic ratio of $^{135}Cs/^{137}Cs$ that acts as a fingerprint for a particular source. It allows for a fine distinction between contaminations caused by nuclear weapon fallout[13,14] and the releases from the Chernobyl nuclear power plant (ChNPP) or Fukushima Daiichi nuclear power plant (FDNPP).[8,15−17] Naturally, global nuclear weapons fallout affected mainly the entire northern hemisphere and hence contributed minute amounts of radiocesium to the Chernobyl and Fukushima signature. Even the fallout of Chernobyl-derived radiocesium was observed in small but discernible amounts in Japan in 1986.[18] In any case, our samples were so highly contaminated that the effects of this mixing of signatures can be deemed negligible. When using highly contaminated materials (and thus large amounts of the analyte), it even allows a distinguishing between the different reactor blocks and spent fuel pools at FDNPP.[6,19] With lower amounts of the analyte, this distinction is much more challenging. For this study, living organisms (moss, fish) were chosen to represent Chernobyl's and Fukushima's contamination because these must have taken up bioavailable radiocesium from the environment.

Despite all advantages, measurement of the ^{135}Cs remains challenging. While activities of ^{134}Cs and ^{137}Cs are easily determinable by gamma spectrometry,[11] ^{135}Cs is a long-lived, pure β^--emitter that exhibits low specific activities in environmental concentrations. Therefore, classical radiometric methods are usually not applicable for this nuclide. Furthermore, also mass spectrometric methods face obstacles in the measurement of radiocesium isotopes because of interfering stable barium isotopes ^{135}Ba (natural abundance 6.59%) and ^{137}Ba (11.23%) and low radiocesium concentrations at moderate contamination levels. Thus, a multistep chemical separation prior to the measurement is imperative, starting with ion exchange reactions of Cs with ammonium molybdophosphate (AMP), followed by anionic and cationic ion exchange resins.[6,7] However, formation of polyatomic interferences in the plasma of an inductively coupled plasma mass spectrometer (ICP-MS) remains a threat for the analysis of trace amounts of Cs isotopes. This is mainly true for Mo ($^{95}Mo^{40}Ar^+$, $^{97}Mo^{40}Ar^+$) that has been introduced into the sample in the form of AMP. Further possible interferences include oxides of ^{121}Sb and ^{119}Sn, as well as hydrides of $^{134/136}Xe$ and $^{134/136}Ba$.[6,14] Therefore, molybdates, along with antimonates and stannates, have to be separated from Cs by anionic exchange resins.

Triple quadrupole ICP-mass spectrometry (ICP-QQQ-MS) has been proven a powerful tool to measure the $^{135}Cs/^{137}Cs$ ratio by taking advantage of chemical shift reactions.[20] Quadrupoles 1 and 3 are set on the detection at an m/z ratio of 135 and 137, respectively, while the central mass filter constitutes a reaction chamber with a gas filling of He and a low percentage of N_2O.[21] Residual barium is likely to form an oxide and hence may be suppressed by several orders of magnitude. In contrast, Cs passes the filter nearly reactionlessly. A combination of chemical separation and online gas reactions warrants the detection of even small amounts of ^{135}Cs and ^{137}Cs. The objective of this study was to investigate the applicability of the $^{135}Cs/^{137}Cs$ isotopic fingerprinting technique to common (Chernobyl, Fukushima) and understudied sources of radiocesium (nuclear weapons fallout) and to find out if the various sources can be discerned by a unique fingerprint.

MATERIALS

Sample Materials. Three major sources of environmental radiocesium were to be covered in this study: atmospheric nuclear weapons fallout as well as the major nuclear accidents at ChNPP and FDNPP. For the analysis, we collected hyperaccumulating mosses from the areas around ChNPP and FDNPP. Some species of moss are notorious for their high affinity for Cs.[22] Furthermore, permission was obtained to catch fish in the Chernobyl cooling pond as a representative of animal tissue, which, due to its higher fat content, is more challenging in the chemical treatment than plant materials. Samples with a "pure" nuclear weapons fallout contamination are hardly accessible nowadays. To exemplify $^{135}Cs/^{137}Cs$ signatures of nuclear weapons fallout, we selected historic materials: historic ashed human lung tissue from the 1960s from Austria as well as commercially available samples of trinitite. Trinitite is a mineral that formed upon the first nuclear weapons test at the Trinity Test Site, NM, USA, and consists of molten glass, crystalline debris, and radionuclides. Before the Trinity Test Site was closed to the public, large amounts of trinitite were collected by mineral and nuclear enthusiasts and are traded still today.

Samples from Chernobyl, Ukraine. Two types of samples were taken from the Chernobyl Exclusion Zone (CEZ), Ukraine. Moss samples were collected in October 2018 in the vicinity of the cooling pond of ChNPP. Wels catfish (*Silurus glanis*) and zander (*Sander lucioperca*) were caught in October 2018, too. Details on samples and sampling locations are compiled in the Supporting Information (SI), see Table S1 and Figures S1 and S2. For the present study, muscle meat from the back of the fish was used.

Samples from Fukushima, Japan. Mosses were collected in Fukushima and neighboring prefectures (Table S2, Figure S3) in July 2019. Samples were weighed, dried at 50 °C, homogenized in a ball mill, and sterilized by autoclave. For a safe transportation to Germany and obeying regulations, they were processed to be sealed products in solidified gel (agar−agar gel). Upon arrival, the gel was removed by heating at 80 °C for 36 h. Afterward, the dried gel film was carefully removed from the moss for measurement. All measurements of radioactivity in sample were conducted in Germany.

Trinitite from the Trinity Test Site, USA. Two specimens of trinitite were purchased form the Mineralogical Research Co. Both samples were recovered from the Trinity Test Site (Tularosa Basin, Alamogordo), NM, USA, where the first nuclear warhead was tested on July 16, 1945. Specifications of the trinitites can be found in Table S3 and Figure S4.

Historic Ashed Human Lung Tissue from Vienna. Sample materials from a historic study of human lung tissue were made available to this study.[23−26] The donators passed away in the early 1960s. The tissue samples were collected by the late Prof. Schönfeld of University of Vienna, ashed, and then analyzed for gamma-emitting fission products. Samples were then put on storage at the University of Vienna from where they were now retrieved (data in Table S4). Five samples from 1963 to 1965 (thus covering the time range of the maximum fallout) were pooled to obtain measurable radiocesium concentrations.

IAEA Reference Materials. For the internal and external comparability of our measurements, homogeneous and commercially available reference materials provided by IAEA

https://dx.doi.org/10.1021/acs.est.1c00180
Environ. Sci. Technol. 2021, 55, 4984−4991

were used. Both reference materials, IAEA-372 (radionuclides in grass) and IAEA-330 (radionuclides in spinach), are from the same farm in Polesskoe, Kiev, Ukraine, and are often used as reference materials for this type of study as they exhibit a $^{135}Cs/^{137}Cs$ ratio characteristic for Chernobyl radiocesium fallout (Table S5).

METHODS

Sample Preparation. Organic samples were incinerated in porcelain crucibles for the utmost removal of the organic matrix. First, they were heated up in a muffle furnace to 350 °C (2 h) and held at this temperature for 2 h. Then, the furnace was heated to 450 °C (2 h) and held for 12 h for final ashing. After cooling, the ashed material was transferred into 110 mL PTFE vessels of the microwave digestion system MARS 6 from CEM Corporation using 4 × 2.5 mL of supra-pure HNO_3 (69%, ROTIPURAN, Supra, Carl Roth). Digestion was performed using a temperature ramp from room temperature to 160 °C within 20 min. This temperature was held for 30 min. After cooling, the solutions were filtered through a Whatman Filter 602 H1/2 (pore size <2 μm) and transferred into PFA vessels. The digestion vessels were washed out with 4 × 5 mL of Merck Millipore Milli-Q water (18.2 MΩcm). Digestion and wash solutions were combined and evaporated to dryness. The residue was redissolved with 10 mL of 1.6 M HNO_3. A 50 μL aliquot was taken as a recovery yield tracer. The tracer was diluted to 2 mL of a 2% HNO_3 solution with sub-boiled HNO_3 for concentration determination. Sub-boiled HNO_3 was prepared from 65% HNO_3 (ROTIPURAN, p.a., Carl Roth).

Trinitite samples were crushed to small particles and put into a 120 mL Savillex PFA vessel. Three × 20 mL HF (48%, Merck EMSURE, ACS) was added and evaporated to dryness after each step. Filtration, evaporation, and recovery yield determination were performed as above.

Cs Separation by AMP. For the Cs extraction from the dissolved sample matrices, solid ammonium molybdophosphate powder ($H_{12}Mo_{12}N_3O_{40}P{\cdot}xH_2O$ ($x \approx 3$); AMP; ACS > 95%) from Alfa Aesar was used. Solutions were brought to 50 mL of 1.6 M HNO_3, and 35 mg of AMP was added. The solution was stirred for 1 h. Thereafter, the samples were filtered thought a 1.2 μm cellulose acetate syringe filter. The AMP(Cs) was dissolved by adding 10 mL of 1.5 M NH_3 solution (20%, ROTIPURAN Supra, Carl Roth) and collected in a PFA breaker.[6,21]

Anion Exchange Resin. In order to remove the interfering elements Mo, Sb, and Sn, the anion exchange resin Dowex 1-X8 (100−200 mesh) from Alfa Aesar was used. Prior to use, the 2 mL resin was cleaned for each sample with 4 × 5 mL of 1.5 M NH_3. Then, the anion exchange resin was conditioned with 2 × 5 mL of 1.5 M NH_3, followed by loading the dissolved AMP(Cs) solution. As a cation, Cs^+ is not trapped in this resin. Residual Cs^+ ions were eluted from the resin by adding 2 × 5 mL of 1.5 M NH_3. Loading and elution solutions were combined and evaporated to dryness in a PFA beaker. Redissolution was achieved with 10 mL of 0.15 M NH_3 as suggested by Zheng et al.[6,21]

Cation Exchange Resin. The cation exchange resin AG 50W-X8 (100−200 mesh) from BioRad Laboratories, Inc. was precleaned by using 4 M sub-boiled HNO_3 to remove unwanted cations during resin production (2 × 5 mL).[27] A volume of 2 mL of the cleaned AG 50W-X8 was packed into an empty column and used for one sample.

The resin was conditioned with 2 × 5 mL 0.15 M NH_3, followed by loading of the redissolved sample solution obtained from the previously described anion exchange procedure. The resin was washed with 2 × 5 mL 0.15 M NH_3 and 18.2 MΩcm H_2O, respectively. Elution of Cs^+ was performed with 6 × 5 mL of 1.5 M sub-boiled HCl (prepared from 37% HCl, ROTIPURAN, p.a., Carl Roth). The Cs containing eluate was collected in a PFA beaker and evaporated to dryness. The dried residue was redissolved in 2 mL of 2% HNO_3. An aliquot of 50 μL was taken for the final calculation of the recovery rate.[6,21]

Gamma Spectrometry for ^{137}Cs Determination. All samples were measured on high-purity germanium (HPGe) detectors at the Institute of Radioecology and Radiation Protection in Hannover, Germany (volume 131 cm^3, relative efficiency 28%, FWHM at 1332 kev of 1.9 keV). Spectra were evaluated using Genie 2000 software from Mirion Technologies, Inc. The certified multinuclide gamma-ray emitting solution QCY-48 from Eckhart and Ziegler Nuclitec GmbH, Germany, was used to calibrate the detector efficiency.

Mass Spectrometry Using ICP-QQQ-MS. Concentrations and isotope ratios were measured using an Agilent 8900 Triple Quadrupole ICP-MS coupled to an SPS4 autosampler using MassHunter 4.4 software, all from Agilent Technologies, Inc. All measurement solutions were prepared from Milli-Q H_2O (18.2 MΩcm) and sub-boiled HNO_3.

Element concentrations as well a recovery rates were measured in a single quadrupole mode without reaction gas. Isotope ratios were measured in triple quadrupole mode with a mixture of He (5N, Linde GmbH) and N_2O (2N, CANGas, Messer Group GmbH) as reactions gas. Parameters are listed in the Supporting Information, Tables S6−S8. Measured values were corrected with a very low processing blank and acid blank (both lower than 1 cps), decay correction of ^{137}Cs to the Fukushima nuclear accident (March 11, 2011), and using the exponential law for mass bias correction.

Residual Ba content after full separation was checked by ICP-MS and was found low enough not to interfere significantly. Mass bias of the plasma was corrected with an external 5 ppb europium reference solution (1000 mg/L, Alfa Aesar) spiked to a blank processed eluate to achieve a comparable matrix like the samples (eq 1 and 2). The β value for this system and measurement was −1.0896,; the reference was the natural Eu ratio.[28]

$$\left(\frac{^{135}Cs}{^{137}Cs}\right)_{corrected} = \left(\frac{^{135}Cs}{^{137}Cs}\right)_{measured} \times \left[\frac{M(^{135}Cs)}{M(^{137}Cs)}\right]^{\beta} \quad (1)$$

$$\beta = \left(\frac{\ln[(^{151}Eu/^{153}Eu)_{reference}/(^{151}Eu/^{153}Eu)_{measured}]}{\ln[(M^{151}Eu)/(M^{153}Eu)]}\right) \quad (2)$$

RESULTS AND DISCUSSION

^{137}Cs Activities and Content of the Samples. The samples analyzed in this study covered not only a wide range of sources but also activity concentrations. Therefore, suitable amounts were chosen to achieve at least some tens of becquerel for a sufficient counting statistic during ICP-QQQ-MS measurement. Activity concentrations of ^{137}Cs obtained by gamma spectrometry (unless certified) are tabulated in Tables S1−S5. Moss samples from Fukushima exhibited the highest activity concentration with more than 2500 Bq/g fresh weight. Similarly, the fish and moss samples collected from CEZ showed reasonably high ^{137}Cs activity concentrations. Very low activities

https://dx.doi.org/10.1021/acs.est.1c00180
Environ. Sci. Technol. 2021, 55, 4984−4991

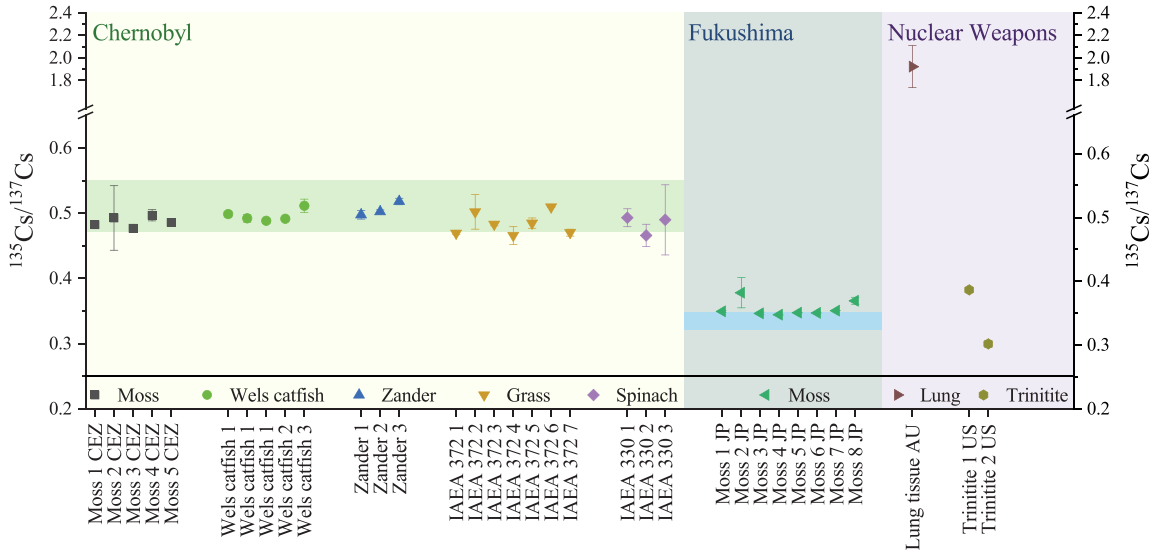

Figure 1. $^{135}Cs/^{137}Cs$ isotopic ratios for samples from different locations. Samples are classified for their origin in Chernobyl, Fukushima, or nuclear weapons. All values are date corrected to March 11, 2011 for better comparison. Darker areas showing previously published values for the $^{135}Cs/^{137}Cs$ ratio for Chernobyl and Fukushima by other techniques and groups.

are found in the samples of ashed human lung tissue with only millibecquerels per gram. The choice of the amount of sample material needed for ICP-QQQ-MS measurements depended on the ^{137}Cs activities or availability of said material.

Concentrations of Analytes and Recovery Yields. Aliquots were taken before and after the separation to determine concentrations and yields of the key elements Cs and its main isobaric interference Ba, as well as Mo, Sn, and Sb. Exact values are listed in Tables S9 and S10 in the SI. Generally, the purification process removed approximately 90% of the initial amount of interfering Mo, Sn, and Sb. For the most sample types, their initial content is just in the range of some tens of nanograms. A few samples appeared to be slightly contaminated by Mo due to the use of AMP. Nevertheless, the residual concentrations proved low enough to not interfere with the determination of the $^{135}Cs/^{137}Cs$ ratio. Barium removal in the separation proved to be highly efficient (99.7%). Losses of Cs through the entire purification process were in the range of 20%. In any case, please note that the initial Cs content is relatively low with only some hundreds of nanograms, compared to the initial Ba content (up to several milligrams). This explains why instrumental suppression of Ba inside the ICP-QQQ-MS alone is insufficient, making the chemical separation crucial to decreasing the Ba content into the lower nanogram range prior to measurement.

$^{135}Cs/^{137}Cs$ Isotopic Ratios. Calculated values for the $^{135}Cs/^{137}Cs$ ratio are shown in Figure 1, together with reference values from the literature (darker area).[6,7,15,16,21] Tabulated values can be found in Table 2, together with activities and the masses of both nuclides. Since the $^{135}Cs/^{137}Cs$ ratio depends on the fairly short half-life of ^{137}Cs, the ratio shifts significantly over the decades. For certain samples, e.g., Chernobyl, Fukushima, or trinitite, an exact release date can be defined. However, for the lung tissue, this is trickier, because the lungs have likely accumulated radiocesium over several years. Table S11 and Figure S5 illustrate the shift of the ratio over time in tabulated and graphical form. Chernobyl samples were compared with the isotope ratio of reference material IAEA-375. This reference material has become the most used international reference for

Table 1. IAEA Reference Materials Comparison with Already Published Values[a]

reference	$^{135}Cs/^{137}Cs$	n	publication	method
IAEA-330	0.52 ± 0.005	2	Snow[13]	TIMS
	0.55 ± 0.031	4	Zheng[29]	ICP-QQQ-MS
	0.56 ± 0.02	3	Dunne[30]	TIMS
	0.58 ± 0.001	3	Bu[20]	TIMS
	0.56 ± 0.02	1	Zhu[31]	ICP-QQQ-MS
	0.48 ± 0.024	3	our work	ICP-QQQ-MS
IAEA-372	0.574 ± 0.008	7	Bu[20]	TIMS
	0.483 ± 0.031	7	our work	ICP-QQQ-MS

[a]Ratios were decay corrected to March 11, 2011. Errors are given with 2 s.d.

$^{135}Cs/^{137}Cs$ isotope measurements. Several groups already published values for this material with values ranging from 0.48 to 0.55 (corrected to March 11, 2011).[6,7,15,16,21] Unfortunately, IAEA-375 is no longer commercially available. As alternatives, IAEA-330 and IAEA-372 that were both contaminated by the Chernobyl nuclear accident are still available and have similar average values ranging between 0.523 and 0.525 (as of March 11, 2011; see Table 1).[14] In the discussion of $^{135}Cs/^{137}Cs$ fingerprints of releases from various sources, the time shift of the ratio complicates comparison of the data. While one may argue that Chernobyl samples should ideally be decay-corrected to April 26, 1986, and Fukushima samples should be decay-corrected to March 11, 2011, we chose the most recent nuclear accident (i.e., the Fukushima) as the uniform reference date for all ratios in this paper. This shows that, whatever the source, their fingerprint remains distinguishable today. On the downside of this uniform reference date, the values spread over a wider range and their uncertainties increase.

Generally, all of our CEZ samples are within the (lower) range of previously published Chernobyl $^{135}Cs/^{137}Cs$ isotope ratios with a value around 0.490 (Figure 1). Deviations are likely due to traces of residual Ba on the resin. Both IAEA reference materials are represented with 10 samples with a slight spread around 0.483. Mosses and fish that were collected inside the

https://dx.doi.org/10.1021/acs.est.1c00180
Environ. Sci. Technol. 2021, 55, 4984−4991

Table 2. $^{135}Cs/^{137}Cs$ Isotope Ratio Values of All Samples Including Analytical Uncertainties[a]

sample	$^{135}Cs/^{137}Cs$	uncert. (±)	^{135}Cs activity [Bq]	^{135}Cs mass [pg]	^{137}Cs activity [Bq]	^{137}Cs mass [pg]
wels catfish 1	0.499	0.004	1.2×10^{-4}	2.9	18.88	5.9
wels catfish 1	0.492	0.006	1.3×10^{-4}	2.9	19.26	6.0
wels catfish 1	0.488	0.003	1.2×10^{-4}	2.9	19.06	5.9
wels catfish 2	0.491	0.002	7.4×10^{-5}	1.7	11.49	3.6
wels catfish 3	0.511	0.010	6.1×10^{-5}	1.4	9.07	2.8
moss 1 CEZ	0.482	0.003	4.2×10^{-5}	1.0	6.57	2.0
moss 2 CEZ	0.493	0.050	8.0×10^{-5}	1.9	12.32	3.8
moss 3 CEZ	0.477	0.001	8.5×10^{-5}	2.0	13.50	4.2
moss 4 CEZ	0.497	0.009	3.1×10^{-4}	7.1	46.91	14.6
moss 5 CEZ	0.486	0.001	1.0×10^{-4}	2.4	16.14	5.0
zander 1	0.498	0.007	1.9×10^{-4}	4.3	28.47	8.9
zander 2	0.502	0.003	5.9×10^{-5}	1.4	8.96	2.8
zander 3	0.518	0.005	5.3×10^{-5}	1.2	7.76	2.4
IAEA 372 1	0.469	0.002	8.6×10^{-5}	2.0	13.91	4.3
IAEA 372 2	0.502	0.026	1.0×10^{-4}	2.3	15.14	4.7
IAEA 372 3	0.483	0.002	9.1×10^{-5}	2.1	14.24	4.4
IAEA 372 4	0.466	0.014	8.8×10^{-5}	2.0	14.26	4.4
IAEA 372 5	0.485	0.008	9.1×10^{-5}	2.1	14.26	4.4
IAEA 372 6	0.509	0.001	1.9×10^{-4}	4.5	28.68	8.9
IAEA 372 7	0.470	0.005	8.8×10^{-5}	2.0	14.12	4.4
IAEA 330 1	0.493	0.014	4.0×10^{-5}	0.9	6.20	1.9
IAEA 330 2	0.466	0.017	3.8×10^{-5}	0.9	6.20	1.9
IAEA 330 3	0.490	0.054	4.7×10^{-5}	1.1	7.27	2.3
moss 1 JP	0.349	0.001	1.3×10^{-2}	302	2830	880
moss 2 JP	0.378	0.023	6.1×10^{-3}	142	1231	383
moss 3 JP	0.346	0.002	7.9×10^{-3}	182	1721	535
moss 4 JP	0.344	0.001	6.7×10^{-3}	156	1476	459
moss 5 JP	0.347	0.001	6.2×10^{-3}	145	1361	423
moss 6 JP	0.347	0.001	1.1×10^{-2}	248	2334	725
moss 7 JP	0.351	0.001	1.1×10^{-3}	26.2	244	75.9
moss 8 JP	0.366	0.005	3.8×10^{-4}	8.9	79.72	24.8
lung AT	1.922	0.187	9.1×10^{-5}	2.1	3.60	1.1
trinitite 1 US	0.382	0.003	1.7×10^{-4}	3.9	32.94	10.2
trinitite 2 US	0.300	0.006	2.3×10^{-4}	5.3	58.10	18.1

[a]Values are date-corrected to March 11, 2011.

CEZ are in good agreement with both reference materials. After more than 30 years since the accident, the environment of the CEZ and its organisms still exhibit the identifiable signature of this release. This makes the $^{135}Cs/^{137}Cs$ ratio a suitable forensic tool for the assignment of a contamination to this accident.

Due to operational and design differences, nuclear power plants are distinguishable via the $^{135}Cs/^{137}Cs$ ratio. Fukushima moss samples exhibit a ratio around 0.358. No IAEA reference material from this region is yet available. Nevertheless, the already published measured values for this ratio are in the range around 0.34−0.36 and hence in good agreement with our data.[21] It should be noted that, unlike Chernobyl, Fukushima's releases are not uniform but involve three different sources, i.e., three reactors. With highly contaminated samples, the minor but characteristic fluctuations of the $^{135}Cs/^{137}Cs$ can be resolved and used to assign the contamination to one reactor.[21] Higher Fukushima-derived ratios were also measured in marine sediments in the Pacific Ocean with values ranging from 0.36 to 0.45.[14] In any case, contaminations caused by the two most notable civilian accidents at Chernobyl and Fukushima are very well distinguishable via the $^{135}Cs/^{137}Cs$ ratio because the gap range between both signatures is big enough.

Fallout from atmospheric nuclear explosions in the 20th century constitutes a third and ubiquitous source of radiocesium. The $^{135}Cs/^{137}Cs$ ratio found in historic ashed human lung tissue samples from the early 1960s was higher (1.9) and thus clearly distinct from Chernobyl's or Fukushima's fingerprints. This value is in agreement with what has been reported previously.[7,8] The higher ratio comes expected as "neutron burning" of ^{135}Xe (the parent nuclide of ^{135}Cs) does not occur in a nuclear explosion due to the short duration of the nuclear chain reaction. It can be expected that the contamination of this historic lung tissue was dominated by nuclear explosions fallout (whereas the 1957 accidents at Windscale and Kyshtym were likely local rather than global sources of atmospheric contamination).

Materials contaminated by nuclear weapons fallout, including both rock samples from the Trinity Test Site, were expected to resemble the high $^{135}Cs/^{137}Cs$ ratio that is characteristic of nuclear weapons fallout of ^{239}Pu warheads. The fast neutron cumulative fission yields of ^{239}Pu are 7.54% for the 135-isobar and 6.35% for the 137-isobar, causing a theoretical $^{135}Cs/^{137}Cs$ ratio of 1.19 for this type of sample material at the time of the detonation.[29] However, in our measurements, both samples exhibited a significantly lower ratio (decay-corrected to 2011 $^{135}Cs/^{137}Cs$ 0.382 ± 0.003 and 0.300 ± 0.006, respectively, or <0.1 at the time of the explosion). The hypothesis of a high $^{135}Cs/^{137}Cs$ ratio hence could *not* be confirmed for the two

https://dx.doi.org/10.1021/acs.est.1c00180
Environ. Sci. Technol. 2021, 55, 4984−4991

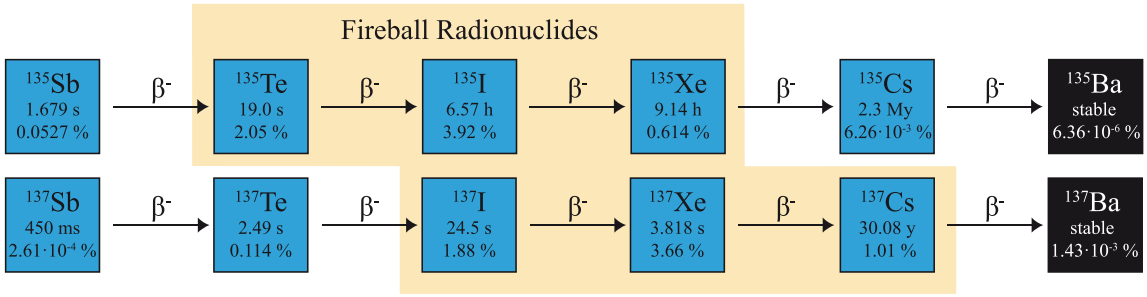

Figure 2. Isobaric decay chains leading to ^{135}Cs and ^{137}Cs, respectively, show that ^{137}Cs is directly produced inside the fireball of a nuclear blast, whereas ^{135}Cs is not. Data presented for each nuclide include half-life and independent fast neutron fission yield of ^{239}Pu in %. Data taken from ref 34.

trinitite samples. The only explanation for this anomalous behavior is a fractionation of radiocesium isotopes that relates to the gaseous nature of some precursor isotopes in the fireball. Not all fission products are formed (either directly by fission or subsequently by the decay of short-lived precursors) during the existence of the fireball following the nuclear explosion. Dominant nuclides in the fireball were those with a sufficient neutron excess, including ^{137}Cs.[30] However, ^{135}Cs with its low neutron excess was not a significant radionuclide constituent of the fireball, but rather its relatively long-lived parent nuclides ^{135}Xe ($T_{1/2}$ = 9.14 h), ^{135}I ($T_{1/2}$ = 6.57 h), or ^{135}Te ($T_{1/2}$ = 19 s; Figure 2). The noble gas ^{135}Xe disperses quickly before it decays to ^{135}Cs, whereas ^{137}Cs condenses together with inert molten material that finally constitutes the glassy matrix of trinitite. The volatility of precursor nuclides has been identified as the reason for unexpected nuclide fractionations previously.[30] Stable isotopic anomalies have also been observed on various occasions where a nuclear release impacted the natural isotopic occurrences.[31,32] For cesium isotopes, only the complementary pattern of this isotopic fractionation had been observed previously:[33] in environmental samples taken from more remote locations downwind from the test site, the ^{135}Cs-rich "far-end" with samples exhibiting a high $^{135}Cs/^{137}Cs$ ratio.[33] Here, to the best of our knowledge, we observe for the first time the complementary ^{137}Cs-rich "near-end" showing the opposite pattern with a low $^{135}Cs/^{137}Cs$ signature. It shows that isotopic fractionation can occur in environmental samples taken in close proximity to the source (e.g., trinitite), leading to deviations that are not observed in samples from more remote locations (e.g., human lung tissue). The impact of this fractionation on the $^{135}Cs/^{137}Cs$ fingerprint is severe. Instead of exhibiting a high $^{135}Cs/^{137}Cs$ ratio typical for nuclear weapons fallout (range 2.0–2.7 in the literature, 1.9 in our study), the trinitite samples studied here exhibit a low ratio that is regarded characteristic for reactors. The nonuniformity of the $^{135}Cs/^{137}Cs$ fingerprint of both samples in this study reflects the great variability of the extent to which ^{135}Cs has been incorporated into the trinitite (vs ^{135}Xe that was blown away with the wind before it decayed to ^{135}Cs). This suggests a dependency of the $^{135}Cs/^{137}Cs$ isotopic ratio on the distance from ground zero of a nuclear blast. We propose a method to estimate the distance/location of a radiocesium-contaminated material of a nuclear explosion from ground zero, by analyzing its $^{135}Cs/^{137}Cs$ fingerprint.

In summary, our results prove the applicability for source attribution of a radiocesium contamination caused by reactor accidents by using the $^{135}Cs/^{137}Cs$ ratio as an isotopic fingerprint. For nuclear weapons fallout, however, the expected "high" $^{135}Cs/^{137}Cs$ ratio could only be found in the "remote" sample of historic human lung tissue from Austria. In a highly contaminated trinitite, a fractionation of cesium nuclides could be observed for the first time. This fractionation causes selective enrichment of the "fireball nuclide" ^{137}Cs in the molten glass in the "near end," whereas the ^{135}Cs-rich "far-end" can be observed only at a distance (allowing for the decay of the relatively long-lived mother ^{135}Xe).[33]

Remaining challenges of the applicability of this $^{135}Cs/^{137}Cs$ fingerprinting include the lack of certified and internationally accepted reference materials for $^{135}Cs/^{137}Cs$ ratios and the lack of a convention for decay-correction (i.e., a uniform reference date).

■ ASSOCIATED CONTENT

Supporting Information

The Supporting Information is available free of charge at https://pubs.acs.org/doi/10.1021/acs.est.1c00180.

Sample material information for samples from Chernobyl (Table S1), from Fukushima (Table S2), trinitite (Table S3), historic ashed human lung tissue (Table S4), and IAEA Reference Materials (Table S5); measurement parameters for ICP-QQQ-MS measurements (Tables S6–S8); concentrations of elements before and after separation (Mo, Sn, Sb, Table S9; Cs, Ba, Table S10); time shifts (Table S11); pictures of sample materials from CEZ (Figures S1 and S2), Fukushima (Figure S3), trinitite (Figure S4); graphical illustration of the time shifts of $^{135}Cs/^{137}Cs$ over various decades (Figure S5) (PDF)

■ AUTHOR INFORMATION

Corresponding Author

Georg Steinhauser − *Leibniz Universität Hannover, Institute of Radioecology and Radiation Protection, 30419 Hannover, Germany*; orcid.org/0000-0002-6114-5890; Email: steinhauser@irs.uni-hannover.de

Authors

Dorian Zok − *Leibniz Universität Hannover, Institute of Radioecology and Radiation Protection, 30419 Hannover, Germany*

Tobias Blenke − *Leibniz Universität Hannover, Institute of Radioecology and Radiation Protection, 30419 Hannover, Germany*

Sandra Reinhard − *Leibniz Universität Hannover, Institute of Radioecology and Radiation Protection, 30419 Hannover, Germany*

https://dx.doi.org/10.1021/acs.est.1c00180
Environ. Sci. Technol. 2021, 55, 4984−4991

Sascha Sprott − *Leibniz Universität Hannover, Institute of Radioecology and Radiation Protection, 30419 Hannover, Germany*
Felix Kegler − *Leibniz Universität Hannover, Institute of Radioecology and Radiation Protection, 30419 Hannover, Germany*
Luisa Syrbe − *Leibniz Universität Hannover, Institute of Radioecology and Radiation Protection, 30419 Hannover, Germany*
Rebecca Querfeld − *Leibniz Universität Hannover, Institute of Radioecology and Radiation Protection, 30419 Hannover, Germany*
Yoshitaka Takagai − *Fukushima University, Faculty of Symbiotic Systems Science, Fukushima 960-1296, Japan;* orcid.org/0000-0002-7760-5636
Vladyslav Drozdov − *State Specialized Enterprise "Ecocentre" (SSE "Ecocentre"), Chernobyl 07270, Ukraine*
Ihor Chyzhevskyi − *State Specialized Enterprise "Ecocentre" (SSE "Ecocentre"), Chernobyl 07270, Ukraine*
Serhii Kirieiev − *State Specialized Enterprise "Ecocentre" (SSE "Ecocentre"), Chernobyl 07270, Ukraine*
Brigitte Schmidt − *University of Vienna, Faculty of Life Sciences, Cell Imaging and Ultrastructure Research, 1090 Vienna, Austria*
Wolfram Adlassnig − *University of Vienna, Faculty of Life Sciences, Cell Imaging and Ultrastructure Research, 1090 Vienna, Austria*
Gabriele Wallner − *University of Vienna, Faculty of Chemistry, Institute of Inorganic Chemistry, 1090 Vienna, Austria*
Sergiy Dubchak − *State Specialized Enterprise "Radon Association", Kyiv 03083, Ukraine*

Complete contact information is available at: https://pubs.acs.org/10.1021/acs.est.1c00180

Notes

The authors declare no competing financial interest.

■ ACKNOWLEDGMENTS

We thank *Deutsche Forschungsgemeinschaft* (DFG) for funding the project (419819104) of radiocesium analytics and the *Stiftung Prof. Joachim Lenz* for financial support of the Chernobyl sampling campaign. We also thank DFG and the State of Lower Saxony for the acquisition of the ICP-QQQ-MS and JSPS for the scholarship for R.Q. (SP19315).

■ REFERENCES

(1) Povinec, P. P.; Aoyama, M.; Biddulph, D.; Breier, R.; Buesseler, K.; Chang, C. C.; Golser, R.; Hou, X. L.; Ješkovský, M.; Jull, A. J. T.; Kaizer, J.; Nakano, M.; Nies, H.; Palcsu, L.; Papp, L.; Pham, M. K.; Steier, P.; Zhang, L. Y. Cesium, Iodine and Tritium in NW Pacific Waters - a Comparison of the Fukushima Impact with Global Fallout. *Biogeosciences* **2013**, *10* (8), 5481−5496.
(2) United Nations Scientific Committee on the Effects of Atomic. Sources and Effects of Ionizing Radiation; *Report to the General Assembly*; United Nations: New York, 2008.
(3) Steinhauser, G.; Brandl, A.; Johnson, T. E. Comparison of the Chernobyl and Fukushima Nuclear Accidents: A Review of the Environmental Impacts. *Sci. Total Environ.* **2014**, *470*−*471*, 800−817.
(4) Jones, S. Windscale and Kyshtym: A Double Anniversary. *J. Environ. Radioact.* **2008**, *99* (1), 1−6.
(5) Steinhauser, G. Environmental Nuclear Forensics: The Need for a New Scientific Discipline. *Environ. Sci. Pollut. Res.* **2019**, *26* (17), 16901−16903.
(6) Zheng, J.; Tagami, K.; Bu, W.; Uchida, S.; Watanabe, Y.; Kubota, Y.; Fuma, S.; Ihara, S. $^{135}Cs/^{137}Cs$ Isotopic Ratio as a New Tracer of Radiocesium Released from the Fukushima Nuclear Accident. *Environ. Sci. Technol.* **2014**, *48* (10), 5433−5438.
(7) Snow, M. S.; Snyder, D. C. $^{135}Cs/^{137}Cs$ Isotopic Composition of Environmental Samples across Europe: Environmental Transport and Source Term Emission Applications. *J. Environ. Radioact.* **2016**, *151*, 258−263.
(8) Russell, B. C.; Croudace, I. W.; Warwick, P. E. Determination of ^{135}Cs and ^{137}Cs in Environmental Samples: A Review. *Anal. Chim. Acta* **2015**, *890*, 7−20.
(9) Lee, T.; Teh-Lung, K.; Hsiao-Ling, L.; Ju-Chin, C. First Detection of Fallout Cs-135 and Potential Applications of Ratios. *Geochim. Cosmochim. Acta* **1993**, *57* (14), 3493−3497.
(10) Ohno, T.; Muramatsu, Y. Determination of Radioactive Cesium Isotope Ratios by Triple Quadrupole ICP-MS and Its Application to Rainwater Following the Fukushima Daiichi Nuclear Power Plant Accident. *J. Anal. At. Spectrom.* **2014**, *29* (2), 347.
(11) Nagy, P.; Vajda, N.; Pintér, T.; Fél, K. Activities of ^{134}Cs, ^{135}Cs and ^{137}Cs in the Primary Coolant of VVER-440 Reactors. *J. Radioanal. Nucl. Chem.* **2016**, *307* (2), 1045−1053.
(12) Merz, S.; Steinhauser, G.; Hamada, N. Anthropogenic Radionuclides in Japanese Food: Environmental and Legal Implications. *Environ. Sci. Technol.* **2013**, *47* (3), 1248−1256.
(13) Snow, M. S.; Snyder, D. C.; Clark, S. B.; Kelley, M.; Delmore, J. E. ^{137}Cs Activities and $^{135}Cs/^{137}Cs$ Isotopic Ratios from Soils at Idaho National Laboratory: A Case Study for Contaminant Source Attribution in the Vicinity of Nuclear Facilities. *Environ. Sci. Technol.* **2015**, *49* (5), 2741−2748.
(14) Bu, W.; Tang, L.; Liu, X.; Wang, Z.; Fukuda, M.; Zheng, J.; Aono, T.; Hu, S.; Wang, X. Ultra-Trace Determination of the $^{135}Cs/^{137}Cs$ Isotopic Ratio by Thermal Ionization Mass Spectrometry with Application to Fukushima Marine Sediment Samples. *J. Anal. At. Spectrom.* **2019**, *34* (2), 301−309.
(15) Yang, G.; Tazoe, H.; Yamada, M. Rapid Determination of 135Cs and Precise $^{135}Cs/^{137}Cs$ Atomic Ratio in Environmental Samples by Single-Column Chromatography Coupled to Triple-Quadrupole Inductively Coupled Plasma-Mass Spectrometry. *Anal. Chim. Acta* **2016**, *908*, 177−184.
(16) Taylor, V. F.; Evans, R. D.; Cornett, R. J. Preliminary Evaluation of $^{135}Cs/^{137}Cs$ as a Forensic Tool for Identifying Source of Radioactive Contamination. *J. Environ. Radioact.* **2008**, *99* (1), 109−118.
(17) Snow, M. S.; Snyder, D. C.; Delmore, J. E. Fukushima Daiichi Reactor Source Term Attribution Using Cesium Isotope Ratios from Contaminated Environmental Samples. *Rapid Commun. Mass Spectrom.* **2016**, *30* (4), 523−532.
(18) Merz, S.; Shozugawa, K.; Steinhauser, G. Effective and ecological half-lives of ^{90}Sr and ^{137}Cs observed in wheat and rice in Japan. *J. Radioanal. Nucl. Chem.* **2016**, *307*, 1807−1810.
(19) Yang, G.; Tazoe, H.; Yamada, M. ^{135}Cs Activity and $^{135}Cs/^{137}Cs$ Atom Ratio in Environmental Samples before and after the Fukushima Daiichi Nuclear Power Plant Accident. *Sci. Rep.* **2016**, *6* (1), 24119.
(20) Bu, W.; Ni, Y.; Steinhauser, G.; Zheng, W.; Zheng, J.; Furuta, N. The Role of Mass Spectrometry in Radioactive Contamination Assessment after the Fukushima Nuclear Accident. *J. Anal. At. Spectrom.* **2018**, *33* (4), 519−546.
(21) Zheng, J.; Bu, W.; Tagami, K.; Shikamori, Y.; Nakano, K.; Uchida, S.; Ishii, N. Determination of ^{135}Cs and $^{135}Cs/^{137}Cs$ Atomic Ratio in Environmental Samples by Combining Ammonium Molybdophosphate (AMP)-Selective Cs Adsorption and Ion-Exchange Chromatographic Separation to Triple-Quadrupole Inductively Coupled Plasma-Mass Spectrom. *Anal. Chem.* **2014**, *86* (14), 7103−7110.
(22) Zhong, Q.; Du, J.; Puigcorbé, V.; Wang, J.; Wang, Q.; Deng, B.; Zhang, F. Accumulation of Natural and Anthropogenic Radionuclides in Body Profiles of Bryidae, a Subgroup of Mosses. *Environ. Sci. Pollut. Res.* **2019**, *26* (27), 27872−27887.
(23) Schönfeld, T.; Liebscher, K.; Karl, F.; Friedmann, C. Radioactive Fission Products in Lungs. *Nature* **1960**, *185* (4707), 192−193.

https://dx.doi.org/10.1021/acs.est.1c00180
Environ. Sci. Technol. 2021, 55, 4984−4991

(24) Liebscher, K.; Schönfeld, T.; Schaller, A. Concentration of Inhaled Cerium-144 in Pulmonary Lymph Nodes of Human Beings. *Nature* **1961**, *192* (4809), 1308−1308.
(25) Irlweck, K.; Friedmann, C.; Schönfeld, T. Plutonium in the Lungs of Austrian Residents. *Health Phys.* **1980**, *39*, 95−99.
(26) Schönfeld, T.; Friedmann, C. Deposition of Inhaled Fission Products in Lungs and Pulmonary Lymph Nodes of Human Beings - Final Report on Research Project under Contract with the IAEA. *Rep. IAEA-R-156*; International Atomic Energy Agency, 1965.
(27) Russell, B. C.; Croudace, I. W.; Warwick, P. E.; Milton, J. A. Determination of Precise $^{135}Cs/^{137}Cs$ Ratio in Environmental Samples Using Sector Field Inductively Coupled Plasma Mass Spectrometry. *Anal. Chem.* **2014**, *86* (17), 8719−8726.
(28) Isnard, H.; Granet, M.; Caussignac, C.; Ducarme, E.; Nonell, A.; Tran, B.; Chartier, F. Comparison of Thermal Ionization Mass Spectrometry and Multiple Collector Inductively Coupled Plasma Mass Spectrometry for Cesium Isotope Ratio Measurements. *Spectrochim. Acta, Part B* **2009**, *64* (11−12), 1280−1286.
(29) IAEA - Nuclear Data Section. Live Chart of Nuclides. https://www-nds.iaea.org/relnsd/vcharthtml/VChartHTML.html (accessed Nov 18, 2020).
(30) Hanson, S. K.; Pollington, A. D.; Waidmann, C. R.; Kinman, W. S.; Wende, A. M.; Miller, J. L.; Berger, J. A.; Oldham, W. J.; Selby, H. D. Measurements of Extinct Fission Products in Nuclear Bomb Debris: Determination of the Yield of the Trinity Nuclear Test 70 y Later. *Proc. Natl. Acad. Sci. U. S. A.* **2016**, *113* (29), 8104−8108.
(31) Hopp, T.; Zok, D.; Kleine, T.; Steinhauser, G. Non-Natural Ruthenium Isotope Ratios of the Undeclared 2017 Atmospheric Release Consistent with Civilian Nuclear Activities. *Nat. Commun.* **2020**, *11* (1), 2744.
(32) Bonamici, C. E.; Hervig, R. L.; Kinman, W. S. Tracking Radionuclide Fractionation in the First Atomic Explosion Using Stable Elements. *Anal. Chem.* **2017**, *89* (18), 9877−9883.
(33) Snyder, D. C.; Delmore, J. E.; Tranter, T.; Mann, N. R.; Abbott, M. L.; Olson, J. E. Radioactive Cesium Isotope Ratios as a Tool for Determining Dispersal and Re-Dispersal Mechanisms Downwind from the Nevada Nuclear Security Site. *J. Environ. Radioact.* **2012**, *110*, 46−52.
(34) Nucleonica. Fission Yields++. https://nucleonica.com/Application/YieldsPlus.aspx (accessed Nov 18, 2020).

https://dx.doi.org/10.1021/acs.est.1c00180
Environ. Sci. Technol. 2021, 55, 4984−4991

Chapter 8

Conclusion

Environmental nuclear forensics is a relatively novel approach towards environmental radioactivity studies, where radiation protection aspects are not longer the ultimate motivation but rather the understanding of the occurrence, source, age, or fate of radioactive contamination. The focus of the present thesis was the understanding of forensic characteristics of two fission products that were released into the environment.

The first radionuclide of interest was an unexpected release of ^{106}Ru that occurred in the fall of 2017. No country has admitted to the release so far and no accident been declared either. However, the informal atmospheric monitoring network "Ring of Five" detected relatively high concentrations of airborne ^{106}Ru (occasionally concurrently with traces of ^{103}Ru) in most European countries. In a first step of obtaining forensic information, the data were compiled, and insight on the radiochemical purity of the released substances (lack of other gamma-emitters or prominent other anthropogenic radionuclides) was established (Masson and Steinhauser *et al.*[13], Publication I, Chapter 3). This insight not only led to excluding a nuclear reactor as the source, but various other hypotheses (burned-down satellite with a radionuclide battery on board or a release on Romanian territory) could be refuted. Rather, the characteristics of the release suggested a nuclear reprocessing facility as the source of the release. Based on a simple HYSPLIT model (Publication I), a release in Eastern Europe was found to be most likely. The data compiled in Publication I ultimately fed atmospheric backtracking models that narrowed down the possible release point to the Southern Urals.[68] Publication I also included the calculation of a model age of the release (calculated as days after the unloading of spent fuel from a nuclear reactor) and provided some basic insight into the chemical characteristics of the released radionuclides by simple solubility and volatilization experiments.

Following this initial step, the hypothesis of a release of ^{106}Ru during nuclear reprocessing had to be tested. The resulting study (Cooke *et al.*[71], Publication II, Chapter 4) was performed in close collaboration with Health Canada. Chemical speciation experiments were conducted using the highly specific reaction of a tridentate terpyridyl ligand with a polychlorinated Ru(III) species. The results (Publication II) showed that a small percentage of the radioruthenium was released in the form of β-$RuCl_3$, which suggested that the release occurred in the course

of trapping of gaseous RuO_4 using HCl. The small percentage suggested that the reaction had stopped abruptly soon after its beginning.

In order to understand the nature of the release, not only radioactive isotopes had been targeted in this thesis. Using instrumental neutron activation analysis (Zok *et al.*[72], Publication III, Chapter 5), it could be shown that no other elements (that can be analyzed using INAA) in addition to Ru were released in significant amounts, as an air filter from before the release showed a similar elemental composition to the radioactive air filter from during the ^{106}Ru episode.

In order to understand the nuclear origin of the radioruthenium and to exclude any military background of the release (most notably the production of weapons-grade Pu), the air filters were tested for the presence of stable, radiogenic Ru isotopes (Hopp and Zok *et al.*[73], Publication IV, Chapter 6). Using MC-ICP-MS, a clearly non-natural isotopic composition of the Ru fraction trapped in the air filter could be observed. The isotopic composition of the Ru in the filter was found to be consistent with the Ru produced in Russian VVER reactor types. A military context, however, could be excluded, primarily because of the onset of stable ^{100}Ru, which serves as a chronometer of burn-up (Publication IV).

A related approach, although with a different element, was tested in the analysis of the environmental radiocesium using the isotopic signature of ^{135}Cs/^{137}Cs (Zok *et al.*[79], Publication V, Chapter 7). Here, the primary factor for the onset of ^{135}Cs in irradiated fuel is not due to burn-up of the fuel but due to the neutron capture of ^{135}Xe (which is the parent nuclide of ^{135}Cs). Under high neutron flux densities, ^{135}Xe is largely burnt off, whereas ^{135}Xe is allowed to decay under low neutron flux scenarios (e.g., shutdown of a reactor) or short intensities of the neutron flux (e.g., nuclear explosions). Most remarkably, the radiocesium fraction trapped in molten glass from the Trinity Test Site ("trinitite") showed an even more pronounced "reactor signature" than a reactor. This unique anomaly was found to be due to fractionation of isotopes in the fireball of the nuclear explosion (Publication V). Whereas ^{137}Cs is produced as a primary fission product with remarkable yield, ^{135}Cs is primarily produced by decay of its gaseous parent ^{135}Xe. The xenon, however is blown away and hence a ^{137}Cs-rich cesium fraction is implanted in the trinitite onsite.

References

[1] G. Steinhauser, "Environmental nuclear forensics: the need for a new scientific discipline", *Environ. Sci. Pollut. Res.*, vol. 26, no. 17, pp. 16 901–16 903, 2019. DOI: 10.1007/s11356-019-04877-w.

[2] APS and AAAS, *"Nuclear Forensics - Role, State of the Art, and Program Needs"*, https://www.aaas.org/sites/default/files/Nuclear_Forensics.pdf, accessed on 22.07.2020.

[3] W. Kinman, R. Steiner, and S. Lamont, *"Nuclear Forensics at Los Alamos National Laboratory"*, https://permalink.lanl.gov/object/tr?what=info:lanl-repo/lareport/LA-UR-16-27544, accessed on 14.04.2020.

[4] M. Franzmann, H. Bosco, L. Hamann, C. Walther, and K. Wendt, "Resonant laser-SNMS for spatially resolved and element selective ultra-trace analysis of radionuclides", *J. Anal. At. Spectrom.*, vol. 33, no. 5, pp. 730–737, 2018. DOI: 10.1039/C7JA00423K.

[5] J. J. Bellucci, M. J. Whitehouse, M. Aleshin, and M. Eriksson, "Simultaneous Pu and U Isotope Nuclear Forensics on an Environmentally Recovered Hot Particle", *Anal. Chem.*, vol. 91, no. 9, pp. 5599–5604, 2019. DOI: 10.1021/acs.analchem.8b04809.

[6] Z. Varga, A. Nicholl, J. Zsigrai, M. Wallenius, and K. Mayer, "Methodology for the Preparation and Validation of Plutonium Age Dating Materials", *Anal. Chem.*, vol. 90, no. 6, pp. 4019–4024, 2018. DOI: 10.1021/acs.analchem.7b05204.

[7] K. Mathew, T. Kayzar-Boggs, Z. Varga, A. Gaffney, J. Denton, *et al.*, "Intercomparison of the Radio-Chronometric Ages of Plutonium-Certified Reference Materials with Distinct Isotopic Compositions", *Anal. Chem.*, vol. 91, no. 18, pp. 11 643–11 652, 2019. DOI: 10.1021/acs.analchem.9b02156.

[8] F. E. Stanley, A. M. Stalcup, and H. B. Spitz, "A brief introduction to analytical methods in nuclear forensics", *J. Radioanal. Nucl. Chem.*, vol. 295, no. 2, pp. 1385–1393, 2013. DOI: 10.1007/s10967-012-1927-3.

[9] T. M. Kayzar-Boggs, K. C. Treinen, A. Okubo, J. S. Denton, A. M. Gaffney, *et al.*, "An interlaboratory collaboration to determine consensus ^{231}Pa/^{235}U model ages of a uranium certified reference material for nuclear forensics", *J. Radioanal. Nucl. Chem.*, vol. 323, no. 3, pp. 1189–1195, 2020. DOI: 10.1007/s10967-020-07030-x.

[10] J. S. Denton, K. C. Treinen, Y. Chen, E. Baransky, A. M. Gaffney, *et al.*, "International cooperation in age-dating uranium standards for nuclear forensics using the ^{231}Pa/^{235}U radiochronometer", *J. Radioanal. Nucl. Chem.*, vol. 324, no. 2, pp. 705–714, 2020. DOI: 10.1007/s10967-020-07084-x.

[11] A. Weller, D. Zok, S. Reinhard, S. K. Woche, G. Guggenberger, *et al.*, "Separation of Ultratraces of Radiosilver from Radiocesium for Environmental Nuclear Forensics", *Anal. Chem.*, vol. 92, no. 7, pp. 5249–5257, 2020. DOI: 10.1021/acs.analchem.9b05776.

[12] GRS, *"Fukushima Daiichi - Unfallablauf, radiologische Folgen GRS-S-56"*, https://www.grs.de/sites/default/files/pdf/grs-s-56.pdf, accessed 14.04.2020.

[13] O. Masson, G. Steinhauser, D. Zok, O. Saunier, H. Angelov, *et al.*, "Airborne concentrations and chemical considerations of radioactive ruthenium from an undeclared major nuclear release in 2017", *Proc. Natl. Acad. Sci. U. S. A.*, vol. 116, no. 34, pp. 16 750–16 759, 2019. DOI: 10.1073/pnas.1907571116.

[14] J. Zheng, K. Tagami, W. Bu, S. Uchida, Y. Watanabe, *et al.*, "^{135}Cs/^{137}Cs Isotopic Ratio as a New Tracer of Radiocesium Released from the Fukushima Nuclear Accident", *Environ. Sci. Technol.*, vol. 48, no. 10, pp. 5433–5438, 2014. DOI: 10.1021/es500403h.

[15] J. Lachner, M. Kasberger, M. Martschini, A. Priller, P. Steier, *et al.*, "Developments towards detection of ^{135}Cs at VERA", *Nucl. Instruments Methods Phys. Res. Sect. B Beam Interact. with Mater. Atoms*, vol. 361, pp. 440–444, 2015. DOI: 10.1016/j.nimb.2015.01.032.

[16] W. Bu, L. Tang, X. Liu, Z. Wang, M. Fukuda, *et al.*, "Ultra-trace determination of the ^{135}Cs/^{137}Cs isotopic ratio by thermal ionization mass spectrometry with application to Fukushima marine sediment samples", *J. Anal. At. Spectrom.*, vol. 34, no. 2, pp. 301–309, 2019. DOI: 10.1039/c8ja00380g.

[17] B. Russell, I. W. Croudace, and P. E. Warwick, "Determination of ^{135}Cs and ^{137}Cs in environmental samples: A review", *Anal. Chim. Acta*, vol. 890, pp. 7–20, 2015. DOI: 10.1016/j.aca.2015.06.037.

[18] J. V. Kratz and K. H. Lieser, *Nuclear and Radiochemistry: Fundamentals and Applications*, 3rd ed. Weinheim: Wiley-VCH, 2013, ISBN: 978-3-527-32901-4.

[19] S. Marguet, *The Physics of Nuclear Reactors*, 1st ed. Cham: Springer, 2017, ISBN: 978-3-319-59559-7.

[20] H. Krieger, *Grundlagen der Strahlungsphysik und des Strahlenschutzes*, 6th ed. Berlin Heidelberg: Springer, 2019, ISBN: 978-3-662-60583-7.

[21] B. C. Reed, *The Physics of the Manhattan Project*, 3rd ed. Berlin Heidelberg: Springer, 2015, ISBN: 978-3-662-43532-8.

[22] Vogt, H. G. and Vahlbruch J. W., *Grundzüge des praktischen Strahlenschutzes*, 7th ed. München: Hanser, 2019, ISBN: 978-3-446-44919-0.

[23] N. Tsoulfanidis, *Nuclear Energy - A Volume in the Encyclopedia of Sustainability Science and Technology Series*, 2nd ed. New York: Springer, 2018, ISBN: 978-1-4939-6617-2.

[24] Nucleonica GmbH, *"Karlsruhe Nuclide Chart Online, KNCO++"*, https://nucleonica.com/Application/KNCOPlus.aspx, accessed 01.04.2020.

[25] IAEA and Nuclear Energy Agency, *"Uranium 2018: Resources, Productionand Demand"*, http://www.oecd-nea.org/ndd/pubs/2018/7413-uranium-2018.pdf, accessed 01.04.2020.

[26] G. Kessler, *Sustainable and Safe Nuclear Fission Energy - Technology and Safety of Fastand Thermal Nuclear Reactors*, 1st ed. Berlin Heidelberg: Springer, 2012, ISBN: 978-3-642-11989-7.

[27] IAEA, *"Nuclear Fuel Cycle Information System - A Directory of Nuclear Fuel Cycle Facilities", IAEA-TECDOC-1613, IAEA, Vienna, 2009*, https://www-pub.iaea.org/MTCD/publications/PDF/te_1613_web.pdf.

[28] United States Nuclear Regulatory Commission, *"Uranium Enrichment"*, https://www.nrc.gov/materials/fuel-cycle-fac/ur-enrichment.html, accessed 04.04.2020.

[29] World Nuclear Association, *"Uranium Enrichment"*, https://www.world-nuclear.org/information-library/nuclear-fuel-cycle/conversion-enrichment-and-fabrication/uranium-enrichment.aspx, accessed 02.04.2020.

[30] IAEA - Power Reactor Information System, *"Operational & Long-Term Shutdown Reactor"s*, https://pris.iaea.org/PRIS/WorldStatistics/OperationalReactorsByType.aspx, accsessed 14.01.2021.

[31] World Nuclear Association, *"Nuclear Power Reactors"*, https://www.world-nuclear.org/information-library/nuclear-fuel-cycle/nuclear-power-reactors/nuclear-power-reactors.aspx, accessed 03.04.2020.

[32] World Nuclear Association, *"Processing of Used Nuclear Fuel"*, https://www.world-nuclear.org/information-library/nuclear-fuel-cycle/fuel-recycling/processing-of-used-nuclear-fuel.aspx, accsessed 03.04.2020.

[33] Nuclear Energy Agency, *"Spent Nuclear Fuel Reprocessing Flowsheet"*, https://www.oecd-nea.org/science/docs/2012/nsc-wpfc-doc2012-15.pdf, accessed 08.04.2020.

[34] K. Motojima, "Removal of Ruthenium from PUREX Process", *J. Nucl. Sci. Technol.*, vol. 26, no. 3, pp. 358–364, 1989. DOI: 10.1080/18811248.1989.9734317.

[35] P. Swain, C. Mallika, R. Srinivasan, U. K. Mudali, and R. Natarajan, "Separation and recovery of ruthenium: a review", *J. Radioanal. Nucl. Chem.*, vol. 298, no. 2, pp. 781–796, 2013. DOI: 10.1007/s10967-013-2536-5.

[36] A. Hollemann, E. Wiberg, and N. Wiberg, *Anorganische Chemie*, 103rd ed. Berlin, Boston: de Gruyter, 2017, ISBN: 978-3-11-049573-7.

[37] M. Balcerzak and E. Swicicka, "Determination of ruthenium and osmium in each other's presence in chloride solutions by direct and third-order derivative spectrophotometry", *Talanta*, vol. 43, no. 3, pp. 471–478, 1996. DOI: 10.1016/0039-9140(95)01776-3.

[38] C. Lefebvre, T. Dumas, M.-C. Charbonnel, and P. Solari, "Speciation of Ruthenium in Organic TBP/TPH Organic Phases: A Study about Acidity of Nitric Solutions", *Procedia Chem.*, vol. 21, pp. 54–60, 2016. DOI: 10.1016/j.proche.2016.10.008.

[39] IAEA, *"History"*, https://www.iaea.org/about/overview/history, accessed 06.04.2020.

[40] R. Avenhaus, N. Kyriakopoulos, M. Richard, and G. Stein, *Verifying Treaty Compliance - Limiting Weapons of Mass Destruction and Monitoring Kyoto Protocol Provisions*, 1st ed. Berlin Heidelberg: Springer, 2006, ISBN: 3-540-33853-5.

[41] L. Maiani, S. Abousahl, and W. Plastino, *International Cooperationfor Enhancing Nuclear Safety, Security, Safeguards and Non-proliferation 60 Years of IAEA and EURATOM*, 1st ed. Berlin Heidelberg: Springer, 2018, ISBN: 978-3-662-57365-5.

[42] IAEA, *"International Nuclear and Radiological Event Scale (INES)"*, https://www.iaea.org/resources/databases/international-nuclear-and-radiological-event-scale, accessed 06.04.2020.

[43] IAEA, *"INES: The International Nuclear and Radiological Event Scale User's Manual"*, https://www.iaea.org/publications/10508/ines-the-international-nuclear-and-radiological-event-scale-users-manual, accessed 06.04.2020.

[44] IAEA, *Fukushima Nuclear Accident Update Log"*, https://www.iaea.org/newscenter/news/fukushima-nuclear-accident-update-log-15, accessed 06.04.2020.

[45] E. Ochiai, *Hiroshima to Fukushima - Biohazards of Radiation*. Berlin Heidelberg: Springer, 2014, ISBN: 978-3-642-38726-5.

[46] CTBTO, *"CTBT: Ending Nuclear Explosions"*, https://www.ctbto.org/fileadmin/user_upload/public_information/2019/CTBT_FactSheet_English_Feb_2019.pdf, accessed 06.04.2020.

[47] CTBTO, *"History: Summary"*, https://www.ctbto.org/the-treaty/history-summary/, accessed 06.04.2020.

[48] CTBTO, *"World Overview"*, https://www.ctbto.org/nuclear-testing/history-of-nuclear-testing/world-overview/, accessed 06.04.2020.

[49] K. Moody, P. Grant, and I. Hutcheon, *Nuclear Forensic Analysis*, 2nd ed. Boca Raton: CRC Press, 2015, ISBN: 978-1-4398-8062-3.

[50] CTBTO, *"Types of nuclear weapons"*, https://www.ctbto.org/nuclear-testing/types-of-nuclear-weapons/, accessed 07.04.2020.

[51] CTBTO, *"Types of nuclear weapon tests"*, https://www.ctbto.org/nuclear-testing/history-of-nuclear-testing/types-of-nuclear-weapons-tests/, accessed 07.04.2020.

[52] A. Sakaguchi, K. Kawai, P. Steier, F. Quinto, K. Mino, *et al.*, "First results on ^{236}U levels in global fallout", *Sci. Total Environ.*, vol. 407, no. 14, pp. 4238–4242, 2009. DOI: 10.1016/j.scitotenv.2009.01.058.

[53] F. Quinto, E. Hrnecek, M. Krachler, W. Shotyk, P. Steier, *et al.*, "Determination of ^{239}Pu, ^{240}Pu, ^{241}Pu and ^{242}Pu at femtogram and attogram levels evidence for the migration of fallout plutonium in an ombrotrophic peat bog profile", *Environ. Sci. Process. Impacts*, vol. 15, no. 4, pp. 839–847, 2013. DOI: 10.1039/c3em30910j.

[54] K. Szymaska and D. Strumiska-Parulska, "Atmospheric fallout impact on ^{210}Po and ^{210}Pb content in wild growing mushrooms", *Environ. Sci. Pollut. Res.*, vol. 27, no. 17, pp. 20 800–20 806, 2020. DOI: 10.1007/s11356-020-08559-w.

[55] K. Hain, P. Steier, M. B. Froehlich, R. Golser, X. Hou, *et al.*, "^{233}U/^{236}U signature allows to distinguish environmental emissions of civil nuclear industry from weapons fallout", *Nat. Commun.*, vol. 11, no. 1, pp. 1–11, 2020. DOI: 10.1038/s41467-020-15008-2.

[56] P. N. Owens, W. H. Blake, and G. E. Millward, "Extreme levels of fallout radionuclides and other contaminants in glacial sediment (cryoconite) and implications for downstream aquatic ecosystems", *Sci. Rep.*, vol. 9, no. 1, pp. 1–9, 2019. DOI: 10.1038/s41598-019-48873-z.

[57] UNSCEAR, *"Sources and effects of ionizing Radiation" - Report to the General Assembly with Scientific Annexes, United Nations, New York, 2000*, https://www.unscear.org/docs/publications/2000/UNSCEAR_2000_Annex-J.pdf.

[58] J. Smith and N. Beresford, *Chernobyl - Catastrophe and Consequences*, 1st ed. Berlin Heidelberg: Springer, 2005, ISBN: 3-540-23866-2.

[59] IAEA, *"INSAG-7 The Chernobyl Accident : Updating of INSAG-1, SAFETY SERIES No. 75-INSAG-7"*, https://www-pub.iaea.org/MTCD/publications/PDF/Pub913e_web.pdf.

[60] M. Malko, *"The Chernobyl Reactor: Design Features and Reasons for Accident"*, https://www.rri.kyoto-u.ac.jp/NSRG/reports/kr79/kr79pdf/Malko1.pdf, accessed 14.04.2020.

[61] G. Steinhauser, A. Brandl, and T. E. Johnson, "Comparison of the Chernobyl and Fukushima nuclear accidents: A review of the environmental impacts", *Sci. Total Environ.*, vol. 470-471, pp. 800–817, 2014. DOI: 10.1016/j.scitotenv.2013.10.029.

[62] M. Dreicer, A. Aarkrog, R. Alexakhin, L. Anspaugh, N. Arkhipov, *et al.*, *"Consequences of the Chernobyl Accident for the Natural and Human Environments"*, https://www.osti.gov/servlets/purl/391712, accsessed 08.04.2020.

[63] UNSCEAR, *Figure XI. Surface ground deposition of caesium-137 released in Europe after the Chernobyl accident"*, https://www.unscear.org/docs/JfigXI.pdf, accessed 08.04.2020.

[64] IAEA, *"The Fukushima Daiichi Accident"*, https://www-pub.iaea.org/MTCD/Publications/PDF/Pub1710-ReportByTheDG-Web.pdf, accessed 14.04.2020.

[65] Extension Site of Distribution Map of Radiation Dose, etc., *"Extension Site of Distribution Map of Radiation Dose, etc."* https://ramap.jmc.or.jp/map/, accessed 04.03.2019.

[66] Roshydromet, *"On emergency, extremely high and high pollution of the environment in the territory of the Russian Federation in the period from 6 to 13 October 2017 (original in Russian,* Об аварином, экстремально высоком и высоком загрязнении окружающе среды на территории Россиско Федерации в период с 6 по 13 октября 2017 года)", http://www.meteorf.ru/product/infomaterials/91/15078/?sphrase_id=134576, accessed 01.03.2018.

[67] IAEA, *"IAEA Press Conference"*, https://iaea.streaming.at/20171123, accessed 30.04.2020.

[68] O. Saunier, D. Didier, A. Mathieu, O. Masson, and J. Dumont Le Brazidec, "Atmospheric modeling and source reconstruction of radioactive ruthenium from an undeclared major release in 2017", *Proc. Natl. Acad. Sci. U. S. A.*, vol. 116, no. 50, pp. 24 991–25 000, 2019. DOI: 10.1073/pnas.1907823116.

[69] Nuclear Engineering International, *"Russian commission says Mayak not the source of Ru-106"*, https://www.neimagazine.com/news/newsrussian-commission-says-mayak-not-the-source-of-ru-106-6000301/, accessed 12.03.2018.

[70] Science News, *"How a 2017 radioactive plume may be tied to Russia and nixed neutrino research"*, https://www.sciencenews.org/article/2017-radioactive-plume-europe-russia-plant-neutrino-experiment, accessed 30.04.2020.

[71] M. W. Cooke, A. Botti, D. Zok, G. Steinhauser, and K. R. Ungar, "Identification of a chemical fingerprint linking the undeclared 2017 release of ^{106}Ru to advanced nuclear fuel reprocessing", *Proc. Natl. Acad. Sci. U. S. A.*, vol. 117, no. 26, pp. 14 703–14 711, 2020. DOI: 10.1073/pnas.2001914117.

[72] D. Zok, J. H. Sterba, and G. Steinhauser, "Chemical and radioanalytical investigations of ^{106}Ru-containing air filters from Vienna in fall 2017: searching for stable element anomalies", *J. Radioanal. Nucl. Chem.*, vol. 318, no. 1, pp. 415–421, 2018. DOI: 10.1007/s10967-018-6132-6.

[73] T. Hopp, D. Zok, T. Kleine, and G. Steinhauser, "Non-natural ruthenium isotope ratios of the undeclared 2017 atmospheric release consistent with civilian nuclear activities", *Nat. Commun.*, vol. 11, no. 1, pp. 1–7, 2020. DOI: 10.1038/s41467-020-16316-3.

[74] IBRAE, *"Meeting of the International Independent Scientific Commission for investigation of Ru-106 case"*, http://en.ibrae.ac.ru/newstext/915/, accessed 30.04.2020.

[75] IBRAE, *Meeting of the International Independent Scientific Commission for investigation of Ru-106 case"*, http://en.ibrae.ac.ru/newstext/911/, accessed 30.04.2020.

[76] Reuters, *"Experts fail to find origin of nuclear pollution cloud over Europe"*, https://www.reuters.com/article/us-russia-nuclearpower-accident/experts-fail-to-find-origin-of-nuclear-pollution-cloud-over-europe-idUSKBN1HN1UH, accessed 30.04.2020.

[77] Rosatom, *"Rosatom Official Statement Ru-106"*, http://www.rosatominternational.com/en/news/2017/11/23-11-2, accsessed 30.03.2020.

[78] S. Taylor and S. McLennan, *The continental crust: its composition and evolution : an examination of the geochemical record preserved in sedimentary rocks*, 1st ed. Oxford: Blackwell Scientific, 1985, ISBN: 0632011483.

[79] D. Zok, T. Blenke, S. Reinhard, S. Sprott, F. Kegler, *et al.*, "Determination of Characteristic vs Anomalous $^{135}Cs/^{137}Cs$ Isotopic Ratios in Radioactively Contaminated Environmental Samples", *Environ. Sci. Technol.*, vol. 55, no. 8, pp. 4984–4991, 2021. DOI: 10.1021/acs.est.1c00180.

[80] W. Bu, J. Zheng, X. Liu, K. Long, S. Hu, *et al.*, "Mass spectrometry for the determination of fission products ^{135}Cs, ^{137}Cs and ^{90}Sr: A review of methodology and applications", *Spectrochim. Acta Part B At. Spectrosc.*, vol. 119, pp. 65–75, 2016. DOI: 10.1016/j.sab.2016.03.008.

[81] V. Taylor, R. Evans, and R. Cornett, "Preliminary evaluation of $^{135}Cs/^{137}Cs$ as a forensic tool for identifying source of radioactive contamination", *J. Environ. Radioact.*, vol. 99, no. 1, pp. 109–118, 2008. DOI: 10.1016/j.jenvrad.2007.07.006.

[82] J. Zheng, W. Bu, K. Tagami, Y. Shikamori, K. Nakano, *et al.*, "Determination of ^{135}Cs and $^{135}Cs/^{137}Cs$ Atomic Ratio in Environmental Samples by Combining Ammonium Molybdophosphate (AMP)-Selective Cs Adsorption and Ion-Exchange Chromatographic Separation to Triple-Quadrupole Inductively Coupled Plasma-Mass Spectrometry", *Anal. Chem.*, vol. 86, no. 14, pp. 7103–7110, 2014. DOI: 10.1021/ac501712m.

[83] M. S. Snow, D. C. Snyder, S. B. Clark, M. Kelley, and J. E. Delmore, "^{137}Cs Activities and ^{135}Cs / ^{137}Cs Isotopic Ratios from Soils at Idaho National Laboratory: A Case Study for Contaminant Source Attribution in the Vicinity of Nuclear Facilities", *Environ. Sci. Technol.*, vol. 49, no. 5, pp. 2741–2748, 2015. DOI: 10.1021/es5058852.

[84] M. S. Snow and D. C. Snyder, "^{135}Cs /^{137}Cs isotopic composition of environmental samples across Europe: Environmental transport and source term emission applications", *J. Environ. Radioact.*, vol. 151, pp. 258–263, 2016. DOI: 10.1016/j.jenvrad.2015.10.025.

[85] G. Yang, H. Tazoe, and M. Yamada, "Rapid determination of ^{135}Cs and precise ^{135}Cs/^{137}Cs atomic ratio in environmental samples by single-column chromatography coupled to triple-quadrupole inductively coupled plasma-mass spectrometry", *Anal. Chim. Acta*, vol. 908, pp. 177–184, 2016. DOI: 10.1016/j.aca.2015.12.041.

[86] D. C. Snyder, J. E. Delmore, T. Tranter, N. R. Mann, M. L. Abbott, *et al.*, "Radioactive cesium isotope ratios as a tool for determining dispersal and re-dispersal mechanisms downwind from the Nevada Nuclear Security Site", *J. Environ. Radioact.*, vol. 110, pp. 46–52, 2012. DOI: 10.1016/j.jenvrad.2012.01.019.

[87] T. Lee, K. Teh-Lung, L. Hsiao-Ling, and C. Ju-Chin, "First detection of fallout Cs-135 and potential applications of ratios", *Geochim. Cosmochim. Acta*, vol. 57, no. 14, pp. 3493–3497, 1993. DOI: 10.1016/0016-7037(93)90555-B.

[88] J. A. Dunne, D. A. Richards, and H.-W. Chen, "Procedures for precise measurements of ^{135}Cs/^{137}Cs atom ratios in environmental samples at extreme dynamic ranges and ultra-trace levels by thermal ionization mass spectrometry", *Talanta*, vol. 174, pp. 347–356, 2017. DOI: 10.1016/j.talanta.2017.06.033.

[89] L. Zhu, X. Hou, and J. Qiao, "Determination of Ultralow Level ^{135}Cs and ^{135}Cs/^{137}Cs Ratio in Environmental Samples by Chemical Separation and Triple Quadrupole ICP-MS", *Anal. Chem.*, vol. 92, no. 11, pp. 7884–7892, 2020. DOI: 10.1021/acs.analchem.0c01153.

[90] J. Zheng, L. Cao, K. Tagami, and S. Uchida, "Triple-Quadrupole Inductively Coupled Plasma-Mass Spectrometry with a High-Efficiency Sample Introduction System for Ultratrace Determination of ^{135}Cs and ^{137}Cs in Environmental Samples at Femtogram Levels", *Anal. Chem.*, vol. 88, no. 17, pp. 8772–8779, 2016. DOI: 10.1021/acs.analchem.6b02150.

[91] B. Jäckel, W. Westmeier, and P. Patzelt, "On the photopeak efficiency of germanium gamma-ray detectors", *Nucl. Instruments Methods Phys. Res. Sect. A Accel. Spectrometers, Detect. Assoc. Equip.*, vol. 261, no. 3, pp. 543–548, 1987. DOI: 10.1016/0168-9002(87)90367-6.

[92] M. D. Glascock, "Neutron Activation Analysis (NAA): Applications in Archaeology", in *Encyclopedia of Global Archaeology*, C. Smith, Ed. New York, NY: Springer New York, 2014, pp. 5239–5247, ISBN: 978-1-4419-0465-2.

[93] J. Gross, *Massenspektrometrie - Ein Lehrbuch*, 3rd ed. Berlin Heidelberg: Springer, 2013, ISBN: 978-3-8274-2980-3.

[94] F. Vanhaecke and P. Degryse, *Isotopic Analysis: Fundamentals and Applications Using ICP-MS*, 1st ed. Weinheim: WILEY-VCH, 2012, ISBN: 978-3-527-32896-3.

[95] H. Andrén, I. Rodushkin, A. Stenberg, D. Malinovsky, and D. C. Baxter, "Sources of mass bias and isotope ratio variation in multi-collector ICP-MS: optimization of instrumental parameters based on experimental observations", *J. Anal. At. Spectrom.*, vol. 19, no. 9, pp. 1217–1224, 2004. DOI: 10.1039/B403938F.

[96] W. M. White, F. Albarède, and P. Télouk, "High-precision analysis of Pb isotope ratios by multi-collector ICP-MS", *Chem. Geol.*, vol. 167, no. 3-4, pp. 257–270, 2000. DOI: 10.1016/S0009-2541(99)00182-5.

[97] M. A. Nouioui, M.-L. Milliand, F. Bessueille-Barbier, A. Hedhili, and L. Ayouni-Derouiche, "Determination of traces of As, Cd, Cr, Hg, Mn, Ni, Sb, Se, Sn and Pb in human hair by triple quadrupole ICP-MS", *Int. J. Environ. Anal. Chem.*, vol. 98, no. 10, pp. 954–976, 2018. DOI: 10.1080/03067319.2018.1517870.

[98] L. Y. D. Tiong and S. Tan, "In situ determination of ^{238}Pu in the presence of uranium by triple quadrupole ICP-MS (ICP-QQQ-MS)", *J. Radioanal. Nucl. Chem.*, vol. 322, no. 2, pp. 399–406, 2019. DOI: 10.1007/s10967-019-06695-3.

[99] C. Walkner, R. Gratzer, T. Meisel, and S. N. H. Bokhari, "Multi-element analysis of crude oils using ICP-QQQ-MS", *Org. Geochem.*, vol. 103, pp. 22–30, 2017. DOI: 10.1016/j.orggeochem.2016.10.009.

[100] G. Yang, H. Tazoe, and M. Yamada, "Improved approach for routine monitoring of ^{129}I activity and ^{129}I/^{127}I atom ratio in environmental samples using TMAH extraction and ICP-MS/MS", *Anal. Chim. Acta*, vol. 1008, no. 2018, pp. 66–73, 2018. DOI: 10.1016/j.aca.2017.12.049.

[101] M. Granet, A. Nonell, G. Favre, F. Chartier, H. Isnard, *et al.*, "Cs-Ba separation using N_2O as a reactant gas in a Multiple Collector-Inductively Coupled Plasma Mass Spectrometer collision-reaction cell: Application to the measurements of Cs isotopes in spent nuclear fuel samples", *Spectrochim. Acta Part B At. Spectrosc.*, vol. 63, no. 11, pp. 1309–1314, 2008. DOI: 10.1016/j.sab.2008.09.011.

[102] U. Ritgen, *Analytische Chemie I*, 1st ed. Berlin Heidelberg: Springer Spektrum, 2019, ISBN: 978-3-662-60494-6.

[103] D. Skoog and J. Leary, *Instrumentelle Analytik*, 1st ed. Berlin Heidelberg: Springer, 1996, ISBN: 978-3-662-07917-1.

[104] M. Gey, *Instrumentelle Analytik und Bioanalytik*, 2nd ed. Berlin Heidelberg: Springer, 2008, ISBN: 978-3-540-73803-9.

[105] U. Müller, *Anorganische Strukturchemie*, 6th ed. Wiesbaden: Vieweg & Teubner, 2016, ISBN: 978-3-8348-0626-0.

[106] B. C. Russell, I. W. Croudace, P. E. Warwick, and J. A. Milton, "Determination of Precise $^{135}Cs/^{137}Cs$ Ratio in Environmental Samples Using Sector Field Inductively Coupled Plasma Mass Spectrometry", *Anal. Chem.*, vol. 86, no. 17, pp. 8719–8726, 2014. DOI: 10.1021/ac501894a.

List of Figures

List of Tables

List of Abbreviations

AAAS	American Association for the Advancement of Science
ACS	American Chemical Society
APS	American Physical Society
AGL	Above Ground Level
AMP	Ammonium Molybophosphate
AMS	Accelerator Mass Spectrometry
BCR	Community Bureau of Reference
	French: Bureau Communautaire de Référence
BOREX	Boron Solar Neutrino Experiment
Borexino	Italian Diminutive of BOREX
BWR	Boiling Water Reactor
CANDU	Canada Deuterium Uranium
CEZ	Chernobyl Exclusion Zone
CFA	Coal Fly Ash
ChNPP	Chernobyl Nuclear Power Plant
CRIIRAD	Commission for Independent Research and Information on Radioactivity
	French: Commission de Recherche et d'information Indépendantes sur la Radioactivité Association Française
COGEMA	General Company for Nuclear Materials
	French: Compagnie Générale des Matières Nucléaires
CTBT	Comprehensive Nuclear-Test-Ban Treaty
CTBTO	Comprehensive Nuclear-Test-Ban Treaty Organization
DBP	Dibutyl Phosphoric Acid
DMF	N,N'-dimethylformamide
DMSO	Dimethyl Sulfoxide
DWR	Pressurized Water Reaactor in *German*: Druckwasserreaktor
EDXS	Energy-Dispersive x-Ray Spectroscopy

EGASMRO	Unified State Automated System for Monitoring the Radiation Situation in the Russian Federation *Russian*: ЕГАСМРО - Единая Государственная Автоматиэироваиииая Система Мониторсинга Радиационной Обстановки на Территории Российской Федерации
ESA	European Space Agency
ESI	Electrospray Ionisation
FDNPP	Fukushima Daiichi Nuclear Power Plant
FSUE	Federal State Unitary Enterprise
FWHM	Full Width at Half Maximum
GDAS	Global Data Assimilation System
GBW	Guobiao Standard China
GRS	Association of Facility and Reactor Safety *German*: Gesellschaft für Anlagen- und Reaktorsicherheit
GSNL	Gran Sasso National Laboratory
HM	Heavy Metal
HPGe	High-Purity Germanium
HPLC	High-Performance Liquid Chromatography
HYSPLIT	Hybrid Single Particle Lagrangian Integrated Trajectory
IAEA	International Atomic Energy Agency
IBRAE	Nuclear Safety Institute of the Russian Academy of Sciences
ICRP	International Commission on Radiological Protection
ICP	Inductively Coupled Plasma
ICP-MS	Inductively Coupled Plasma Mass Spectrometry
ICP-QQQ-MS	Inductively Coupled Plasma Triple Quadrupole Mass Spectrometry
IMS	International Monitoring System
IMS2	Inorganics in Marine Sediment
INAA	Instrumental Neutron Activation Analysis
INES	International Nuclear and Radiological Event Scale
IP	Imaging Plate
IRFU	Institute for Research on the fundamental laws of the universe, of the Fundamental Researchs *French*: Institut de recherche sur les lois fondamentales de l'Univer
IRS	Institute of Radioecology and Radiation Protection
IRSN	Institute of Radioprotection and Nuclear Safety *French*: Institut de Radioprotection et de Sûreté Nucléaire
KGR	Nuclear Power Plant Greifswald, in *German*: Kernkraftwerk Greifswald
KKR	Nuclear Power Plant Rheinsberg, in *German*: Kernkraftwerk Rheinsberg
LC	Liquid Chromatography

Lc	Critical Limit
Ld	Detection Limit
LOD	Limit of Detection
LSS	Light Sandy Soil
LTBT	Limited Test Ban Treaty
Magnox	Magnesium Not Oxidising
MC-ICP-MS	Multicollector Inductively Coupled Plasma Mass Spectrometry
MOX	Mixed Oxide
MS	Mass Spectrometry
NIST	National Institute of Standards and Technology
NM	New Mexico
NMR	Nuclear Magnetic Resonance Spectroscopy
NOAA	National Oceanic and Atmospheric Administration
NPP	Nuclear Power Plant
NTI	Nuclear Threat Initiative
PE	Polyethylene
PFA	Perfluoralkoxy
PHWR	Pressurized Heavy Water Reactor
PP	Polypropylene
PTBT	Partial Test Ban Treaty
PTFE	Polytetrafluoroethylene
PUREX	Plutonium Uranium Extraction
PWR	Pressurized Water Reactor
RBMK	High-Power Channel-Type Reactor *Russian*: Реактор Большой Мощности Канальный
Roshydromet	Russian Federal Service for Hydrometeorology and Environmental Monitoring
RTG	Radioisotope Thermoelectric Generator
Ro5	Ring of 5
SAGe	Small Anode Germanium
SEM	Scanning Electron Microscopy
SF	Spontaneous Fission
SI	Supporting Information
SIMS	Secondary Ionization Mass Spectrometry
SOX	Short Distance Neutrino Oscillations with Borexino
SRM	Standard Reference Material
STE	Stratosphere To Troposphere Exchanges
SUF	Serum Ultrafiltrate Fluid
SWR	Boiling Water Reactor in *German*: Siedewasserreaktor

TBACl	Tetrabutylammonium Chloride
TBP	Tri-*n*-butyl Phosphate
TEPCO	Tokyo Electric Power Company
TIA	Titanium Alloy
TIMS	Thermal Ionisation Mass Spectrometry
TLC	Thin Layer Chromatography
TNT	2,4,6-trinitrotoluene
TOF	Time of Flight
TRIGA	Training, Research, Isotopes, General Atomic
ttpy	4'-p-tolyl-2,2';6',2"-terpyridine
UNOOSA	United Nations Office for Outer Space Affairs
UNSCEAR	United Nations Scientific Committee on the Effects of Atomic Radiation
USA	United States of America
USNRC	United States Nuclear Regulatory Commission
USIE	Unified System for Information Exchange in Incidents and Emergencies
UTC	Coordinated Universal Time
VERA	Vienna Environmental Research Accelerator
VVER	Water-Water-Energetic-Reactor *Russian*: Водо-Водяной Энергетический Реактор

Appendix

Appendix A

Publication I

Supporting Information

Airborne Concentrations and Chemical Considerations of Radioactive Ruthenium from an Undeclared Major Nuclear Release in 2017

Supporting Information for

Radioactive Ruthenium from an Undeclared Major Nuclear Release in 2017, Part 1: Airborne Concentrations and Chemical Considerations

Table of contents

Table S1: Airborne ^{106}Ru activity concentrations (mBq·m^{-3}). Results are usually given with 2σ. Uncertainty in %.

Country	Location	Latitude (decimal)	Longitude (decimal)	Start date	Start hour	End date	End hour	^{106}Ru (mBq·m^{-3})	± (%)
Austria	Alt Prerau	48.7964	16.4753	25/09/17	06:03	02/10/17	06:09	11.1	8
Austria	Alt Prerau	48.7964	16.4753	25/09/17	06:03	02/10/17	06:09	0.003	43
Austria	Bregenz	47.5048	9.7264	25/09/17	06:40	02/10/17	09:00	<0.1	
Austria	Bregenz	47.5048	9.7264	26/09/17	06:40	03/10/17	09:00	<0.017	
Austria	Graz	47.0755	15.4505	25/09/17	11:53	02/10/17	08:20	9.1	6
Austria	Graz	47.0755	15.4505	02/10/17	10:16	03/10/17	10:16	36.2	7
Austria	Graz	47.0755	15.4505	03/10/17	10:20	04/10/17	07:50	12.4	6
Austria	Graz	47.0755	15.4505	04/10/17	08:00	05/10/17	07:00	1.3	36
Austria	Graz	47.0755	15.4505	05/10/17	07:05	06/10/17	07:15	0.8	36
Austria	Graz	47.0755	15.4505	06/10/17	07:30	09/10/17	07:30	<0.1	
Austria	Innsbruck	47.2600	11.3566	25/09/17	07:15	02/10/17	06:55	<0.014	
Austria	Innsbruck	47.2600	11.3566	02/10/17	07:03	04/10/17	06:29	<0.3	
Austria	Innsbruck	47.2600	11.3566	04/10/17	06:30	05/10/17	07:22	<1	
Austria	Innsbruck	47.2600	11.3566	05/10/17	07:27	06/10/17	07:15	<1	
Austria	Innsbruck	47.2600	11.3566	06/10/17	07:27	09/10/17	07:36	<0.6	
Austria	Klagenfurt	46.6484	14.3184	25/09/17	10:02	02/10/17	08:18	4.9	7
Austria	Klagenfurt	46.6484	14.3184	25/09/17	10:02	02/10/17	08:18	0.002	49
Austria	Laa an der Thaya	48.7317	16.3917	28/09/17	17:45	29/09/17	18:46	<4.6	
Austria	Laa an der Thaya	48.7317	16.3917	29/09/17	18:46	30/09/17	19:50	<4.5	
Austria	Laa an der Thaya	48.7317	16.3917	30/09/17	19:50	01/10/17	20:52	38	13
Austria	Laa an der Thaya	48.7317	16.3917	01/10/17	20:52	02/10/17	10:13	40	26
Austria	Laa an der Thaya	48.7317	16.3917	02/10/17	18:45	03/10/17	09:32	23	11
Austria	Leopoldschlag	48.6182	14.5018	28/09/17	12:13	29/09/17	12:31	<4.9	
Austria	Leopoldschlag	48.6182	14.5018	29/09/17	12:31	30/09/17	12:49	<4.6	
Austria	Leopoldschlag	48.6182	14.5018	30/09/17	12:49	01/10/17	13:07	<4.5	
Austria	Leopoldschlag	48.6182	14.5018	01/10/17	13:07	02/10/17	16:25	<4.2	
Austria	Linz	48.2675	14.2800	25/09/17	09:50	02/10/17	09:52	0.7	7
Austria	Linz	48.2675	14.2800	02/10/17	10:00	03/10/17	10:25	8.2	8
Austria	Linz	48.2675	14.2800	03/10/17	10:28	04/10/17	09:32	0.3	27
Austria	Linz	48.2675	14.2800	04/10/17	09:35	05/10/17	09:30	<0.2	
Austria	Linz	48.2675	14.2800	05/10/17	09:33	06/10/17	09:36	<0.1	
Austria	Linz	48.2675	14.2800	06/10/17	09:36	09/10/17	09:47	<0.1	
Austria	Retz	48.7549	15.9506	25/09/17	18:55	02/10/17	11:43	13	-
Austria	Retz	48.7549	15.9506	25/09/17	18:11	03/10/17	11:53	12.1	6
Austria	Retz	48.7549	15.9506	25/09/17	18:11	03/10/17	11:53	0.003	44
Austria	Salzburg	47.7909	13.0526	25/09/17	08:30	02/10/17	08:20	<0.0096	
Austria	Sonnblick	47.0500	12.9666	02/10/17	00:01	02/10/17	23:59	0.173	64
Austria	Straß in der Steiermark	46.7259	15.6248	25/09/17	10:02	03/10/17	08:18	9.5	6

Country	Location	Latitude (decimal)	Longitude (decimal)	Start date	Start hour	End date	End hour	^{106}Ru (mBq·m^{-3})	± (%)
Austria	Straß in der Steiermark	46.7259	15.6248	25/09/17	10:02	03/10/17	08:18	0.003	21
Austria	Vienna	48.2561	16.4828	25/09/17	09:10	02/10/17	09:05	12.9	6
Austria	Vienna	48.2561	16.4828	25/09/17	09:13	02/10/17	09:10	13.3	5
Austria	Vienna	48.2345	16.4175	28/09/17	12:24	04/10/17	08:14	21.7	-
Austria	Vienna	48.2561	16.4828	02/10/17	09:10	03/10/17	09:22	41.6	5
Austria	Vienna	48.2561	16.4828	03/10/17	09:30	04/10/17	09:05	10.2	6
Austria	Vienna	48.2561	16.4828	04/10/17	09:10	05/10/17	08:47	<0.1	
Austria	Vienna	48.2565	16.4829	05/10/17	08:51	06/10/17	08:54	<0.2	
Austria	Vienna	48.2565	16.4829	02/10/17	09:05	09/10/17	08:55	8	9
Austria	Vienna	48.2561	16.4828	06/10/17	08:57	09/10/17	08:57	<0.4	
Austria	Vienna	48.1200	16.2500	02/10/17	08:00	02/10/17	20:40	32.6	4
Austria	Vienna	48.1200	16.2500	03/10/17	08:00	03/10/17	20:40	12.7	10
Belarus	Braslav	55.6333	27.0333	01/10/17	-	02/10/17	-	<LOD	
Belarus	Braslav	55.6333	27.0333	02/10/17	-	03/10/17	-	<LOD	
Belarus	Braslav	55.6333	27.0333	03/10/17	-	04/10/17	-	2.7	-
Belarus	Braslav	55.6333	27.0333	04/10/17	-	05/10/17	-	<LOD	
Belarus	Braslav	55.6333	27.0333	05/10/17	-	06/10/17	-	<LOD	
Belarus	Gomel	52.4400	30.9900	01/10/17	-	02/10/17	-	<LOD	
Belarus	Gomel	52.4400	30.9900	02/10/17	-	03/10/17	-	<LOD	
Belarus	Gomel	52.4400	30.9900	03/10/17	-	04/10/17	-	0.21	-
Belarus	Gomel	52.4400	30.9900	04/10/17	-	05/10/17	-	0.16	-
Belarus	Gomel	52.4400	30.9900	05/10/17	-	06/10/17	-	<LOD	
Belarus	Minsk	53.9030	27.5640	01/10/17	-	02/10/17	-	<LOD	
Belarus	Minsk	53.9030	27.5640	02/10/17	-	03/10/17	-	<LOD	
Belarus	Minsk	53.9030	27.5640	03/10/17	-	04/10/17	-	<LOD	
Belarus	Minsk	53.9030	27.5640	04/10/17	-	05/10/17	-	<LOD	
Belarus	Minsk	53.9030	27.5640	05/10/17	-	06/10/17	-	<LOD	
Belarus	Mstislavl	54.0176	31.7230	01/10/17	-	02/10/17	-	<LOD	
Belarus	Mstislavl	54.0176	31.7230	02/10/17	-	03/10/17	-	<LOD	
Belarus	Mstislavl	54.0176	31.7230	03/10/17	-	04/10/17	-	<LOD	
Belarus	Mstislavl	54.0176	31.7230	04/10/17	-	05/10/17	-	<LOD	
Belarus	Mstislavl	54.0176	31.7230	05/10/17	-	06/10/17	-	<LOD	
Belarus	Pinsk	52.1244	26.0797	01/10/17	-	02/10/17	-	<LOD	
Belarus	Pinsk	52.1244	26.0797	02/10/17	-	03/10/17	-	<LOD	
Belarus	Pinsk	52.1244	26.0797	03/10/17	-	04/10/17	-	3.5	-
Belarus	Pinsk	52.1244	26.0797	04/10/17	-	05/10/17	-	0.05	-
Belarus	Pinsk	52.1244	26.0797	05/10/17	-	06/10/17	-	<LOD	
Belgium	Mol	51.2171	5.0904	29/09/17	07:00	30/09/17	07:00	<1.7	
Belgium	Mol	51.2171	5.0904	30/09/17	07:00	01/10/17	07:00	<1.4	

Country	Location	Latitude (decimal)	Longitude (decimal)	Start date	Start hour	End date	End hour	^{106}Ru (mBq·m^{-3})	± (%)
Belgium	Mol	51.2171	5.0904	01/10/17	07:00	02/10/17	07:00	<1.2	
Belgium	Mol	51.2171	5.0904	02/10/17	07:00	03/10/17	07:00	<0.5	
Bosnia and Herzegovina	Sarajevo	43.8639	18.4175	22/09/17	-	02/10/17	-	4.76	8
Bosnia and Herzegovina	Sarajevo	43.8639	18.4176	02/10/17	-	09/10/17	-	3.17	12
Bosnia and Herzegovina	Sarajevo	43.8639	18.4177	09/10/17	-	17/10/17	-	<0.05	
Bosnia and Herzegovina	Sarajevo	43.8639	18.4178	17/10/17	-	25/10/17	-	<0.07	
Bulgaria	Buhovo	42.7660	23.5660	29/09/17	-	02/10/17	-	29.1	20
Bulgaria	Burgas	42.5000	27.4660	29/09/17	12:00	04/10/17	06:00	11.8	5
Bulgaria	Kozloduy	43.7461	23.7706	29/09/17	12:00	02/10/17	06:00	58.9	-
Bulgaria	Kozloduy	43.7461	23.7706	15/09/17	13:00	02/10/17	06:00	10.9	-
Bulgaria	Montana	43.4166	23.2333	25/09/17	12:00	02/10/17	06:00	2.6	12
Bulgaria	Moussala Peak	42.1833	23.5833	03/10/17	08:30	03/10/17	17:00	1.75	25
Bulgaria	Pleven	43.4166	24.6000	02/10/17	12:00	04/10/17	06:00	24	10
Bulgaria	Vratsa	43.2166	23.5500	02/10/17	12:00	04/10/17	06:00	4.1	20
Bulgaria	Yana	42.7330	23.5660	29/09/17	12:00	04/10/17	06:00	17.6	6
Croatia	Zagreb	45.8338	15.9783	01/09/17	10:00	29/09/17	09:53	<0.0008	
Croatia	Zagreb	45.8338	15.9783	29/09/17	09:57	09/10/17	10:36	13.3	1
Cyprus	Lefkosia	35.1754	33.3710	25/09/17	-	02/10/17	-	0.0461	14
Cyprus	Lefkosia	35.1754	33.3710	03/10/17	08:10	13/10/17	-	0.245	13
Czech Rep.	Brno	49.2000	16.6000	26/09/17	07:00	03/10/17	07:00	21.1	20
Czech Rep.	Brno	49.2000	16.6000	03/10/17	14:00	04/10/17	12:30	0.84	15
Czech Rep.	Brno	49.2000	16.6000	04/10/17	14:00	10/10/17	12:30	<0.005	
Czech Rep.	Brno	49.2000	16.6000	17/10/17	06:00	24/10/17	06:00	0.057	8
Czech Rep.	Brno	49.2000	16.6000	07/11/17	06:00	14/11/17	06:00	0.0099	20
Czech Rep.	České Budějovice	48.9667	14.4667	26/09/17	05:00	03/10/17	05:00	1.90	20
Czech Rep.	České Budějovice	48.9667	14.4667	03/10/17	05:10	03/10/17	15:30	<0.1	
Czech Rep.	České Budějovice	48.9667	14.4667	03/10/17	15:30	04/10/17	13:30	<0.1	
Czech Rep.	České Budějovice	48.9667	14.4667	04/10/17	13:30	10/10/17	05:30	<0.05	
Czech Rep.	Cheb	50.0800	12.4000	03/10/17	09:50	04/10/17	12:30	<0.052	
Czech Rep.	Cheb	50.0800	12.4000	04/10/17	12:30	10/10/17	10:25	<0.02	
Czech Rep.	Holešov	49.3167	17.5667	25/09/17	05:20	02/10/17	05:07	7.9	10
Czech Rep.	Holešov	49.3167	17.5667	02/10/17	05:22	05/10/17	06:28	21.2	20
Czech Rep.	Holešov	49.3167	17.5667	05/10/17	06:29	09/10/17	05:07	0.018	40
Czech Rep.	Holešov	49.3167	17.5667	09/10/17	05:00	16/10/17	05:45	0.005	15
Czech Rep.	Hradec Králové	50.2453	15.8696	26/09/17	04:46	03/10/17	04:47	10.90	10
Czech Rep.	Hradec Králové	50.2453	15.8696	26/09/17	04:46	03/10/17	04:47	0.0026	30
Czech Rep.	Hradec Králové	50.2333	15.8696	29/09/17	06:25	03/10/17	04:47	24.90	10
Czech Rep.	Hradec Králové	50.2453	15.8696	03/10/17	04:50	03/10/17	11:50	4.19	10

Country	Location	Latitude (decimal)	Longitude (decimal)	Start date	Start hour	End date	End hour	^{106}Ru (mBq·m^{-3})	± (%)
Czech Rep.	Hradec Králové	50.2453	15.8696	03/10/17	11:54	04/10/17	11:40	<0.3	
Czech Rep.	Hradec Králové	50.2453	15.8696	04/10/17	11:40	05/10/17	11:40	<0.3	
Czech Rep.	Hradec Králové	50.2453	15.8696	05/10/17	11:40	10/10/17	04:30	<0.011	
Czech Rep.	Kamenná	49.6160	14.0000	25/09/17	05:30	02/10/17	05:30	3.74	10
Czech Rep.	Kamenná	49.6160	14.0000	02/10/17	07:10	04/10/17	12:12	1.31	20
Czech Rep.	Kamenná	49.6160	14.0000	04/10/17	12:12	09/10/17	07:10	<0.02	10
Czech Rep.	Ostrava	49.8333	18.2833	25/09/17	04:00	02/10/17	04:00	3.82	10
Czech Rep.	Ostrava	49.8333	18.2833	02/10/17	04:00	03/10/17	13:00	40.00	10
Czech Rep.	Ostrava	49.8333	18.2833	03/10/17	13:00	04/10/17	13:00	1.10	10
Czech Rep.	Ostrava	49.8333	18.2833	04/10/17	13:00	05/10/17	04:30	<0.15	
Czech Rep.	Ostrava	49.8333	18.2833	05/10/17	04:30	05/10/17	12:30	<0.48	
Czech Rep.	Ostrava	49.8333	18.2833	05/10/17	12:30	06/10/17	04:00	<0.3	
Czech Rep.	Ostrava	49.8333	18.2833	06/10/17	04:00	09/10/17	04:00	<0.03	
Czech Rep.	Plzeň	49.7333	13.3667	26/09/17	07:00	03/10/17	07:00	0.62	20
Czech Rep.	Plzeň	49.7333	13.3667	04/10/17	06:00	10/10/17	06:00	<0.004	
Czech Rep.	Praha	50.0667	14.4500	26/09/17	06:00	03/10/17	06:05	0.00062	30
Czech Rep.	Praha	50.0667	14.4500	26/09/17	06:00	03/10/17	06:05	6.21	10
Czech Rep.	Praha	50.0670	14.4500	29/09/17	04:45	02/10/17	14:35	13.10	10
Czech Rep.	Praha	50.0670	14.4500	01/10/17	09:00	02/10/17	02:00	57.70	10
Czech Rep.	Praha	50.0667	14.4500	02/10/17	14:40	02/10/17	18:25	1.38	10
Czech Rep.	Praha	50.0667	14.4500	02/10/17	18:25	03/10/17	06:10	0.96	30
Czech Rep.	Praha	50.0667	14.4500	03/10/17	06:10	03/10/17	13:00	<0.04	
Czech Rep.	Praha	50.0667	14.4500	03/10/17	13:05	04/10/17	06:00	<0.1	
Czech Rep.	Praha	50.0667	14.4500	04/10/17	06:00	05/10/17	06:05	<0.01	
Czech Rep.	Praha	50.0667	14.4500	05/10/17	06:05	06/10/17	04:40	<0.006	
Czech Rep.	Praha	50.0667	14.4500	06/10/17	04:40	07/10/17	08:30	<0.08	
Czech Rep.	Praha	50.0667	14.4500	07/10/17	08:40	10/10/17	08:45	<0.03	
Czech Rep.	Praha	50.0667	14.4500	10/10/17	05:50	13/10/17	04:50	<0.03	
Czech Rep.	Ústí nad Labem	50.6667	14.0333	26/09/17	09:00	04/10/17	07:00	4.23	7
Czech Rep.	Ústí nad Labem	50.6667	14.0333	04/10/17	06:58	05/10/17	08:28	<0.252	
Czech Rep.	Ústí nad Labem	50.6667	14.0333	17/10/17	10:05	24/10/17	07:35	0.016	30
Denmark	Allinge	55.2700	14.8000	27/09/17	-	04/10/17	-	1.8	20
Denmark	Haderslev	55.2300	9.5000	30/09/17	-	30/09/17	23:00	<LOD	
Denmark	Roskilde	55.6830	12.1000	26/09/17	12:00	02/10/17	12:00	0.0008	60
Denmark	Roskilde	55.6830	12.1000	02/10/17	12:00	10/10/17	12:00	<0.01	60
Estonia	Harku	59.4625	28.0450	24/09/17	-	01/10/17	-	<LOD	
Estonia	Harku	59.4625	28.0450	26/09/17	11:00	03/10/17	-	<LOD	
Estonia	Harku	59.4625	28.0450	01/10/17	-	08/10/17	-	0.18	6

5

Country	Location	Latitude (decimal)	Longitude (decimal)	Start date	Start hour	End date	End hour	^{106}Ru (mBq·m^{-3})	± (%)
Estonia	Narva-Joesuu	59.4625	28.0450	26/09/17	11:00	03/10/17	09:00	0.0107	10
Estonia	Narva-Joesuu	59.4625	28.0450	03/10/17	09:00	10/10/17	09:00	0.111	6
Estonia	Toravere	58.2644	26.4617	25/09/17	-	02/10/17	-	<LOD	
Estonia	Toravere	58.2644	26.4617	02/10/17	-	09/10/17	-	0.214	7
Finland	Böle	60.3711	26.3934	26/09/17	-	04/10/17	-	0.192	-
Finland	Haapasaari	61.1725	21.4777	27/09/17	-	11/10/17	-	0.17	-
Finland	Hankkila	61.1959	21.5530	20/09/17	-	04/10/17	-	0.168	-
Finland	Helsinki	60.2100	25.0500	28/09/17	10:57	03/10/17	04:29	0.064	9
Finland	Helsinki	60.2100	25.0500	03/10/17	09:01	04/10/17	08:58	0.849	4
Finland	Helsinki	60.2100	25.0500	03/10/17	09:01	05/10/17	08:58	0.45	4
Finland	Helsinki	60.2100	25.0500	05/10/17	-	06/10/17	-	<LOD	4
Finland	Imatra	61.1300	28.8300	03/10/17	02:33	05/10/17	09:30	0.288	8
Finland	Ivalo	68.6400	27.5700	02/10/17	05:27	05/10/17	03:21	0.138	4
Finland	Kajaani	67.4136	26.5910	02/10/17	-	09/10/17	-	0.045	-
Finland	Keitala	60.4219	26.3659	26/09/17	-	04/10/17	-	0.192	-
Finland	Korvensuo	61.2400	21.4819	27/09/17	-	11/10/17	-	0.16	-
Finland	Kotka	60.4800	26.9200	11/09/17	11:50	04/10/17	09:10	0.016	10
Finland	Kuivalahti	61.2739	21.5699	20/09/17	-	04/10/17	-	0.163	-
Finland	Kuopio	62.8900	27.6300	02/10/17	06:08	05/10/17	06:10	0.217	4
Finland	Loviisa NPP	60.3778	26.3222	26/09/17	-	10/10/17	-	0.135	-
Finland	Määrlahti	60.4499	26.2607	26/09/17	-	10/10/17	-	0.109	-
Finland	Rovaniemi	66.5100	25.6800	02/10/17	05:15	09/10/17	04:57	0.061	3
Finland	Sodankylä	67.3700	26.6300	02/10/17	04:51	05/10/17	04:38	0.107	8
France	Ajaccio	41.9183	8.7928	18/09/17	09:30	25/09/17	09:10	<0.048	
France	Ajaccio	41.9183	8.7928	25/09/17	09:11	02/10/17	09:30	<0.0043	
France	Ajaccio	41.9183	8.7928	02/10/17	09:00	09/10/17	09:00	0.0082	34
France	Ajaccio	41.9183	8.7928	09/10/17	09:00	16/10/17	09:00	<0.009	
France	Alençon	48.4324	0.0911	26/09/17	11:20	03/10/17	12:00	<0.0004	
France	Alençon	48.4324	0.0911	03/10/17	12:05	10/10/17	11:00	<0.00024	
France	Alençon	48.4324	0.0911	10/10/17	11:00	17/10/17	11:00	0.000277	58
France	Alençon	48.4324	0.0911	17/10/17	11:00	24/10/17	11:43	<0.00026	
France	Bordeaux	44.8271	-0.7043	25/09/17	15:30	02/10/17	15:15	<0.00022	
France	Bordeaux	44.8271	-0.7043	02/10/17	15:30	09/10/17	14:30	<0.00022	
France	Bordeaux	44.8271	-0.7043	09/10/17	14:30	16/10/17	15:08	<0.00025	
France	Bordeaux	44.8271	-0.7043	16/10/17	15:08	23/10/17	14:00	<0.00031	
France	Bugey	45.7907	5.2667	18/09/17	06:19	25/09/17	06:12	<0.050	
France	Bugey	45.7907	5.2667	25/09/17	06:12	02/10/17	06:19	<0.013	
France	Bugey	45.7907	5.2667	02/10/17	06:34	09/10/17	09:11	<0.031	
France	Bugey	45.7907	5.2667	09/10/17	11:00	16/10/17	12:00	<0.025	

Country	Location	Latitude (decimal)	Longitude (decimal)	Start date	Start hour	End date	End hour	^{106}Ru (mBq·m^{-3})	± (%)
France	Bure	48.4872	5.3550	25/09/17	12:40	02/10/17	13:25	<0.00021	
France	Bure	48.4872	5.3550	02/10/17	13:30	05/10/17	09:00	<0.00038	
France	Bure	48.4872	5.3550	05/10/17	09:05	09/10/17	12:23	<0.00018	
France	Bure	48.4872	5.3550	09/10/17	12:27	16/10/17	12:29	<0.00011	
France	Bure	48.4872	5.3550	16/10/17	12:32	23/10/17	13:55	0.00043	36
France	Cadarache	43.7001	5.7471	18/09/17	08:15	29/09/17	07:45	<0.050	
France	Cadarache	43.7001	5.7471	25/09/17	07:45	02/10/17	08:20	<0.029	
France	Cadarache	43.7001	5.7471	02/10/17	08:20	09/10/17	07:35	<0.012	
France	Cadarache	43.7001	5.7471	09/10/17	07:35	16/10/17	08:05	<0.015	
France	Cattenom	49.4203	6.2269	18/09/17	07:55	25/09/17	07:34	<0.048	
France	Cattenom	49.4203	6.2269	25/09/17	07:34	02/10/17	08:06	<0.024	
France	Cattenom	49.4203	6.2269	02/10/17	08:00	09/10/17	07:59	<0.021	
France	Cattenom	49.4203	6.2269	09/10/17	08:00	16/10/17	07:55	<0.05	
France	Charleville-Mézières	49.9378	4.7028	26/09/17	11:50	03/10/17	13:15	<0.00027	
France	Charleville-Mézières	49.9378	4.7028	03/10/17	13:15	10/10/17	12:35	0.00017	71
France	Charleville-Mézières	49.9378	4.7028	10/10/17	12:40	17/10/17	15:10	<0.00023	
France	Charleville-Mézières	49.9378	4.7028	17/10/17	15:15	24/10/17	12:24	0.00017	70
France	Chooz	50.0949	4.7917	02/10/17	07:46	09/10/17	09:51	<0.06	
France	Cruas	44.6263	4.7516	02/10/17	08:30	05/10/17	08:45	<0.008	
France	Cruas	44.6263	4.7516	09/10/17	09:27	16/10/17	09:29	<0.008	
France	Dijon	47.3180	5.0382	13/09/17	13:00	02/10/17	13:35	<0.00024	
France	Dijon	47.3180	5.0382	13/09/17	13:00	02/10/17	13:35	0.00328	16
France	Dijon	47.3180	5.0382	02/10/17	13:35	05/10/17	08:00	<0.00068	
France	Dijon	47.3180	5.0382	05/10/17	08:00	12/10/17	13:30	<0.0003	
France	Dijon	47.3180	5.0382	12/10/17	13:30	19/10/17	14:45	0.000245	78
France	Dijon	47.3180	5.0382	19/10/17	14:45	27/10/17	15:00	<0.00018	
France	Fessenheim	47.9163	7.5662	18/09/17	08:45	25/09/17	08:41	<0.049	
France	Fessenheim	47.9163	7.5662	25/09/17	08:41	02/10/17	08:45	<0.023	
France	Fessenheim	47.9163	7.5662	02/10/17	08:45	09/10/17	08:53	<0.021	
France	Fessenheim	47.9163	7.5662	09/10/17	08:53	16/10/17	08:50	<0.018	
France	Gravelines	50.9974	2.1435	25/09/17	09:05	02/10/17	09:25	<0.00029	
France	Grenoble	45.2020	5.7050	18/09/17	08:03	22/09/17	07:16	<0.140	
France	Grenoble	45.2020	5.7050	22/09/17	07:17	25/09/17	07:13	<0.140	
France	Grenoble	45.2020	5.7050	25/09/17	07:15	29/09/17	07:17	<0.048	
France	Grenoble	45.2020	5.7050	29/09/17	07:19	02/10/17	07:25	<0.050	
France	Grenoble	45.2113	5.6833	02/10/17	07:26	06/10/17	08:12	<0.014	
France	Grenoble	45.2113	5.6833	09/10/17	07:15	12/10/17	07:20	<0.01	
France	Grenoble	45.2113	5.6833	13/10/17	07:09	16/10/17	07:52	<0.016	
France	La Seyne sur Mer	43.1068	5.8847	26/09/17	08:25	03/10/17	11:30	0.0074	19

Country	Location	Latitude (decimal)	Longitude (decimal)	Start date	Start hour	End date	End hour	^{106}Ru (mBq·m^{-3})	± (%)
France	La Seyne sur Mer	43.1068	5.8847	03/10/17	11:30	11/10/17	10:35	0.0197	17
France	La Seyne sur Mer	43.1068	5.8847	11/10/17	10:35	13/10/17	11:42	0.00155	45
France	La Seyne sur Mer	43.1068	5.8847	13/10/17	11:43	17/10/17	14:30	0.001034	38
France	La Seyne sur Mer	43.1068	5.8847	17/10/17	16:18	24/10/17	14:18	<0.00028	
France	Marcoule	44.1237	4.7027	18/09/17	09:01	21/09/17	08:46	<0.120	
France	Marcoule	44.1237	4.7027	21/09/17	08:47	25/09/17	09:20	<0.080	
France	Marcoule	44.1237	4.7027	25/09/17	09:21	28/09/17	09:25	<0.021	
France	Marcoule	44.1237	4.7027	28/09/17	09:21	02/10/17	09:25	<0.023	
France	Marcoule	44.1237	4.7027	02/10/17	09:26	05/10/17	08:39	<0.0082	
France	Marcoule	44.1237	4.7027	05/10/17	08:40	09/10/17	09:15	<0.011	
France	Marcoule	44.1237	4.7027	09/10/17	09:16	12/10/17	16:50	<0.018	
France	Marcoule	44.1237	4.7027	12/10/17	07:51	16/10/17	08 :59	<0.023	
France	Marcoule	44.1237	4.7027	16/10/17	09:01	19/10/17	08:36	<0.024	
France	Nancy	48.6879	6.2215	18/09/17	12:10	25/09/17	12:08	<0.048	
France	Nancy	48.6879	6.2215	25/09/17	12:09	02/10/17	12:30	<0.011	
France	Nancy	48.6879	6.2215	02/10/17	12:31	09/10/17	11:38	<0.011	
France	Nancy	48.6879	6.2215	09/10/17	11:40	16/10/17	11:48	<0.0046	
France	Nice	43.6492	7.2092	18/09/17	09:00	25/09/17	09:00	<0.047	
France	Nice	43.6492	7.2092	25/09/17	09:00	02/10/17	15:20	0.0068	39
France	Nice	43.6492	7.2092	02/10/17	13:55-	09/10/17	14:40	0.046	17
France	Nice	43.6492	7.2092	09/10/17	15:40	16/10/17	07:43	<0.007	
France	Omonville	49.6949	-1.8733	09/10/17	08:50	16/10/17	15:00	<0.022	
France	Opme	45.7070	3.0937	27/09/17	09:38	03/10/17	10:02	< 0.0005	
France	Opme	45.7070	3.0937	03/10/17	10:04	11/10/17	10:32	<0.0003	
France	Opme	45.7070	3.0937	11/10/17	10:36	18/10/17	09:26	0.00035	83
France	Opme	45.7070	3.0937	18/10/17	09:29	25/10/17	10:48	<0.00032	
France	Orsay	48.7061	2.1783	27/09/17	13:30	03/10/17	9:10	<0.00035	
France	Orsay	48.7061	2.1783	03/10/17	9:13	11/10/17	13:38	<0.00035	
France	Orsay	48.7061	2.1783	11/10/17	13:40	18/10/17	13:56	< 0.00028	
France	Orsay	48.7061	2.1783	18/10/17	13:58	25/10/17	13:32	<0.00022	
France	Orsay	48.7061	2.1783	25/10/17	13:33	31/10/17	13:51	<0.00021	
France	Penly	49.9761	1.2247	18/09/17	08:30	25/09/17	08:40	<0.048	
France	Penly	49.9761	1.2247	25/09/17	08:40	02/10/17	08:38	<0.023	
France	Penly	49.9761	1.2247	02/10/17	08:40	09/10/17	08:20	<0.022	
France	Penly	49.9761	1.2247	09/10/17	07:23	16/10/17	07:23	<0.027	
France	Prevessin	46.2668	6.1142	18/09/17	14:12	25/09/17	14:06	<0.046	
France	Prevessin	46.2668	6.1142	25/09/17	14:11	02/10/17	14:32	<0.007	
France	Prevessin	46.2668	6.1142	02/10/17	14:36	06/10/17	10:31	<0.033	
France	Puy de Dôme	45.7723	2.9645	27/09/17	13:59	03/10/17	09:37	<0.00045	

Country	Location	Latitude (decimal)	Longitude (decimal)	Start date	Start hour	End date	End hour	^{106}Ru (mBq·m^{-3})	± (%)
France	Puy de Dôme	45.7723	2.9645	03/10/17	09:39	11/10/17	13:06	<0.00028	
France	Puy de Dôme	45.7723	2.9645	11/10/17	13:08	18/10/17	13:07	<0.00031	
France	Puy de Dôme	45.7723	2.9645	18/10/17	13:09	25/10/17	12:47	0.00062	50
France	Puy de Dôme	45.7723	2.9645	25/10/17	12:49	02/11/17	14:33	0.000373	54
France	Saint Alban	45.3957	4.7581	18/09/17	07:35	25/09/17	07:33	<0.046	
France	Saint Alban	45.3957	4.7581	25/09/17	07:33	02/10/17	07:43	<0.032	
France	Saint Alban	45.3957	4.7581	02/10/17	08:58	09/10/17	08:07	<0.024	
France	Saint Alban	45.3957	4.7581	09/10/17	07:25	16/10/17	07:39	<0.026	
France	Saint Laurent	47.7267	1.5993	09/10/17	09:10	16/10/17	09:05	<0.027	
France	Tricastin	44.3222	4.7308	18/09/17	08:54	25/09/17	09:03	<0.048	
France	Tricastin	44.3222	4.7308	25/09/17	09:45	02/10/17	09:45	<0.026	
France	Tricastin	44.3222	4.7308	02/10/17	08:31	06/10/17	07:46	<0.010	
France	Tricastin	44.3222	4.7308	09/10/17	09:45	16/10/17	09:45	<0.016	
France	Villeneuve d'Ascq	50.6091	3.1327	19/09/17	12:05	22/09/17	08:45	<0.140	
France	Villeneuve d'Ascq	50.6091	3.1327	22/09/17	08:49	26/09/17	11:23	<0.100	
France	Villeneuve d'Ascq	50.6091	3.1327	26/09/17	11:24	29/09/17	08:20	<0.160	
France	Villeneuve d'Ascq	50.6091	3.1327	29/09/17	08:21	03/10/17	11:10	<0.060	
France	Villeneuve d'Ascq	50.6091	3.1327	03/10/17	11:10	06/10/17	13:14	<0.050	
France	Villeneuve d'Ascq	50.6091	3.1327	06/10/17	-	13/10/17	-	<0.012	
France	Villeneuve d'Ascq	50.6091	3.1327	13/10/17	-	17/10/17	-	<0.1	
Germany	Aachen-Orsbach	50.7983	6.0244	25/09/17	09:00	02/10/17	08:00	<0.00743	
Germany	Aachen-Orsbach	50.7983	6.0244	02/10/17	09:00	04/10/17	08:00	<0.053	
Germany	Aachen-Orsbach	50.7983	6.0244	04/10/17	08:00	09/10/17	09:00	<0.0101	
Germany	Angermünde	53.0315	13.9908	25/09/17	09:00	02/10/17	09:00	0.160	8
Germany	Angermünde	53.0315	13.9908	02/10/17	09:00	09/10/17	09:00	0.050	11
Germany	Arkona	54.6792	13.4343	25/09/17	09:00	02/10/17	09:00	0.014	29
Germany	Arkona	54.6792	13.4343	02/10/17	09:00	04/10/17	08:00	<0.0942	29
Germany	Arkona	54.6792	13.4343	04/10/17	08:00	09/10/17	09:00	<0.0299	29
Germany	Artern	51.3745	11.2920	25/09/17	09:00	02/10/17	09:00	<0.0139	29
Germany	Artern	51.3745	11.2920	02/10/17	09:00	09/10/17	09:00	<0.021	29
Germany	Braunschweig	52.3000	10.4660	25/09/17	-	02/10/17	-	<0.00023	
Germany	Braunschweig	52.3000	10.4660	02/10/17	-	05/10/17	-	0.000299	25
Germany	Braunschweig	52.3000	10.4660	09/10/17	05:40	16/10/17	05:17	<LOD	
Germany	Braunschweig	52.3000	10.4660	16/10/17	05:40	23/10/17	05:17	0.0005	19
Germany	Bremen	53.0450	8.7979	25/09/17	09:00	02/10/17	09:00	<0.0193	
Germany	Bremen	53.0450	8.7979	02/10/17	09:00	09/10/17	09:00	<0.0196	
Germany	Brocken	51.7986	10.6183	25/09/17	09:00	02/10/17	09:00	<0.0198	
Germany	Brocken	51.7986	10.6181	02/10/17	09:00	09/10/17	09:00	<0.0193	
Germany	Brocken	51.7986	10.6181	16/10/17	09:00	23/10/17	09:00	<0.0185	

Country	Location	Latitude (decimal)	Longitude (decimal)	Start date	Start hour	End date	End hour	^{106}Ru (mBq·m^{-3})	± (%)
Germany	Cottbus	51.7760	14.3168	25/09/17	09:00	02/10/17	09:00	0.677	7
Germany	Cottbus	51.7760	14.3168	02/10/17	09:00	09/10/17	09:00	0.167	9
Germany	Essen-Bredeney	51.4041	6.9677	25/09/17	09:00	02/10/17	09:00	<0.0239	
Germany	Essen-Bredeney	51.4041	6.9677	02/10/17	09:00	04/10/17	08:00	<0.09	
Germany	Essen-Bredeney	51.4041	6.9677	04/10/17	08:00	09/10/17	09:00	<0.0217	
Germany	Fehmarn	54.5284	11.1404	25/09/17	09:00	02/10/17	09:00	<0.0154	
Germany	Fürstenzell	48.5451	13.3531	25/09/17	09:00	02/10/17	09:00	0.0198	17
Germany	Fürstenzell	48.5442	13.3531	02/10/17	09:00	09/10/17	09:00	<0.0195	
Germany	Garmisch-Partenkirchen	47.4831	11.0623	25/09/17	09:00	02/10/17	09:00	<0.0231	
Germany	Garmisch-Partenkirchen	47.4831	11.0623	02/10/17	09:00	04/10/17	09:00	<0.0349	
Germany	Garmisch-Partenkirchen	47.4831	11.0623	04/10/17	09:00	09/10/17	09:00	<0.0855	
Germany	Gera-Leumnitz	50.8813	12.1289	25/09/17	09:00	02/10/17	09:00	<0.0336	
Germany	Gera-Leumnitz	50.8813	12.1289	02/10/17	09:00	04/10/17	09:00	<0.103	
Germany	Gera-Leumnitz	50.8813	12.1289	04/10/17	09:00	09/10/17	09:00	<0.0409	
Germany	Görlitz	51.1622	14.9506	25/09/17	09:00	02/10/17	09:00	4.91	6
Germany	Görlitz	51.1622	14.9506	02/10/17	09:00	04/10/17	08:00	4.57	7
Germany	Görlitz	51.1622	14.9506	04/10/17	09:00	09/10/17	09:00	<0.0349	
Germany	Greifswald	54.0967	13.4056	25/09/17	09:00	02/10/17	09:00	0.009	6
Germany	Greifswald	54.0967	13.4056	02/10/17	09:00	09/10/17	09:00	<0.0147	
Germany	Hamburg-Fuhlsbüttel	53.6332	9.9881	25/09/17	09:00	02/10/17	09:00	<0.0292	
Germany	Hamburg-Fuhlsbüttel	53.6332	9.9881	02/10/17	09:00	04/10/17	13:20	<0.0782	
Germany	Hamburg-Fuhlsbüttel	53.6332	9.9881	04/10/17	13:30	09/10/17	09:00	<0.043	
Germany	Hof	50.3122	11.8761	25/09/17	09:00	02/10/17	09:00	<0.0115	
Germany	Hof	50.3122	11.8761	02/10/17	09:00	04/10/17	08:00	<0.0378	
Germany	Hof	50.3122	11.8761	04/10/17	09:00	09/10/17	09:00	<0.0167	
Germany	Kahler Asten	51.1803	8.4891	25/09/17	09:00	02/10/17	09:00	<0.0133	
Germany	Kahler Asten	51.1803	8.4891	02/10/17	09:00	09/10/17	09:00	<0.0138	
Germany	Konstanz	47.6774	9.1901	25/09/17	09:00	02/10/17	09:00	<0.0414	
Germany	Konstanz	47.6774	9.1901	02/10/17	09:00	04/10/17	08:00	<0.197	
Germany	Konstanz	47.6774	9.1901	04/10/17	09:00	09/10/17	09:00	<0.00561	
Germany	Lahr	48.3647	7.8280	25/09/17	09:00	02/10/17	09:00	<0.00953	
Germany	Lahr	48.3647	7.8280	02/10/17	09:00	04/10/17	08:00	<0.0661	
Germany	Lahr	48.3647	7.8280	04/10/17	09:00	09/10/17	09:00	<0.0114	
Germany	Lingen	52.5181	7.3081	25/09/17	09:00	02/10/17	09:00	<0.0164	
Germany	Lingen	52.5181	7.3081	02/10/17	09:00	09/10/17	09:00	<0.0164	
Germany	Lippspringe. Bad	51.7855	8.8388	25/09/17	09:00	02/10/17	09:00	<0.0128	
Germany	Lippspringe. Bad	51.7855	8.8388	02/10/17	09:00	09/10/17	09:00	<0.0133	
Germany	Magdeburg	52.1029	11.5827	25/09/17	09:00	02/10/17	09:00	<0.020	
Germany	Magdeburg	52.1029	11.5827	25/09/17	09:00	02/10/17	09:00	<0.0254	

10

Country	Location	Latitude (decimal)	Longitude (decimal)	Start date	Start hour	End date	End hour	^{106}Ru (mBq·m^{-3})	± (%)
Germany	Neuherberg	48.2500	11.5500	22/09/17	14:05	29/09/17	12:02	<0.00256	
Germany	Neuherberg	48.2500	11.5500	29/09/17	12:05	03/10/17	12:30	<0.00671	
Germany	Norderney	53.7123	7.1519	25/09/17	09:00	02/10/17	09:00	<0.0359	
Germany	Norderney	53.7123	7.1519	02/10/17	09:00	04/10/17	08:00	<0.115	
Germany	Norderney	53.7123	7.1519	04/10/17	09:00	09/10/17	09:00	<0.0438	
Germany	Nürburg-Barweiler	50.3601	6.9533	25/09/17	09:00	02/10/17	09:00	<0.0137	
Germany	Nürburg-Barweiler	50.3601	6.9533	02/10/17	09:00	09/10/17	09:00	<0.0157	
Germany	Nürnberg	49.5030	11.0549	25/09/17	09:00	02/10/17	09:00	<0.032	
Germany	Nürnberg	49.5030	11.0549	02/10/17	09:00	04/10/17	08:00	<0.0914	
Germany	Nürnberg	49.5030	11.0549	04/10/17	09:00	09/10/17	09:00	<0.0461	
Germany	Oberschleißheim	48.2446	11.5525	25/09/17	09:00	02/10/17	09:00	<0.0148	
Germany	Oberschleißheim	48.2446	11.5525	02/10/17	09:00	04/10/17	08:00	<0.0425	
Germany	Oberschleißheim	48.2446	11.5525	04/10/17	09:00	09/10/17	09:00	<0.00874	
Germany	Potsdam	52.3813	13.0622	25/09/17	09:00	02/10/17	09:00	0.00921	9
Germany	Potsdam	52.3813	13.0622	02/10/17	09:00	04/10/17	08:00	<0.0394	
Germany	Potsdam	52.3813	13.0622	04/10/17	09:00	09/10/17	09:00	<0.0014	
Germany	Regensburg	49.0424	12.1021	25/09/17	09:00	02/10/17	09:00	<0.0144	
Germany	Regensburg	49.0424	12.1021	02/10/17	09:00	09/10/17	09:00	<0.0159	
Germany	Rheinstetten	48.9726	8.3301	25/09/17	09:00	02/10/17	09:00	<0.0579	
Germany	Rheinstetten	48.9726	8.3301	02/10/17	09:00	04/10/17	08:00	<0.154	
Germany	Rheinstetten	48.9726	8.3301	04/10/17	09:00	09/10/17	09:00	<0.0542	
Germany	Rostock-Warnemünde	54.1803	12.0808	25/09/17	09:00	02/10/17	09:00	<0.0245	
Germany	Rostock-Warnemünde	54.1803	12.0808	02/10/17	09:00	04/10/17	08:00	<0.0648	
Germany	Rostock-Warnemünde	54.1803	12.0808	04/10/17	09:00	09/10/17	09:00	<0.0164	
Germany	Saarbrücken-Ensheim	49.2128	7.1077	25/09/17	09:00	02/10/17	09:00	<0.023	
Germany	Saarbrücken-Ensheim	49.2128	7.1077	02/10/17	09:00	09/10/17	09:00	<0.024	
Germany	Schauinsland	47.9100	7.8900	25/09/17	-	02/10/17	-	<0.01	
Germany	Schleswig	54.5275	9.5487	25/09/17	09:00	02/10/17	09:00	<0.00716	
Germany	Schleswig	54.5275	9.5487	02/10/17	09:00	04/10/17	08:00	<0.0285	
Germany	Schleswig	54.5275	9.5487	04/10/17	09:00	09/10/17	09:00	<0.00973	
Germany	Seehausen	52.8911	11.7297	25/09/17	09:00	02/10/17	09:00	<0.032	
Germany	Seehausen	52.8911	11.7297	02/10/17	09:00	04/10/17	08:00	<0.0737	
Germany	Seehausen	52.8911	11.7297	04/10/17	09:00	09/10/17	09:00	<0.02	
Germany	Seehausen	52.8911	11.7297	02/10/17	09:00	09/10/17	09:00	0.00957	-
Germany	Stötten	48.6657	9.8646	25/09/17	09:00	02/10/17	09:00	<0.0206	
Germany	Stötten	48.6657	9.8646	02/10/17	09:00	09/10/17	09:00	<0.0218	
Germany	Trier-Petrisberg	49.7479	6.6582	25/09/17	09:00	02/10/17	09:00	<0.0357	
Germany	Trier-Petrisberg	49.7479	6.6582	02/10/17	09:00	04/10/17	08:00	<0.141	
Germany	Trier-Petrisberg	49.7479	6.6582	04/10/17	09:00	09/10/17	09:00	<0.0456	

Country	Location	Latitude (decimal)	Longitude (decimal)	Start date	Start hour	End date	End hour	^{106}Ru (mBq·m^{-3})	± (%)
Germany	Wasserkuppe	50.4973	9.9428	25/09/17	09:00	02/10/17	09:00	<0.00561	
Germany	Wasserkuppe	50.4973	9.9428	02/10/17	09:00	04/10/17	08:00	<0.03	
Germany	Wasserkuppe	50.4973	9.9428	04/10/17	09:00	09/10/17	09:00	<0.00712	
Germany	Würzburg	49.7703	9.9577	25/09/17	09:00	02/10/17	09:00	<0.0154	
Germany	Würzburg	49.7703	9.9577	02/10/17	09:00	09/10/17	09:00	<0.0142	
Germany	Zinnwald-Georgenfeld	50.7314	13.7516	25/09/17	09:00	02/10/17	09:00	<0.0159	
Germany	Zinnwald-Georgenfeld	50.7314	13.7516	25/09/17	09:00	02/10/17	09:00	<0.0112	
Germany	Zugspitze	47.4209	10.9847	25/09/17	09:00	02/10/17	09:00	<0.0256	
Germany	Zugspitze	47.4209	10.9847	02/10/17	09:00	09/10/17	09:00	<0.0245	
Greece	Athens	37.9950	23.81599	27/09/17	13:27	03/10/17	10:00	2.64	24
Greece	Athens	37.9950	23.81599	03/10/17	11:10	04/10/17	14:40	0.19	14
Greece	Athens	37.9950	23.81599	04/10/17	14:53	06/10/17	14:17	0.11	13
Greece	Athens	37.9950	23.81599	06/10/17	14:25	11/10/17	15:10	0.04	13
Greece	Athens	37.9998	23.8159	05/10/17	17:43	10/10/17	17:13	<0.2	
Greece	Athens	37.9766	23.7851	09/10/17	13:00	11/10/17	09:00	<0.1	
Greece	Athens	37.9766	23.7851	10/10/17	16:00	17/10/17	17:00	<0.1	
Greece	Helmos Kalavrita	37.9842	22.1964	27/09/17	-	29/09/17	-	0.99	20
Hungary	Budapest	47.5011	19.0465	29/09/17	-	02/10/17	-	33.76	-
Hungary	Budapest	47.5011	19.0465	02/10/17	-	03/10/17	-	27.58	-
Hungary	Budapest	47.5011	19.0465	03/10/17	-	04/10/17	-	9.9	-
Hungary	Budapest	47.5011	19.0465	04/10/17	-	05/10/17	-	2.08	-
Hungary	Budapest	47.5011	19.0465	25/09/17	-	02/10/17	-	11.95	5
Hungary	Budapest	47.5011	19.0465	25/09/17	-	02/10/17	-	14.67	2
Hungary	Budapest	47.5011	19.0465	02/10/17	-	05/10/17	-	9.21	3
Hungary	Budapest	47.5011	19.0465	05/10/17	-	09/10/17	-	0.271	-
Hungary	Budapest	47.5011	19.0465	09/10/17	-	16/10/17	-	0.0114	3
Hungary	Budapest *	47.4891	18.9537	25/09/17	10:00	02/10/17	10:00	10.7	6
Hungary	Budapest *	47.4891	18.9537	02/10/17	10:00	03/10/17	10:00	24.1	7
Hungary	Budapest *	47.4891	18.9537	03/10/17	10:00	04/10/17	10:00	11.9	8
Hungary	Budapest *	47.4891	18.9537	04/10/17	10:00	05/10/17	10:00	<1.2	
Hungary	Budapest *	47.4891	18.9537	02/10/17	10:00	09/10/17	10:00	3.9	5
Hungary	Budapest *	47.4891	18.9537	09/10/17	10:00	16/10/17	10:00	<0.19	
Hungary	Győr	47.6850	17.6530	26/09/17	-	03/10/17	-	14.3	5
Hungary	Miskolc	48.1000	20.7700	29/09/17	-	05/10/17	-	14.6	5
Hungary	Paks	46.5742	18.8496	25/09/17	-	02/10/17	-	13.5	-
Hungary	Paks	46.5742	18.8496	30/09/17	-	02/10/17	-	49.4	-
Ireland	Belfield	53.3090	-6.2247	28/09/17	-	09/10/17	-	<0.00257	
Italy	Belluno	46.1650	12.2460	29/09/17	07:00	02/10/17	07:00	2.62	23
Italy	Belluno	46.1650	12.2460	02/10/17	07:00	03/10/17	07:00	18.6	20

Country	Location	Latitude (decimal)	Longitude (decimal)	Start date	Start hour	End date	End hour	^{106}Ru (mBq·m^{-3})	± (%)
Italy	Belluno	46.1650	12.2460	03/10/17	07:00	04/10/17	07:00	9.3	24
Italy	Belluno	46.1650	12.2460	04/10/17	07:00	05/10/17	07:00	2.97	34
Italy	Belluno	46.1650	12.2460	05/10/17	07:00	06/10/17	07:00	2.17	32
Italy	Bergamo	45.6970	9.6794	29/09/17	07:00	02/10/17	07:00	3.8	16
Italy	Bergamo	45.6970	9.6794	02/10/17	07:00	03/10/17	07:00	12.2	18
Italy	Bergamo	45.6970	9.6794	03/10/17	07:00	03/10/17	21:00	6.9	19
Italy	Firenze	43.7772	11.2486	30/09/17	-	02/10/17	-	0.5	40
Italy	Firenze	43.7772	11.2486	02/10/17	-	03/10/17	-	1.4	29
Italy	Firenze	43.7772	11.2486	03/10/17	-	04/10/17	-	<0.2	
Italy	Firenze	43.7772	11.2486	04/10/17	-	05/10/17	-	<0.3	
Italy	Genova	44.4070	8.9460	29/09/17	-	02/10/17	-	0.5	40
Italy	Gorizia	45.9371	13.6162	29/09/17	-	29/09/17	23:59	<4.1	
Italy	Gorizia	45.9371	13.6162	30/10/17	-	30/10/17	23:59	<3.9	
Italy	Gorizia	45.9371	13.6162	01/10/17	-	01/10/17	23:59	48.4	13
Italy	Gorizia	45.9371	13.6162	02/10/17	-	02/10/17	23:59	6.3	17
Italy	Gorizia	45.9371	13.6162	03/10/17	-	03/10/17	23:59	39.5	11
Italy	Gorizia	45.9371	13.6162	04/10/17	-	04/10/17	23:59	9.2	34
Italy	Gorizia	45.9371	13.6162	05/10/17	-	05/10/17	23:59	5.3	34
Italy	Gorizia	45.9371	13.6162	06/10/17	-	06/10/17	23:59	<4.3	
Italy	Ivrea	45.4742	7.8742	27/09/17	-	03/10/17	-	0.88	68
Italy	Ivrea	45.4742	7.8742	05/10/17	-	06/10/17	-	1.17	77
Italy	Milano	45.4731	9.2225	25/09/17	07:00	02/10/17	07:00	1.09	25
Italy	Milano	45.4731	9.2225	29/09/17	07:00	02/10/17	07:00	2.49	17
Italy	Milano	45.4731	9.2225	02/10/17	07:30	09/10/17	07:30	1.64	24
Italy	Milano	45.4731	9.2225	02/10/17	07:30	02/10/17	15:00	6.3	23
Italy	Milano	45.4731	9.2225	02/10/17	15:00	03/10/17	07:30	3.6	33
Italy	Milano	45.4731	9.2225	03/10/17	07:30	04/10/17	07:30	3.5	34
Italy	Milano	45.4731	9.2225	04/10/17	07:30	05/10/17	07:30	3.09	34
Italy	Milano	45.4731	9.2225	05/10/17	07:30	06/10/17	07:30	<1.7	
Italy	Milano	45.4731	9.2225	06/10/17	07:30	09/10/17	07:30	<0.62	
Italy	Milano	45.4731	9.2225	09/10/17	07:30	10/10/17	07:30	<2.4	
Italy	Milano	45.4731	9.2225	10/10/17	07:30	11/10/17	07:30	<2.4	
Italy	Milano	45.4731	9.2225	11/10/17	07:30	12/10/17	07:30	<2.6	
Italy	Milano	45.4731	9.2225	12/10/17	07:30	13/10/17	07:30	<3.1	
Italy	Milano	45.4731	9.2225	13/10/17	07:30	16/10/17	07:30	<1.1	
Italy	Milano	45.4731	9.2225	16/10/17	07:30	17/10/17	07:30	<4.4	
Italy	Milano	45.4731	9.2225	17/10/17	07:30	18/10/17	07:30	<3.7	
Italy	Milano	45.4731	9.2225	18/10/17	07:30	19/10/17	07:30	<2.8	
Italy	Milano	45.4731	9.2225	19/10/17	07:30	20/10/17	07:30	<2.8	

Country	Location	Latitude (decimal)	Longitude (decimal)	Start date	Start hour	End date	End hour	^{106}Ru (mBq·m^{-3})	± (%)
Italy	Milano	45.4731	9.2225	20/10/17	07:30	23/10/17	07:30	<0.5	
Italy	Milano	45.4731	9.2225	23/10/17	07:30	24/10/17	07:30	<2.1	
Italy	Milano	45.4731	9.2225	24/10/17	07:30	25/10/17	07:30	<2.4	
Italy	Milano	45.4731	9.2225	25/10/17	07:30	26/10/17	07:30	<3.5	
Italy	Milano	45.4731	9.2225	26/10/17	07:30	27/10/17	07:30	<2.7	
Italy	Milano	45.4731	9.2225	27/10/17	07:30	30/10/17	07:30	<0.78	
Italy	Milano	45.4731	9.2225	30/10/17	07:30	31/10/17	07:30	<2.3	
Italy	Perugia	43.0819	12.3380	29/09/17	-	02/10/17	-	0.91	22
Italy	Perugia	43.0819	12.3380	02/10/17	-	03/10/17	-	6.2	21
Italy	Perugia	43.0819	12.3380	03/10/17	-	04/10/17	-	<0.13	
Italy	Porcia	45.9576	12.6187	29/09/17	-	29/09/17	21:59	<3.8	
Italy	Porcia	45.9576	12.6187	30/10/17	-	30/10/17	21:59	<3.8	
Italy	Porcia	45.9576	12.6187	01/10/17	-	01/10/17	21:59	16.6	19
Italy	Porcia	45.9576	12.6187	02/10/17	-	02/10/17	21:59	53.5	20
Italy	Porcia	45.9576	12.6187	03/10/17	-	03/10/17	21:59	38.3	11
Italy	Porcia	45.9576	12.6187	04/10/17	-	04/10/17	21:59	15.7	21
Italy	Porcia	45.9576	12.6187	05/10/17	-	05/10/17	21:59	6.8	35
Italy	Porcia	45.9576	12.6187	06/10/17	-	06/10/17	21:59	4.8	33
Italy	Trino	45.1953	8.2961	29/09/17	-	02/10/17	-	1.14	35
Italy	Udine	46.0710	13.2340	29/09/17	07:00	02/10/17	07:00	12.5	24
Italy	Udine	46.0710	13.2340	02/10/17	07:00	03/10/17	07:00	49.1	24
Italy	Udine	46.0710	13.2340	03/10/17	07:10	03/10/17	13:30	54.3	37
Italy	Udine	46.0710	13.2340	03/10/17	13:30	04/10/17	07:05	30	30
Italy	Udine	46.0710	13.2340	04/10/17	07:10	04/10/17	13:30	4.2	35
Italy	Udine	46.0710	13.2340	04/10/17	13:30	05/10/17	07:00	5.2	29
Italy	Udine	46.0710	13.2340	05/10/17	07:10	06/10/17	07:00	3.3	45
Italy	Udine	46.0710	13.2340	06/10/17	07:10	07/10/17	06:00	<1.1	
Italy	Udine	46.0710	13.2340	07/10/17	06:00	09/10/17	06:00	<1.5	
Italy	Udine	46.0710	13.2340	09/10/17	06:00	10/10/17	06:00	<1.3	
Italy	Udine	46.0661	13.2408	29/09/17	-	29/09/17	21:59	<4.23	
Italy	Udine	46.0661	13.2408	30/10/17	-	30/10/17	21:59	<4.77	
Italy	Udine	46.0661	13.2408	01/10/17	-	01/10/17	21:59	41.6	22
Italy	Udine	46.0661	13.2408	02/10/17	-	02/10/17	21:59	50.4	11
Italy	Udine	46.0661	13.2408	03/10/17	-	03/10/17	21:59	33.7	22
Italy	Udine	46.0661	13.2408	04/10/17	-	04/10/17	21:59	6.3	21
Italy	Udine	46.0661	13.2408	05/10/17	-	05/10/17	21:59	9.2	26
Italy	Ugovizza	46.5101	13.4747	29/09/17	-	29/09/17	21:59	<2.4	
Italy	Ugovizza	46.5101	13.4747	30/10/17	-	30/10/17	21:59	10.2	26
Italy	Ugovizza	46.5101	13.4747	01/10/17	-	01/10/17	21:59	35.4	10

Country	Location	Latitude (decimal)	Longitude (decimal)	Start date	Start hour	End date	End hour	^{106}Ru (mBq·m^{-3})	± (%)
Italy	Ugovizza	46.5101	13.4747	02/10/17	-	02/10/17	21:59	27.5	16
Italy	Ugovizza	46.5101	13.4747	03/10/17	-	03/10/17	21:59	6	37
Italy	Vercelli	45.3099	8.4077	29/09/17	-	05/10/17	-	1.25	32
Italy	Verona	45.4260	10.9920	29/09/17	07:00	02/10/17	07:00	5.58	16
Italy	Verona	45.4260	10.9920	02/10/17	07:00	03/10/17	07:00	19.1	22
Italy	Verona	45.4260	10.9920	03/10/17	07:00	04/10/17	07:00	17.4	29
Italy	Verona	45.4260	10.9920	04/10/17	07:00	05/10/17	07:00	7.07	42
Italy	Verona	45.4260	10.9920	05/10/17	07:00	06/10/17	07:00	<1.93	
Italy	Vicenza	45.5460	11.5620	29/09/17	07:00	02/10/17	07:00	8.4	18
Italy	Vicenza	45.5460	11.5620	02/10/17	07:00	03/10/17	07:00	25.2	7
Italy	Vicenza	45.5460	11.5620	03/10/17	07:00	04/10/17	07:00	23	13
Italy	Vicenza	45.5460	11.5620	04/10/17	07:00	05/10/17	07:00	6	32
Italy	Vicenza	45.5460	11.5620	05/10/17	07:00	06/10/17	07:00	<3.10	
Lithuania	Ignalina NPP	55.6043	26.5601	25/09/17	-	03/10/17	-	0.021	-
Lithuania	Ignalina NPP	55.6043	26.5601	03/10/17	-	05/10/17	-	1.7	-
Lithuania	Utena	55.4932	25.6220	29/09/17	-	02/10/17	-	<0.0243	
Lithuania	Utena	55.4932	25.6220	02/10/17	-	05/10/17	-	1.21	-
Luxembourg	Luxembourg-ville	49.6114	6.1231	18/09/17	-	26/09/17	-	<0.021	
Luxembourg	Luxembourg-ville	49.6114	6.1231	26/09/17	-	02/10/17	-	<0.023	
Luxembourg	Luxembourg-ville	49.6114	6.1231	02/10/17	-	09/10/17	-	<0.021	
Luxembourg	Luxembourg-ville	49.6114	6.1231	09/10/17	-	16/10/17	-	<0.019	
Netherlands	Bilthoven	52.1365	5.2104	21/09/17	08:29	28/09/17	08:10	<0.0043	
Netherlands	Bilthoven	52.1365	5.2104	28/09/17	08:10	03/10/17	07:00	<0.0076	
Netherlands	Bilthoven	52.1365	5.2104	03/10/17	07:00	05/10/17	07:58	<0.0241	
Netherlands	Bilthoven	52.1365	5.2104	05/10/17	07:58	06/10/17	11:26	<0.0215	
North Macedonia	Skopje	41.9900	21.4240	25/09/17	-	02/10/17	-	5.773	8
Norway	Ørland	63.6900	9.6100	25/09/17	10:00	02/10/17	10:00	0.074	4
Norway	Ørland	63.6900	9.6100	02/10/17	10:00	03/10/17	10:00	0.213	4
Norway	Ørland	63.6900	9.6100	03/10/17	10:00	09/10/17	10:00	0.003	14
Norway	Ørland	63.6900	9.6100	09/10/17	10:00	16/10/17	10:00	<0.001	
Norway	Oslo	59.9482	10.6032	25/09/17	10:00	02/10/17	10:00	0.2	-
Norway	Østerås	59.9400	10.6000	25/09/17	10:00	02/10/17	10:00	0.184	4
Norway	Østerås	59.9400	10.6000	25/09/17	10:00	02/10/17	10:00	0.0006	18
Norway	Østerås	59.9400	10.6000	02/10/17	10:00	03/10/17	10:00	0.024	10
Norway	Østerås	59.9400	10.6000	03/10/17	10:00	04/10/17	10:00	<0.003	
Norway	Østerås	59.9400	10.6000	04/10/17	10:00	06/10/17	10:00	<0.055	
Norway	Østerås	59.9400	10.6000	06/10/17	10:00	09/10/17	10:00	<0.005	
Norway	Sola	58.8800	5.6400	22/09/17	10:00	29/09/17	10:00	<0.001	

Country	Location	Latitude (decimal)	Longitude (decimal)	Start date	Start hour	End date	End hour	^{106}Ru (mBq·m^{-3})	± (%)
Norway	Sola	58.8800	5.6400	29/09/17	10:00	03/10/17	10:00	<0.002	
Norway	Skibotn	69.3700	20.3000	25/09/17	10:00	02/10/17	10:00	<0.003	
Norway	Skibotn	69.3700	20.3000	02/10/17	10:00	09/10/17	10:00	0.094	6
Norway	Skibotn	69.3700	20.3000	09/10/17	10:00	16/10/17	10:00	0.004	6
Norway	Skibotn	69.3700	20.3000	16/10/17	10:00	23/10/17	10:00	<0.002	
Norway	Sola	58.8800	5.6400	03/10/17	10:00	06/10/17	10:00	<0.002	
Norway	Svanhovd	69.4500	30.0400	13/10/17	10:00	16/10/17	10:00	<0.01	
Norway	Viksjofjell	69.6200	30.8100	24/09/17	10:00	01/10/17	10:00	<0.002	
Norway	Viksjofjell	69.6200	30.8100	01/10/17	10:00	08/10/17	10:00	<0.04	
Poland	Białystok	53.1279	23.1649	25/09/17	10:00	02/10/17	10:00	0.23	4
Poland	Białystok	53.1279	23.1649	02/10/17	10:00	09/10/17	10:00	1.752	3
Poland	Gdynia	54.5210	18.5463	25/09/17	10:00	02/10/17	10:00	3.62	2
Poland	Gdynia	54.5210	18.5463	02/10/17	10:00	09/10/17	10:00	2.536	2
Poland	Katowice	50.2707	19.0268	25/09/17	10:00	02/10/17	10:00	0.6	5
Poland	Katowice	50.2707	19.0268	02/10/17	10:00	09/10/17	10:00	4.65	3
Poland	Kraków	50.0902	19.8886	25/09/17	09:18	02/10/17	09:46	3.11	7
Poland	Kraków	50.0902	19.8886	25/09/17	09:12	02/10/17	09:41	1.67	7
Poland	Kraków	50.0902	19.8886	02/10/17	09:50	03/10/17	11:35	16.7	7
Poland	Kraków	50.0902	19.8886	03/10/17	12:00	04/10/17	10:12	2.44	7
Poland	Kraków	50.0902	19.8886	04/10/17	10:30	05/10/17	09:53	<0.0103	
Poland	Kraków	50.0902	19.8886	05/10/17	10:00	06/10/17	08:33	<0.0073	
Poland	Kraków	50.0902	19.8886	06/10/17	08:37	09/10/17	09:08	0.0045	67
Poland	Kraków	50.0902	19.8886	02/10/17	09:45	09/10/17	09:02	3.11	7
Poland	Łódź	51.7446	19.4501	25/09/17	10:00	02/10/17	10:00	7.63	32
Poland	Łódź	51.7446	19.4501	02/10/17	10:00	09/10/17	10:00	12.19	3
Poland	Lublin	51.2610	22.5127	25/09/17	10:00	02/10/17	10:00	7.16	3
Poland	Lublin	51.2610	22.5127	02/10/17	10:00	09/10/17	10:00	3.36	1
Poland	Sanok	49.5501	22.2011	25/09/17	10:00	02/10/17	10:00	6.52	6
Poland	Sanok	49.5501	22.2011	02/10/17	10:00	09/10/17	10:00	4.83	6
Poland	Szczecin	53.4207	14.5351	25/09/17	10:00	02/10/17	10:00	0.36	3
Poland	Szczecin	53.4207	14.5351	02/10/17	10:00	09/10/17	10:00	0.09	3
Poland	Torun	53.0167	18.7779	26/09/17	11:00	03/10/17	11:00	9.93	4
Poland	Torun	53.0167	18.7779	02/10/17	10:00	09/10/17	11:00	0.0008	26
Poland	Warszawa	52.3016	20.9879	25/09/17	10:00	02/10/17	10:00	4.09	1
Poland	Warszawa	52.3016	20.9879	02/10/17	10:00	09/10/17	10:00	2.456	2
Poland	Wrocław	51.1060	17.0629	25/09/17	10:00	02/10/17	10:00	3.03	2
Poland	Wrocław	51.1060	17.0629	02/10/17	10:00	09/10/17	10:00	2.97	2
Poland	Zielona Gora	51.9435	15.5302	25/09/17	12:00	02/10/17	12:00	3.99	3
Poland	Zielona Gora	51.9435	15.5302	02/10/17	10:00	09/10/17	10:00	1.54	2

Country	Location	Latitude (decimal)	Longitude (decimal)	Start date	Start hour	End date	End hour	^{106}Ru (mBq·m^{-3})	± (%)
Portugal	Lisboa	38.7200	-9.1300	-	-	-	-	<LOD	
Romania	Alba Iulia	46.0780	23.5780	29/09/17	01:00	29/09/17	12:00	<LOD	
Romania	Alba Iulia	46.0780	23.5780	30/09/17	01:00	30/09/17	12:00	32.81	-
Romania	Alba Iulia	46.0780	23.5780	01/10/17	01:00	01/10/17	12:00	75.42	-
Romania	Alba Iulia	46.0780	23.5780	02/10/17	01:00	02/10/17	12:00	39.42	-
Romania	Alba Iulia	46.0780	23.5780	03/10/17	01:00	03/10/17	12:00	15.02	-
Romania	Alba Iulia	46.0780	23.5780	04/10/17	01:00	04/10/17	12:00	<LOD	
Romania	Alba Iulia	46.0780	23.5780	05/10/17	01:00	05/10/17	12:00	<LOD	
Romania	Arad	46.1910	21.3260	28/09/17	01:00	28/09/17	12:00	<LOD	
Romania	Arad	46.1910	21.3260	29/09/17	01:00	29/09/17	12:00	<LOD	
Romania	Arad	46.1910	21.3260	30/09/17	01:00	30/09/17	12:00	<LOD	
Romania	Arad	46.1910	21.3260	01/10/17	01:00	01/10/17	12:00	64.42	-
Romania	Arad	46.1910	21.3260	02/10/17	01:00	02/10/17	12:00	30.41	-
Romania	Arad	46.1910	21.3260	03/10/17	01:00	03/10/17	12:00	9.31	-
Romania	Arad	46.1910	21.3260	04/10/17	01:00	04/10/17	12:00	<LOD	
Romania	Arad	46.1910	21.3260	05/10/17	01:00	05/10/17	12:00	<LOD	
Romania	Babele	45.4320	25.4520	29/09/17	01:00	30/09/17	00:00	<LOD	
Romania	Babele	45.4320	25.4520	30/09/17	01:00	01/10/17	00:00	<LOD	
Romania	Babele	45.4320	25.4520	01/10/17	01:00	02/10/17	00:00	<LOD	
Romania	Babele	45.4320	25.4520	02/10/17	01:00	03/10/17	00:00	<LOD	
Romania	Babele	45.4320	25.4520	03/10/17	01:00	04/10/17	00:00	<LOD	
Romania	Babele	45.4320	25.4520	04/10/17	01:00	05/10/17	00:00	<LOD	
Romania	Babele	45.4320	25.4520	05/10/17	01:00	06/10/17	00:00	<LOD	
Romania	Bacau	46.5710	26.9240	29/09/17	01:00	29/09/17	12:00	<LOD	
Romania	Bacau	46.5710	26.9240	30/09/17	01:00	30/09/17	12:00	39.3	-
Romania	Bacau	46.5710	26.9240	01/10/17	01:00	01/10/17	12:00	24.31	-
Romania	Bacau	46.5710	26.9240	02/10/17	01:00	02/10/17	12:00	<LOD	
Romania	Bacau	46.5710	26.9240	03/10/17	01:00	03/10/17	12:00	<LOD	
Romania	Bacau	46.5710	26.9240	04/10/17	01:00	04/10/17	12:00	<LOD	
Romania	Bacau	46.5710	26.9240	05/10/17	01:00	05/10/17	12:00	<LOD	
Romania	Baia Mare	47.6540	23.5890	28/09/17	01:00	28/09/17	12:00	<LOD	
Romania	Baia Mare	47.6540	23.5890	29/09/17	01:00	29/09/17	12:00	<LOD	
Romania	Baia Mare	47.6540	23.5890	30/09/17	01:00	30/09/17	12:00	<LOD	
Romania	Baia Mare	47.6540	23.5890	01/10/17	01:00	01/10/17	12:00	47.47	-
Romania	Baia Mare	47.6540	23.5890	02/10/17	01:00	02/10/17	12:00	38.21	-
Romania	Baia Mare	47.6540	23.5890	03/10/17	01:00	03/10/17	12:00	24.6	-
Romania	Baia Mare	47.6540	23.5890	04/10/17	01:00	04/10/17	12:00	<LOD	
Romania	Baia Mare	47.6540	23.5890	05/10/17	01:00	05/10/17	12:00	< LOD	
Romania	Bechet	43.7820	23.9500	28/09/17	01:00	29/09/17	00:00	<LOD	

Country	Location	Latitude (decimal)	Longitude (decimal)	Start date	Start hour	End date	End hour	^{106}Ru (mBq·m^{-3})	± (%)
Romania	Bechet	43.7820	23.9500	29/09/17	01:00	30/09/17	00:00	66.6	-
Romania	Bechet	43.7820	23.9500	30/09/17	01:00	01/10/17	00:00	127.57	-
Romania	Bechet	43.7820	23.9500	01/10/17	01:00	02/10/17	00:00	18.1	-
Romania	Bechet	43.7820	23.9500	02/10/17	01:00	03/10/17	00:00	<LOD	
Romania	Bechet	43.7820	23.9500	03/10/17	01:00	04/10/17	00:00	<LOD	
Romania	Bechet	43.7820	23.9500	04/10/17	01:00	05/10/17	00:00	<LOD	
Romania	Botosani	47.7460	26.6670	29/09/17	01:00	29/09/17	12:00	<LOD	
Romania	Botosani	47.7460	26.6670	30/09/17	01:00	30/09/17	12:00	51.81	-
Romania	Botosani	47.7460	26.6670	01/10/17	01:00	01/10/17	12:00	<LOD	
Romania	Botosani	47.7460	26.6670	02/10/17	01:00	02/10/17	12:00	<LOD	
Romania	Botosani	47.7460	26.6670	03/10/17	01:00	03/10/17	12:00	<LOD	
Romania	Botosani	47.7460	26.6670	04/10/17	01:00	04/10/17	12:00	<LOD	
Romania	Botosani	47.7460	26.6670	05/10/17	01:00	05/10/17	12:00	<LOD	
Romania	Brasov	45.6560	25.6100	29/09/17	01:00	29/09/17	12:00	<LOD	
Romania	Brasov	45.6560	25.6100	30/09/17	01:00	30/09/17	12:00	113.03	-
Romania	Brasov	45.6560	25.6100	01/10/17	01:00	01/10/17	12:00	54.74	-
Romania	Brasov	45.6560	25.6100	02/10/17	01:00	02/10/17	12:00	17.44	-
Romania	Brasov	45.6560	25.6100	03/10/17	01:00	03/10/17	12:00	<LOD	
Romania	Brasov	45.6560	25.6100	04/10/17	01:00	04/10/17	12:00	<LOD	
Romania	Brasov	45.6560	25.6100	05/10/17	01:00	05/10/17	12:00	<LOD	
Romania	București	44.4310	26.1220	28/09/17	01:00	28/09/17	12:00	<LOD	
Romania	București	44.4310	26.1220	29/09/17	01:00	29/09/17	12:00	<LOD	
Romania	București	44.4310	26.1220	30/09/17	01:00	30/09/17	12:00	145	-
Romania	București	44.4310	26.1220	01/10/17	01:00	01/10/17	12:00	18.1	-
Romania	București	44.4310	26.1220	02/10/17	01:00	02/10/17	12:00	<LOD	
Romania	București	44.4310	26.1220	03/10/17	01:00	03/10/17	12:00	<LOD	
Romania	București	44.4310	26.1220	04/10/17	01:00	04/10/17	12:00	<LOD	
Romania	Buzau	45.1490	26.8240	29/09/17	01:00	29/09/17	12:00	<LOD	
Romania	Buzau	45.1490	26.8240	30/09/17	01:00	30/09/17	12:00	120.45	-
Romania	Buzau	45.1490	26.8240	01/10/17	01:00	01/10/17	12:00	<LOD	
Romania	Buzau	45.1490	26.8240	02/10/17	01:00	02/10/17	12:00	<LOD	
Romania	Buzau	45.1490	26.8240	03/10/17	01:00	03/10/17	12:00	<LOD	
Romania	Buzau	45.1490	26.8240	04/10/17	01:00	04/10/17	12:00	<LOD	
Romania	Buzau	45.1490	26.8240	05/10/17	01:00	05/10/17	12:00	<LOD	
Romania	Calarasi	44.2050	27.3350	29/09/17	01:00	29/09/17	12:00	38.01	-
Romania	Calarasi	44.2050	27.3350	30/09/17	01:00	30/09/17	12:00	86.81	-
Romania	Calarasi	44.2050	27.3350	01/10/17	01:00	01/10/17	12:00	<LOD	
Romania	Calarasi	44.2050	27.3350	02/10/17	01:00	02/10/17	12:00	<LOD	
Romania	Calarasi	44.2050	27.3350	03/10/17	01:00	03/10/17	12:00	<LOD	

Country	Location	Latitude (decimal)	Longitude (decimal)	Start date	Start hour	End date	End hour	^{106}Ru (mBq·m^{-3})	± (%)
Romania	Calarasi	44.2050	27.3350	04/10/17	01:00	04/10/17	12:00	<LOD	
Romania	Calarasi	44.2050	27.3350	05/10/17	01:00	05/10/17	12:00	<LOD	
Romania	Cernavodă	44.3490	28.0490	29/09/17	01:00	30/09/17	00:00	81.28	-
Romania	Cernavodă	44.3177	28.0523	30/09/17	01:00	01/10/17	00:00	47.23	-
Romania	Cernavodă	44.3490	28.0490	01/10/17	01:00	02/10/17	00:00	<LOD	
Romania	Cernavodă	44.3490	28.0490	02/10/17	01:00	03/10/17	00:00	<LOD	
Romania	Cernavodă	44.3490	28.0490	03/10/17	01:00	04/10/17	00:00	<LOD	
Romania	Cernavodă	44.3490	28.0490	04/10/17	01:00	05/10/17	00:00	<LOD	
Romania	Cernavodă	44.3490	28.0490	05/10/17	01:00	06/10/17	00:00	<LOD	
Romania	Cluj Napoca	46.7770	23.5990	29/09/17	01:00	30/09/17	00:00	<LOD	
Romania	Cluj Napoca	46.7770	23.5990	30/09/17	01:00	01/10/17	00:00	<LOD	
Romania	Cluj Napoca	46.7770	23.5990	01/10/17	01:00	02/10/17	00:00	29.08	-
Romania	Cluj Napoca	46.7770	23.5990	02/10/17	01:00	03/10/17	00:00	<LOD	
Romania	Cluj Napoca	46.7770	23.5990	03/10/17	01:00	04/10/17	00:00	<LOD	
Romania	Cluj Napoca	46.7770	23.5990	04/10/17	01:00	05/10/17	00:00	<LOD	
Romania	Cluj Napoca	46.7770	23.5990	05/10/17	01:00	06/10/17	00:00	<LOD	
Romania	Constanța	44.1730	28.6350	28/09/17	01:00	29/09/17	00:00	<LOD	
Romania	Constanța	44.1730	28.6350	29/09/17	01:00	30/09/17	00:00	88.1	-
Romania	Constanța	44.1730	28.6350	30/09/17	01:00	01/10/17	00:00	44.31	-
Romania	Constanța	44.1730	28.6350	01/10/17	01:00	02/10/17	00:00	<LOD	
Romania	Constanța	44.1730	28.6350	02/10/17	01:00	03/10/17	00:00	<LOD	
Romania	Constanța	44.1730	28.6350	03/10/17	01:00	04/10/17	00:00	<LOD	
Romania	Constanța	44.1730	28.6350	04/10/17	01:00	05/10/17	00:00	<LOD	
Romania	Craiova	44.3250	23.8140	28/09/17	01:00	29/09/17	00:00	<LOD	
Romania	Craiova	44.3250	23.8140	29/09/17	01:00	30/09/17	00:00	59.81	-
Romania	Craiova	44.3250	23.8140	30/09/17	01:00	01/10/17	00:00	106.27	-
Romania	Craiova	44.3250	23.8140	01/10/17	01:00	02/10/17	00:00	33.12	-
Romania	Craiova	44.3250	23.8140	02/10/17	01:00	03/10/17	00:00	<LOD	
Romania	Craiova	44.3250	23.8140	03/10/17	01:00	04/10/17	00:00	<LOD	
Romania	Craiova	44.3250	23.8140	04/10/17	01:00	05/10/17	00:00	<LOD	
Romania	Deva	45.8870	22.9070	29/09/17	01:00	29/09/17	12:00	<LOD	
Romania	Deva	45.8870	22.9070	30/09/17	01:00	30/09/17	12:00	<LOD	
Romania	Deva	45.8870	22.9070	01/10/17	01:00	01/10/17	12:00	35.8	-
Romania	Deva	45.8870	22.9070	02/10/17	01:00	02/10/17	12:00	22.7	-
Romania	Deva	45.8870	22.9070	03/10/17	01:00	03/10/17	12:00	<LOD	
Romania	Deva	45.8870	22.9070	04/10/17	01:00	04/10/17	12:00	<LOD	
Romania	Deva	45.8870	22.9070	05/10/17	01:00	05/10/17	12:00	<LOD	
Romania	Drobeta Turnu Severin	44.6350	22.6660	29/09/17	01:00	29/09/17	12:00	<LOD	
Romania	Drobeta Turnu Severin	44.6350	22.6660	30/09/17	01:00	30/09/17	12:00	123.5	-

Country	Location	Latitude (decimal)	Longitude (decimal)	Start date	Start hour	End date	End hour	^{106}Ru (mBq·m^{-3})	± (%)
Romania	Drobeta Turnu Severin	44.6350	22.6660	01/10/17	01:00	01/10/17	12:00	47.56	-
Romania	Drobeta Turnu Severin	44.6350	22.6660	02/10/17	01:00	02/10/17	12:00	<LOD	
Romania	Drobeta Turnu Severin	44.6350	22.6660	03/10/17	01:00	03/10/17	12:00	<LOD	
Romania	Drobeta Turnu Severin	44.6350	22.6660	04/10/17	01:00	04/10/17	12:00	<LOD	
Romania	Drobeta Turnu Severin	44.6350	22.6660	05/10/17	01:00	05/10/17	12:00	<LOD	
Romania	Fetesti	44.3833	27.8333	06/09/17	-	06/10/17	-	3.18	50
Romania	Focsani	45.7010	27.1880	29/09/17	01:00	29/09/17	12:00	15.17	-
Romania	Focsani	45.7010	27.1880	30/09/17	01:00	30/09/17	12:00	82.81	-
Romania	Focsani	45.7010	27.1880	01/10/17	01:00	01/10/17	12:00	24.22	-
Romania	Focsani	45.7010	27.1880	02/10/17	01:00	02/10/17	12:00	<LOD	
Romania	Focsani	45.7010	27.1880	03/10/17	01:00	03/10/17	12:00	<LOD	
Romania	Focsani	45.7010	27.1880	04/10/17	01:00	04/10/17	12:00	<LOD	
Romania	Focsani	45.7010	27.1880	05/10/17	01:00	05/10/17	12:00	<LOD	
Romania	Galati	45.4350	28.0390	29/09/17	01:00	29/09/17	12:00	35.94	-
Romania	Galati	45.4350	28.0390	30/09/17	01:00	30/09/17	12:00	37.38	-
Romania	Galati	45.4350	28.0390	01/10/17	01:00	01/10/17	12:00	<LOD	
Romania	Galati	45.4350	28.0390	02/10/17	01:00	02/10/17	12:00	<LOD	
Romania	Galati	45.4350	28.0390	03/10/17	01:00	03/10/17	12:00	<LOD	
Romania	Galati	45.4350	28.0390	04/10/17	01:00	04/10/17	12:00	<LOD	
Romania	Galati	45.4350	28.0390	05/10/17	01:00	05/10/17	12:00	<LOD	
Romania	Gherghina	44.3226	28.1819	05/09/17	-	05/10/17	-	3.39	37
Romania	Iași	47.1810	27.5830	28/09/17	01:00	29/09/17	00:00	<LOD	
Romania	Iași	47.1810	27.5830	29/09/17	01:00	30/09/17	00:00	80.75	-
Romania	Iași	47.1810	27.5830	30/09/17	01:00	01/10/17	00:00	65.8	-
Romania	Iași	47.1810	27.5830	01/10/17	01:00	02/10/17	00:00	<LOD	
Romania	Iași	47.1810	27.5830	02/10/17	01:00	02/10/17	00:00	<LOD	
Romania	Iași	47.1810	27.5830	03/10/17	01:00	03/10/17	00:00	<LOD	
Romania	Iași	47.1810	27.5830	04/10/17	01:00	05/10/17	00:00	<LOD	
Romania	Medgidia	44.2500	28.2833	07/09/17	-	07/10/17	-	3.39	48
Romania	Miercurea Ciuc	46.3680	25.8140	29/09/17	01:00	29/09/17	12:00	<LOD	
Romania	Miercurea Ciuc	46.3680	25.8140	30/09/17	01:00	30/09/17	12:00	61.76	-
Romania	Miercurea Ciuc	46.3680	25.8140	01/10/17	01:00	01/10/17	12:00	46.97	-
Romania	Miercurea Ciuc	46.3680	25.8140	02/10/17	01:00	02/10/17	12:00	<LOD	
Romania	Miercurea Ciuc	46.3680	25.8140	03/10/17	01:00	03/10/17	12:00	<LOD	
Romania	Miercurea Ciuc	46.3680	25.8140	04/10/17	01:00	04/10/17	12:00	<LOD	
Romania	Miercurea Ciuc	46.3680	25.8140	05/10/17	01:00	05/10/17	12:00	<LOD	
Romania	Mircea Voda	44.2833	28.1667	05/09/17	-	05/10/17	-	3.1	47
Romania	Oradea	47.0630	21.9180	29/09/17	01:00	29/09/17	12:00	<LOD	
Romania	Oradea	47.0630	21.9180	30/09/17	01:00	30/09/17	12:00	<LOD	

Country	Location	Latitude (decimal)	Longitude (decimal)	Start date	Start hour	End date	End hour	^{106}Ru (mBq·m^{-3})	± (%)
Romania	Oradea	47.0630	21.9180	01/10/17	01:00	01/10/17	12:00	75.06	-
Romania	Oradea	47.0630	21.9180	02/10/17	01:00	02/10/17	12:00	45.77	-
Romania	Oradea	47.0630	21.9180	03/10/17	01:00	03/10/17	12:00	<LOD	
Romania	Oradea	47.0630	21.9180	04/10/17	01:00	04/10/17	12:00	<LOD	
Romania	Oradea	47.0630	21.9180	05/10/17	01:00	05/10/17	12:00	<LOD	
Romania	Piatra Neamt	46.9490	26.3820	29/09/17	01:00	29/09/17	12:00	<LOD	
Romania	Piatra Neamt	46.9490	26.3820	30/09/17	01:00	30/09/17	12:00	31.73	-
Romania	Piatra Neamt	46.9490	26.3820	01/10/17	01:00	01/10/17	12:00	38.83	-
Romania	Piatra Neamt	46.9490	26.3820	02/10/17	01:00	02/10/17	12:00	<LOD	
Romania	Piatra Neamt	46.9490	26.3820	03/10/17	01:00	03/10/17	12:00	<LOD	
Romania	Piatra Neamt	46.9490	26.3820	04/10/17	01:00	04/10/17	12:00	<LOD	
Romania	Piatra Neamt	46.9490	26.3820	05/10/17	01:00	05/10/17	12:00	<LOD	
Romania	Ploiesti	44.9360	26.0360	29/09/17	01:00	29/09/17	12:00	<LOD	
Romania	Ploiesti	44.9360	26.0360	30/09/17	01:00	30/09/17	12:00	138.18	-
Romania	Ploiesti	44.9360	26.0360	01/10/17	01:00	01/10/17	12:00	46.07	-
Romania	Ploiesti	44.9360	26.0360	02/10/17	01:00	02/10/17	12:00	<LOD	
Romania	Ploiesti	44.9360	26.0360	03/10/17	01:00	03/10/17	12:00	<LOD	
Romania	Ploiesti	44.9360	26.0360	04/10/17	01:00	04/10/17	12:00	<LOD	
Romania	Ploiesti	44.9360	26.0360	05/10/17	01:00	05/10/17	12:00	<LOD	
Romania	Resita	45.2920	21.8920	29/09/17	01:00	29/09/17	12:00	<LOD	
Romania	Resita	45.2920	21.8920	30/09/17	01:00	30/09/17	12:00	50.36	-
Romania	Resita	45.2920	21.8920	01/10/17	01:00	01/10/17	12:00	44.42	-
Romania	Resita	45.2920	21.8920	02/10/17	01:00	02/10/17	12:00	<LOD	
Romania	Resita	45.2920	21.8920	03/10/17	01:00	03/10/17	12:00	<LOD	
Romania	Resita	45.2920	21.8920	04/10/17	01:00	04/10/17	12:00	<LOD	
Romania	Resita	45.2920	21.8920	05/10/17	01:00	05/10/17	12:00	<LOD	
Romania	Saligny	44.2833	28.0833	07/09/17	-	03/10/17	-	4.54	34
Romania	Satu Mare	47.7850	22.8840	29/09/17	01:00	29/09/17	12:00	<LOD	
Romania	Satu Mare	47.7850	22.8840	30/09/17	01:00	30/09/17	12:00	<LOD	
Romania	Satu Mare	47.7850	22.8840	01/10/17	01:00	01/10/17	12:00	35.35	-
Romania	Satu Mare	47.7850	22.8840	02/10/17	01:00	02/10/17	12:00	<LOD	
Romania	Satu Mare	47.7850	22.8840	03/10/17	01:00	03/10/17	12:00	<LOD	
Romania	Satu Mare	47.7850	22.8840	04/10/17	01:00	04/10/17	12:00	<LOD	
Romania	Satu Mare	47.7850	22.8840	05/10/17	01:00	05/10/17	12:00	<LOD	
Romania	Seimeni	44.4018	28.0876	06/09/17	-	04/10/17	-	5.34	29
Romania	Sf.Gheorghe - Tulcea	44.9040	29.6080	29/09/17	01:00	29/09/17	12:00	69.55	-
Romania	Sf.Gheorghe - Tulcea	44.9040	29.6080	30/09/17	01:00	30/09/17	12:00	34.45	-
Romania	Sf.Gheorghe - Tulcea	44.9040	29.6080	01/10/17	01:00	01/10/17	12:00	<LOD	
Romania	Sf.Gheorghe - Tulcea	44.9040	29.6080	02/10/17	01:00	02/10/17	12:00	<LOD	

Country	Location	Latitude (decimal)	Longitude (decimal)	Start date	Start hour	End date	End hour	^{106}Ru (mBq·m^{-3})	± (%)
Romania	Sf.Gheorghe - Tulcea	44.9040	29.6080	03/10/17	01:00	03/10/17	12:00	<LOD	
Romania	Sf.Gheorghe - Tulcea	44.9040	29.6080	04/10/17	01:00	04/10/17	12:00	<LOD	
Romania	Sf.Gheorghe - Tulcea	44.9040	29.6080	05/10/17	01:00	05/10/17	12:00	<LOD	
Romania	Sibiu	45.7880	24.1420	29/09/17	01:00	29/09/17	12:00	<LOD	
Romania	Sibiu	45.7880	24.1420	30/09/17	01:00	30/09/17	12:00	<LOD	
Romania	Sibiu	45.7880	24.1420	01/10/17	01:00	01/10/17	12:00	<LOD	
Romania	Sibiu	45.7880	24.1420	02/10/17	01:00	02/10/17	12:00	<LOD	
Romania	Sibiu	45.7880	24.1420	03/10/17	01:00	03/10/17	12:00	<LOD	
Romania	Sibiu	45.7880	24.1420	04/10/17	01:00	04/10/17	12:00	<LOD	
Romania	Sibiu	45.7880	24.1420	05/10/17	01:00	05/10/17	12:00	<LOD	
Romania	Slobozia	44.5700	27.3800	29/09/17	01:00	29/09/17	12:00	55.63	-
Romania	Slobozia	44.5700	27.3800	30/09/17	01:00	30/09/17	12:00	118.78	-
Romania	Slobozia	44.5700	27.3800	01/10/17	01:00	01/10/17	12:00	<LOD	
Romania	Slobozia	44.5700	27.3800	02/10/17	01:00	02/10/17	12:00	<LOD	
Romania	Slobozia	44.5700	27.3800	03/10/17	01:00	03/10/17	12:00	<LOD	
Romania	Slobozia	44.5700	27.3800	04/10/17	01:00	04/10/17	12:00	<LOD	
Romania	Slobozia	44.5700	27.3800	05/10/17	01:00	05/10/17	12:00	<LOD	
Romania	Suceava	47.6420	26.2580	29/09/17	01:00	29/09/17	12:00	<LOD	
Romania	Suceava	47.6420	26.2580	30/09/17	01:00	30/09/17	12:00	22.81	-
Romania	Suceava	47.6420	26.2580	01/10/17	01:00	01/10/17	12:00	52.28	-
Romania	Suceava	47.6420	26.2580	02/10/17	01:00	02/10/17	12:00	<LOD	
Romania	Suceava	47.6420	26.2580	03/10/17	01:00	03/10/17	12:00	<LOD	
Romania	Suceava	47.6420	26.2580	04/10/17	01:00	04/10/17	12:00	<LOD	
Romania	Suceava	47.6420	26.2580	05/10/17	01:00	05/10/17	12:00	<LOD	
Romania	Târgu Mures	46.5410	24.5650	29/09/17	01:00	29/09/17	12:00	<LOD	
Romania	Târgu Mures	46.5410	24.5650	30/09/17	01:00	30/09/17	12:00	<LOD	
Romania	Târgu Mures	46.5410	24.5650	01/10/17	01:00	01/10/17	12:00	42.33	-
Romania	Târgu Mures	46.5410	24.5650	02/10/17	01:00	02/10/17	12:00	<LOD	
Romania	Târgu Mures	46.5410	24.5650	03/10/17	01:00	03/10/17	12:00	<LOD	
Romania	Târgu Mures	46.5410	24.5650	04/10/17	01:00	04/10/17	12:00	<LOD	
Romania	Târgu Mures	46.5410	24.5650	05/10/17	01:00	05/10/17	12:00	<LOD	
Romania	Timisoara	45.7560	21.2370	29/09/17	01:00	29/09/17	12:00	<LOD	
Romania	Timisoara	45.7560	21.2370	30/09/17	01:00	30/09/17	12:00	30.03	-
Romania	Timisoara	45.7560	21.2370	01/10/17	01:00	01/10/17	12:00	82.88	-
Romania	Timisoara	45.7560	21.2370	02/10/17	01:00	02/10/17	12:00	31.99	-
Romania	Timisoara	45.7560	21.2370	03/10/17	01:00	03/10/17	12:00	<LOD	
Romania	Timisoara	45.7560	21.2370	04/10/17	01:00	04/10/17	12:00	<LOD	
Romania	Timisoara	45.7560	21.2370	05/10/17	01:00	05/10/17	12:00	<LOD	
Romania	Toaca	46.9753	25.9487	29/09/17	01:00	30/09/17	00:00	<LOD	

Country	Location	Latitude (decimal)	Longitude (decimal)	Start date	Start hour	End date	End hour	^{106}Ru (mBq·m^{-3})	± (%)
Romania	Toaca	46.9753	25.9487	30/09/17	01:00	01/10/17	00:00	58.28	-
Romania	Toaca	46.9753	25.9487	01/10/17	01:00	02/10/17	00:00	12.86	-
Romania	Toaca	46.9753	25.9487	02/10/17	01:00	03/10/17	00:00	12.9	-
Romania	Toaca	46.9753	25.9487	03/10/17	01:00	04/10/17	00:00	<LOD	
Romania	Toaca	46.9753	25.9487	04/10/17	01:00	05/10/17	00:00	<LOD	
Romania	Toaca	46.9753	25.9487	05/10/17	01:00	06/10/17	00:00	<LOD	
Romania	Topalu Bucureşti	44.4323	26.1063	06/09/17	-	06/10/17	-	2.94	22
Romania	Tulcea	45.1800	28.8050	29/09/17	01:00	29/09/17	12:00	50.01	-
Romania	Tulcea	45.1800	28.8050	30/09/17	01:00	30/09/17	12:00	82.57	-
Romania	Tulcea	45.1800	28.8050	01/10/17	01:00	01/10/17	12:00	<LOD	
Romania	Tulcea	45.1800	28.8050	02/10/17	01:00	02/10/17	12:00	<LOD	
Romania	Tulcea	45.1800	28.8050	03/10/17	01:00	03/10/17	12:00	<LOD	
Romania	Tulcea	45.1800	28.8050	04/10/17	01:00	04/10/17	12:00	<LOD	
Romania	Tulcea	45.1800	28.8050	05/10/17	01:00	05/10/17	12:00	<LOD	
Romania	Vaslui	46.6440	27.7400	29/09/17	01:00	29/09/17	12:00	44.22	-
Romania	Vaslui	46.6440	27.7400	30/09/17	01:00	30/09/17	12:00	132.77	-
Romania	Vaslui	46.6440	27.7400	01/10/17	01:00	01/10/17	12:00	21.79	-
Romania	Vaslui	46.6440	27.7400	02/10/17	01:00	02/10/17	12:00	<LOD	
Romania	Vaslui	46.6440	27.7400	03/10/17	01:00	03/10/17	12:00	<LOD	
Romania	Vaslui	46.6440	27.7400	04/10/17	01:00	04/10/17	12:00	<LOD	
Romania	Vaslui	46.6440	27.7400	05/10/17	01:00	05/10/17	12:00	<LOD	
Romania	Zimnicea	43.6660	25.3660	29/09/17	01:00	29/09/17	12:00	<LOD	
Romania	Zimnicea	43.6660	25.3660	30/09/17	01:00	30/09/17	12:00	176.09	-
Romania	Zimnicea	43.6660	25.3660	01/10/17	01:00	01/10/17	12:00	<LOD	
Romania	Zimnicea	43.6660	25.3660	02/10/17	01:00	02/10/17	12:00	<LOD	
Romania	Zimnicea	43.6660	25.3660	03/10/17	01:00	03/10/17	12:00	<LOD	
Romania	Zimnicea	43.6660	25.3660	04/10/17	01:00	04/10/17	12:00	<LOD	
Romania	Zimnicea	43.6660	25.3660	05/10/17	01:00	05/10/17	12:00	<LOD	
Russia	Argayash	55.4860	60.8750	26/09/17	-	01/10/17	-	46	-
Russia	Argayash	55.4860	60.8750	26/09/17	-	01/10/17	-	30.78	-
Russia	Argayash	55.4860	60.8750	26/09/17	-	01/10/17	-	21	-
Russia	Argayash	55.4860	60.8750	26/09/17	-	01/10/17	-	29.4	-
Russia	Arkhangelsk	64.5521	40.5203	25/09/17	-	06/10/17	-	<LOD	
Russia	Balakovo NPP	52.0880	47.9830	01/09/17	-	02/10/17	-	27.7	-
Russia	Balakovo NPP	52.0880	47.9830	01/09/17	-	02/10/17	-	33.2	-
Russia	Balakovo NPP	52.0880	47.9830	02/10/17	-	02/11/17	-	63.6	-
Russia	Bilibino NPP	68.0514	166.5401	09/10/17	-	12/10/17	-	<0.066	
Russia	Bolshaya Murta	56.9090	93.1206	04/10/17	-	05/10/17	-	0.0785	
Russia	Bolshaya Murta	56.9090	93.1206	06/10/17	-	07/10/17	-	0.1128	-

Country	Location	Latitude (decimal)	Longitude (decimal)	Start date	Start hour	End date	End hour	^{106}Ru (mBq·m^{-3})	± (%)
Russia	Dimitrovgrad NIIAR_facility	54.2210	49.3955	29/09/17	-	06/10/17	-	<LOD	
Russia	Kola NPP	67.4653	32.4811	28/09/17	-	05/10/17	-	19	-
Russia	Kola NPP	67.4653	32.4811	28/09/17	-	05/10/17	-	16.8	-
Russia	Kola NPP	67.4653	32.4811	01/10/17	-	31/10/17	-	<LOD	
Russia	Leningrad NPP	59.8307	29.0570	25/09/17	-	06/10/17	-	0.073	-
Russia	Leningrad NPP	59.8307	29.0570	01/10/17	-	31/10/17	-	<0.005	
Russia	Leningrad NPP	59.8697	29.0814	29/09/17	-	31/10/17	-	0.14	-
Russia	Novogornyy	55.6330	60.7870	26/09/17	-	01/10/17	-	18	-
Russia	Novogornyy	55.6330	60.7870	26/09/17	-	01/10/17	-	20.27	-
Russia	Rostov NPP2	47.6040	42.3739	29/09/17	-	13/10/17	-	4.41	-
Russia	Rostov NPP1	47.6040	42.3739	20/06/17	-	12/10/17	-	0.0532	-
Russia	Rostov NPP2	47.6040	42.3739	20/06/17	-	12/10/17	-	4.41	-
Russia	Rostov NPP Dubrovskoe	47.5000	42.1800	29/09/17	-	13/10/17	-	2.76	-
Russia	Rostov NPP Volgodonsk	47.5000	42.1800	20/06/17	-	13/11/17	-	3.17	-
Russia	Severodvinsk	64.5660	39.8500	25/09/17	-	06/10/17	-	<LOD	
Russia	Smolensk NPP	54.1658	33.2334	01/09/17	-	30/09/17	-	<LOD	
Russia	Smolensk NPP	54.1658	33.2334	01/10/17	-	31/10/17	-	<LOD	
Russia	Sosnovy Bor	59.8500	29.0090	01/10/17	-	31/10/17	-	<LOD	
Russia	Sukhobuzimsky	56.5142	93.2740	06/10/17	-	07/10/17	-	0.2076	-
Russia	Tsimlyansk	47.6300	42.1200	26/09/17	-	01/10/17	-	13.6	-
Russia	Tsimlyansk	47.6300	42.1200	26/09/17	-	01/10/17	-	19	-
Russia	Volgograd	48.7000	44.5000	26/09/17	-	01/10/17	-	19	-
Russia	Volgograd	48.7000	44.5000	26/09/17	-	01/10/17	-	13.6	-
San Marino	San Marino	43.9696	12.4802	02/10/17	00:00	02/10/17	23:59	13.47	39
Serbia	Beograd	44.7608	20.6000	03/10/17	07:00	04/10/17	07:00	5	20
Serbia	Beograd	44.7608	20.6000	04/10/17	07:00	05/10/17	07:00	< 0.2	
Serbia	Beograd	44.7608	20.6000	06/10/17	07:00	09/10/17	07:00	< 0.1	
Serbia	Beograd	44.7608	20.6000	09/10/17	07:00	10/10/17	07:00	< 0.2	
Serbia	Beograd	44.7608	20.6000	11/10/17	07:00	12/10/17	07:00	< 0.3	
Serbia	Institute Vinča 1	44.7608	20.6000	01/09/17	07:00	30/09/17	07:00	4.5	9
Serbia	Institute Vinča 1	44.7608	20.6000	29/09/17	07:00	02/10/17	07:00	40	8
Serbia	Institute Vinča 1	44.7608	20.6000	01/10/17	07:00	31/10/17	07:00	0.9	7
Serbia	Institute Vinča 2	44.7608	20.6000	01/09/17	07:00	30/09/17	07:00	5.2	15
Serbia	Institute Vinča 2	44.7608	20.6000	01/10/17	07:00	31/10/17	07:00	1.1	9
Serbia	Institute Vinča 3	44.7608	20.6000	01/09/17	07:00	30/09/17	07:00	7	14
Serbia	Institute Vinča 3	44.7608	20.6000	01/10/17	07:00	31/10/17	07:00	0.81	11
Serbia	Institute Vinča 4	44.7000	20.5000	01/09/17	07:00	30/09/17	07:00	< 0.013	
Serbia	Niš	43.3192	21.8961	01/09/17	07:00	30/09/17	07:00	< 0.008	
Serbia	Niš	43.3192	21.8961	01/10/17	07:00	31/10/17	07:00	0.047	13

Country	Location	Latitude (decimal)	Longitude (decimal)	Start date	Start hour	End date	End hour	^{106}Ru (mBq·m^{-3})	± (%)
Serbia	Palić	46.1237	19.7583	01/09/17	07:00	30/09/17	07:00	< 0.008	
Serbia	Palić	46.1237	19.7583	01/10/17	07:00	31/10/17	07:00	7.8	6
Serbia	Vranje	42.5333	21.9000	28/09/17	07:00	30/09/17	07:00	2.1	14
Serbia	Vranje	42.5333	21.9000	01/09/17	07:00	30/09/17	07:00	0.21	19
Serbia	Vranje	42.5333	21.9000	01/10/17	07:00	31/10/17	07:00	5.2	8
Serbia	Zaječar	43.9333	22.3000	27/09/17	07:00	29/09/17	07:00	< 0.2	
Serbia	Zaječar	43.9333	22.3000	01/09/17	07:00	30/09/17	07:00	< 0.03	
Serbia	Zaječar	43.9333	22.3000	01/10/17	07:00	31/10/17	07:00	6.9	6
Serbia	Zeleno Brdo	44.7869	20.5219	01/09/17	07:00	30/09/17	07:00	4.8	8
Serbia	Zeleno Brdo	44.7869	20.5219	02/10/17	07:00	03/10/17	07:00	18	25
Serbia	Zeleno Brdo	44.7869	20.5219	01/10/17	07:00	31/10/17	07:00	0.61	7
Serbia	Zlatibor	43.7333	19.7167	01/09/17	07:00	30/09/17	07:00	0.18	17
Serbia	Zlatibor	43.7333	19.7167	28/09/17	07:00	30/09/17	07:00	1	10
Serbia	Zlatibor	43.7333	19.7167	01/10/17	07:00	31/10/17	07:00	7	14
Slovakia	Bohunice NPP 1	48.4914	17.6774	27/09/17	09:00	04/10/17	15:00	10.52	4
Slovakia	Bohunice NPP 2	48.4914	17.6774	27/09/17	09:00	04/10/17	15:00	8.98	4
Slovakia	Bohunice NPP 3	48.4914	17.6774	27/09/17	09:00	04/10/17	15:00	9.8	4
Slovakia	Bohunice NPP 4	48.4914	17.6774	27/09/17	09:00	04/10/17	15:00	8.32	3
Slovakia	Bohunice NPP 5	48.4914	17.6774	27/09/17	09:00	04/10/17	15:00	10.99	4
Slovakia	Bohunice NPP 6	48.4914	17.6774	25/09/17	09:00	02/10/17	15:00	2.78	50
Slovakia	Bratislava	48.1439	17.1097	27/09/17	14:00	03/10/17	14:00	9.8	5
Slovakia	Bratislava	48.1439	17.1097	29/09/17	10:00	05/10/17	14:00	16	5
Slovakia	Bratislava	48.1439	17.1097	03/10/17	14:00	06/10/17	14:00	1.27	7
Slovakia	Bratislava	48.1439	17.1097	06/10/17	14:00	11/10/17	14:00	0.011	20
Slovakia	Červený Hrádok	48.2999	18.3833	27/09/17	09:00	04/10/17	15:00	4.89	7
Slovakia	Jaslovské Bohunice NPP 1	48.4773	17.6473	29/09/17	09:00	06/10/17	15:00	10.3	5
Slovakia	Jaslovské Bohunice NPP 2	48.4773	17.6473	29/09/17	09:00	06/10/17	15:00	9.46	6
Slovakia	Jaslovské Bohunice NPP 3	48.4773	17.6473	27/09/17	09:00	04/10/17	15:00	10.74	3
Slovakia	Kátlovce	48.5265	17.6111	27/09/17	09:00	04/10/17	15:00	9.83	3
Slovakia	Levice	48.2174	18.6000	27/09/17	09:00	04/10/17	15:00	3.67	7
Slovakia	Mochovce NPP	48.2697	18.4533	25/09/17	09:00	05/10/17	15:00	5.78	7
Slovakia	Nižná	49.3103	19.5211	27/09/17	09:00	04/10/17	15:00	9.06	3
Slovakia	Nový Tekov	48.2440	18.5166	27/09/17	09:00	04/10/17	15:00	3.99	7
Slovakia	Pečeňady	48.4822	17.7198	27/09/17	09:00	04/10/17	15:00	11.88	3
Slovakia	Trakovice	48.4397	17.7092	27/09/17	09:00	04/10/17	15:00	8.88	3
Slovakia	Tajná	48.2625	18.3617	27/09/17	09:00	04/10/17	15:00	4.23	7
Slovakia	Veľké Kostoľany 1	48.5110	17.7227	27/09/17	09:00	04/10/17	15:00	9.54	3
Slovakia	Veľké Kostoľany 2	48.5110	17.7227	27/09/17	09:00	04/10/17	15:00	9.76	3
Slovenia	Jareninski Vrh	46.6406	15.6958	01/09/17	-	30/09/17	-	1.5	-

25

Country	Location	Latitude (decimal)	Longitude (decimal)	Start date	Start hour	End date	End hour	^{106}Ru (mBq·m^{-3})	± (%)
Slovenia	Ljubljana	46.0558	14.5083	01/09/17	-	30/09/17	-	3.1	-
Slovenia	Ljubljana	46.0425	14.4875	02/10/17	11:50	04/10/17	10:30	37	5
Slovenia	Ljubljana	46.0425	14.4875	04/10/17	10:30	05/10/17	10:30	4	8
Slovenia	Ljubljana	46.0425	14.4875	05/10/17	10:30	06/10/17	10:30	3.3	6
Slovenia	Ljubljana	46.0425	14.4875	06/10/17	11:50	09/10/17	11:50	<0.03	
Spain	Barcelona	41.3800	2.1100	-	-	04/10/17	-	<LOD	
Spain	Caceres	39.4800	-6.3400	-	-	05/10/17	-	<LOD	
Spain	Madrid	40.4500	-3.7160	02/10/17	-	08/10/17	-	<LOD	
Spain	Sevilla	37.3600	-5.9800	-	-	04/10/17	-	<LOD	
Sweden	Gävle	60.6700	17.1900	26/09/17	10:10	29/09/17	11:45	<0.01	
Sweden	Gävle	60.6700	17.1900	29/09/17	11:45	03/10/17	05:00	4.07	4
Sweden	Gävle	60.6700	17.1900	29/09/17	11:45	03/10/17	05:00	0.001	40
Sweden	Gävle	60.6700	17.1900	03/10/17	05:00	06/10/17	08:00	<0.12	
Sweden	Kista	59.4020	17.9450	30/09/17	11:45	01/10/17	05:00	4.08	3
Sweden	Kista	59.4020	17.9450	01/10/17	05:00	03/10/17	03:45	16.63	3
Sweden	Kista	59.4020	17.9450	01/10/17	05:00	03/10/17	03:45	0.004	39
Sweden	Kiruna	67.8400	20.4200	25/09/17	10:40	02/10/17	05:02	<0.003	
Sweden	Kiruna	67.8400	20.4200	29/09/17	08:00	02/10/17	08:00	<0.11	
Sweden	Kiruna	67.8400	20.4200	02/10/17	05:02	06/10/17	08:47	0.092	7
Sweden	Ljungbyhed	56.0800	13.2200	25/09/17	06:35	29/09/17	06:10	<0.004	
Sweden	Ljungbyhed	56.0800	13.2200	29/09/17	06:10	02/10/17	06:50	0.98	4
Sweden	Stockholm	59.3900	17.9600	29/09/17	15:44	30/09/17	19:44	<0.034	
Sweden	Stockholm	59.3900	17.9600	30/09/17	19:44	01/10/17	23:44	7.59	5
Sweden	Stockholm	59.3900	17.9600	01/10/17	23:44	03/10/17	03:44	16.7	4
Sweden	Stockholm	59.3900	17.9600	01/10/17	23:44	03/10/17	03:44	0.004	39
Sweden	Stockholm	59.3900	17.9600	03/10/17	03:44	04/10/17	07:44	<0.025	
Sweden	Stockholm	59.3900	17.9600	04/10/17	07:44	05/10/17	11:44	<0.044	
Sweden	Stockholm (SEP63)**	59.3900	17.9600	30/09/17	08:42	01/10/17	08:42	0.039	51
Sweden	Stockholm (SEP63)**	59.3900	17.9600	01/10/17	08:42	02/10/17	08:42	20.58	4
Sweden	Stockholm (SEP63)**	59.3900	17.9600	01/10/17	08:42	02/10/17	08:42	0.0047	30
Sweden	Stockholm (SEP63)**	59.3900	17.9600	02/10/17	08:42	03/10/17	08:42	11.89	4
Sweden	Stockholm (SEP63)**	59.3900	17.9600	02/10/17	08:42	03/10/17	08:42	0.0048	4
Sweden	Umeå	63.8500	20.3400	25/09/17	11:01	02/10/17	08:41	<0.005	
Sweden	Umeå	63.8500	20.3400	29/09/17	08:00	02/10/17	08:00	<0.09	
Sweden	Umeå	63.8500	20.3400	02/10/17	08:41	06/10/17	05:10	0.621	5
Sweden	Visby	57.6150	18.3210	25/09/17	06:00	28/09/17	06:00	<0.01	
Sweden	Visby	57.6150	18.3210	28/09/17	06:00	02/10/17	06:30	5.87	4
Sweden	Visby	57.6150	18.3210	28/09/17	06:00	02/10/17	06:30	0.0014	20
Sweden	Visby	57.6150	18.3210	02/10/17	06:30	05/10/17	08:10	5.28	4

Country	Location	Latitude (decimal)	Longitude (decimal)	Start date	Start hour	End date	End hour	^{106}Ru (mBq·m^{-3})	± (%)
Switzerland	Bern	46.9160	7.3500	25/09/17	08:00	02/10/17	08:00	< 0.02	
Switzerland	Cadenazzo	46.1602	8.9345	18/09/17	06:12	25/09/17	05:50	<0.0031	
Switzerland	Cadenazzo	46.1602	8.9345	25/09/17	05:50	02/10/17	06:45	0.0503	15
Switzerland	Cadenazzo	46.1602	8.9345	02/10/17	06:45	03/10/17	09:12	1.872	11
Switzerland	Cadenazzo	46.1602	8.9345	03/10/17	09:21	04/10/17	11:56	0.481	12
Switzerland	Cadenazzo	46.1602	8.9345	04/10/17	12:02	05/10/17	13:50	0.467	12
Switzerland	Cadenazzo	46.1602	8.9345	05/10/17	13:56	06/10/17	14:07	0.315	12
Switzerland	Cadenazzo	46.1602	8.9345	06/10/17	14:07	09/10/17	06:30	<0.0577	
Switzerland	Cadenazzo	46.1602	8.9345	09/10/17	06:36	16/10/17	06:01	<0.0029	
Switzerland	CERN	46.2289	6.0559	18/09/17	08:48	25/09/17	08:52	<0.0019	
Switzerland	CERN	46.2289	6.0559	25/09/17	08:52	02/10/17	12:24	<0.0053	
Switzerland	CERN	46.2289	6.0559	02/10/17	12:24	04/10/17	12:32	<0.0107	
Switzerland	CERN	46.2289	6.0559	04/10/17	12:32	09/10/17	13:20	<0.0046	
Switzerland	CERN	46.2289	6.0559	09/10/17	13:10	16/10/17	13:12	<0.0029	
Switzerland	Güttingen	47.6016	9.2799	18/09/17	11:05	25/09/17	11:05	<0.0027	
Switzerland	Güttingen	47.6016	9.2799	25/09/17	11:10	02/10/17	10:45	<0.0037	
Switzerland	Güttingen	47.6016	9.2799	02/10/17	10:50	03/10/17	10:15	<0.0257	
Switzerland	Güttingen	47.6010	9.2790	03/10/17	10:20	04/10/17	16:20	<0.0181	
Switzerland	Güttingen	47.6010	9.2790	04/10/17	16:20	09/10/17	11:05	<0.0031	
Switzerland	Güttingen	47.6010	9.2790	09/10/17	11:10	16/10/17	11:10	<0.0031	
Switzerland	Jungfraujoch	46.5470	7.9830	22/09/17	17:42	29/09/17	17:42	<0.0521	
Switzerland	Jungfraujoch	46.5470	7.9830	29/09/17	17:42	06/10/17	17:42	<0.0404	
Switzerland	Jungfraujoch	46.5470	7.9830	06/10/17	17:42	27/10/17	17:42	<0.0163	
Switzerland	Klingnau	47.5940	8.2240	20/09/17	06:15	27/09/17	05:30	<0.004	
Switzerland	Klingnau	47.5940	8.2240	27/09/17	05:35	04/10/17	05:25	<0.0036	
Switzerland	Klingnau	47.5940	8.2240	04/10/17	05:30	11/10/17	05:40	<0.003	
Switzerland	Liebefeld	46.9296	7.4228	25/09/17	07:56	02/10/17	08:00	<0.0053	
Switzerland	Liebefeld	46.9296	7.4228	02/10/17	08:00	03/10/17	06:25	<0.0704	
Switzerland	Liebefeld	46.9296	7.4228	03/10/17	06:30	04/10/17	07:32	<0.057	
Switzerland	Liebefeld	46.9296	7.4228	04/10/17	07:37	09/10/17	08:29	<0.009	
Switzerland	Liebefeld	46.9296	7.4228	09/10/17	08:33	16/10/17	08:09	<0.0023	
Switzerland	Posieux	46.7680	7.1000	20/09/17	04:55	27/09/17	05:00	<0.0036	
Switzerland	Posieux	46.7680	7.1000	27/09/17	05:00	04/10/17	05:00	<0.0026	
Switzerland	Posieux	46.7680	7.1000	04/10/17	05:00	11/10/17	05:00	<0.003	
UK	Chilton	51.5747	-1.3188	02/10/17	11:00	09/10/17	09:40	<0.034	
UK	Glasgow	55.8625	-4.3450	28/09/17	08:15	09/10/17	10:40	<0.021	
Ukraine	Ahronomiya	47.7681	31.3114	27/09/17	-	04/10/17	-	17	
Ukraine	Arbunzynka	47.9079	31.3151	26/09/17	-	03/10/17	-	29	
Ukraine	Baryshivka	50.3507	31.3189	29/09/17	-	03/10/17	-	13.9	-

Country	Location	Latitude (decimal)	Longitude (decimal)	Start date	Start hour	End date	End hour	^{106}Ru (mBq·m^{-3})	± (%)
Ukraine	Bil′s′ka Volya	51.4384	25.8159	28/09/17	06:50	06/10/17	06:45	1.02	5
Ukraine	Buz'ke	47.6036	31.2061	27/09/17	-	04/10/17	-	24	-
Ukraine	Chernobyl	51.2763	30.2219	29/09/17	-	03/10/17	-	2.5	-
Ukraine	Chtchors	51.8159	31.9582	29/09/17	-	01/10/17	-	0.1	-
Ukraine	Ivanivka	47.4807	34.7565	28/09/17	-	05/10/17	-	1.3	-
Ukraine	Kamianka Dniprovska	47.4863	34.4169	25/09/17	-	02/10/17	-	30	-
Ukraine	Khmelnitsky NPP	50.3024	26.6522	29/09/17	-	03/10/17	-	1.4	-
Ukraine	Kostyukhnivka	51.3499	25.7634	28/09/17	07:20	10/10/17	10:20	0.689	6
Ukraine	Kyiv	50.4501	30.5234	28/09/17	-	30/09/17	-	2.2	14
Ukraine	Kyiv	50.4501	30.5234	29/09/17	-	03/10/17	-	2.2	-
Ukraine	Lyubakhy	51.3743	26.0286	29/09/17	06:55	06/10/17	07:35	1.20	5
Ukraine	Manevychi	51.2856	25.5242	28/09/17	10:50	10/10/17	07:37	0.489	8
Ukraine	Nikopol	47.5567	34.4019	28/09/17	-	05/10/17	-	15	-
Ukraine	Novovodyane	47.4349	34.6822	25/09/17	-	02/10/17	-	36	-
Ukraine	Odesa	46.3846	30.7433	28/09/17	-	30/09/17	-	45	16
Ukraine	Polytsi	51.2581	26.0650	28/09/17	12:05	06/10/17	08:45	1.14	7
Ukraine	Rakhiv	48.0552	24.2135	27/09/17	-	29/09/17	-	2.6	-
Ukraine	Rivne NPP 1	51.3281	25.8898	28/09/17	07:40	06/10/17	06:55	1.19	5
Ukraine	Rivne NPP 2	51.3219	25.8815	28/09/17	07:15	06/10/17	06:45	1.06	5
Ukraine	Rivne NPP Heliport	51.3581	25.9194	29/09/17	06:30	06/10/17	07:13	1.39	5
Ukraine	Rivne NPP Heliport	51.3581	25.9194	06/10/17	07:13	11/10/17	07:10	0.0028	62
Ukraine	Rivne NPP Pump Station	51.3174	25.8773	28/09/17	08:25	06/10/17	06:35	1.13	6
Ukraine	Ryabokoneve	48.1063	31.2831	26/09/17	-	03/10/17	-	14	-
Ukraine	Sopachiv	51.4110	25.8912	28/09/17	06:20	06/10/17	06:18	0.953	5
Ukraine	South Ukraine NPP	47.8209	31.1862	22/09/17	-	29/09/17	-	3.9	-
Ukraine	South Ukraine NPP	47.8197	31.2238	28/09/17	-	05/10/17	-	24	-
Ukraine	South Ukraine NPP	47.8167	31.2167	29/09/17	-	03/10/17	-	29	-
Ukraine	Staryy Chartoryys′k	51.2289	25.8880	28/09/17	10:05	10/10/17	06:56	0.725	8
Ukraine	Sukhovolya	51.3413	25.9667	29/09/17	07:15	06/10/17	07:50	1.26	6
Ukraine	Tokmak	47.2500	35.7108	26/09/17	-	03/10/17	-	36	-
Ukraine	Varash	51.3363	25.8548	28/09/17	06:15	04/10/17	12:15	1.23	5
Ukraine	Varash	51.3363	25.8548	04/10/17	12:15	06/10/17	07:40	0.041	74
Ukraine	Velyka Vedmezhka	51.3079	25.7994	28/09/17	07:45	10/10/17	09:50	0.646	6
Ukraine	Velykyy Zholudsk	51.3107	26.0933	29/09/17	08:05	06/10/17	08:55	1.05	6
Ukraine	Vodyane	47.4819	34.5042	27/09/17	-	04/10/17	-	27	-
Ukraine	Volya	47.8035	30.8883	28/09/17	-	05/10/17	-	24	-
Ukraine	Yaroshivka	48.8047	31.2596	26/09/17	-	03/10/17	-	23	-
Ukraine	Zabolottya	51.3225	25.9141	28/09/17	08:05	06/10/17	07:20	0.914	8
Ukraine	Zaporizhzhya NPP	47.5047	34.5853	29/09/17	-	03/10/17	-	13	-

Country	Location	Latitude (decimal)	Longitude (decimal)	Start date	Start hour	End date	End hour	^{106}Ru (mBq·m^{-3})	± (%)
Ukraine	Zaporizhzhya NPP	47.4814	34.5723	26/09/17	-	03/10/17	-	40	-
Ukraine	Zaporizhzhya NPP	47.4998	34.5705	25/09/17	-	02/10/17	-	23	-
Ukraine	Zaporizhzhya NPP	47.5147	34.5945	25/09/17	-	02/10/17	-	18	-
Ukraine	Zaporizhzhya NPP	47.4919	34.6370	26/09/17	-	03/10/17	-	27	-
Ukraine	Zaporizhzhya NPP	47.5221	34.6552	04/10/17	-	05/10/17	-	30	-

All time stamps are unified to UTC.
Other data from Monaco, Malta, and Turkey exist but are not publicly available.
LOD: Limit of Detection
***:** Data published in (1)
******: Data for Sweden from the IMS network have been published in (2)
"–" or blank cell: Information not provided

Table S2: Airborne ^{103}Ru activity concentrations (mBq·m^{-3}) and ^{103}Ru/^{106}Ru isotopic ratio. Results are usually with 2σ. Uncertainty in %.

Country	Location	Latitude (decimal)	Longitude (decimal)	Start sampling	End sampling	^{103}Ru (mBq·m^{-3})	± (%)	^{103}Ru/^{106}Ru
Austria	Alt Prerau	48.7964	16.4753	25/09/17	02/10/17	0.0030	43	$2.70\cdot10^{-4}$
Austria	Klagenfurt	46.6484	14.3184	25/09/17	02/10/17	0.0020	49	$4.08\cdot10^{-4}$
Austria	Retz	48.7549	15.9506	25/09/17	03/10/17	0.0030	44	$2.48\cdot10^{-4}$
Austria	Straß in der Steiermark	46.7259	15.6248	25/09/17	03/10/17	0.0030	21	$3.16\cdot10^{-4}$
Austria	Vienna	48.2345	16.4175	28/09/17	04/10/17	0.0073	30	$3.37\cdot10^{-4}$
Czech Rep.	Praha	50.0667	14.4500	26/09/17	03/10/17	0.00062	30	$1.0\cdot10^{-4}$
Czech Rep.	Hradec Králové	50.2453	15.8696	26/09/17	03/10/17	0.0026	30	$2.36\cdot10^{-4}$
Czech Rep.	Ústí nad Labem	50.6667	14.0333	26/09/17	04/10/17	0.0012	30	$2.81\cdot10^{-4}$
Poland	Krakow	50.0660	19.9660	25/09/17	02/10/17	0.00085	26	$5.09\cdot10^{-4}$
Poland	Krakow	50.0660	19.9660	02/10/17	09/10/17	0.0001	20	$2.47\cdot10^{-4}$
Poland	Lublin	51.2610	22.5127	25/09/17	02/10/17	0.00039	95	$0.55\cdot10^{-4}$
Poland	Torun	53.0167	18.7779	26/09/17	03/10/17	0.00084	26	$0.85\cdot10^{-4}$
Sweden	Gävle	60.6700	17.1900	29/09/17	03/10/17	0.0010	40	$2.46\cdot10^{-4}$
Sweden	Kista	59.4020	17.9450	01/10/17	03/10/17	0.0040	39	$2.41\cdot10^{-4}$
Sweden	Stockholm	59.3900	17.9600	01/10/17	03/10/17	0.0040	39	$2.77\cdot10^{-4}$
Sweden	Stockholm (SEP63)*	59.3900	17.9600	01/10/17	02/10/17	0.0047	30	$2.41\cdot10^{-4}$
Sweden	Stockholm (SEP63)*	59.3900	17.9600	02/10/17	03/10/17	0.0048	4	$4.90\cdot10^{-4}$
Sweden	Visby	57.6150	18.3210	28/09/17	02/10/17	0.0014	20	$2.38\cdot10^{-4}$

*: data from the IMS network have been published in (2)

Table S3: Dry + wet fallout/deposition of ^{106}Ru (Bq·m^{-2}) and ^{106}Ru activity concentrations in rainwater (Bq·L^{-1}). Results are usually given with 2σ. Uncertainty in %.

Country	Location	Latitude (decimal)	Longitude (decimal)	Type of deposition	Start date	End date	^{106}Ru	± (%)	Unit
Austria	Linz	48.2675	14.2800	Rain water	04/10/17	05/10/17	<1.0		Bq·m^{-2}
Austria	Linz	48.2675	14.2800	Rain water	01/09/17	02/10/17	<0.12		Bq·m^{-2}
Austria	Linz	48.2675	14.2800	Rain water	02/10/17	04/10/17	0.50	19	Bq·m^{-2}
Austria	Vienna	48.2561	16.4828	Dry + wet	03/10/17	05/10/17	5.0	47	Bq·m^{-2}
Austria	Vienna	48.2561	16.4828	Rain water	05/10/17	06/10/17	<1.1		Bq·m^{-2}
Czech Rep.	České Budějovice	48.9667	14.4667	Rain water	29/09/17	03/10/17	<1.0		Bq·m^{-2}
Czech Rep.	Hradec Kralove	50.2453	15.8696	Rain water	02/10/17	03/10/17	9.0	20	Bq·m^{-2}
Czech Rep.	Hradec Kralove	50.2453	15.8696	Dry + wet	03/10/17	04/10/17	<1.1		Bq·m^{-2}
Czech Rep.	Hradec Kralove	50.2453	15.8696	Rain water	04/10/17	05/10/17	<1.2		Bq·m^{-2}
Czech Rep.	Ostrava	49.8333	18.2833	Rain water	02/10/17	03/10/17	40.0	15	Bq·m^{-2}
Czech Rep.	Praha	50.0670	14.4500	Rain water	02/10/17	03/10/17	<1.6		Bq·m^{-2}
Czech Rep.	Praha	50.0670	14.4500	Rain water	29/09/17	04/10/17	<1.1		Bq·m^{-2}
Finland	Böle	60.3711	26.3934	Dry + wet	28/09/17	28/12/17	72.0	-	Bq·m^{-2}
Finland	Helsinki	60.1654	24.9411	Dry + wet	02/10/17	06/11/17	66.0	-	Bq·m^{-2}
Finland	Helsinki	60.1654	24.9411	Dry + wet	02/10/17	02/01/18	56.0	-	Bq·m^{-2}
Finland	Imatra	61.1891	28.7595	Dry + wet	02/10/17	02/01/18	5.8	-	Bq·m^{-2}
Finland	Kajaani	64.2186	27.7351	Dry + wet	02/10/17	02/01/18	2.8	-	Bq·m^{-2}
Finland	Keitala	60.4219	26.3659	Dry + wet	28/09/17	28/12/17	79.0	-	Bq·m^{-2}
Finland	Kotka	60.4940	26.9006	Dry + wet	03/07/17	02/10/17	27.0	-	Bq·m^{-2}
Finland	Kuopio	62.8921	27.6715	Dry + wet	02/10/17	02/01/18	9.7	-	Bq·m^{-2}
Finland	Loviisa	60.4532	26.2197	Dry + wet	28/09/17	31/10/17	87.0	-	Bq·m^{-2}
Finland	Olkiluoto NPP	61.2428	21.4302	Dry + wet	27/09/17	25/10/17	38.0	-	Bq·m^{-2}
Finland	Rovaniemi	66.4894	25.6842	Dry + wet	02/10/17	28/11/17	1.9	-	Bq·m^{-2}
Finland	Sodankyla	67.4136	26.5910	Dry + wet	02/10/17	02/01/18	5.3	-	Bq·m^{-2}
Finland	Smoltti	60.3741	26.3487	Dry + wet	28/09/17	31/10/17	79.0	-	Bq·m^{-2}
Germany	Hanover	52.3817	9.7179	Rain water	20/10/17	20/10/17	<0.05		Bq·L^{-1}
Hungary	Budapest *	47.48910	18.95370	Dry + wet	25/09/17	02/10/17	<2.1		Bq·m^{-2}
Hungary	Budapest *	47.48910	18.95370	Dry + wet	02/10/17	09/10/17	11.3	19	Bq·m^{-2}
Hungary	Budapest *	47.48910	18.95370	Dry + wet	09/10/17	16/10/17	<2.5		Bq·m^{-2}
Hungary	Budapest *	47.48910	18.95370	Dry + wet	04/09/17	02/10/17	<2.8		Bq·m^{-2}
Hungary	Budapest *	47.48910	18.95370	Dry + wet	02/10/17	06/11/17	11.3	13	Bq·m^{-2}
Italy	Udine	46.0788	13.2316	Dry + wet	01/09/17	30/09/17	1.14	22	Bq·m^{-2}
Italy	Udine	46.0633	13.2358	Dry + wet	01/10/17	31/10/17	6.69	5	Bq·m^{-2}
Italy	Udine	46.0633	13.2358	Dry + wet	01/11/17	30/11/17	0.757	38	Bq·m^{-2}
Italy	Udine	46.0633	13.2358	Dry + wet	01/12/17	31/12/17	0.19	45	Bq·m^{-2}
Italy	Udine	46.0633	13.2358	Dry + wet	01/01/18	31/01/18	0.099	40	Bq·m^{-2}
Italy	Udine	46.0633	13.2358	Dry + wet	01/02/18	28/02/18	0.134	28	Bq·m^{-2}
Norway	Østerås	59.9400	10.6000	Dry + wet	08/09/17*	02/10/17	22	-	Bq·m^{-2}
Norway	Østerås	59.9400	10.6000	Rain water	08/09/17	02/10/17	0.222	-	Bq·L^{-1}
Poland	Gdynia	54.5207	18.5462	Dry + wet	01/10/17	31/10/17	<0.9		Bq·m^{-2}
Poland	Krakow	50.0902	19.8886	Dry + wet	02/10/17	04/10/17	0.912	3	Bq·L^{-1}
Poland	Krakow	50.0902	19.8886	Dry + wet	02/10/17	04/10/17	9.7	3	Bq·m^{-2}
Poland	Mikolajki	53.7904	21.5897	Dry + wet	02/10/17	03/10/17	5.7	9	Bq·m^{-2}
Poland	Poznan	52.4192	16.8770	Dry + wet	01/10/17	02/10/17	12.1	1	Bq·m^{-2}
Poland	Warszawa	52.2809	20.9614	Dry + wet	02/10/17	03/10/17	14.5	8	Bq·m^{-2}
Poland	Warszawa	52.2809	20.9614	Dry + wet	03/10/17	04/10/17	3.0	12	Bq·m^{-2}

Country	Location	Latitude (decimal)	Longitude (decimal)	Type of deposition	Start date	End date	^{106}Ru	± (%)	Unit
Poland	Wlodawa	51.5542	23.5305	Dry + wet	03/10/17	04/10/17	19.7	8	Bq·m^{-2}
Poland	Whole country			Dry + wet	01/09/17	30/09/17	0.24	8	Bq·m^{-2}
Poland	Whole country			Dry + wet	01/10/17	31/10/17	6.32	2	Bq·m^{-2}
Poland	Whole country			Dry + wet	01/11/17	30/11/17	0.12	11	Bq·m^{-2}
Poland	Whole country			Dry + wet	01/12/17	31/12/17	0.16	11	Bq·m^{-2}
Russia	Argayash	55.4860	60.8750	Dry + wet	25/09/17	26/09/17	115.5	-	Bq·m^{-2}
Russia	Argayash	55.4860	60.8750	Dry + wet	25/09/17	26/09/17	13.9	-	Bq·m^{-2}
Russia	Argayash	55.4860	60.8750	Dry + wet	25/09/17	26/09/17	15.6	-	Bq·m^{-2}
Russia	Argayash	55.4860	60.8750	Dry + wet	25/09/17	26/09/17	32.6	-	Bq·m^{-2}
Russia	Argayash	55.4860	60.8750	Dry + wet	26/09/17	27/09/17	112.0	-	Bq·m^{-2}
Russia	Argayash	55.4860	60.8750	Dry + wet	26/09/17	27/09/17	11.0	-	Bq·m^{-2}
Russia	Argayash	55.4860	60.8750	Dry + wet	26/09/17	27/09/17	109.7	-	Bq·m^{-2}
Russia	Argayash	55.4860	60.8750	Dry + wet	26/09/17	27/09/17	24.6	-	Bq·m^{-2}
Russia	Bugulma	54.5360	52.7980	Dry + wet	26/09/17	27/09/17	16.0	-	Bq·m^{-2}
Russia	Bugulma	54.5360	52.7980	Dry + wet	27/09/17	28/09/17	30.0	-	Bq·m^{-2}
Russia	Bugulma	54.5360	52.7980	Dry + wet	26/09/17	27/09/17	20.9	-	Bq·m^{-2}
Russia	Bugulma	54.5360	52.7980	Dry + wet	27/09/17	28/09/17	20.8	13	Bq·m^{-2}
Russia	Bugulma	54.5360	52.7980	Dry + wet	26/09/17	27/09/17	11.3	13	Bq·m^{-2}
Russia	Dema-Oufa	54.7140	55.8770	Dry + wet	26/09/17	27/09/17	17.0	-	Bq·m^{-2}
Russia	Khudaiberdinskiy	55.6110	60.9240	Dry + wet	27/09/17	28/09/17	74.0	-	Bq·m^{-2}
Russia	Khudaiberdinskiy	55.6110	60.9240	Dry + wet	29/09/17	30/09/17	24.7	-	Bq·m^{-2}
Russia	Khudaiberdinskiy	55.6110	60.9240	Dry + wet	29/09/17	30/09/17	54.0	-	Bq·m^{-2}
Russia	Khudaiberdinskiy	55.6110	60.9240	Dry + wet	27/09/17	28/09/17	19.8	-	Bq·m^{-2}
Russia	Khudaiberdinskiy	55.6110	60.9240	Dry + wet	27/09/17	28/09/17	9.1	-	Bq·m^{-2}
Russia	Khudaiberdinskiy	55.6110	60.9240	Dry + wet	29/09/17	30/09/17	230.9	-	Bq·m^{-2}
Russia	Khudaiberdinskiy	55.6110	60.9240	Dry + wet	26/09/17	27/09/17	8.6	-	Bq·m^{-2}
Russia	Kyshtym	55.7142	60.8445	Dry + wet	23/09/17	24/09/17	62.0	-	Bq·m^{-2}
Russia	Kyshtym	55.7142	60.8445	Dry + wet	23/09/17	24/09/17	50.7	-	Bq·m^{-2}
Russia	Kyshtym	55.7142	60.8445	Dry + wet	23/09/17	24/09/17	17.6	-	Bq·m^{-2}
Russia	Metlino	55.7890	60.9800	Dry + wet	26/09/17	27/09/17	343.3	-	Bq·m^{-2}
Russia	Metlino	55.7890	60.9800	Dry + wet	26/09/17	27/09/17	330.0	-	Bq·m^{-2}
Russia	Metlino	55.7890	60.9800	Dry + wet	26/09/17	27/09/17	37.1	-	Bq·m^{-2}
Russia	Metlino	55.7890	60.9800	Dry + wet	26/09/17	27/09/17	79.6	-	Bq·m^{-2}
Russia	Morozovsk	48.3500	41.8700	Dry + wet	28/09/17	29/09/17	17.1	-	Bq·m^{-2}
Russia	Novogornyy	55.6330	60.7870	Dry + wet	26/09/17	27/09/17	203.0	-	Bq·m^{-2}
Russia	Novogornyy	55.6330	60.7870	Dry + wet	26/09/17	27/09/17	184.8	-	Bq·m^{-2}
Russia	Novogornyy	55.6330	60.7870	Dry + wet	26/09/17	27/09/17	52.1	-	Bq·m^{-2}
Russia	Novogornyy	55.6330	60.7870	Dry + wet	26/09/17	27/09/17	30.9	-	Bq·m^{-2}
Russia	Novogornyy	55.6330	60.7870	Dry + wet	29/09/17	30/09/17	28.0	-	Bq·m^{-2}
Russia	Novogornyy	55.6330	60.7870	Dry + wet	27/09/17	28/09/17	14.7	-	Bq·m^{-2}
Russia	Novogornyy	55.6330	60.7870	Dry + wet	27/09/17	28/09/17	7.9	-	Bq·m^{-2}
Serbia	Kragujevac	44.0100	20.9100	Dry + wet	01/09/17	30/09/17	<0.8		Bq·m^{-2}
Serbia	Kragujevac	44.0100	20.9100	Dry + wet	01/10/17	31/10/17	<0.3		Bq·m^{-2}
Serbia	Niš	43.3192	21.8961	Dry + wet	01/09/17	30/09/17	<1.0		Bq·m^{-2}
Serbia	Niš	43.3192	21.8961	Dry + wet	01/10/17	31/10/17	<0.3		Bq·m^{-2}
Serbia	Novi Sad	45.2671	19.8335	Dry + wet	01/10/17	31/10/17	3.7	30	Bq·m^{-2}
Serbia	Novi Sad	45.2671	19.8335	Dry + wet	01/09/17	30/09/17	0.9	20	Bq·m^{-2}
Serbia	Palić	46.1237	19.7583	Dry + wet	01/09/17	30/09/17	<0.7		Bq·m^{-2}

Country	Location	Latitude (decimal)	Longitude (decimal)	Type of deposition	Start date	End date	^{106}Ru	± (%)	Unit
Serbia	Palić	46.1237	19.7583	Dry + wet	01/10/17	31/10/17	<0.7		$Bq \cdot m^{-2}$
Serbia	Vinča	44.7608	20.6000	Dry + wet	01/09/17	30/09/17	1.0	30	$Bq \cdot m^{-2}$
Serbia	Vinča	44.7608	20.6000	Dry + wet	05/10/17	06/10/17	<2.6		$Bq \cdot L^{-1}$
Serbia	Vinča	44.7608	20.6000	Dry + wet	01/10/17	31/10/17	<0.4		$Bq \cdot m^{-2}$
Serbia	Vinča	44.7000	20.5000	Dry + wet	01/09/17	30/09/17	<0.4		$Bq \cdot m^{-2}$
Serbia	Vinča. Vodovod	44.7000	20.5000	Dry + wet	01/09/17	30/09/17	<0.3		$Bq \cdot m^{-2}$
Serbia	Vinča. Vodovod	44.7000	20.5000	Dry + wet	01/10/17	31/10/17	<0.3		$Bq \cdot m^{-2}$
Serbia	Vinča	44.8000	20.6000	Dry + wet	01/09/17	30/09/17	<0.1		$Bq \cdot m^{-2}$
Serbia	Vinča.	44.7000	20.5000	Dry + wet	01/10/17	31/10/17	<0.1		$Bq \cdot m^{-2}$
Serbia	Vinča	44.8000	20.6000	Dry + wet	01/09/17	30/09/17	<0.01		$Bq \cdot m^{-2}$
Serbia	Vinča	44.8000	20.6000	Dry + wet	01/10/17	31/10/17	0.2	24	$Bq \cdot m^{-2}$
Serbia	Vranje	42.5333	21.9000	Dry + wet	01/09/17	30/09/17	<0.2		$Bq \cdot m^{-2}$
Serbia	Vranje	42.5333	21.9000	Dry + wet	01/10/17	31/10/17	<0.2		$Bq \cdot m^{-2}$
Serbia	Zaječar	43.9333	22.3000	Dry + wet	01/09/17	30/09/17	<0.7		$Bq \cdot m^{-2}$
Serbia	Zaječar	43.9333	22.3000	Dry + wet	01/10/17	31/10/17	<0.3		$Bq \cdot m^{-2}$
Serbia	Zeleno brdo	44.7869	20.5219	Dry + wet	01/09/17	30/09/17	<0.3		$Bq \cdot m^{-2}$
Serbia	Zeleno brdo	44.7869	20.5219	Dry + wet	01/10/17	31/10/17	2.6	19	$Bq \cdot m^{-2}$
Serbia	Zlatibor	43.7333	19.7167	Dry + wet	01/09/17	30/09/17	<5.0		$Bq \cdot m^{-2}$
Serbia	Zlatibor	43.7333	19.7167	Dry + wet	01/10/17	31/10/17	<0.7		$Bq \cdot m^{-2}$
Slovakia	Bratislava	48.1439	17.1097	Dry + wet	03/10/17	10/10/17	0.17	25	$Bq \cdot L^{-1}$
Slovakia	Bratislava	48.1439	17.1097	Dry + wet	20/09/17	27/09/17	0.02	10	$Bq \cdot L^{-1}$
Slovakia	Bratislava	48.1439	17.1097	Rain water	20/09/17	27/09/17	0.02	10	$Bq \cdot L^{-1}$
Slovakia	Bratislava	48.1439	17.1097	Rain water	03/10/17	10/10/17	0.17	5	$Bq \cdot L^{-1}$
Slovakia	Bratislava	48.1439	17.1097	Rain water	03/10/17	10/10/17	7.9	8	$Bq \cdot m^{-2}$
Slovakia	Bratislava	48.1439	17.1097	Rain water	20/09/17	10/10/17	8.2	7	$Bq \cdot m^{-2}$
Slovenia	Krško – Location	45.9195	15.4981	Rain water	01/02/18	01/03/18	0.02	11	$Bq \cdot L^{-1}$
Slovenia	Krško – Location	45.9195	15.4981	Dry + wet	01/02/18	01/03/18	2.5	12	$Bq \cdot m^{-2}$
Slovenia	Krško	45.9511	15.5031	Rain water	01/02/18	01/03/18	0.008	52	$Bq \cdot L^{-1}$
Slovenia	Krško	45.9511	15.5031	Dry + wet	01/02/18	01/03/18	1.2	42	$Bq \cdot m^{-2}$
Slovenia	Krško reference	45.9061	15.0508	Rain water	01/02/18	01/03/18	0.0011	18	$Bq \cdot L^{-1}$
Slovenia	Krško reference	45.9061	15.0508	Dry + wet	01/02/18	01/03/18	1.6	13	$Bq \cdot m^{-2}$
Slovenia	Ljubljana	46.0425	14.4875	Rain water	01/02/18	01/03/18	0.01	30	$Bq \cdot L^{-1}$
Slovenia	Ljubljana	46.0425	14.4875	Dry + wet	01/02/18	01/03/18	1.3	31	$Bq \cdot m^{-2}$
Sweden	Gävle	60.6700	17.1900	Rain water	26/09/17	03/10/17	18.7	6	$Bq \cdot m^{-2}$
Sweden	Gävle	60.6700	17.1900	Rain water	03/10/17	09/10/17	0.7	10	$Bq \cdot m^{-2}$
Sweden	Gävle	60.6700	17.1900	Rain water	09/10/17	16/10/17	0.13	29	$Bq \cdot m^{-2}$
Sweden	Kiruna	67.8400	20.4200	Rain water	02/10/17	09/10/17	3.36	7	$Bq \cdot m^{-2}$
Sweden	Ljungbyhed	56.0800	13.2200	Rain water	25/09/17	02/10/17	<0.07		$Bq \cdot m^{-2}$
Sweden	Ljungbyhed	56.0800	13.2200	Rain water	02/10/17	10/10/17	<0.12		$Bq \cdot m^{-2}$
Sweden	Stockholm	59.3900	17.9600	Rain water	02/10/17	04/10/17	20.8	7	$Bq \cdot m^{-2}$
Sweden	Stockholm	59.3900	17.9600	Rain water	04/10/17	09/10/17	0.46	24	$Bq \cdot m^{-2}$

– : not provided

* : data from Budapest have been published in (1)

Table S4: ^{106}Ru deposition on plant and soil (Bq·m-2 or Bq·kg-1 fresh). Results are usually given with 2σ. Uncertainty in %.

Country	Location	Latitude (decimal)	Longitude (decimal)	Deposit	Start date	End date	^{106}Ru activity	± (%)	Unit
Austria	Vienna	48.2502	16.3393	Red maple dry	13/10/17	13/10/17	1.30	31	Bq·kg^{-1}
Austria	Vienna	48.2502	16.3393	Red maple wet	14/10/17	14/10/17	1.70	24	Bq·kg^{-1}
Austria	Vienna	48.2502	16.3393	Paulownia	22/10/17	22/10/17	4.00	28	Bq·kg^{-1}
Austria	Vienna	48.2502	16.3393	Grass	13/10/17	13/10/17	2.80	39	Bq·kg^{-1}
Austria	Vienna	48.2502	16.3393	Grass	13/10/17	13/10/17	3.60	33	Bq·kg^{-1}
Austria	Vienna	48.2502	16.3393	Grass	13/10/17	13/10/17	0.70	29	Bq·m^{-2}
Bulgaria	Glavan	42.068	26.1070	Pine needles	08/10/18	08/10/18	0.43	37	Bq·kg^{-1}
Bulgaria	Glavan	42.068	26.1070	Oak leaf litter	08/10/18	08/10/18	14.47	10	Bq·kg^{-1}
Bulgaria	Glavan	42.068	26.1070	Pine needles	08/10/18	08/10/18	19.0	5	Bq·kg^{-1}
Bulgaria	Harmanli	41.933	25.9250	Oak leaf litter	07/10/18	07/10/18	<22.0		Bq·kg^{-1}
Bulgaria	Harmanli	41.933	25.9250	Oak leaf litter	07/10/18	07/10/18	10.0	16	Bq·kg^{-1}
Bulgaria	Harmanli	41.933	25.9250	Pine needle litter	07/10/18	07/10/18	3.6	16	Bq·kg^{-1}
Bulgaria	Harmanli	41.933	25.9250	Pine needles	07/10/18	07/10/18	0.83	28	Bq·kg^{-1}
Bulgaria	Harmanli	41.933	25.9250	Tall grass	07/10/18	07/10/18	<1.56		Bq·kg^{-1}
Bulgaria	Haskovo	41.9275	25.5472	Pine needles	07/10/18	07/10/18	0.47	43	Bq·kg^{-1}
Bulgaria	Haskovo	41.9275	25.5472	Pine needle litter	07/10/18	07/10/18	3.5	10	Bq·kg^{-1}
Bulgaria	Rila Mountain	42.1747	23.5587	Lichen	07/11/17	07/11/17	0.14	20	Bq·kg^{-1}
Bulgaria	Rila Mountain	42.1747	23.5587	Moss	07/11/17	07/11/17	0.14	19	Bq·kg^{-1}
Bulgaria	Rila Mountain	42.1747	23.5587	Juniper	07/11/17	07/11/17	0.06	6	Bq·kg^{-1}
Bulgaria	Rila Mountain	42.1747	23.5587	Dwarf pine	07/11/17	07/11/17	0.03	20	Bq·kg^{-1}
Bulgaria	Sofia	42.6528	23.3844	Wild briar	12/10/17	12/10/17	0.0006	23	Bq·kg^{-1}
Bulgaria	Sofia	42.6528	23.3844	Hawthorn	12/10/17	12/10/17	0.0007	24	Bq·kg^{-1}
Bulgaria	Sofia	42.6528	23.3844	Fir-tree	19/12/17	19/12/17	0.0032	19	Bq·kg^{-1}
Bulgaria	Sveti Vlas	42.7134	27.7588	Short grass	13/09/18	13/09/18	1.73	32	Bq·kg^{-1}
Bulgaria	Sveti Vlas	42.7134	27.7588	Topsoil layer	12/09/18	12/09/18	55.60	11	Bq·m^{-2}
Bulgaria	Sveti Vlas	42.7134	27.7588	Topsoil layer	12/09/18	12/09/18	39.35	11	Bq·kg^{-1}
Bulgaria	Sveti Vlas	42.7134	27.7588	Larch needles	12/09/18	12/09/18	4.91	21	Bq·kg^{-1}
Bulgaria	Svilengrad	41.788	26.1920	Pine needle litter	07/10/18	07/10/18	5.46	24	Bq·kg^{-1}
Bulgaria	Svilengrad	41.788	26.1920	Pine needles	07/10/18	07/10/18	0.51	37	Bq·kg^{-1}
Czech Rep.	Frýdlant- Větrov	50.8905	15.0706	Grass	19/10/17	19/10/17	0.27	41	Bq·m^{-2}
Czech Rep.	Frýdlant- Větrov	50.8905	15.0706	Grass	19/10/17	19/10/17	0.63	40	Bq·kg^{-1}
Czech Rep.	Frýdlant- Větrov	50.8905	15.0706	Grass	19/10/17	19/10/17	2.41	40	Bq·kg^{-1}
Czech Rep.	Frýdlant- Větrov	50.8915	15.0698	Grass	19/10/17	19/10/17	0.79	25	Bq·m^{-2}
Czech Rep.	Frýdlant- Větrov	50.8915	15.0698	Grass	19/10/17	19/10/17	1.43	24	Bq·kg^{-1}
Czech Rep.	Frýdlant- Větrov	50.8915	15.0698	Grass	19/10/17	19/10/17	6.57	25	Bq·kg^{-1}
Czech Rep.	Jeřmanice	50.6882	15.1208	Grass	20/10/17	20/10/17	0.21	19	Bq·m^{-2}
Czech Rep.	Jeřmanice	50.6882	15.1208	Grass	20/10/17	20/10/17	0.50	20	Bq·kg^{-1}
Czech Rep.	Jeřmanice	50.6882	15.1208	Grass	20/10/17	20/10/17	3.88	21	Bq·kg^{-1}
Czech Rep.	Višňová	50.9650	15.0178	Grass	22/10/17	22/10/17	<0.10		Bq·m^{-2}
Czech Rep.	Višňová	50.9650	15.0178	Grass	22/10/17	22/10/17	<0.11		Bq·kg^{-1}
Czech Rep.	Višňová	50.9650	15.0178	Grass	22/10/17	22/10/17	<0.99		Bq·kg^{-1}
Germany	Hanover	52.3817	9.7179	Spanish chestnut	11/11/17	11/11/17	<1.5		Bq·kg^{-1}
Greece	Kamena Vourla*	38.7785	22.7466	Soil (0-1 cm)	17/10/17	17/10/17	27.2	2	Bq·kg^{-1}
Greece	Kamena Vourla*	38.7785	22.7466	Soil (1-2 cm)	17/10/17	17/10/17	27.2	2	Bq·kg^{-1}
Greece	Kamena Vourla*	38.7785	22.7466	Soil (2-3 cm)	17/10/17	17/10/17	11.9	2	Bq·kg^{-1}
Greece	Kamena Vourla*	38.7785	22.7466	Soil (3-4 cm)	17/10/17	17/10/17	12.1	2	Bq·kg^{-1}

Country	Location	Latitude (decimal)	Longitude (decimal)	Deposit	Start date	End date	^{106}Ru activity	± (%)	Unit
Greece	Thermopylae*	38.7927	22.5261	Soil	17/10/17	17/10/17	12.1	2	Bq·kg^{-1}
Hungary	Budapest **	47.4300	19.0300	Grass	03/10/17	03/10/17	5.28	-	Bq·kg^{-1}
Hungary	Budapest **	47.48910	18.95370	Grass	09/10/17	09/10/17	<3.20		Bq·kg^{-1}
Hungary	Budapest **	47.48910	18.95370	Grass	16/10/17	16/10/17	<4.60		Bq·kg^{-1}
Italy	Taipana	46.2738	13.3097	Moss	30/05/18	30/05/18	9.60	15	Bq·m^{-2}
Italy	Taipana	46.2738	13.3097	Moss	01/06/18	01/06/18	4.40	41	Bq·m^{-2}
Italy	Taipana	46.2728	13.3088	Moss	07/06/18	07/06/18	9.10	56	Bq·m^{-2}
Poland	Krakow	50.0902	19.8886	Grass	16/10/17	16/10/17	8.8	25	Bq·kg^{-1}
Poland	Krakow	50.0902	19.8886	Grass	16/10/17	16/10/17	0.283	25	Bq·m^{-2}
Slovakia	Bratislava	48.1439	17.1097	Grass	17/10/17	17/10/17	0.58	2	Bq·m^{-2}
Sweden	Umeå	63.8500	20.3400	Topsoil + grass	15/10/17	15/11/17	48.50	16	Bq·m^{-2}
Sweden	Umeå	63.8500	20.3400	Topsoil + grass	15/10/17	15/11/17	25.50	17	Bq·m^{-2}
Sweden	Umeå	63.8500	20.3400	Topsoil + grass	15/10/17	15/11/17	28.40	17	Bq·m^{-2}
Sweden	Umeå	63.8500	20.3400	Topsoil + grass	15/10/17	15/11/17	44.70	17	Bq·m^{-2}
Sweden	Umeå	63.8500	20.3400	Topsoil + grass	15/10/17	15/11/17	34.50	23	Bq·m^{-2}
Sweden	Umeå	63.8500	20.3400	Topsoil + grass	15/10/17	15/11/17	8.50	115	Bq·m^{-2}
Switzerland	Mezzovico -Vira	46.0918	8.9217	Forage, grass	04/10/17	04/10/17	<2.6		Bq·kg^{-1}
Switzerland	Mezzovico -Vira	46.0918	8.9217	Soil	04/10/17	04/10/17	<8.2		Bq·kg^{-1}
Switzerland	Cevio	46.3171	8.6017	Forage, grass	04/10/17	04/10/17	<3.5		Bq·kg^{-1}
Switzerland	Cevio	46.3171	8.6017	Soil	04/10/17	04/10/17	<4.1		Bq·kg^{-1}
Switzerland	Prato Leventina	46.4829	8.7567	Forage, grass	04/10/17	04/10/17	<5.3		Bq·kg^{-1}
Switzerland	Prato Leventina	46.4829	8.7567	Soil	04/10/17	04/10/17	<14.8		Bq·kg^{-1}

* Data from Kamena Vourla and from Thermopylae (Greece) have been taken from (3)

** Data from Budapest have been taken from (1)

Datasets used

The dataset used in this study comprises mostly data from laboratory members involved in the Ro5 network, personal communications as well as publicly available data from the internet. Most notably, this includes data that have been provided only to IAEA-USIE but that can be found on various websites:
https://blog.safecast.org/2017/11/about-that-radioactive-plume-of-ru-106/
http://geoenergetics.ru/2017/10/19/magate-stavit-tochku-v-skandale-vokrug-ruteniya/
http://www.criirad.org/accident-et-pollutions/som-accidents&pollutions.html.

Data only reported through IAEA-USIE include the following countries:

- Albania (no value >LOD)
- Estonia
- Iceland (no value >LOD)
- Ireland
- Kazakhstan
- Turkey

Radioactive properties and use of ^{106}Ru

Both ruthenium isotopes are anthropogenic fission products of fissile materials. The ratio between the most notable fission nuclides ^{103}Ru and ^{106}Ru allows dating of the production of the radioactive batch, as ^{103}Ru has the higher fission yield (3.1% for thermal ^{235}U fission and 6.9% for ^{239}Pu fission, respectively) but shorter half-life ($T_{1/2}$ = 39.25 d) compared with ^{106}Ru ($T_{1/2}$ = 371.8 d) (fission yields; 0.41% for ^{235}U and 4.2% for ^{239}Pu, respectively). The detection of ruthenium isotopes alone excludes the possibility of an accident release from a nuclear reactor which would have resulted in the presence of much more other radionuclides. The origin of this radioelement is therefore to be found either in nuclear fuel reprocessing facilities or in radioactive sources (e.g. for nuclear medicine purposes like radiotherapy of eye tumors (4)). This isotope can also be used as reference source to test radiation monitoring equipment but as for the previous case, there is no need for very high activity source to make such tests.

Discussion of a possible satellite re-entry

Several organizations concluded that no satellite went missing during the ^{106}Ru episode. The IAEA concluded that no satellite containing ^{106}Ru had fallen back on earth during this period (5, 6). Several space agencies, among them the European Space Agency (ESA) and the Russian Space Agency (Roskosmos) (7), registered a constant number of satellites before and after the ^{106}Ru episode (8). The United Nations Office for Outer Space Affairs (UNOOSA) also confirmed that no satellite or other re-entries of objects containing ^{106}Ru RTGs had taken place. Previous disintegration of satellites fueled with radioactive material during their atmospheric re-entry have dispersed most of radioactive debris in the high stratosphere (at about 50 km in 1964 for the satellite SNAP-9A fueled with ^{238}Pu (9), at altitudes about 39 and 36 km for the Kosmos-954 and Kosmos-1402 satellites, fueled with enriched ^{235}U, during their re-entry in the earth's atmosphere in 1978 and 1983, respectively.
A re-entry of a disintegrating satellite would cause a vertical decreasing gradient in activity concentration from the disintegration altitude (the higher the altitude, the higher the concentration). Similar scenarios are observed for ^{7}Be, a cosmogenic radionuclide whose production takes place in the lower stratosphere and upper troposphere and for which concentrations at mountain sites are higher than in lowland.
Aircraft samplings were also performed on September 27 and October 30, 2017, in the lower stratosphere (11,700 and 13,100 m) above Switzerland but no ^{106}Ru was detected. However, these investigations were probably too early or too late to be compared with the probable date of the event. Stratosphere to troposphere exchanges (STE) can be tracked by looking at the ^{7}Be and ^{22}Na cosmogenic radionuclide concentrations which should have exhibited higher concentrations and based on their activity ratio. No significant and simultaneous increase of cosmogenic radionuclides which could have resulted from downdraft was noticed during the ^{106}Ru detections. Finally, assuming this re-entry had occurred several months or even some years before its detection in the lower troposphere one should not expect such a "high" concentration range at ground level.

Sequence of airborne ^{106}Ru detections in Ukraine

In Ukraine, thirty-eight detections occurred between 09/26 and 10/3 (or 09/28 and 10/5), however most of these filters were changed on a weekly basis, thus offering little time resolution. At four locations, however, ^{106}Ru was detected on filters having sampling duration as short as 1 to 2 days. This made it possible to demonstrate, in addition with daily detections in surrounding countries (Romania and Russia) that the plume duration was of the order of also 1 to 2 days only. This statement implicitly indicates similar or even shorter release duration upwind. It is thus obvious that proper comparison of the airborne ^{106}Ru concentration from different monitoring networks in Europe requires a correction for sampling periods longer than the plume duration. For instance, most ^{106}Ru results were based on weekly sampling and even as long as one month leading to a strong effect on the average estimated concentration with regards to the plume duration.

Correction for plume duration

Several aerosol filters have been changed on a daily basis even before the first detection of ^{106}Ru. The example in Fig. S1 shows that the radioruthenium plume was present on three consecutive filters, which is also another argument in favor of a ground-based release.

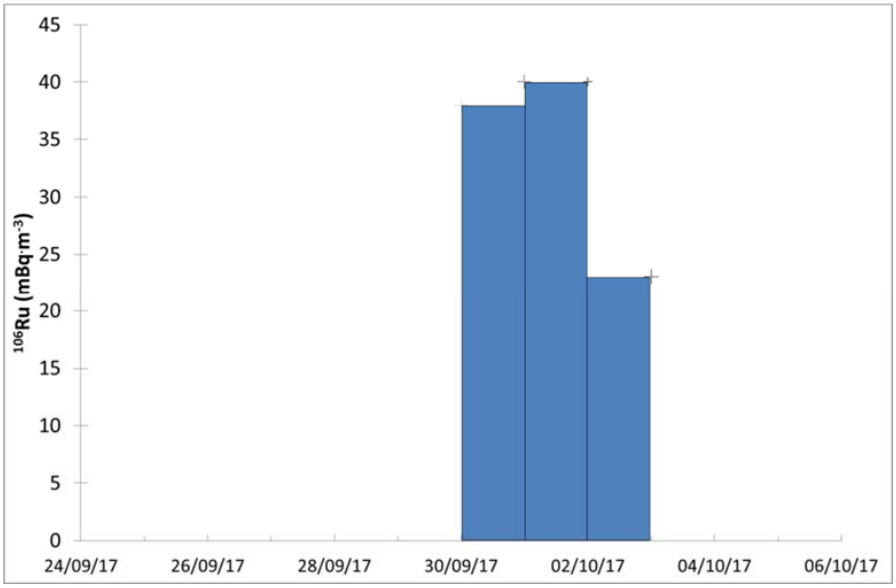

Fig. S1. Typical pattern of activity concentrations of ^{106}Ru detections on three consecutive filters.

Chemistry of ruthenium and solubility experiments

Ruthenium exhibits a rather complicated chemistry with multiple oxidation states. The release scenario most likely involved the most volatile oxidation state +VIII, mainly in the form of RuO_4, which is volatilized just above room temperature. The lack of any concomitant radionuclides of other elements suggests that the radioruthenium experienced a purification via the gas phase (before or during the release). Under highly oxidizing conditions, as they often occur in spent nuclear fuel reprocessing, highly volatile and reactive (oxidizing) RuO_4 is formed. Due to its volatility, it may easily escape under "normal" industrial conditions. Upon contact with organic (and even inorganic) substances (which includes natural aerosols and dust particles), airborne RuO_4 is quickly reduced to RuO_2 which exhibits both low volatility and solubility in water. In nuclear fuel processing, measures have to be taken to stabilize and trap the highly volatile RuO_4 by chemical reactions (trapping in acids or bases). This means that, even though RuO_4 had been involved in the release scenario at some point, it may already have been brought to react to a lower oxidation state at the time of release.

Ruthenium-106 trapped on aerosol filters was found to be quite readily soluble in water. A part of glass fibre filter with 30.5±1.3 Bq of ^{106}Ru (as of 13.11.2017) collected in the period 29.9. - 2.10. 2017 in the Czech Republic was subjected to dissolution in serum ultra filtrate fluid (SUF) as defined in (10). The lung dissolution test was performed using the static method (Fig. S2). The filter was submerged in 80 ml of SUF solution. At specified time intervals sufficient to determine a half-life on the order of minutes to hours the solution was filtered through a membrane filter with a pore size of 120 nm and was replaced with a fresh simulant solution.

Rapid dissolution fraction of 0.91 with dissolution rate 6.03 h^{-1} ($T_{1/2}$ = 0.115 h) and slow dissolution fraction of 0.09 with dissolution rate 0.06 h^{-1} ($T_{1/2}$ = 10.7 h) were found.

Possible phagocytation of aerosol particles has not been considered.

		y= undissolved fraction $y = (1-r_2)\cdot e^{-s1\cdot t} + r_2\cdot e^{-s2\cdot t}$	t=time (h)	$T_{1/2}$ (h)
r_1 (= 1-r_2)	0.0866			
s_1	0.0646	h^{-1}		10.7
r_2	0.913			
s_2	6.033	h^{-1}		0.115

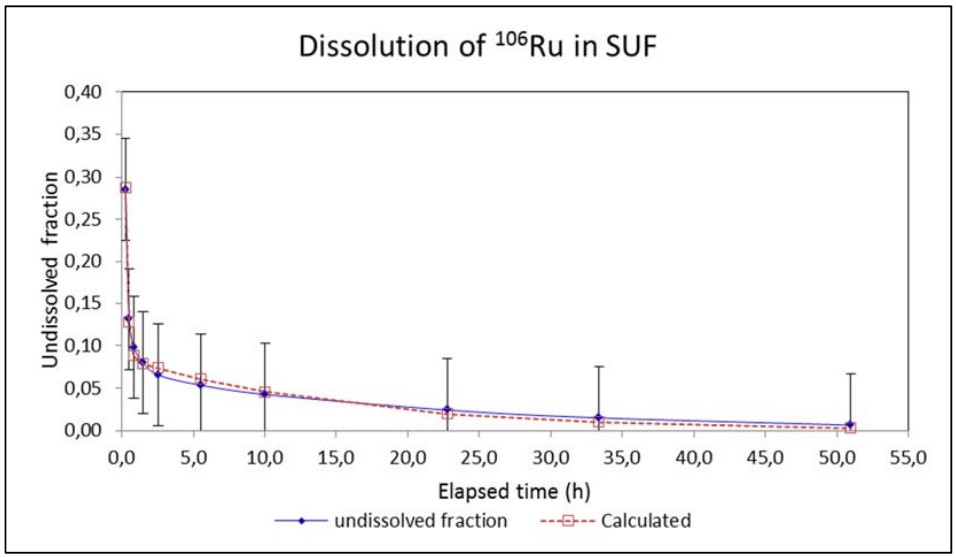

Fig. S2. Dissolution kinetics of ^{106}Ru from an aerosol filter in SUF

Volatilization experiments

An air filter from a high volume sampler from Austria with an aerosol ^{106}Ru activity concentration of 21.7 $mBq \cdot m^{-3}$ were used to provide chemical information about the released Ru species. Ruthenium has multiple oxidation states, most notably Ru^{III}, Ru^{IV}, and Ru^{VIII}. Under highly oxidizing conditions, highly volatile and reactive (oxidizing) RuO_4 is formed. Due to its volatility, it may easily escape under "normal" industrial conditions above room temperature. Upon contact with organic substances (which likely includes natural aerosols and dust particles), RuO_4 is quickly reduced to RuO_2 which exhibits both low volatility and solubility in water.

Heating experiments were performed in air. Filters fragments containing about 30 Bq were placed in quartz crucibles and heated for 60 min at the given temperatures (see Fig. S3.). In the course of the heating experiments, the polypropylene (Blown MicroFiber) filter melted and decomposed, causing deformation of the material, which, at least partially, had to be accounted for in the gamma measurements.

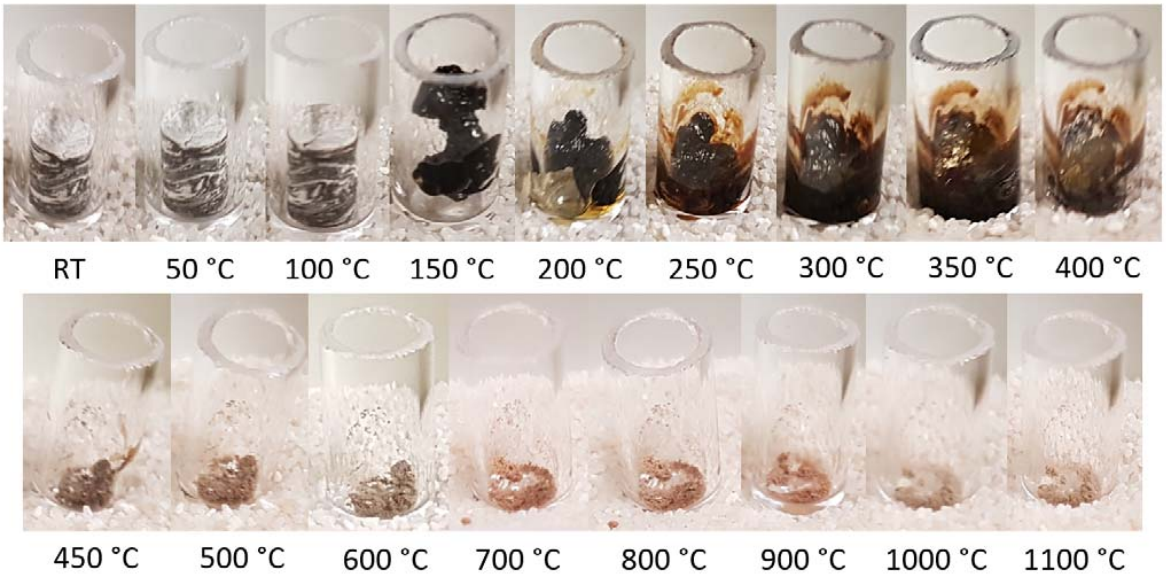

Fig. S3. An air filter fragment after being heated in air for 60 min at the given temperature in a minuscule quartz glass vial. It illustrates the changing geometry (which partially could be accounted for during the gamma measurement) and the loss of matter through ashing

Imaging Plate (IP) Autoradiography

IP Autoradiography (Fig. S4) of a ^{106}Ru-contaminated filter from Germany reveals an extremely finely and homogeneously dispersed ^{106}Ru fraction, which is largely responsible for the darkening of the IP. The light grey spot represents a blank filter, which is only marginally darkened due to the electrostatic adhesion of natural airborne ^{210}Pb on the polypropylene fibres.

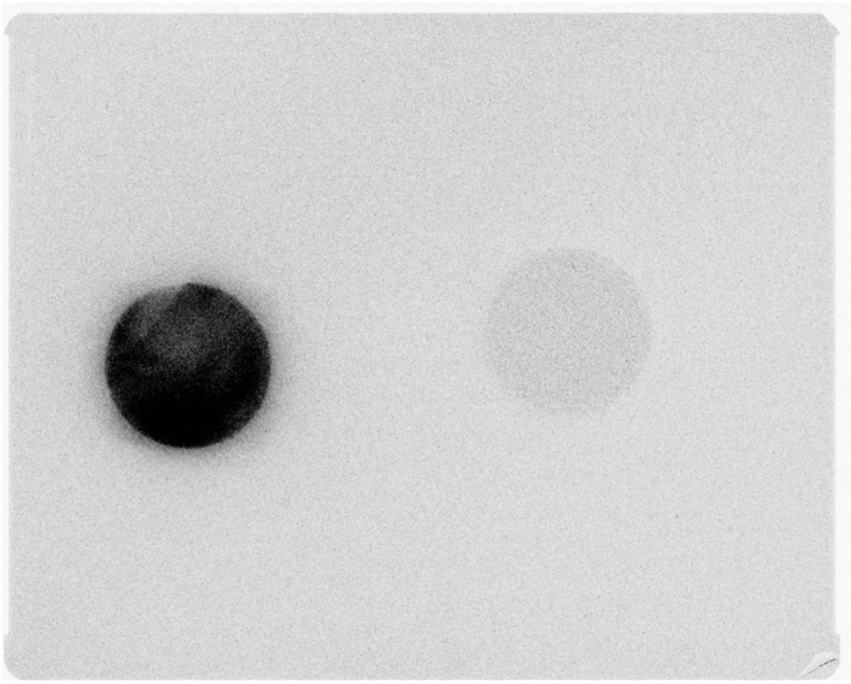

Fig. S4. IP autoradiograph of a ^{106}Ru containing aerosol filter (left) from Cottbus, Germany and blank (right). The ^{106}Ru containing sample was collected from 2017/09/25 to 2017/10/02 with a sample volume of 25194 m^3. From gamma spectrometry analysis the filter was determined to contain 18.7 Bq of ^{106}Ru, 11.4 Bq of ^{7}Be, and 17.2 Bq of ^{210}Pb.

Scanning electron microscopic imaging of the filter surface

Electron microscopy (Fig. S5) revealed only particles on the air filter (from Vienna, see above) that are typically found in dust. They include soil particles, pollen, fibres etc. No unusual particles containing high-*Z* elements were found.

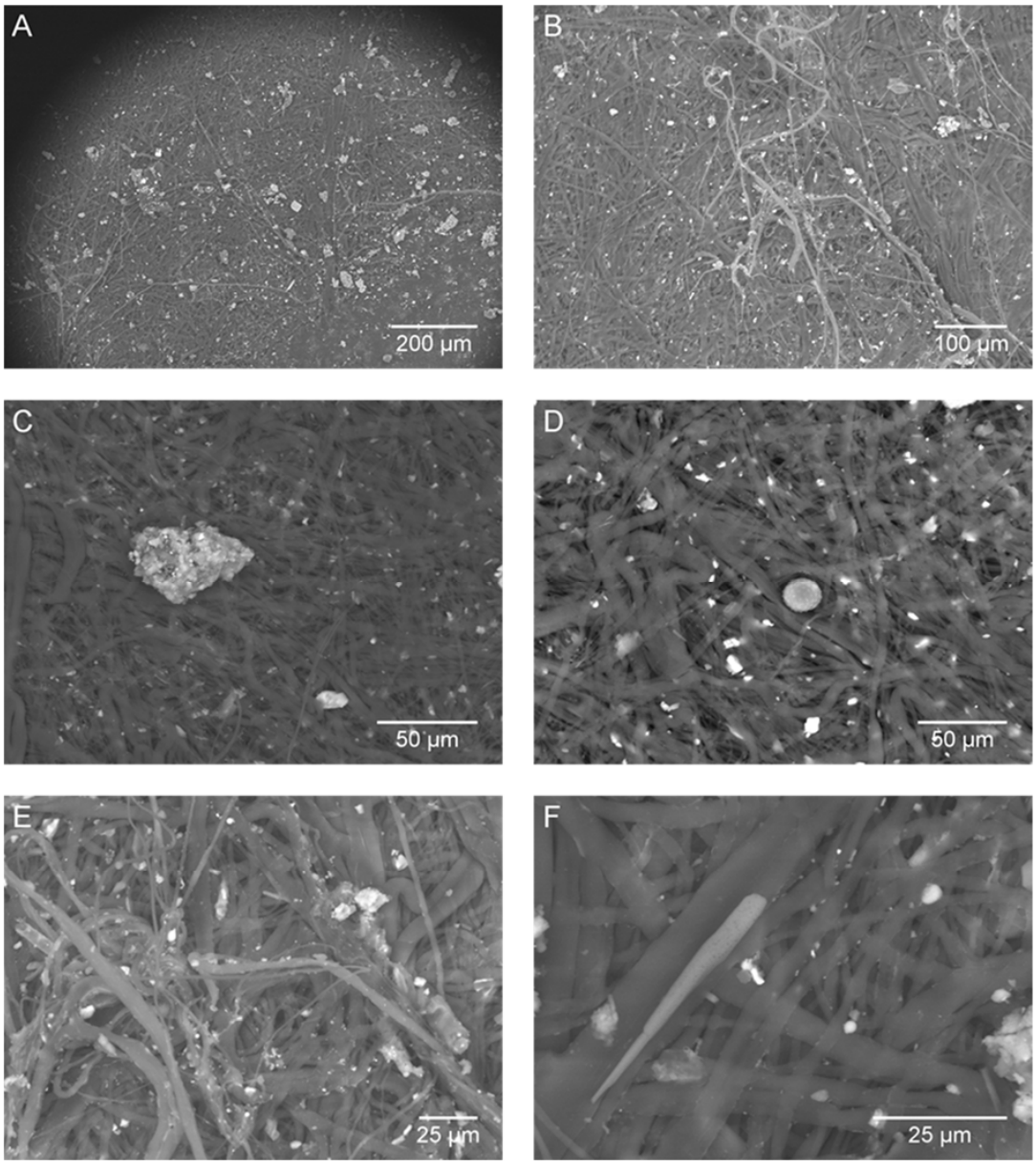

Fig. S5. Selection of scanning electron microscopic images of an air filter from Vienna, Austria (sampling period 2017/09/29 to 2017/10/04).

Gamma spectrum

A gamma spectrum exhibiting detectable activities of both ^{103}Ru (9.7 µBq·m^{-3}) and ^{106}Ru (42 mBq·m^{-3}) is shown in Fig. S6. The most intense peak of ^{106}Rh (^{106}Ru) at 511.9 keV coincides with the unavoidable 511 keV annihilation peak that is typically found in gamma spectra. Thus, activities of ^{106}Ru are typically calculated using the undisturbed photopeak at 621.9 keV. The activities of ^{214}Bi at 609.3 keV did not interfere with this photopeak, because activities of ^{214}Bi proved to be too low and energy resolution in modern gamma detectors allows for the distinction of both peak areas (if the 609.3 keV was present at all). The spectrum also exhibits the characteristic photopeaks of natural radionuclides, including ^{212}Pb, ^{7}Be, and ^{40}K.

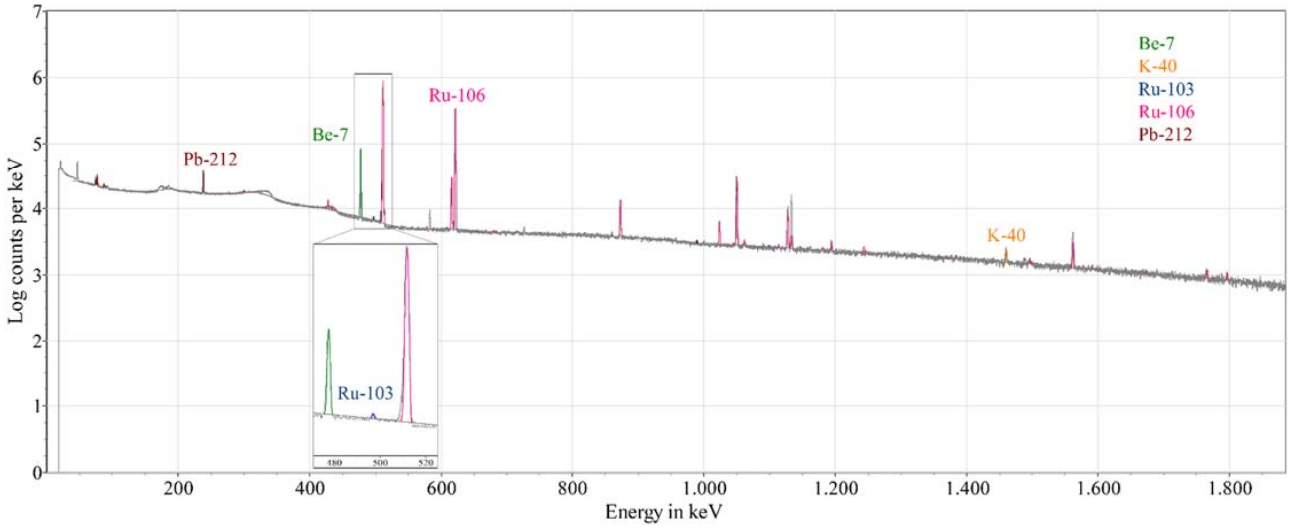

Fig. S6. A gamma spectrum of an air filter from Vienna, Austria (sampling period 2017/10/02 to 2017/10/03). Measurement duration was 250,000 s. Peak areas and gamma intensities for each nuclide are fitted using Visual RobFit™ software from Snakedance Scientific™.

References

1. Jakab D, *et al.* (2018) Methods, results and dose consequences of ^{106}Ru detection in the environment in Budapest, Hungary. *J. Environ. Radioact.* 192:543-550.
2. Ramebäck H, *et al.* (2018) Measurements of ^{106}Ru in Sweden during the autumn 2017: Gamma-ray spectrometric measurements of air filters, precipitation and soil samples, and in situ gamma-ray spectrometry measurement. *Appl. Radiat. Isot.* 140:179-184.
3. Padovani S, Mitsios I, Anagnostakis M, & Mostacci D (2018) Analysis of the vertical distribution and size fractionation of natural and artificial radionuclides in soils in the vicinity of hot springs. *Radiat. Eff. Defects Solids* 173(9-10):794-806.
4. Abouzeid H, *et al.* (2008) ^{106}Ruthenium brachytherapy for retinoblastoma. *Int. J. Radiat. Oncol. Biol. Phys.* 71(3):821-828.
5. IAEA (2017) *Status of Measurements of Ru-106 in Europe* (IAEA, Vienna) p 5.
6. IAEA (2017) *Status of Measurements of Ru-106 in Europe* (IAEA, Vienna) p 19.
7. Roshydromet (2017) Report on the causes and source of ruthenium-106 on the territory of Russia in September-October 2017 (Отчет по определению причин и источника рутения-106 на территории России в сентябре-октябре 2017 года) (in Russian). http://egasmro.ru/files/documents/reports/report_28_12_2017.pdf (accessed accessed May 2018).
8. Bastida Virgili B (2017) Nuage radioactif : Pourquoi l'hypothèse russe de la chute d'un satellite ne tient pas la route (in French). https://www.sciencesetavenir.fr/espace/nuage-radioactif-pourquoi-l-hypothese-russe-de-la-chute-d-un-satellite-ne-tient-pas-la-route_119345 (accessed June 2018).
9. Telegadas K (1969) *The seasonal stratospheric distribution of plutonium-238 and strontium-90, March through November 1967* (U.S. Atomic Energy Commission).
10. Ansoborlo E, Hengé-Napoli MH, Chazel V, Gibert R, & Guilmette RA (1999) Review and critical analysis of available in vitro dissolution tests. *Health Phys.* 77(6):638-645.

Appendix B

Publication II

Supporting Information

Identification of a Chemical Fingerprint Linking the Undeclared 2017 Release of ^{106}Ru to Advanced Nuclear Fuel Reprocessing

Supporting Information Appendix:

Identification of a Chemical Fingerprint Linking the Undeclared 2017 Release of 106Ru to Advanced Nuclear Fuel Reprocessing

Michael W. Cooke[1*], Adrian Botti[1], Dorian Zok[2], Georg Steinhauser[2], Kurt R. Ungar[1]

[1]*Radiation Protection Bureau, Health Canada, 775 Brookfield Rd., Ottawa, ON, Canada, K1A 1C1.*

[2]*Institute of Radioecology and Radiation Protection, Leibniz Universität Hannover, Herrenhäuser Str. 2, 30419 Hannover, Germany.* [*]*Email: michaelw.cooke@canada.ca*

[*]Corresponding author: Michael W. Cooke

Email: michaelw.cooke@canada.ca

Table of Contents

http://www.pnas.org/cgi/doi/10.1073/pnas.2001914117

1. ^{1}H NMR Spectra

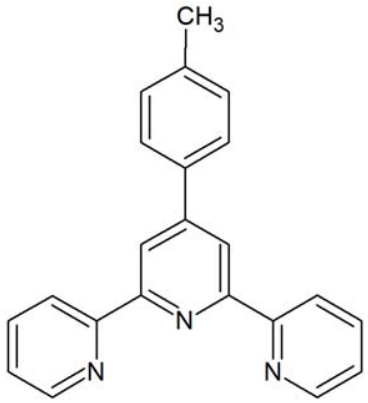

4'-p-tolyl-2,2';6',2"-terpyridine (ttpy)

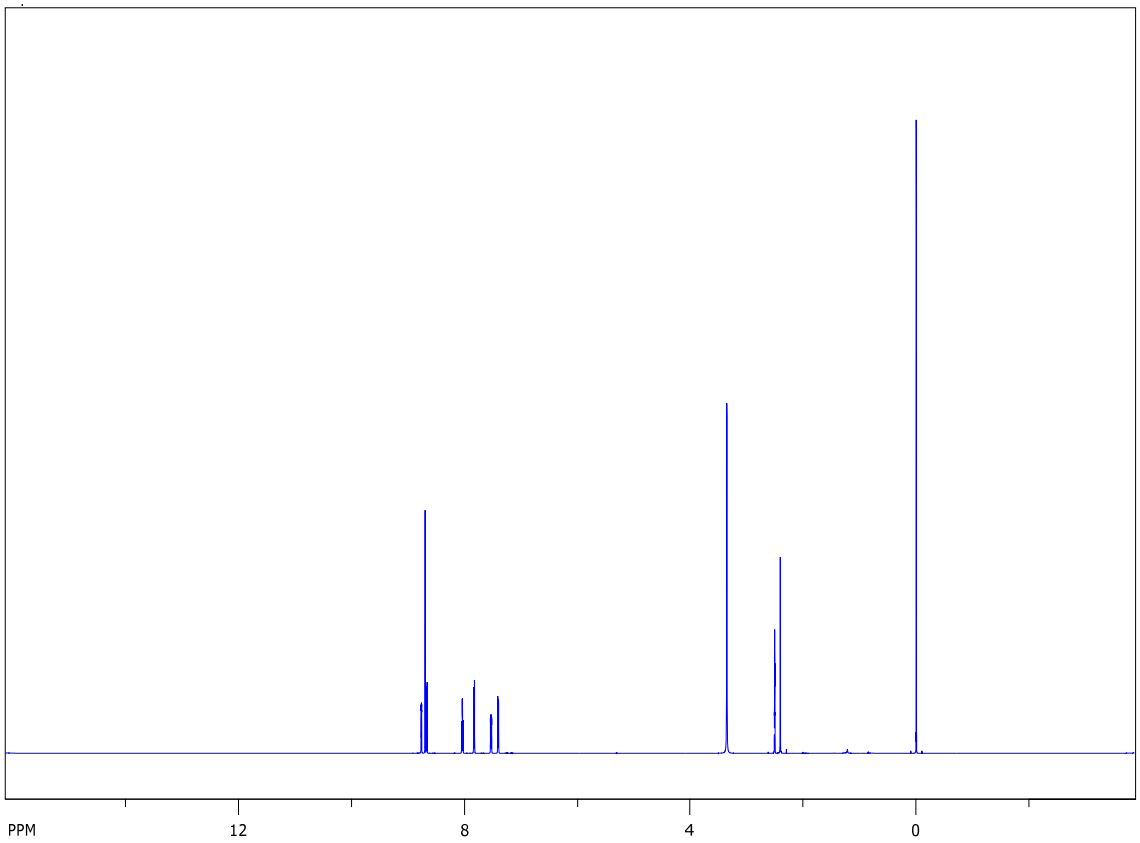

Figure S.1. ^{1}H NMR of 4'-p-tolyl-2,2';6',2"-terpyridine (600 MHz, full spectrum) in d_6-DMSO.

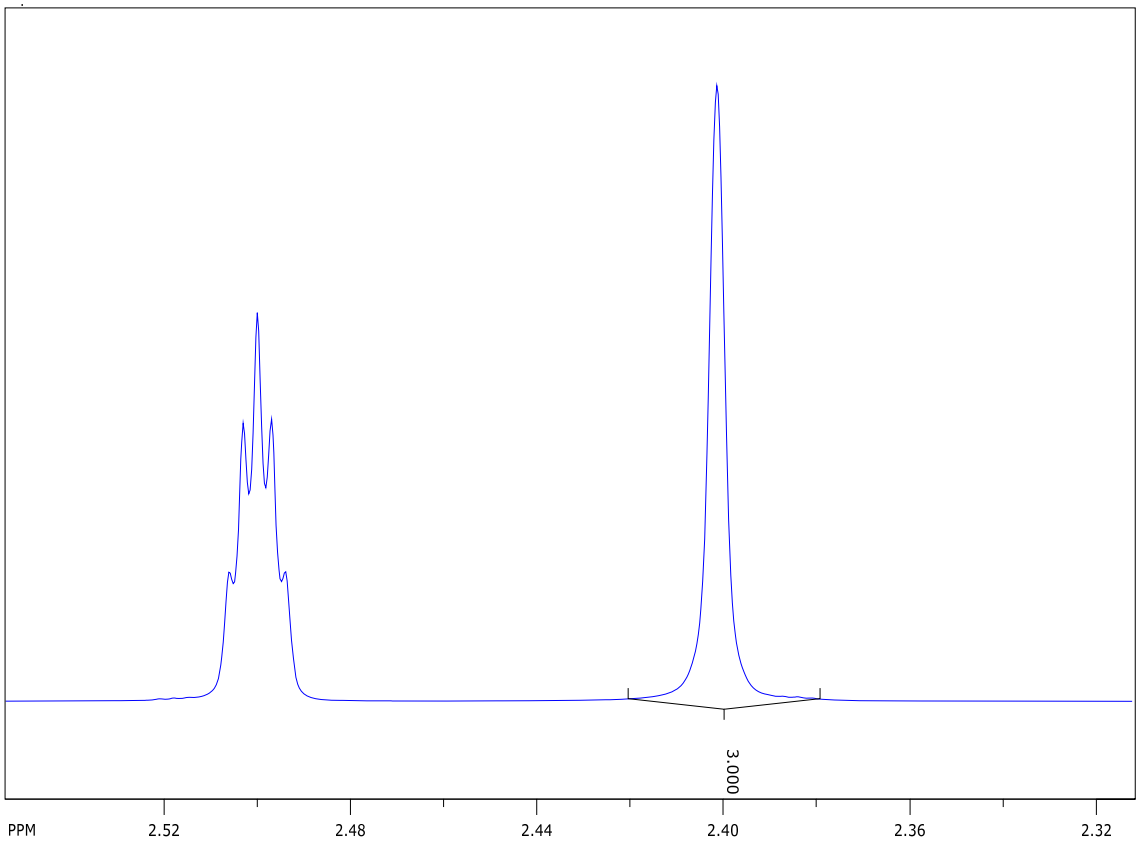

Figure S.2. 1H NMR of 4'-p-tolyl-2,2';6',2"-terpyridine (600 MHz, aliphatic region) in d_6-DMSO.

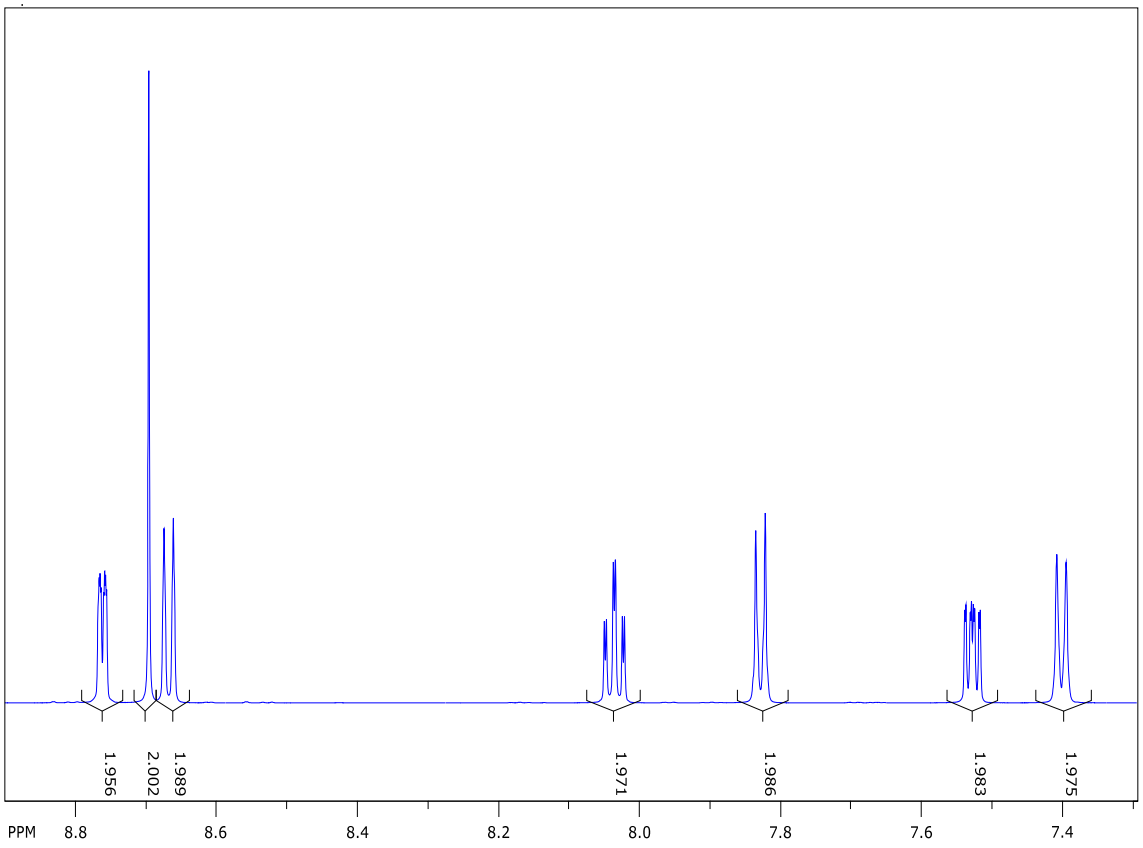

Figure S.3. ^{1}H NMR of 4'-p-tolyl-2,2';6',2"-terpyridine (600 MHz, aromatic region) in d_6-DMSO.

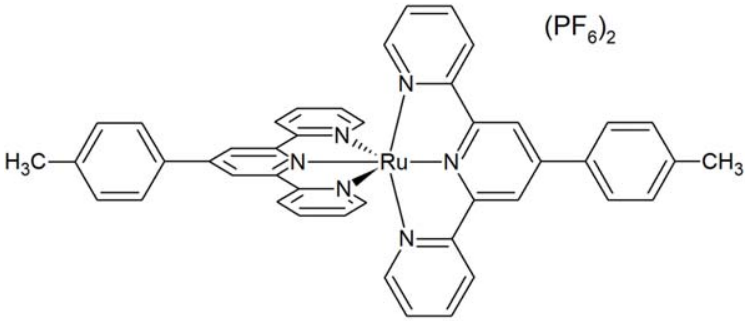

[Ru(ttpy)$_2$](PF$_6$)$_2$

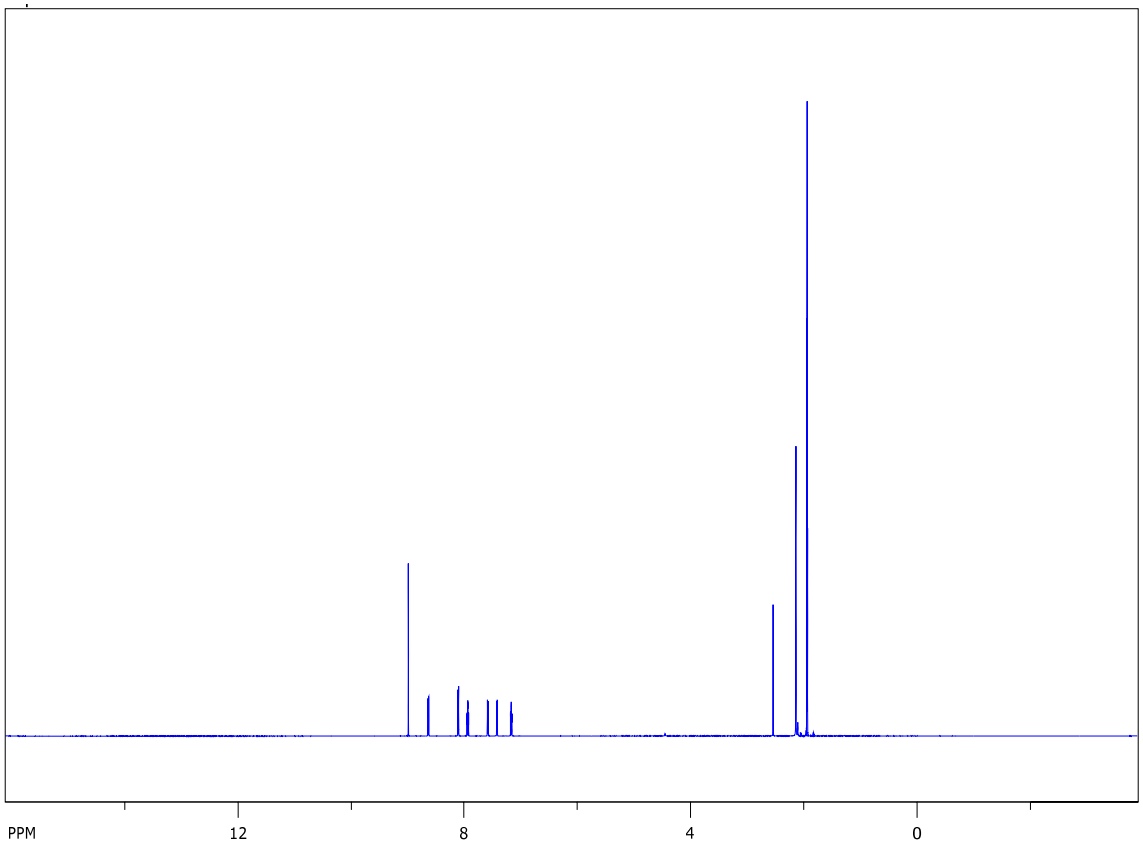

Figure S.4. ^{1}H NMR of [Ru(ttpy)$_2$](PF$_6$)$_2$ (600 MHz, full spectrum) in d_3-acetonitrile.

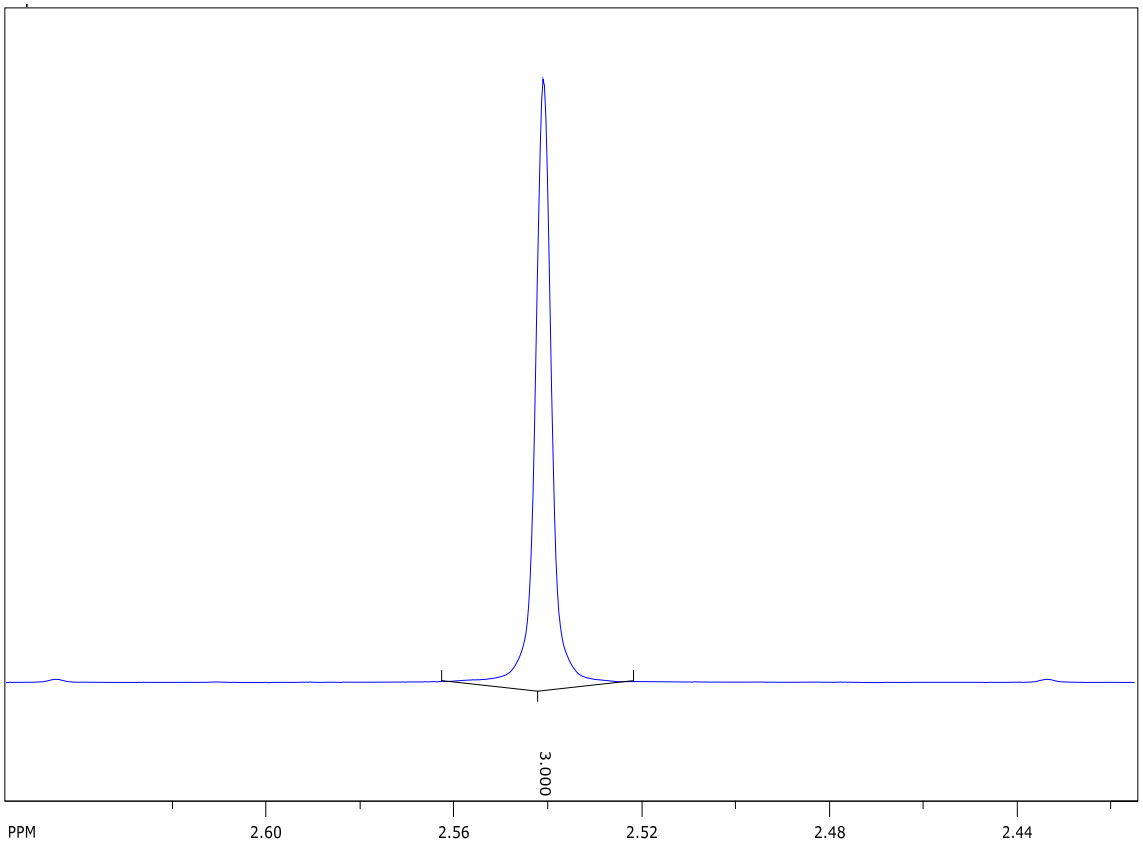

Figure S.5. ^{1}H NMR of $[Ru(ttpy)_2](PF_6)_2$ (600 MHz, aliphatic region) in d_3-acetonitrile.

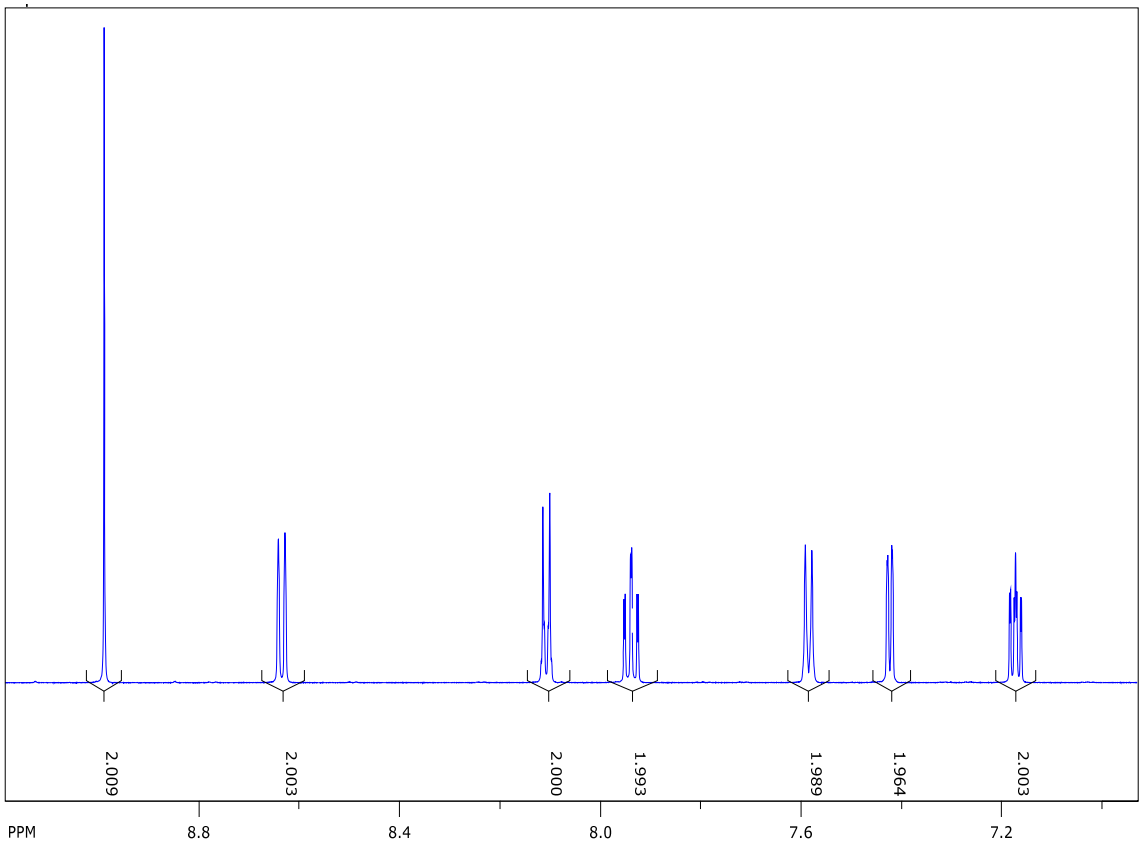

Figure S.6. ^{1}H NMR of $[Ru(ttpy)_2](PF_6)_2$ (600 MHz, aromatic region) in d_3-acetonitrile.

2. Electrospray Ionization Mass Spectrometry

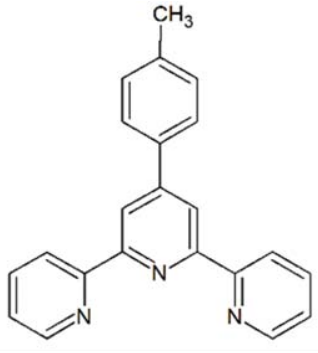

4'-p-tolyl-2,2';6',2"-terpyridine (ttpy)

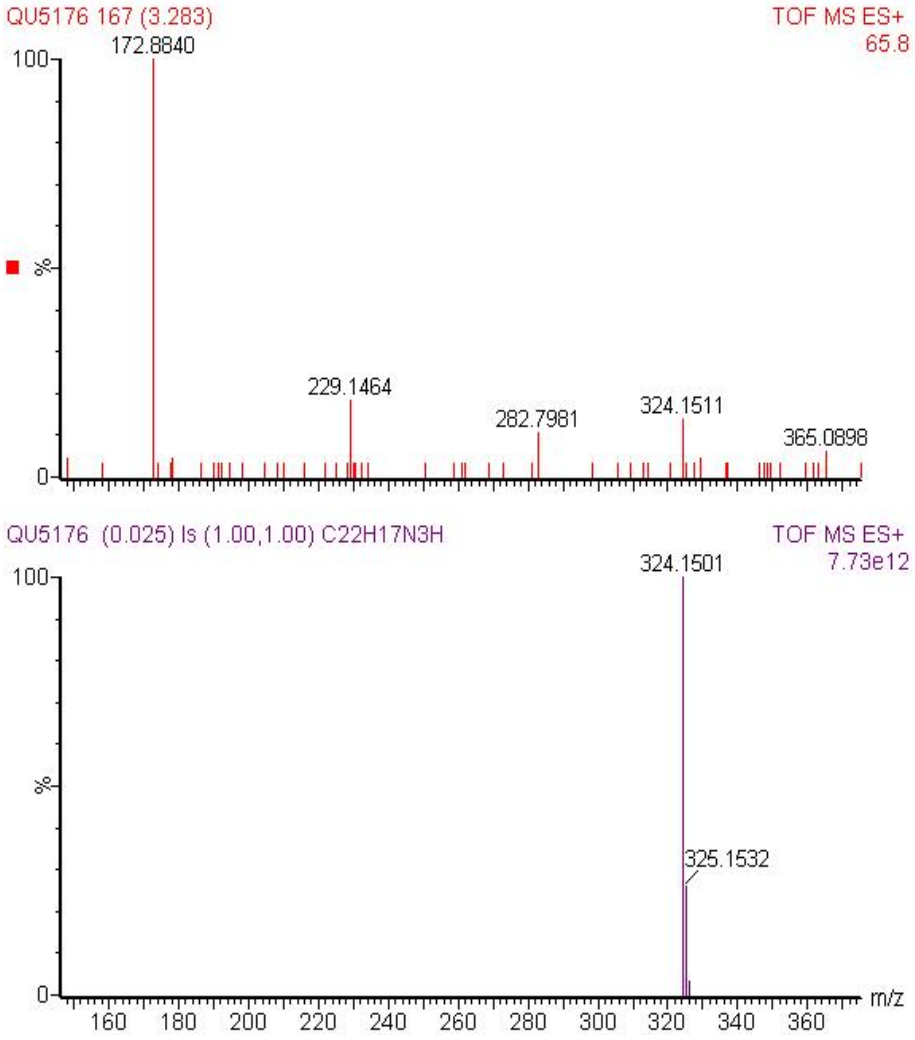

Figure S.7. ESI-MS of ttpy. Actual (top) and calculated (bottom) for $C_{22}H_{17}N_3$.

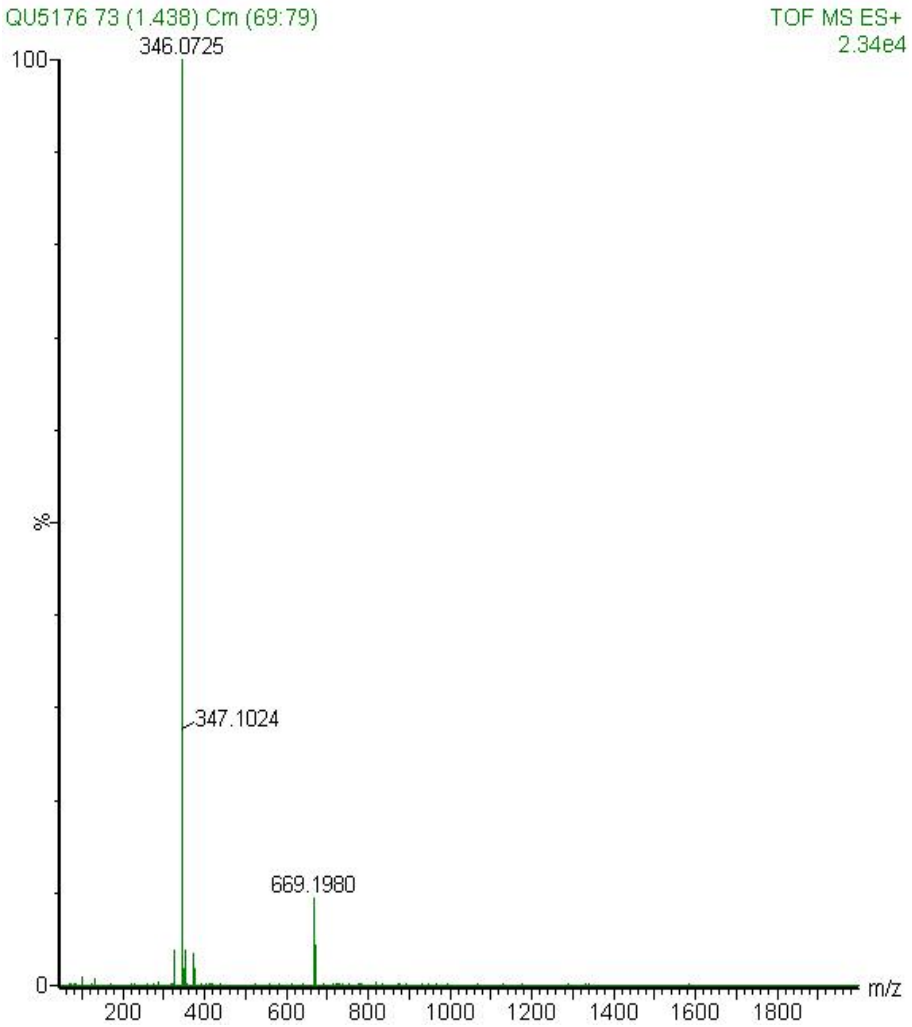

Figure S.8. ESI-MS for ttpy. $C_{22}H_{17}N_3Na^+$ (m/z = 346.0725); $(C_{22}H_{17}N_3)_2Na^+$ (m/z = 669.1980)

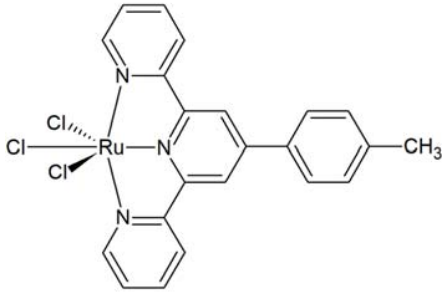

ttpyRuCl₃

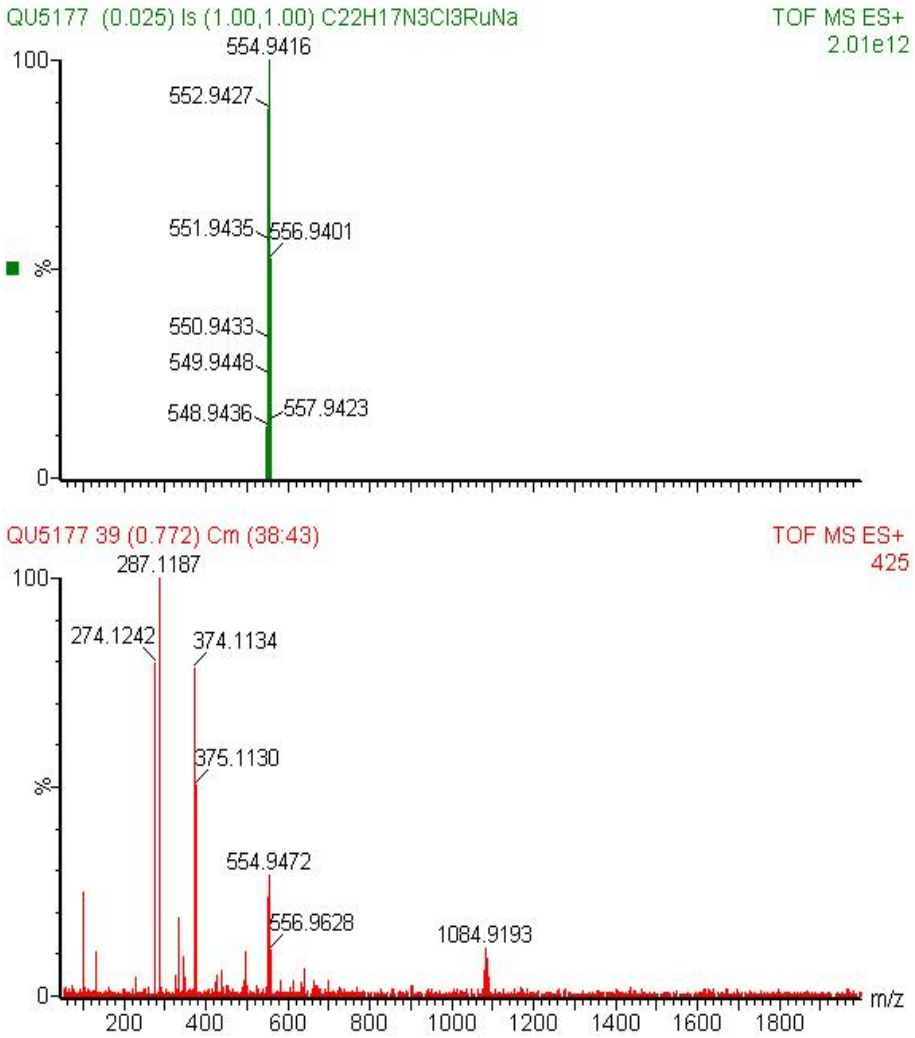

Figure S.9. ESI-MS for ttpyRuCl₃. At bottom, $C_{22}H_{17}N_3RuCl_3Na^+$ (m/z = 554.9472), $(C_{22}H_{17}N_3RuCl_3)_2Na^+$ (m/z = 1084.9193). At top, calculated spectrum for $C_{22}H_{17}N_3RuCl_3Na^+$.

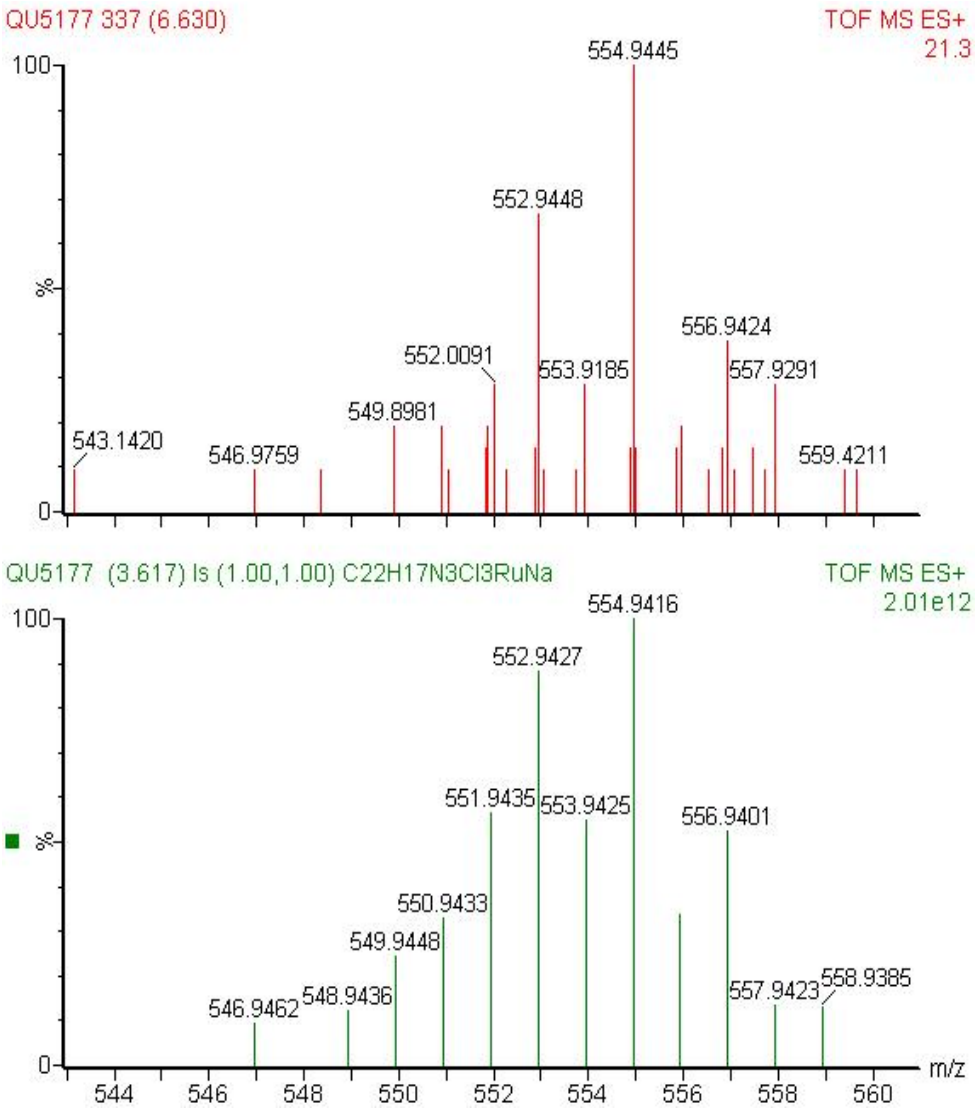

Figure S.10. ESI-MS for ttpyRuCl$_3$. At bottom, calculated for $C_{22}H_{17}N_3RuCl_3Na^+$. At top, actual for $C_{22}H_{17}N_3RuCl_3Na^+$.

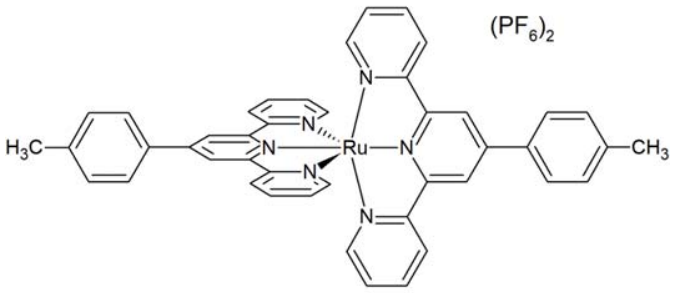

[Ru(ttpy)$_2$](PF$_6$)$_2$

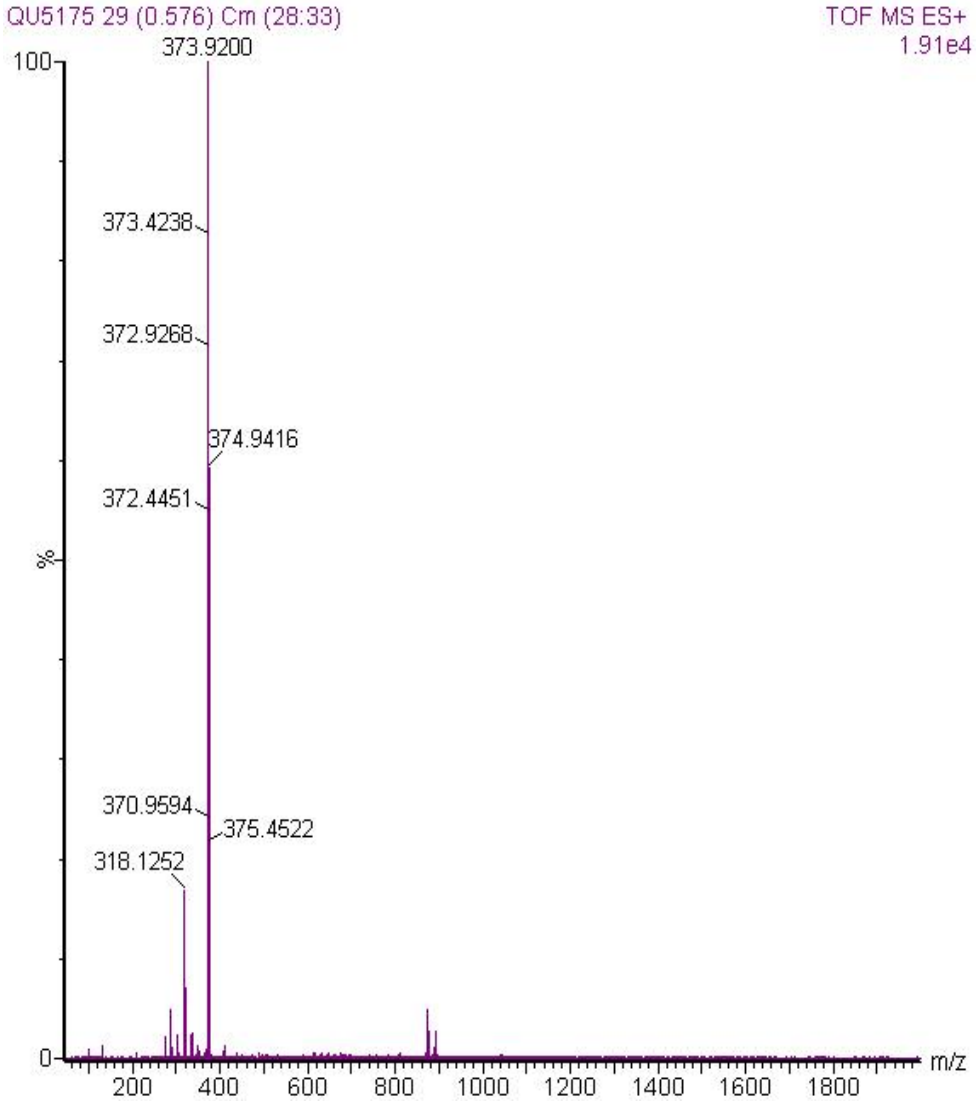

Figure S.11. ESI-MS for [Ru(ttpy)$_2$](PF$_6$)$_2$ (actual).

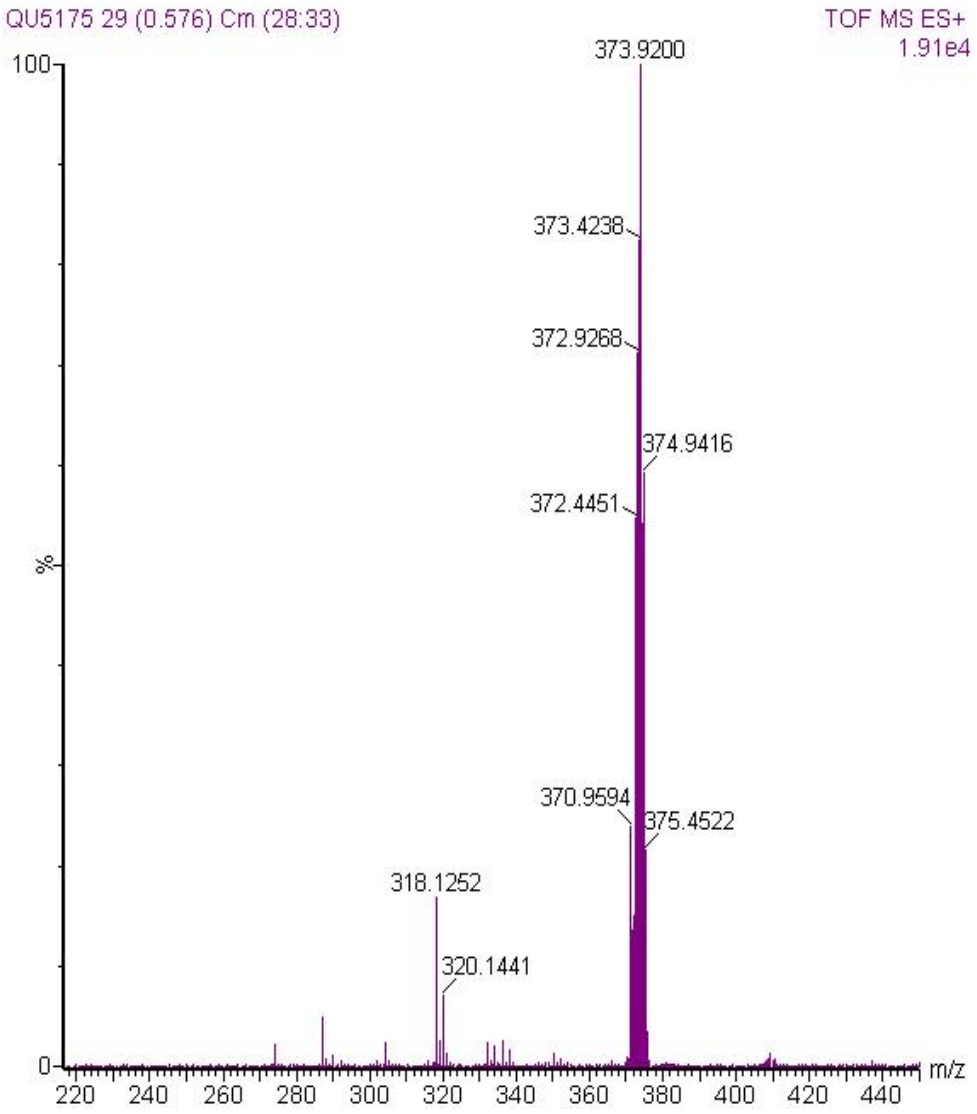

Figure S.12. ESI-MS (actual) of $[Ru(ttpy)_2](PF_6)_2$, depicting $C_{44}H_{34}N_6Ru^{2+}$ (m/z = 373.9200).

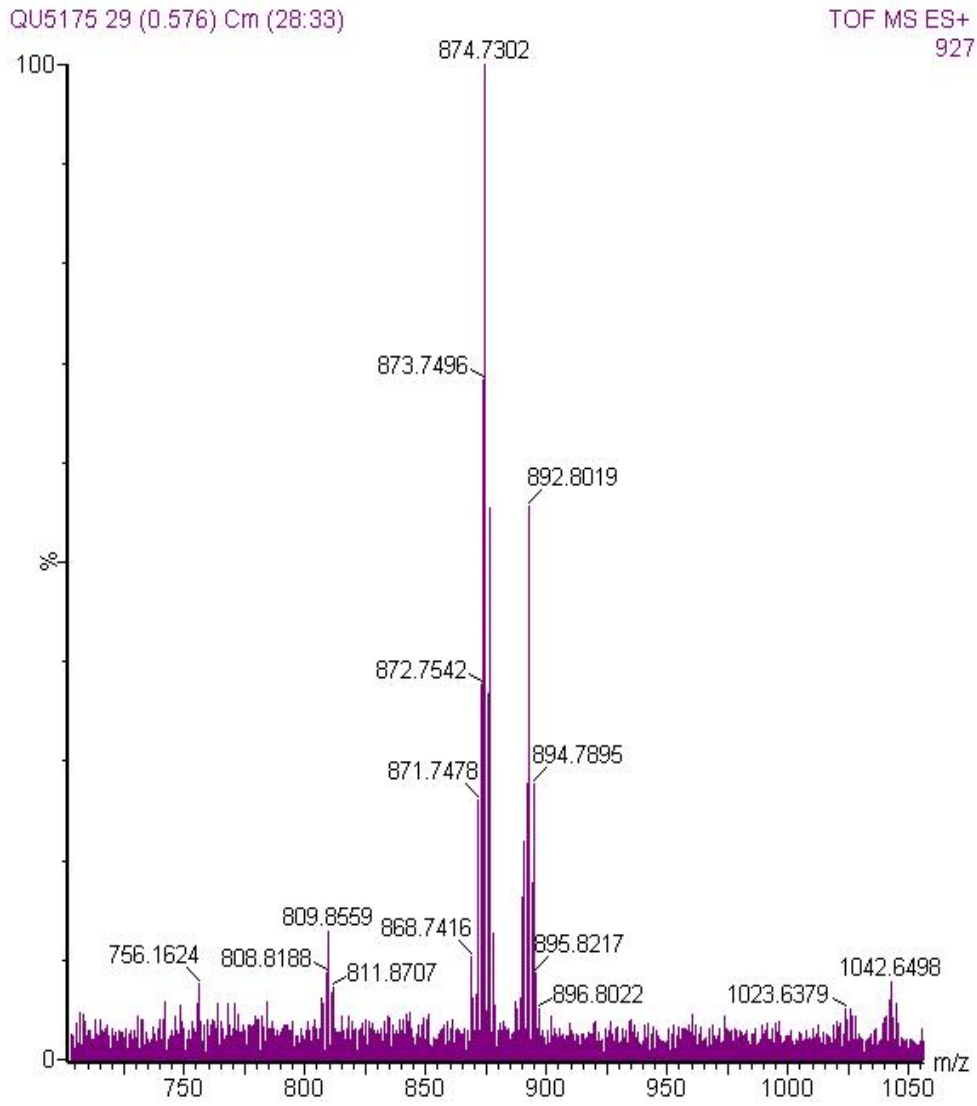

Figure S.13. ESI-MS (actual) of $[Ru(ttpy)_2](PF_6)_2$, depicting $C_{44}H_{34}N_6Ru(PF_5)^+$ (m/z = 874.7302) and $C_{44}H_{34}N_6Ru(PF_6)^+$ (m/z = 892.8019).

3. HPLC

Method development considerations for separation of $ttpyRuCl_3$ and $Ru(ttpy)_2^{2+}$:

To ensure long-term solubility of $ttpyRuCl_3$, the proportion of DMF in the mobile phase was required to be high (no less than 70% when paired with methanol). A 90:10 (DMF:MeOH) mixture was found to be optimal with respect to the retention of $ttpyRuCl_3$. The ionic strength of the solution, provided by the addition of tetrabutylammonium chloride (TBACl), was integral to achieve adequate separation, where the retention of $ttpyRuCl_3$ was shown to be invariant (Figure S.14).

The crude $ttpyRuCl_3$ containing ^{106}Ru that was purified by HPLC (108 mg, 88% yield) was not ideally suited to the separation method developed, which was limited to 0.4 mg of $ttpyRuCl_3$ per injection. However, it was found that smaller scale reactions, targeting a more manageable 2 – 5 mg of the complex in 0.5 – 1.0 ml of concentrated ethanol filter extract, produced little to no discernable $ttpyRuCl_3$. This result was contrasted by initial, similarly scaled model reactions (i.e. using ethanol not in contact with the filter media) that produced the target complex in high-yield. This observation indicated that some ethanol-soluble component of the filter media works to inhibit or transform the target complex under the reaction conditions used. For this reason, a larger scale reaction was adopted to ensure that the target complex was produced in acceptable yield.

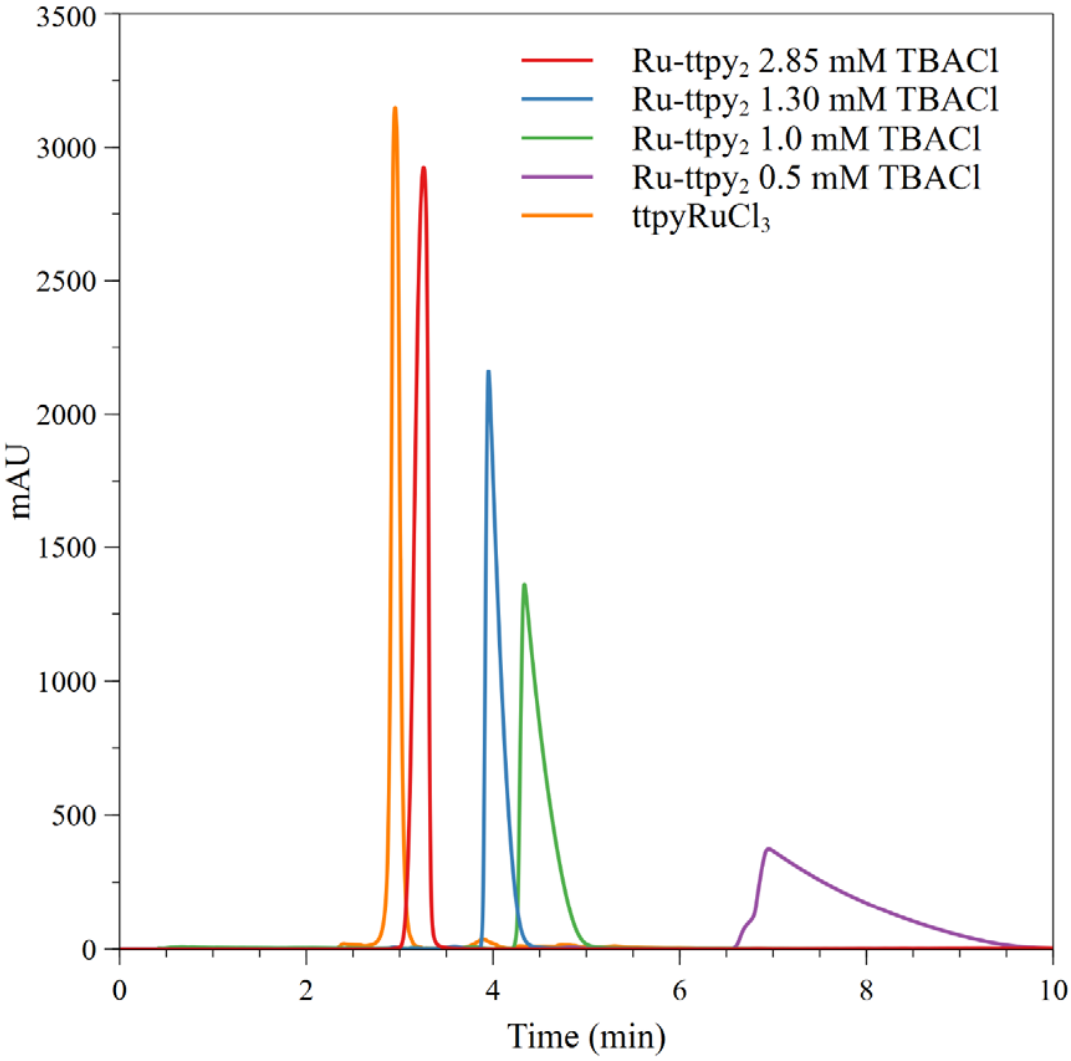

Figure S.14. Overlay of HPLC chromatograms depicting $ttpyRuCl_3$ and $Ru(ttpy)_2^{2+}$ elution times as a function of TBACl concentration. C_{18} reverse-phase, semi-preparatory scale column; 90:10 (DMF:MeOH) mobile phase at a flow rate of 4.0 mL/min; $\lambda = 450$ nm. Injection concentrations and volumes for both $ttpyRuCl_3$ and $[Ru(ttpy)_2](PF_6)_2$ correspond to 1.0 mg/mL at 250 µl.

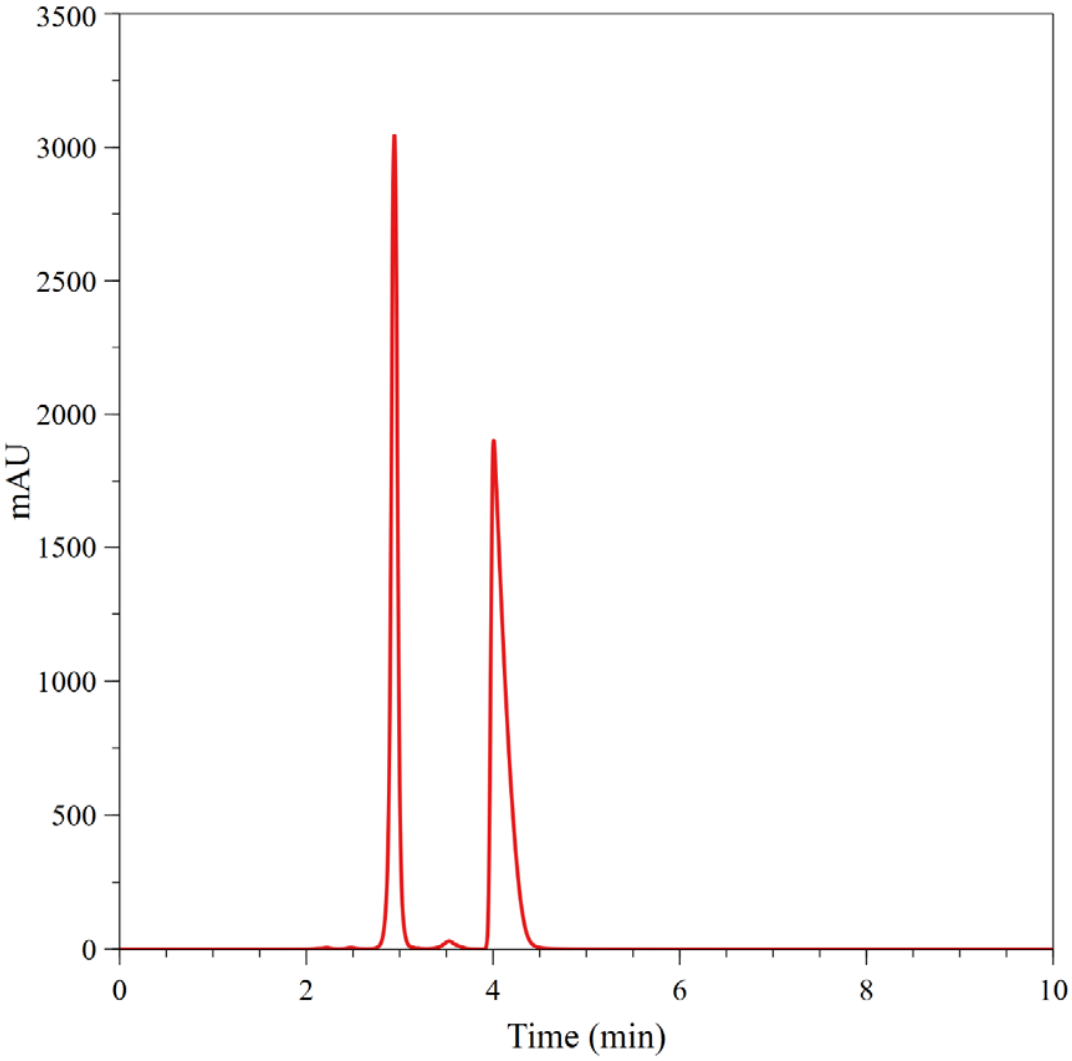

Figure S.15. Co-injection and elution of ttpyRuCl$_3$ and [Ru(ttpy)$_2$](PF$_6$)$_2$ at 1.0 mg/mL from DMF solution. R_t = 2.96, R_t = 4.01 min, respectively. C_{18} reverse-phase, semi-preparatory scale column; 90:10 (DMF:MeOH) at 1.30 mM TBACl and 4.0 mL/min; λ = 450 nm. Injection concentrations and volumes correspond to 1.0 mg/mL at 250 µl.

4. Radiochemistry with ^{106}Ru

Reactions with β-$RuCl_3$:

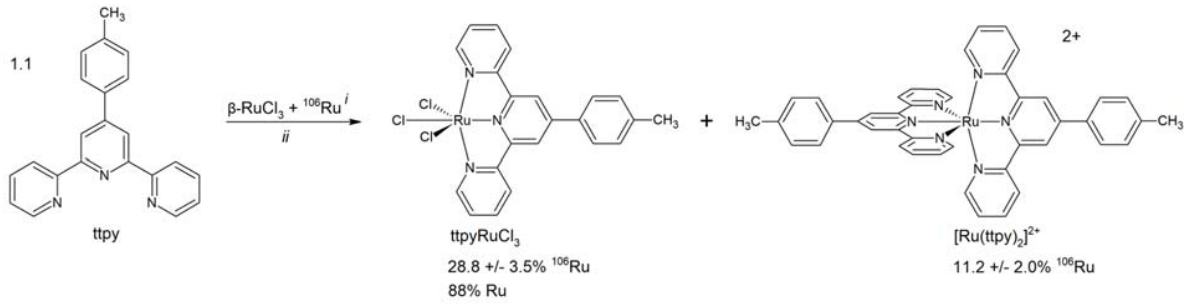

Figure S.16. Reaction of ^{106}Ru (ethanol extract) with β-$RuCl_3$ to form $ttpyRuCl_3$ and $[Ru(ttpy)_2]^{2+}$.

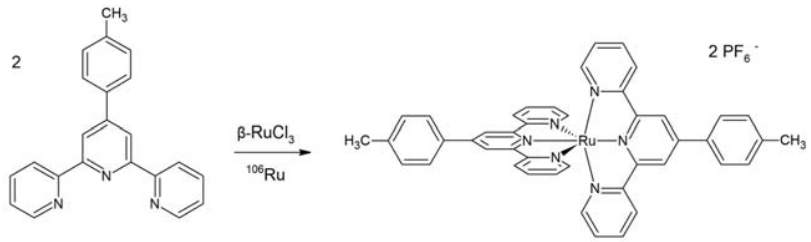

Figure S.17. Reaction of ^{106}Ru (filter piece or aqueous extract) with β-$RuCl_3$ to form $[Ru(ttpy)_2](PF_6)_2$.

Carrier-Free Reaction:

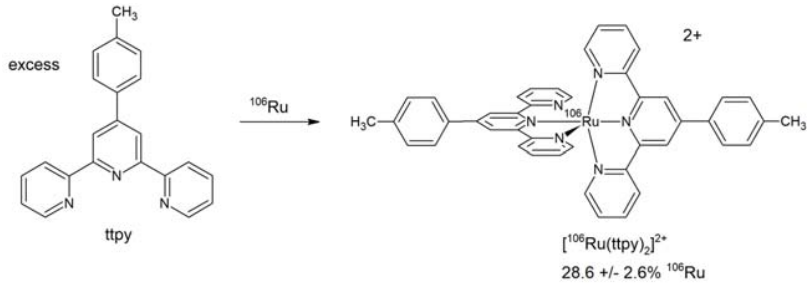

Figure S.18. Reaction of ^{106}Ru (ethanol extract) with ttpy.

5. Gamma Spectrometry

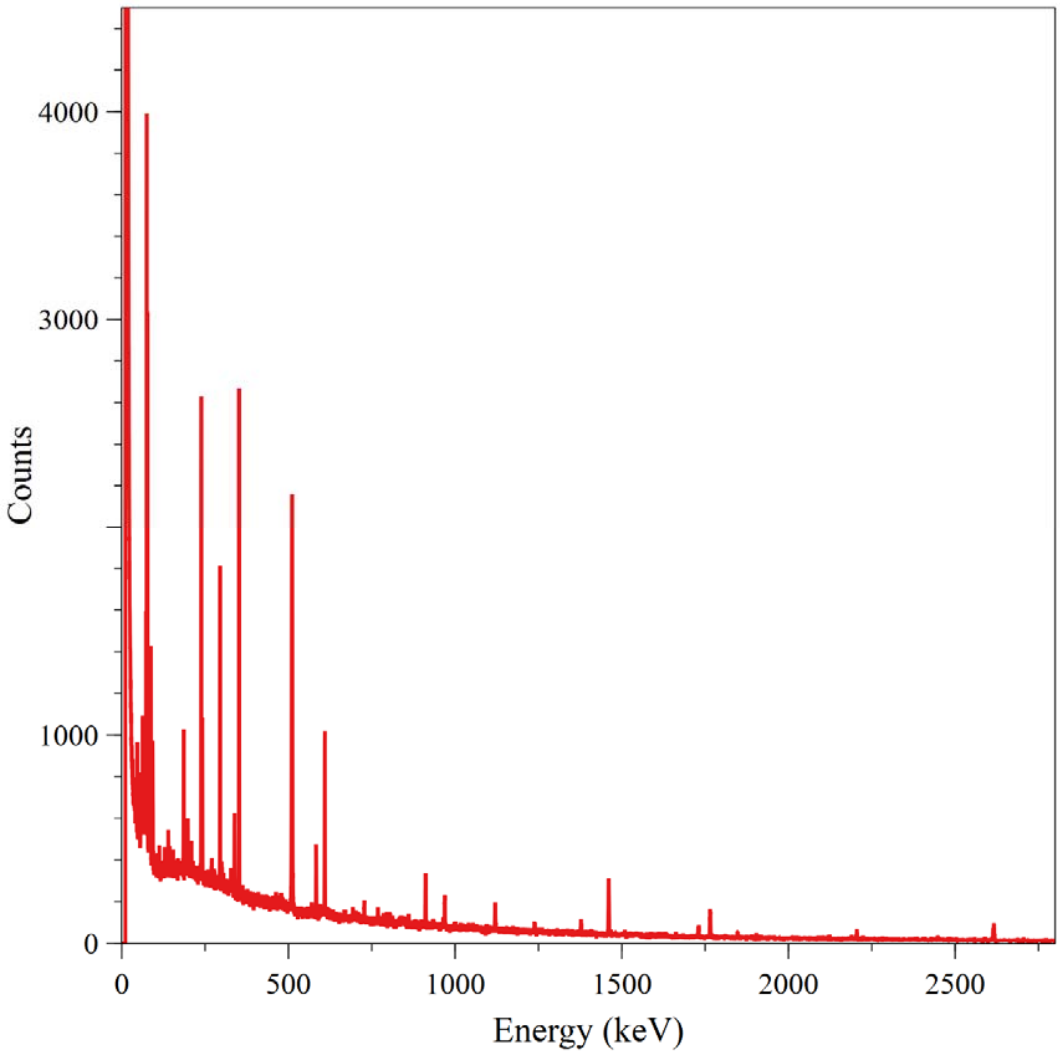

Figure S.19. Full energy gamma spectrum (0 – 2800 keV) of collected HPLC fraction representing column dead-volume (R_t = 0 – 2 min.)

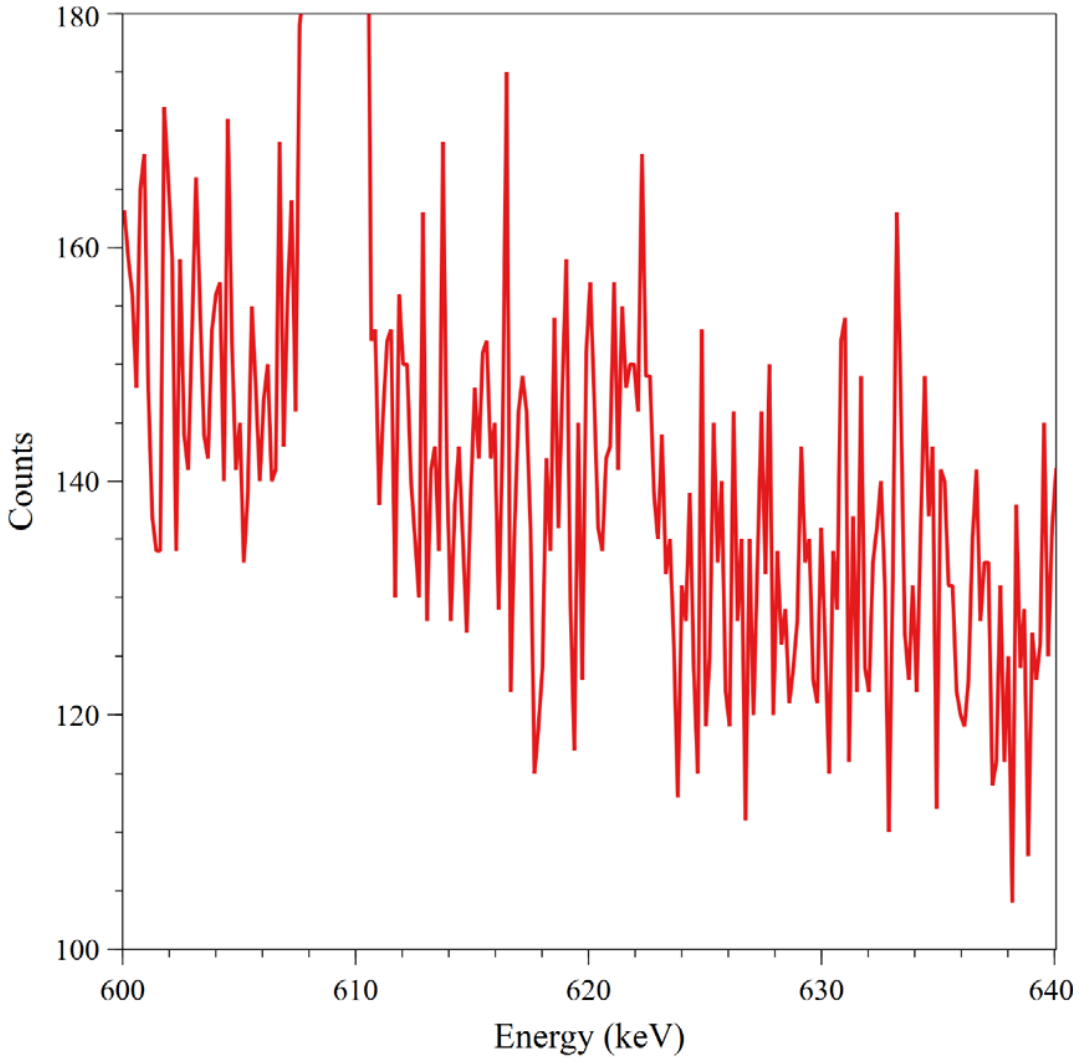

Figure S.20. Gamma spectrum (600 – 640 keV) of the collected HPLC fraction representing the column dead-volume (R_t = 0 – 2 min.) Depicted are gamma emission peaks corresponding to ^{214}Bi (609.2 keV, off-scale), and ^{106}Ru (622 keV).

6. Radiography

Qualitative Radiographic Observations of Filters Bearing the ^{106}Ru contaminant: Filter material contaminated with ^{106}Ru produce noticeably darker images when exposed to phosphor imaging plates. More importantly, the activity appears to be uniformly distributed. This is consistent with aqueous and ethanolic extraction experiments of filter pieces, which showed ^{106}Ru partitioning with very good reproducibility.

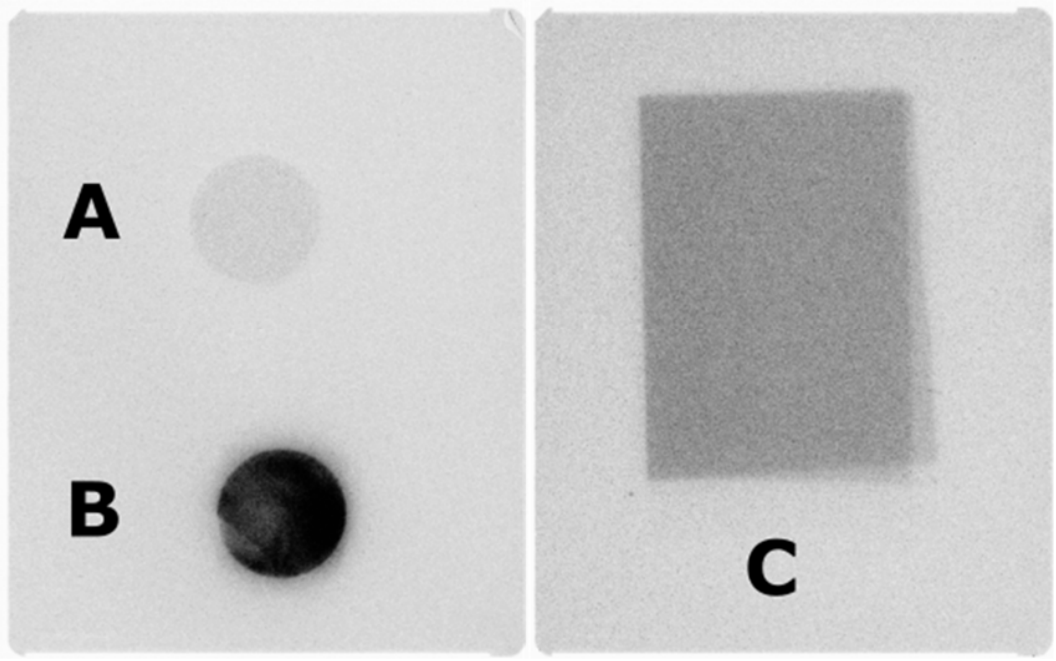

Figure S.21. (A) Blank and (B) ^{106}Ru contaminated monitoring network samples from Germany, pressed into standard cylindrical geometries. (C) Filter from the Swedish monitoring network.

Radio-Thin Layer Chromatography:

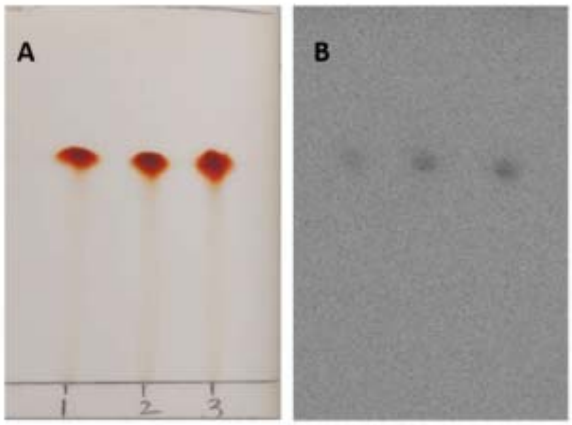

Figure S.22. Preparative-scale TLC (silica) depicting the elution of $[Ru(ttpy)_2](PF_6)_2$ (A) and its subsequent autoradiographic image (B). Reaction products pertain to: direct reaction with a filter piece (left); reaction with aqueous extract of filter piece (center); reaction with filter piece after aqueous wash (right). SiO2 substrate using an acetonitrile/potassium nitrate (7:1) mobile phase.

Appendix C

Publication IV

Supporting Information

Non-Natural Ruthenium Isotope Ratios of the Undeclared 2017 Atmospheric Release consistent with Civilian Nuclear Activities

Supplementary Information

Non-natural ruthenium isotope ratios of the undeclared 2017 atmospheric release consistent with civilian nuclear activities

Hopp & Zok *et al.*

Supplementary Notes

Supplementary Note 1. Analyses

To estimate the true external reproducibility of used air filter samples, standard deviation (2 s.d.) of the Ru isotope ratios determined for the reference air filters can be calculated (Supplementary Table 3). This more conservative uncertainty estimate using the standard deviation (2 s.d.) on the Ru isotope ratios of all four reference air filters may include some natural variations of the Ru isotopic composition in the atmospheric Ru over time (i.e., atmospheric Ru may partly originate from vehicle catalytic converters that may have led to isotope fractionation). However, the overall good agreement of all four filter samples collected from 2015 to 2018 can be used to describe and characterize the general isotopic composition of "background Ru" in the atmosphere over Vienna, Austria (Supplementary Table 3). Measurements of 10 ppb and 1 ppb solutions of the standard solution and several of the air filters show good reproducibility and accuracy of the measurements and no systematic differences due to low amount of Ru analyzed by 1 ppb solution measurements (Supplementary Figure 2; Supplementary Tables 2 and 3).

The air filter containing the non-natural Ru from the nuclear release in 2017 could also be analyzed twice, using 10 ppb and 1 ppb solutions, respectively. The two measurements agree very well with each other and reveal highly non-natural Ru isotopic composition of the Ru collected by this air filter for all Ru isotope ratios (Supplementary Table 3).

Supplementary Note 2. Isotopic composition of fission-generated Ru

Supplementary Table 4 summarizes the Ru isotopic composition of fission-generated Ru from different reactor types and the thermal neutron fission yields expected for low-burnup ^{239}Pu production. These values were derived from actual measurements of nuclear fuels, nuclear waste, contaminated ground water, or calculated based on fission product yields[1-4]. Fission-

generated Ru does not have significant abundances of ^{96}Ru, ^{98}Ru, and ^{99}Ru, because long-lived or stable molybdenum and technetium isotopes inhibit the beta-decay along the respective isobars, respectively. Artificial generation of these lighter Ru isotopes are possible at trace levels only due to (rather improbable) independent fission events yielding these Ru isotopes directly (or by the extremely slow decay of ^{99}Tc, respectively). In contrast, the heavier Ru isotopes (^{101}Ru, ^{102}Ru, and ^{104}Ru) are produced in higher abundances than the natural abundances because their production path along the isobar is not blocked by any long-lived or stable isotope. The isotopic deviation of fission-generated Ru vs. naturally abundant Ru is greatest for the isotope ^{101}Ru (Supplementary Table 4). Hence, the ^{i}Ru/^{101}Ru ratios can be used to distinguish between various origins of fission-generated Ru and thus were favored for the illustration of the nuclear impact on the isotopic Ru composition in Fig. 1.

Available data of ^{102}Ru/^{101}Ru in low-burnup nuclear fuel[2] and the Hanford Site groundwater[1] allow deriving an estimate for the expected Ru isotopic composition generated during the production of weapons-grade ^{239}Pu (Supplementary Table 4). This estimate is in good agreement with the calculated ^{102}Ru/^{101}Ru of ^{235}U thermal neutron fission yields, with minor contributions of ^{239}Pu thermal neutron fission (Supplementary Table 4). The estimated ^{102}Ru/^{101}Ru ratio for Ru produced during ^{239}Pu production is different from any of the ^{102}Ru/^{101}Ru signatures of civilian reactors (Supplementary Table 4). Moreover, during low-burnup and thermal neutron fission of ^{235}U or ^{239}Pu, no significant amount of ^{100}Ru is produced, hence, the ^{100}Ru/^{101}Ru ratio of Ru from civilian reactors is also a distinctive signature for tracing the origin of fission-generated Ru (Supplementary Table 4).

Supplementary Note 3. Ru isotopic fingerprints of various reactor types

In preparation of the German nuclear waste repository, the ‘Gesellschaft für Anlagen- und Reaktorsicherheit’ (GRS)[4] modelled and published the isotopic inventory of all spent nuclear fuel from all reactor types that have ever been in operation in Germany. The link

https://www.grs.de/en/node/1749 will bring you to the root menu, from where the tabulated data can be found under "Anhang GRS-278." For this study, we used "Waste from the utilization of power reactors" (1 Abfälle aus der Nutzung von Leistungsreaktoren), "Irradiated nuclear fuel elements" (Bestrahlte Brennelemente), "Nuclear fuel" (Kernbrennstoff). The reactor types used for this study are "Pressurized water reactors" with both MOX and UO_2 as fuel (DWR-MOX and DWR-UO2, respectively), Boiling water reactors" (SWR-MOX and SWR-UO2, respectively), VVER-210 (KKR), and VVER-440 (KGR).

The enrichment and burnup parameters used in the GRS modelling are tabulated in Supplementary Table 5. Chemical impurities are listed in Supplementary Table 6. Fuel cladding was Zircaloy 4. Nuclear cross sections were taken from the library ENDF/B VI.

Supplementary Note 4. Estimate of non-natural Ru fraction

The non-natural Ru isotopic composition in the air filter can be explained by mixing of fission-generated Ru from the undeclared atmospheric release in 2017 with natural Ru. The determined isotopic composition falls closest to mixing lines of the Ru expected to be produced by a VVER reactor and natural Ru. The fraction of fission-generated Ru required can be estimated by mass-balance calculations using the calculated Ru isotope abundances (Supplementary Table 7) and is, depending on the Ru isotope used in the calculation, ~66-90 % (excluding ^{104}Ru due to possible larger interference effects from ^{104}Pd). This means that 10 to 34 % of the Ru analyzed in the sample solution was natural atmospheric Ru collected from the air or added as analytical blank during digestion and chemical separation (despite using ultra-high-purity chemicals). In any case, the majority of the Ru analyzed in this filter sample was generated in a nuclear reactor.

To better estimate the absolute amount of Ru that was collected by the air filter station in Vienna, Austria, during the week of the 2017/09/28 to 2017/10/04, we analyzed a small aliquot (2 %) of the sample solution for its Ru concentration using a ThermoScientific *X-Series 2* quadrupole ICPMS at the Institut für Planetologie in Münster. The measured intensity of the

sample solution was compared to a standard solution to estimate the total amount of Ru in the sample aliquot. To calculate a true estimate of the Ru content, the non-natural isotopic composition of the Ru in the air filter has to be taken into account (Supplementary Table 7). After correction for the non-natural isotopic composition, the amount of Ru in the sample solution is estimated to be ~5 ng (±20 %). Hence, during chemical separation and removal of Mo and Pd interferences, up to 50 % of the Ru was lost. If we assume that ~66 to 90 % of the total Ru trapped on the filter is fission-generated, it translates to 3-4.5 ng in the ~2.5 g filter material digested (Supplementary Table 1). Since the fission-generated Ru was homogeneously distributed (as shown in [5]), we can estimate the total amount of fission-generated Ru collected in the complete filter (total mass 9.7 g) to be 11.6-17.5 ng. The total amount of Ru released into the atmosphere during the undeclared release is not well known, but can be estimated to ~110 g, based on the Ru isotopic composition of spent fuel and the ^{106}Ru source term of 250 TBq. In combination with these estimations, a fraction of ~1x10^{-10} of the total released stable Ru and ~8 x10^{-12} of the radioactive Ru was collected on the air filter with 94444 m³ of air collected from 2017/09/28 to 2017/10/04.

The radioactive ^{106}Ru content is estimated to be 250 TBq (specific activity of 1.22x10^{14} Bq/g, equals to 2 g)[5]. However, the total amount of Ru on the filter is measured with 2.03 kBq (equal to 16.6 pg). The estimated mass of ^{103}Ru released from the source is about 60 µg.

Supplementary Note 5. Russia's nuclear power reactor fleet

At the time of the incident, 35 nuclear power reactors were listed as active in the Russian Federation (Supplementary Table 8; [6]). The VVER-210 is the discontinued lower-power version of the VVER family, whereas VVER-440 is still frequently used. The related isotopic characteristics of both reactor types illustrate the great similarities within the early VVER families (Fig. 3). The reactors of the Russian power reactor fleet are operated with different grades of enriched uranium. Fuel for VVER-1000 reactors is enriched to 4.3 % ^{235}U; VVER-

440 fuel to 3.6 %; fuel for High Power Channel-type Reactors (RBMK) is enriched to 2.0 %; and the fast breeder reactor BN-600 fuel to 20 % [6].

According to Bolshov[7], spent nuclear fuel from VVER-440 and BN-600 reactors is reprocessed at the Production Association Mayak, whereas VVER-1100 fuel is sent for centralized wet storage at the Krasnoyarsk MCC (information as of 2007). Fuel from RBMK and EPG reactors is stored in the NPP repositories. Russia also possesses a significant inventory of spent nuclear fuel from its naval fleet, which is also processed at the Mayak facility[7].

Supplementary Figures

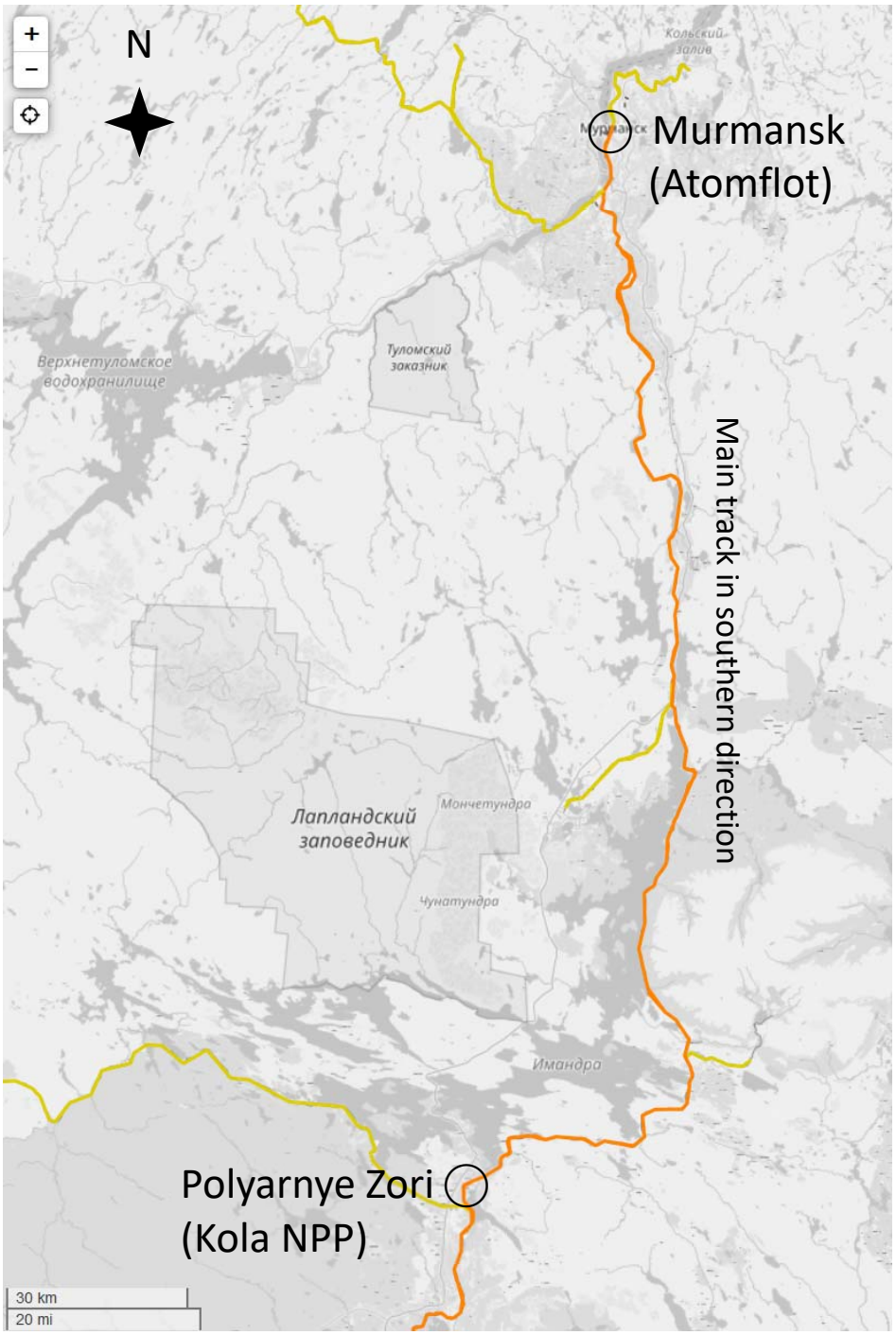

Supplementary Figure 1. Main railway connections on the Kola Peninsula that may be used to connect Murmansk in southern direction. Data © OpenStreetMap contributors (ODbL), map image OpenStreetMap/OpenRailwayMap (CC-BY-SA 2.0)[8].

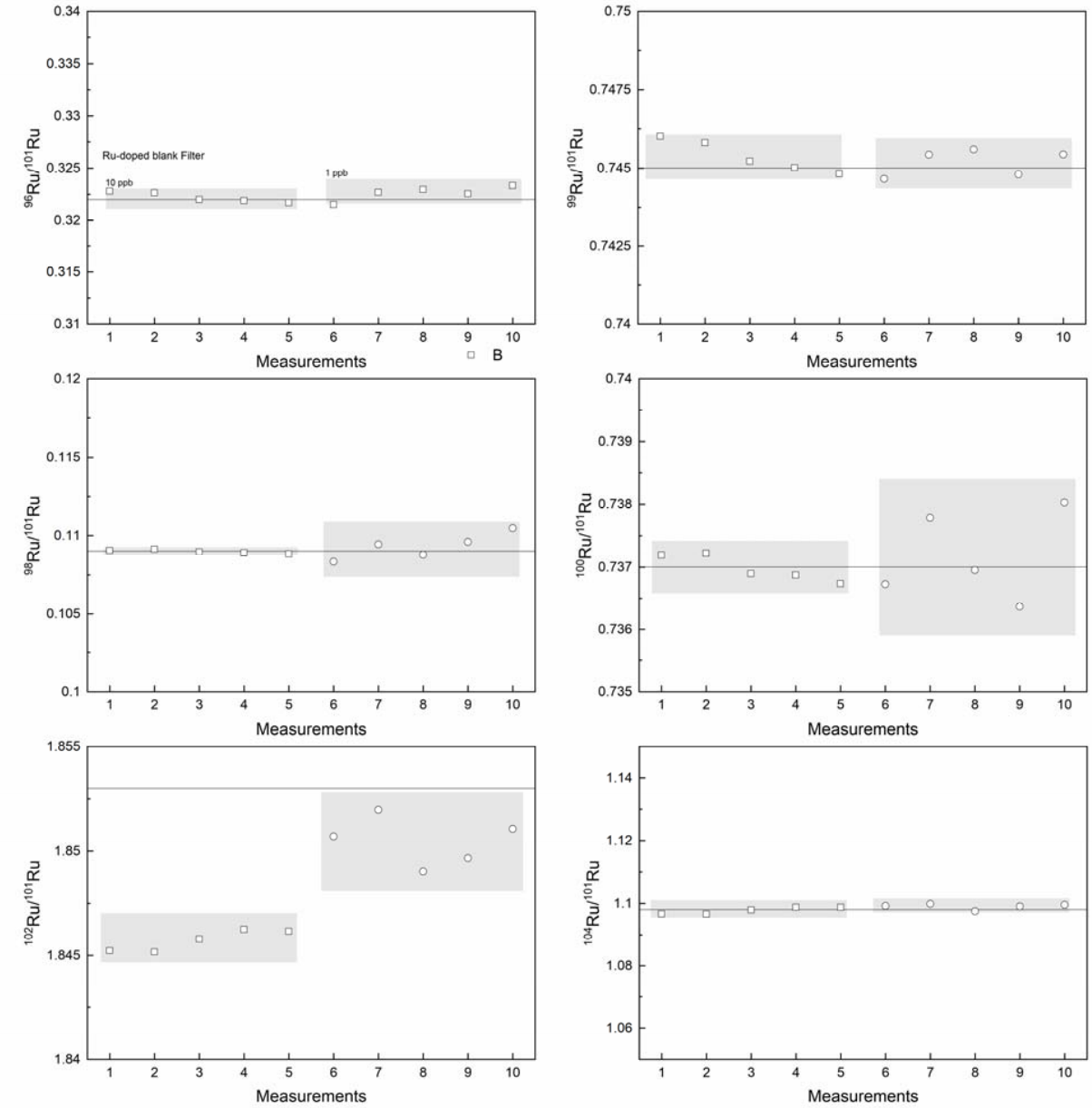

Supplementary Figure 2. Reproducibility and accuracy of Ru isotopic composition measurements of a Ru-doped air filters by MC-ICPMS. Gray boxes give the standard deviation (2 s.d.) on the determined isotope ratios for 10 ppb and 1 ppb solution measurements, respectively. The solid lines define the natural Ru isotope composition[9]. Deviation from the natural $^{102}Ru/^{101}Ru$ is produced by larger Pd interferences during the measurements of the 10 ppb solution.

Supplementary Tables

Supplementary Table 1. Air filter collection dates, passed air volume, weights of samples, and measured activity of ^{103}Ru and ^{106}Ru.

Start of collection	End of collection	Weight [g]	Passed air volume [m³]	^{103}Ru/^{106}Ru acitivity [Bq]
2015/07/19	2015/07/19	2.49909	20000	-
2017/09/27	2017/09/28	2.48189	20000	-
2017/09/28	2017/10/04	2.51576	94444	0.66/2030 (as of 2017/09/26)
2018/01/24	2018/01/25	2.53357	20000	-
2018/02/26	2018/02/27	2.46478	19099	-
Blank filter		2.4895	0	-

Supplementary Table 2. Ruthenium isotopic composition of the Alfa Aesar standard solutions and Ru-doped blank filter measured by MC-ICPMS. Instrumental mass bias was corrected by normalizing the bracketing standards to $^{99}Ru/^{101}Ru$ of 0.745 and using the average isotope fractionation factor (β) of the bracketing standards on the sample measurements (for details see Supplementary Note 2).

Sample	n	$^{96}Ru/^{101}Ru$	$^{98}Ru/^{101}Ru$	$^{99}Ru/^{101}Ru$	$^{100}Ru/^{101}Ru$	$^{102}Ru/^{101}Ru$	$^{104}Ru/^{101}Ru$
Alfa Aesar standard							
10 ppb (2 s.d.)	103	0.3220(3)	0.1090(2)	0.7451	0.7370(1)	1.8532(4)	1.0978(3)
1 ppb (2 s.d.)	74	0.321(2)	0.109(1)	0.7451	0.737(1)	1.854(2)	1.098(2)
Ru-doped blank Filter							
10 ppb		0.323	0.109	0.746	0.737	1.845	1.097
10 ppb		0.323	0.109	0.746	0.737	1.845	1.097
10 ppb		0.322	0.109	0.745	0.737	1.846	1.098
10 ppb		0.322	0.109	0.745	0.737	1.846	1.099
10 ppb		0.322	0.109	0.745	0.737	1.846	1.099
Average (2 s.d.)	5	0.322(1)	0.1090(2)	0.745(1)	0.7370(4)	1.846(1)	1.098(2)
1 ppb		0.322	0.108	0.745	0.737	1.851	1.099
1 ppb		0.323	0.109	0.745	0.738	1.852	1.100
1 ppb		0.323	0.109	0.746	0.737	1.849	1.097
1 ppb		0.323	0.110	0.745	0.736	1.850	1.099
1 ppb		0.323	0.110	0.745	0.738	1.851	1.100
Average (2 s.d.)	5	0.323(1)	0.109(2)	0.745(1)	0.737(1)	1.850(1)	1.099(2)

Supplementary Table 3. Ruthenium isotopic composition of air filters measured by MC-ICPMS. Instrumental mass bias was corrected by normalizing the bracketing standards to $^{99}Ru/^{101}Ru$ of 0.745 and using the average isotope fractionation factor (β) of the bracketing standards on the sample measurements (for details see Supplementary Note 2). Denoted errors (parentheses) are the standard error (2 s.e.) for n < 3 (measurements) or the standard deviation (2 s.d.) for n ≥ 3.

Sample	n	$^{96}Ru/^{101}Ru$	$^{98}Ru/^{101}Ru$	$^{99}Ru/^{101}Ru$	$^{100}Ru/^{101}Ru$	$^{102}Ru/^{101}Ru$	$^{104}Ru/^{101}Ru$
Reference filters							
2015/07/19-2015/07/20							
1 ppb		0.330	0.111	0.786	0.735	1.848	1.096
1 ppb		0.331	0.112	0.785	0.736	1.847	1.095
1 ppb		0.328	0.110	0.784	0.734	1.849	1.097
Average (2 s.d.)	3	0.330(3)	0.111(3)	0.785(2)	0.735(2)	1.848(1)	1.096(2)
2017/09/27-2017/09/28							
1ppb (2 s.e.)	1	0.3211(1)	0.1150(1)	0.762(1)	0.743(1)	1.848(1)	1.095(1)
2018/01/24-2018/01/25							
10 ppb		0.322	0.113	0.787	0.737	1.852	1.098
1 ppb		0.324	0.114	0.788	0.737	1.851	1.096
1 ppb		0.322	0.112	0.784	0.736	1.854	1.100
1 ppb		0.322	0.113	0.787	0.737	1.852	1.098
1 ppb		0.324	0.114	0.787	0.737	1.853	1.097
1 ppb		0.323	0.112	0.786	0.737	1.852	1.098
Average (2 s.d.)	6	0.323(2)	0.113(1)	0.787(3)	0.7369(8)	1.853(2)	1.098(3)
2018/02/26-2018/02/27							
10 ppb		0.325	0.113	0.801	0.736	1.849	1.096
1 ppb		0.324	0.111	0.802	0.735	1.847	1.095
1 ppb		0.324	0.111	0.802	0.735	1.848	1.096
Average (2 s.d.)	3	0.3244(4)	0.112(3)	0.802(1)	0.735(1)	1.848(2)	1.096(2)
Average all filters (2 s.d.)	4	0.325(8)	0.113(4)	0.784(32)	0.738(7)	1.849(4)	1.096(2)
Non-natural Ru air filter							
2017/09/28-2018/10/04							
10 ppb		0.0616(1)	0.02048(8)	0.1424(2)	0.2161(2)	1.1306(2)	0.6894(1)
1 ppb		0.0619(3)	0.0207(4)	0.1427(3)	0.2164(3)	1.1300(4)	0.6888(2)
Wdt. Average	2	0.0616(1)	0.0205(1)	0.1425(14)	0.2162(1)	1.131(3)	0.689(3)

Supplementary Table 4. Ruthenium isotopic compositions of civilian reactor types, low-burnup nuclear fuel, Hanford Site groundwater, and ^{235}U thermal fission yields.

Type of production	$^{96}Ru/^{101}Ru$	$^{98}Ru/^{101}Ru$	$^{99}Ru/^{101}Ru$	$^{100}Ru/^{101}Ru$	$^{102}Ru/^{101}Ru$	$^{104}Ru/^{101}Ru$
PWR[a]-MOX[b]	0	0	0	0.143	1.171	1.129
BWR[c]-MOX	0	0	0	0.137	1.155	1.109
PWR-UO_2[d]	0	0	0	0.188	1.08	0.775
BWR-UO_2	0	0	0	0.182	1.078	0.792
VVER[e] 440	0	0	0	0.108	0.999	0.682
VVER[e] 210	0	0	0	0.086	0.996	0.733
low-burnup nuclear fuel[f]	0	0	0	-	0.826	-
Hanford Site groundwater[g]	0	0	0	-	0.801(21)	-
^{235}U thermal fission[h]	0	0	0	-	0.829	-
^{239}Pu thermal fission[h]	0	0	0	-	0.984	-

[a]Pressurized water reactor, after [5], [b]Mixed oxide fuel, after [5], [c]Boiling water reactor, after [5], [d]Uranium dioxide fuel, after [5], [e]Water-water energetic reactor, after [5], [f]Average of values from[2], [g]Average of Hanford Site groundwater samples from [1], [h]Calculated or measured thermal neutron fission yields following[3].

Supplementary Table 5. Enrichment and burn up parameters for the simulated reactor types.[4]

Reactor type –Fuel type	Nuclide	U enrichment or Pu/U composition %	Burnup GWd/t heavy metal
PWR-MOX	Pu total Nat. U	8.6 91.4	55
BWR-MOX	Pu total Nat. U	6.3 93.6	50
PWR-UO_2	^{235}U	4.4	55
BWR-UO_2	^{235}U	3.5	50
VVER 440	^{235}U	3.6	30
VVER 210	^{235}U	2.0	20

Supplementary Table 6. Fuel impurities in the fuel.[4]

Impurity	F	H_2O	B	Fe	Si	Ni	N	C	Cl	Ca	Ag	Bi	Co	Cu	Mg	Mo
mg/kg	4	2	0.5	15	6	3.5	30	4	4.5	10	5	5	5	5	5	5

Impurity	Na	Pb	Sn	V	Zn	Ti	Th	Ta	P	W	Li	Al	K	Cr	Mn
mg/kg	5	5	5	5	5	5	5	5	5	5	1	21	10	3	1

Supplementary Table 7. Ruthenium isotope abundances of air filter samples and fission-generated Ru from VVER reactors relative to natural Ru abundances used in Fig. 2.

Sample	^{96}Ru [%]	^{98}Ru [%]	^{99}Ru [%]	^{100}Ru [%]	^{101}Ru [%]	^{102}Ru [%]	^{104}Ru [%]
Natural Ru[a]	5.54(14)	1.87(3)	12.76(14)	12.60(7)	17.06(2)	31.55(14)	18.62(27)
Alfa Aesar standard	5.49(1)	1.859(3)	12.706(2)	12.567(2)	17.053(3)	31.603(5)	18.721(4)
Ru-doped blank filter	5.50(2)	1.861(4)	12.73(2)	12.583(8)	17.074(2)	31.51(1)	18.74(3)
Reference filters							
2015/07/19-2015/07/20	5.59(4)	1.88(5)	13.29(3)	12.45(2)	16.935(2)	31.30(5)	18.56(5)
2017/09/27-2017/09/28	5.46(1)	1.95(2)	12.96(1)	12.62(1)	16.99(1)	31.41(1)	18.61(1)
2018/01/24-2018/01/25	5.46(2)	1.91(2)	13.31(5)	12.47(1)	16.922(7)	31.35(4)	18.58(5)
2018/02/26-2018/02/27	5.483(1)	1.88(4)	13.55(3)	12.43(1)	16.90(2)	31.236(5)	18.52(2)
Average all filters (2 s.d.)	5.50(12)	1.91(7)	13.28(48)	12.49(18)	16.94(8)	31.32(15)	18.57(7)
Non-natural Ru air filter							
2017/09/28-2017/10/04	1.89(1)	0.63(1)	4.37(1)	6.63(1)	30.67(1)	34.67(2)	21.13(2)
VVER[b] reactors							
440	0	0	0	4.03	29.40	33.96	32.61
210	0	0	0	5.96	32.77	35.32	25.95

[a]Data from [9], [b]Water-water energetic reactor data calculated from [4].

Supplementary Table 8. Russia's power reactors (active in 2017), modified after[6].

Reactor/NPP	Type	MWe net, each	Commercial operation since	Licensed to, or scheduled closure
Balakovo 1	VVER-1000/320	988	5/86	2043
Balakovo 2	VVER-1000/320	988	1/88	2033
Balakovo 3	VVER-1000/320	988	4/89	2049
Balakovo 4	VVER-1000/320	988	12/93	2053
Beloyarsk 3	BN-600 FBR	560	11/81	2025
Beloyarsk 4	BN-800 FBR	789	10/16	2056
Bilibino 1-4	LWGR EGP-6	11 × 4	12/74-1/77	12/2021
Kalinin 1	VVER-1000/338	988	6/85	2045
Kalinin 2	VVER-1000/338	988	3/87	2047
Kalinin 3	VVER-1000/320	988	11/2005	2065
Kalinin 4	VVER-1000/320	988	9/2012	2072
Kola 1	VVER-440/230	432	12/73	2033
Kola 2	VVER-440/230	411	2/75	2029
Kola 3	VVER-440/213	440	12/82	2027
Kola 4	VVER-440/213	440	12/84	2039
Kursk 1	RBMK	971	10/77	2022
Kursk 2	RBMK	971	8/79	2024
Kursk 3	RBMK	971	3/84	2029
Kursk 4	RBMK	925	2/86	2031
Leningrad 1	RBMK	971	11/74	2018
Leningrad 2	RBMK	971	2/76	2021
Leningrad 3	RBMK	971	6/80	2025
Leningrad 4	RBMK	925	8/81	2026
Novovoronezh 4	VVER-440/179	385	3/73	2032
Novovoronezh 5	VVER-1000/187	950	2/81	2035
Novovoronezh II-1*	VVER-1200/392M	1114	2/2017	2077
Smolensk 1	RBMK	925	9/83	2028
Smolensk 2	RBMK	925	7/85	2030
Smolensk 3	RBMK	925	1/90	2050
Rostov 1	VVER-1000/320	990	3/2001	2030?
Rostov 2	VVER-1000/320	990	10/2010	2040
Rostov 3	VVER-1000/320	1011	9/2015	2045
Total: 35			**26,911 MWe**	

Supplementary References

1 Dresel, P. E., Evans, J. C. & Farmer, O. T. *Investigation of isotopic signatures for sources of groundwater contamination at the Hanford Site*, https://www.pnnl.gov/main/publications/external/technical_reports/pnnl-13763.pdf (2002).

2 Byerly, B. *et al.* Determination of initial fuel state and number of reactor shutdowns in archived low-burnup uranium targets. *J. Radioanal. Nucl. Chem.* **307**, 1871-1876 (2016).

3 Shima, M., Thode, H. G. & Tomlinson, R. H. Cumulative yields of stable and long-lived isotopes of ruthenium and palladium in neutron-induced fission. *Can. J. Phys.* **56**, 1340-1352 (1978).

4 Pfeiffer, F. *et al. Abfallspezifikation und Mengengerüst, GRS-278 (in German)*, https://www.grs.de/en/node/1749 (2011).

5 Masson, O. *et al.* Airborne concentrations and chemical considerations of radioactive ruthenium from an undeclared major nuclear release in 2017. *Proc. Natl. Acad. Sci. USA* **116**, 16750-16759 (2019).

6 World Nuclear Association. *Russia's nuclear fuel cycle*, https://www.world-nuclear.org/information-library/country-profiles/countries-o-s/russia-nuclear-fuel-cycle.aspx (2019).

7 Bolshov, L. *Safety for nuclear fuel cycle in the Russian Federation*, http://www.oecd-nea.org/nsd/workshops/fcsafety/proceedings/documents/Session_3_2_Presentation_4.pdf (2007).

8 *Open Railway Map*, https://www.openrailwaymap.org/ (2019).

9 Berglund, M. & Wieser, M. E. Isotopic compositions of the elements 2009 (IUPAC technical report). *Pure Appl. Chem.* **83**, 397-410 (2011).

Appendix D

Publication V

Supporting Information

Determination of Characteristic vs. Anomalous $^{135}Cs/^{137}Cs$ Isotopic Ratios in Radioactively Contaminated Environmental Samples

Supporting Information

Determination of Characteristic vs. Anomalous $^{135}Cs/^{137}Cs$ Isotopic Ratios in Radioactively Contaminated Environmental Samples

Dorian Zok,[1] Tobias Blenke,[1] Sandra Reinhard,[1] Sascha Sprott,[1] Felix Kegler,[1] Luisa Syrbe,[1]

Rebecca Querfeld,[1] Yoshitaka Takagai,[2] Vladyslav Drozdov,[3] Ihor Chyzhevskyi,[3]

Serhii Kirieiev,[3] Brigitte Schmidt,[4] Wolfram Adlassnig,[4] Gabriele Wallner,[5] Sergiy Dubchak,[6]

Georg Steinhauser[1*]

[1] Leibniz Universität Hannover, Institute of Radioecology and Radiation Protection, 30419 Hannover, Germany

[2] Fukushima University, Faculty of Symbiotic Systems Science, Fukushima 960-1296, Japan

[3] State Specialized Enterprise "Ecocentre" (SSE "Ecocentre"), Chernobyl 07270, Ukraine

[4] University of Vienna, Faculty of Life Sciences, Cell Imaging and Ultrastructure Research, 1090 Vienna, Austria

[5] University of Vienna, Faculty of Chemistry, Institute of Inorganic Chemistry, 1090 Vienna, Austria

[6] State Specialized Enterprise "Radon Association", Kyiv 03083, Ukraine

*Correspondence to: steinhauser@irs.uni-hannover.de

Table of Contents

1. Supporting Tables

1.1 Sample Materials

Table S1: Overview of the moss and fish samples from the Chernobyl cooling pond and its vicinity. Date of measurement is the date of reference for the activities. Dates are given as dd/mm/yyyy.

Name	Fresh mass [g]	Ash mass [g]	Used mass [g]	Location	Species	Activity conc. ^{137}Cs $[Bq/g]_{Fresh}$	Date of measurement
Wels catfish 1	341.9	37.8	2.05514	Pond	*Silurus glanis*	9.19 ± 0.20	08/10/2018
Wels catfish 1	341.9	37.8	2.09562	Pond	*Silurus glanis*	9.19 ± 0.20	08/10/2018
Wels catfish 1	341.9	37.8	2.07429	Pond	*Silurus glanis*	9.19 ± 0.20	08/10/2018
Wels catfish 2	1260.4	122	2.20130	Pond	*Silurus glanis*	5.22 ± 0.12	08/10/2018
Wels catfish 3	626.6	59.4	2.11406	Pond	*Silurus glanis*	4.29 ± 0.10	10/10/2018
Moss 1 CEZ	0.1125	-	0.02647	Pond island	*Bryum imbricatum*	248 ± 13	09/10/2018
Moss 2 CEZ	0.484	-	0.33193	Pond island	*Bryum argenteum*	37.1 ± 6.3	09/10/2018
Moss 3 CEZ	0.1805	-	0.08597	Pond island	*Bryum cf. badium*	157 ± 9.06	09/10/2018
Moss 4 CEZ	0.2562	-	0.25356	Southwest bank	*Marchantia polymorpha*	185 ± 31	10/10/2018
Moss 5 CEZ	0.1414	-	0.05434	Southwest bank	*Bryum x intermedium*	297 ± 20	10/10/2018
Zander 1	159.1	8.5276	6.00560	Pond	*Sander lucioperca*	4.74 ± 0.16	31/07/2020
Zander 2	127.5	7.45145	3.36806	Pond	*Sander lucioperca*	2.66 ± 0.11	03/08/2020
Zander 3	122.2	8.48135	2.14952	Pond	*Sander lucioperca*	3.61 ± 0.15	03/08/2020

Table S2: Overview of the moss samples from Fukushima prefecture. Date of measurement is the date of reference.

Name	Fresh mass [g]	Dry mass [g]	Used mass [g]	Location	Species	Activity concentration ^{137}Cs $[Bq/g]_{Dry}$	Date of measurement
Moss 1 JP	2.75	2.59374	1.11866	Okuma Town	*Dichodontium cf pellucidum*	2,530 ± 13	02/07/2019
Moss 2 JP	11.40	10.01203	2.01922	Okuma Town	*Plagiomnium cuspidatum*	610 ± 2.3	02/07/2019
Moss 3 JP	5.59	5.37601	1.02753	Okuma Town	*Hydrogonium javanicum*	1675 ± 8	02/07/2019
Moss 4 JP	12.0	11.72470	1.44368	Futaba Town	*Hydrogonium javanicum*	1,023 ± 6	23/07/2019
Moss 5 JP	16.8	16.36428	1.45720	Futaba Town	*Brachythecium sakuraii*	934 ± 5	23/07/2019
Moss 6 JP	6.09	5.96036	1.25518	Futaba Town	*Ptychomitrium sinense*	1,860 ± 11	23/07/2019
Moss 7 JP	11.2	11.09095	11.09095	Iwaki Town	*Dichodontium pellucidum*	22.0 ± 0.53	30/07/2019
Moss 8 JP	13.5	13.32702	1.67838	Iwaki Town	*Trichostomum weisioides*	47.5 ± 0.58	30/07/2019

Table S3: Overview of trinitite samples. Date of measurement is the date of reference.

Sample name	Size [cm]			Mass [g]	Activity conc. ^{137}Cs [Bq/g]	Date of measurement
	Length	Width	Thickness			
Trinitite 1 US	4.52	2.47	0.98	6.25	5.27 ± 0.19	14/07/2020
Trinitite 2 US	4.42	2.09	1.11	6.35	9.15 ± 0.21	14/07/2020

Table S4: Overview of the samples of ashed human lung tissue from Vienna, Austria, that were used for pooling. Date of measurement is the date of reference.

Running no. after Schönfeld	Date of passing	Fresh mass [kg]	Ash mass [g]	Used mass [g]	Activity conc. ^{137}Cs $[Bq/g]_{Ash}$	Date of measurement
388	27/04/1963	1.25	15.1390	3.21430	0.12 ± 0.01	03/05/2018
505	01/06/1964	0.65	7.9000	4.85644	0.24 ± 0.03	25/04/2018
544	25/10/1964	1.1	11.3920	3.47686	0.35 ± 0.05	07/05/2018
604	01/06/1965	0.8	11.0860	4.49724	0.13 ± 0.02	11/05/2018
642	17/10/1965	0.7	8.445	1.07975	0.16 ± 0.01	30/04/2018
Lung AT				17.125	0.21 ± 0.03	

Table S5: Overview of the reference materials from IAEA.

Name	Sample Type	Mass [g]	Certified activity concentration ^{137}Cs [Bq/g]	Reference Date for Certification
IAEA 372 1*	Grass	1.22882	11.320 ± 0.360	01/06/2006
IAEA 372 2*	Grass	1.33706	11.320 ± 0.360	01/06/2006
IAEA 372 3*	Grass	1.25814	11.320 ± 0.360	01/06/2006
IAEA 372 4*	Grass	1.25972	11.320 ± 0.360	01/06/2006
IAEA 372 5*	Grass	1.25969	11.320 ± 0.360	01/06/2006
IAEA 372 6*	Grass	2.53396	11.320 ± 0.360	01/06/2006
IAEA 372 7*	Grass	1.24774	11.320 ± 0.360	01/06/2006
IAEA 330 1#	Spinach	5.01816	1.235 ± 0.035	15/10/2007
IAEA 330 2#	Spinach	5.01816	1.235 ± 0.035	15/10/2007
IAEA 330 3#	Spinach	5.89019	1.235 ± 0.035	15/10/2007

* Data from https://nucleus.iaea.org/sites/ReferenceMaterials/Pages/IAEA-372.aspx
# Data from https://nucleus.iaea.org/sites/ReferenceMaterials/Pages/IAEA-330.aspx

2. Measurement Parameters for ICP-QQQ-MS

Table S6: Elements and integration time for concentration determination.

Element	Isobar	Integration time [s]
Mo	95	0.0300
Sn	118	0.3000
Sb	121	0.3000
Cs	133	0.0300
Ba	137	0.0300

Table S7: Targeted isobars for isotope ratio measurement and mass bias correction.

Target isotope	Q1 Isobar	Q2 Isobar	Integration time [s]
^{133}Cs	133	133	0.9999
^{135}Cs	135	135	5.0001
^{137}Cs	137	137	5.0001
^{151}Eu	151	151	5.0001
^{153}Eu	153	153	5.0001

Table S8: ICP-QQQ-MS parameters for the concentration and isotope ratio measurements, respectively.

Parameter	Concentration	Isotope ratio
Sample Introduction		
Stabilisation time	40 s	15 s
Sample uptake	45 s, 0.3 rpm	30 s, 0.5 rpm
Probe rinse	90 s, 0.3 rpm	90 s, 0.3 rpm
Spectrum Acquisition		
Q2 peak pattern	3 Points	3 Points
Replicates	5	5
Sweeps/replicate	100	1000
Plasma	Low Matrix	
RF power		1550 W
RF matching		1.40 V
Sample depth		10.0 mm
Nebulizer gas		1.07 L/min
Nebulizer pump		0.10 rps
S/C temperature		2 °C
Makeup gas		0.25 L/min
Lenses		
Extract 1	-12.8 V	-23.0 V
Extract 2	-250 V	-250 V
Omega bias	-140 V	-145 V
Omega lens	9.4 V	8.6 V
Q1 exit	3.0 V	1.0 V
Cell focus	-3.0 V	1.0 V
Deflect	15.2 V	6.8 V
Cell entrance		-62 V
Cell exit		-51 V
Plate bias		-52 V
Q1		
Q1 bias	-9.0 V	-2 V
Q1 pre-filter	-9.5 V	-5.6 V
Q1 post-filter	-10.0 V	-10 V
Cell		
He flow		1 mL/min
3rd gas flow (N_2O)		6 % (0.6 mL/min)

1.2. Elemental Concentrations of Mo, Sn, Sb, Cs and Ba before and after Separation

Table S9: Masses and recovery rates of potential polyatomic interfering elements during measurement, before and after chemical separation.

Sample	Mo			Sn			Sb		
	Before [ng]	After [ng]	Recov. [%]	Before [ng]	After [ng]	Recov. [%]	Before [ng]	After [ng]	Recov. [%]
Wels catfish 1	44.3 ± 5.7	20.9 ± 1.2	47.2	20.9 ± 1.2	3.54 ± 0.19	16.9	17.8 ± 1.3	2.95 ± 0.36	16.5
Wels catfish 1	66.3 ± 0.6	13.8 ± 0.8	20.8	33.6 ± 0.8	5.32 ± 0.10	15.9	31.8 ± 1.2	3.00 ± 0.15	9.4
Wels catfish 1	95.7 ± 4.5	5.96 ± 0.95	6.2	30.2 ± 1.9	4.70 ± 0.22	15.6	31.8 ± 0.9	2.92 ± 0.44	9.2
Wels catfish 2	77.7 ± 8.7	70.9 ± 2.2	91.3	15.2 ± 0.8	2.50 ± 0.16	16.4	16.6 ± 1.3	2.89 ± 0.29	17.5
Wels catfish 3	31.4 ± 4.7	54.8 ± 1.6	174.5	15.5 ± 1.5	3.03 ± 0.22	19.6	21.5 ± 1.6	3.37 ± 0.17	15.7
Moss 1 CEZ	45.0 ± 7.2	19.6 ± 3.2	43.6	7.54 ± 0.50	2.60 ± 0.12	34.5	13.8 ± 1.9	4.04 ± 0.35	29.2
Moss 2 CEZ	89.2 ± 10.5	51.5 ± 2.6	57.8	14.3 ± 0.3	2.22 ± 0.14	15.6	34.0 ± 2.3	3.65 ± 0.30	10.7
Moss 3 CEZ	103 ± 5	50.5 ± 4.0	48.8	9.52 ± 0.49	2.33 ± 0.12	24.5	18.2 ± 1.1	2.96 ± 0.30	16.3
Moss 4 CEZ	61.0 ± 4.8	25.4 ± 0.9	41.6	8.79 ± 0.71	1.85 ± 0.19	21.0	24.7 ± 1.8	3.35 ± 0.36	13.6
Moss 5 CEZ	71.1 ± 12.4	28.8 ± 2.7	40.5	8.18 ± 0.73	2.29 ± 0.15	28.0	16.9 ± 1.6	2.89 ± 0.54	17.2
Zander 1	2139 ± 19	64.9 ± 0.9	3.0	441 ± 8	4.85 ± 0.09	1.1	192 ± 1	3.10 ± 0.20	1.6
Zander 2	80.0 ± 8.2	85.7 ± 2.4	107.2	42.3 ± 0.6	6.92 ± 0.07	16.4	103 ± 1	3.24 ± 0.14	3.1
Zander 3	78.7 ± 7.7	84.0 ± 1.2	106.8	35.0 ± 0.6	5.60 ± 0.17	16.0	146 ± 1	2.99 ± 0.06	2.0
IAEA 372 1	540 ± 12	10.1 ± 1.4	1.9	36.7 ± 1.3	2.21 ± 0.16	6.0	16.1 ± 2.1	3.36 ± 0.17	20.8
IAEA 372 2	555 ± 12	18.2 ± 1.3	3.3	30.5 ± 1.6	1.69 ± 0.08	5.5	15.6 ± 1.0	3.18 ± 0.30	20.4
IAEA 372 3	506 ± 9	25.4 ± 0.8	5.0	301 ± 1	4.85 ± 0.15	1.6	24.8 ± 0.7	2.95 ± 0.31	11.9
IAEA 372 4	532 ± 11	41.7 ± 1.6	7.8	50.4 ± 0.5	4.82 ± 0.10	9.6	18.9 ± 1.6	2.94 ± 0.30	15.6
IAEA 372 5	894 ± 14	20.6 ± 1.2	2.3	42.1 ± 0.6	4.84 ± 0.15	11.5	17.9 ± 0.6	2.98 ± 0.15	16.6
IAEA 372 6	1290 ± 32	22.2 ± 0.9	1.7	68.7 ± 1.3	5.43 ± 0.18	7.9	20.4 ± 1.1	2.97 ± 0.07	14.6
IAEA 372 7	529 ± 16	15.7 ± 1.0	3.0	30.4 ± 0.4	4.35 ± 0.05	14.3	24.7 ± 2.1	2.93 ± 0.17	11.9
IAEA 330 1	927 ± 6	4.65 ± 0.30	0.5	109 ± 2	5.63 ± 0.22	5.2	37.8 ± 0.4	2.93 ± 0.23	7.8

IAEA 330 2	736 ± 21	27.0 ± 0.6	3.7	87.3 ± 0.7	3.99 ± 0.14	4.6	34.6 ± 2.0	3.63 ± 0.12	10.5
IAEA 330 3	850 ± 15	50.1 ± 0.4	5.9	98.4 ± 1.1	4.77 ± 0.10	4.8	36.7 ± 0.4	2.95 ± 0.14	8.0
Moss 1 JP	3440 ± 140	13.8 ± 0.6	0.4	2696 ± 31	6.19 ± 0.06	0.2	292 ± 10	3.12 ± 0.28	1.1
Moss 2 JP	859 ± 62	35.7 ± 1.9	4.2	263 ± 10	6.66 ± 0.21	2.5	300 ± 53	2.95 ± 0.30	1.0
Moss 3 JP	1313 ± 67	24.5 ± 0.7	1.9	712 ± 14	4.14 ± 0.11	0.6	199 ± 27	2.98 ± 0.13	1.5
Moss 4 JP	1510 ± 48	19.6 ± 1.1	1.3	643 ± 9	4.76 ± 0.11	0.7	201 ± 24	2.94 ± 0.11	1.5
Moss 5 JP	1930 ± 110	16.0 ± 1.5	0.8	661 ± 6	4.38 ± 0.19	0.7	198 ± 21	2.89 ± 0.22	1.5
Moss 6 JP	1454 ± 46	21.5 ± 0.9	1.5	804 ± 15	4.36 ± 0.10	0.5	263 ± 27	2.98 ± 0.27	1.1
Moss 7 JP	6970 ± 330	42.2 ± 1.0	0.6	3051 ± 37	4.90 ± 0.17	0.2	687 ± 41	3.06 ± 0.24	0.4
Moss 8 JP	1710 ± 120	11.0 ± 0.8	0.8	402 ± 9	3.91 ± 0.14	1.0	193 ± 14	2.81 ± 0.27	1.5
Lung tissue AT	27390 ± 470	31.8 ± 2.9	0.1	91470 ± 230	2.66 ± 0.08	0.0	13340 ± 60	2.90 ± 0.22	0.0
Trinitite 1 US	2640 ± 130	4.48 ± 0.26	0.2	2338 ± 51	4.07 ± 0.13	0.2	2392 ± 61	3.29 ± 0.17	0.1
Trinitite 2 US	1280 ± 120	4.29 ± 0.50	0.3	1634 ± 28	4.23 ± 0.16	0.3	1419 ± 23	3.18 ± 0.14	0.2

Table S10: Masses and recovery rates of cesium and interfering barium before and after chemical separation.

Sample	Cs			Ba		
	Before [ng]	After [ng]	Recov. [%]	Before [ng]	After [ng]	Recov. [%]
Wels catfish 1	279 ± 5	277 ± 4	99.1	1225 ± 29	11.0 ± 0.3	0.9
Wels catfish 1	315 ± 20	230 ± 12	73.0	711 ± 14	16.2 ± 0.4	2.3
Wels catfish 1	325 ± 22	228 ± 21	70.3	994 ± 21	15.5 ± 0.1	1.6
Wels catfish 2	222 ± 5	209 ± 2	94.1	1276 ± 28	13.0 ± 0.3	1.0
Wels catfish 3	229 ± 8	64.3 ± 1.4	28.0	2417 ± 48	14.9 ± 0.3	0.6
Moss 1 CEZ	56.1 ± 3.4	45.3 ± 1.1	80.8	1358 ± 21	13.9 ± 0.2	1.0
Moss 2 CEZ	56.9 ± 3.3	43.5 ± 0.8	76.5	16780 ± 280	24.6 ± 0.4	0.1
Moss 3 CEZ	79.1 ± 2.1	65.2 ± 0.8	82.4	2861 ± 28	13.0 ± 0.1	0.5
Moss 4 CEZ	182 ± 4	161 ± 3	88.4	12180 ± 120	11.9 ± 0.1	0.1
Moss 5 CEZ	108 ± 4	89.9 ± 1.8	83.4	2674 ± 79	26.4 ± 0.8	1.0
Zander 1	437 ± 6	238 ± 4	54.5	6975 ± 57	4.51 ± 0.04	0.4
Zander 2	185 ± 2	144 ± 1	77.8	2195 ± 28	10.3 ± 0.1	0.5
Zander 3	158 ± 3	143 ± 1	90.5	1424 ± 27	5.33 ± 010	0.1
IAEA 372 1	71.7 ± 2.9	48.7 ± 0.4	67.9	40630 ± 380	43.1 ± 0.4	0.1
IAEA 372 2	70.5 ± 2.6	51.6 ± 0.4	73.2	41346 ± 46	11.7 ± 0.1	0.0
IAEA 372 3	67.1 ± 1.0	45.7 ± 1.8	68.1	39947 ± 15	11.4 ± 0.1	0.0
IAEA 372 4	122 ± 1	96.3 ± 1.8	79.0	42100 ± 200	11.3 ± 0.1	0.0
IAEA 372 5	65.4 ± 2.3	44.6 ±0.3	68.2	43440 ± 180	12.4 ± 0.1	0.0
IAEA 372 6	116 ± 3	97.6 ± 0.8	84.5	85630 ± 510	18.4 ± 0.1	0.0
IAEA 372 7	50.5 ± 2.1	3.98 ± 0.02	7.9	26420 ± 750	12.9 ± 0.1	0.0
IAEA 330 1	100 ± 3	79.5 ± 0.8	79.8	24110 ± 110	18.0 ± 0.1	0.1
IAEA 330 2	61.5 ± 1.6	56.9 ± 3.7	92.6	16160 ± 420	12.7 ± 0.1	0.1
IAEA 330 3	69.8 ± 1.2	51.7 ± 3.2	74.1	23760 ± 220	2.47 ± 0.02	0.0
Moss 1 JP	2770 ± 140	2241 ± 68	80.9	78700 ± 1300	26.0 ± 0.1	0.0
Moss 2 JP	3740 ± 140	3120 ± 300	83.5	65500 ± 830	18.3 ± 0.1	0.0
Moss 3 JP	2110 ± 50	2000 ± 130	94.9	58300 ± 1400	15.8 ± 0.1	0.0
Moss 4 JP	1728 ± 68	1660 ± 60	95.8	35460 ± 580	23.5 ± 0.1	0.1
Moss 5 JP	1631 ± 95	1600 ± 120	98.3	30540 ± 520	18.5 ± 0.1	0.1
Moss 6 JP	2240 ± 160	2090 ± 100	93.2	50800 ± 830	21.0 ± 0.2	0.0
Moss 7 JP	1916 ± 53	1854 ± 180	96.8	70630 ± 380	12.8 ± 0.1	0.0
Moss 8 JP	11970 ± 720	2170 ± 150	18.1	447900 ± 5800	4.79 ± 0.04	0.0
Lung AT	5590 ± 460	4230 ± 210	75.7	170700 ± 2400	13.0 ± 0.1	0.0
Trinitite 1 US	6460 ± 700	5830 ± 240	90.3	1463000 ± 26000	4.06 ± 0.02	0.0
Trinitite 2 US	6300 ± 360	6020 ± 320	95.6	1183000 ± 16000	43.65 ± 0.02	0.0

1.3 $^{135}Cs/^{137}Cs$ Isotope Ratio Time Dependence

Since the $^{135}Cs/^{137}Cs$ ratio, depends on the fairly short half-life of ^{137}Cs, the ratio shifts significantly over the decades. For certain samples, e.g., Chernobyl, Fukushima or trinitite, an exact release date can be defined. For the lung tissue, this is trickier, because the lungs have likely accumulated radiocesium over several years. Table S12 and Fig S5 show the shift of the ratio over time.

Table S11: $^{135}Cs/^{137}Cs$ isotope ratio values for various dates including analytical uncertainties.

Sample Date	$^{135}Cs/^{137}Cs$ 16/07/1945	$^{135}Cs/^{137}Cs$ 01/01/1963	$^{135}Cs/^{137}Cs$ 26/04/1986	$^{135}Cs/^{137}Cs$ 11/03/2011	$^{135}Cs/^{137}Cs$ 01/01/2020
Moss CEZ 1			0.272 ± 0.001	0.482 ± 0.003	0.591 ± 0.003
Moss CEZ 2			0.278 ± 0.028	0.493 ± 0.050	0.604 ± 0.061
Moss CEZ 3			0.269 ± 0.001	0.477 ± 0.001	0.584 ± 0.001
Moss CEZ 4			0.280 ± 0.005	0.497 ± 0.009	0.609 ± 0.011
Moss CEZ 5			0.274 ± 0.001	0.486 ± 0.001	0.595 ± 0.002
Wels catfish 1			0.281 ± 0.002	0.499 ± 0.004	0.611 ± 0.005
Wels catfish 1			0.277 ± 0.003	0.492 ± 0.006	0.603 ± 0.007
Wels catfish 1			0.275 ± 0.002	0.488 ± 0.003	0.598 ± 0.004
Wels catfish 2			0.277 ± 0.001	0.491 ± 0.002	0.602 ± 0.003
Wels catfish 3			0.288 ± 0.006	0.511 ± 0.010	0.626 ± 0.013
Zander 1			0.281 ± 0.004	0.498 ± 0.007	0.610 ± 0.008
Zander 2			0.283 ± 0.002	0.502 ± 0.003	0.615 ± 0.004
Zander 3			0.292 ± 0.003	0.518 ± 0.005	0.635 ± 0.006
IAEA 372 1			0.265 ± 0.001	0.469 ± 0.002	0.575 ± 0.002
IAEA 372 2			0.283 ± 0.015	0.502 ± 0.026	0.615 ± 0.032
IAEA 372 3			0.272 ± 0.001	0.483 ± 0.002	0.592 ± 0.003
IAEA 372 4			0.263 ± 0.008	0.466 ± 0.014	0.571 ± 0.017
IAEA 372 5			0.273 ± 0.004	0.485 ± 0.008	0.594 ± 0.010
IAEA 372 6			0.287 ± 0.000	0.509 ± 0.000	0.624 ± 0.001
IAEA 372 7			0.265 ± 0.003	0.470 ± 0.005	0.576 ± 0.007
IAEA 330 1			0.278 ± 0.008	0.493 ± 0.014	0.604 ± 0.017
IAEA 330 2			0.263 ± 0.010	0.466 ± 0.017	0.571 ± 0.021
IAEA 330 3			0.276 ± 0.030	0.490 ± 0.054	0.600 ± 0.066
Moss JP 1			0.197 ± 0.001	0.349 ± 0.001	0.428 ± 0.002
Moss JP 2			0.213 ± 0.013	0.378 ± 0.023	0.463 ± 0.028
Moss JP 3			0.195 ± 0.001	0.346 ± 0.002	0.424 ± 0.003
Moss JP 4			0.194 ± 0.001	0.344 ± 0.001	0.422 ± 0.001
Moss JP 5			0.196 ± 0.000	0.347 ± 0.000	0.426 ± 0.000
Moss JP 6			0.196 ± 0.001	0.347 ± 0.001	0.425 ± 0.002
Moss JP 7			0.198 ± 0.000	0.351 ± 0.000	0.430 ± 0.000
Moss JP 8			0.206 ± 0.003	0.366 ± 0.005	0.448 ± 0.007
Lung tissue AT	0.423 ± 0.039	0.648 ± 0.059	1.084 ± 0.105	1.922 ± 0.187	2.355 ± 0.229
Trinitite 1 US	0.084 ± 0.001	0.129 ± 0.001	0.216 ± 0.002	0.382 ± 0.003	0.468 ± 0.003
Trinitite 2 US	0.066 ± 0.001	0.101 ± 0.002	0.169 ± 0.003	0.300 ± 0.006	0.367 ± 0.007

2. Sample Figures

2.1 Chernobyl Samples

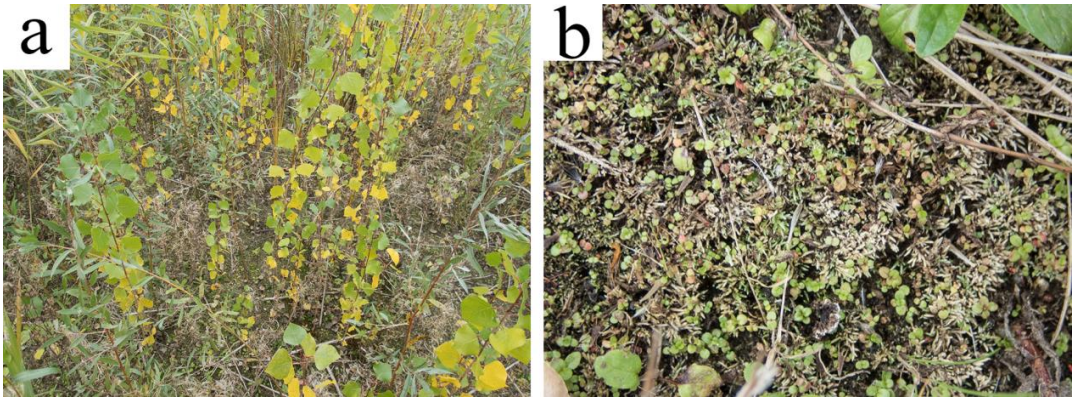

Figure S1: Moss 1 CEZ & 3 CEZ (a) and Moss 2 CEZ (b) on pond island.

Figure S2: Catch (a) 138 cm/ 13 kg wels catfish 1 and (b) 45 cm/ 0.65 kg zander 4 from CEZ.

2.2 Fukushima Samples

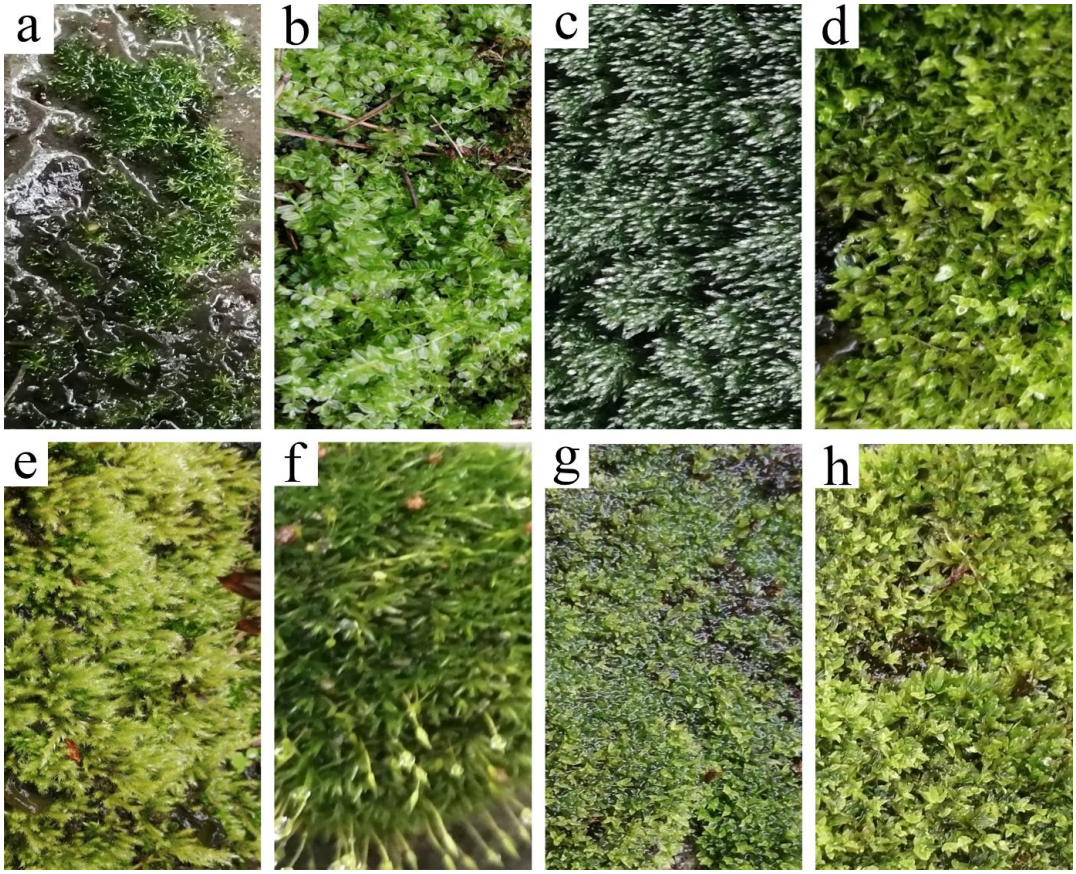

Figure S3: Moss 1 JP (a), Moss 2 JP (b), Moss 3 JP (c), Moss 4 JP (d), Moss 5 JP (e), Moss 6 JP (f), Moss 7 JP (g), Moss 8 JP (h)

2.3 Trinitite Samples

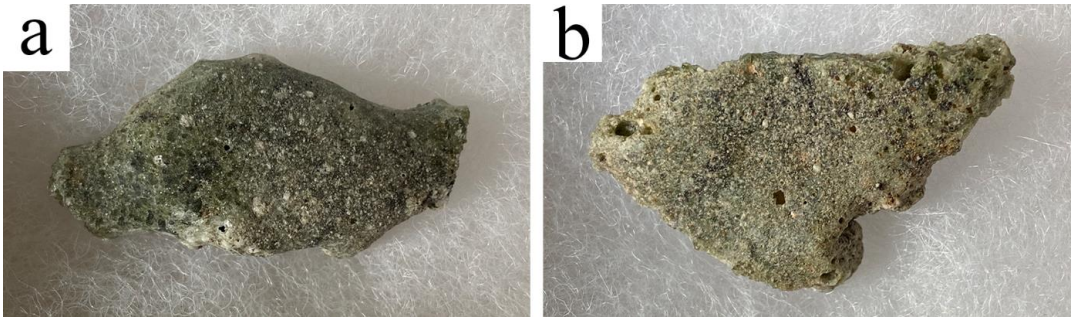

Figure S4: Pictures of used trinitite specimens. Trinitite 1 US (a) and Trinitite 2 US (b).

2.4 $^{135}Cs/^{137}Cs$ Ratio Shift over Time

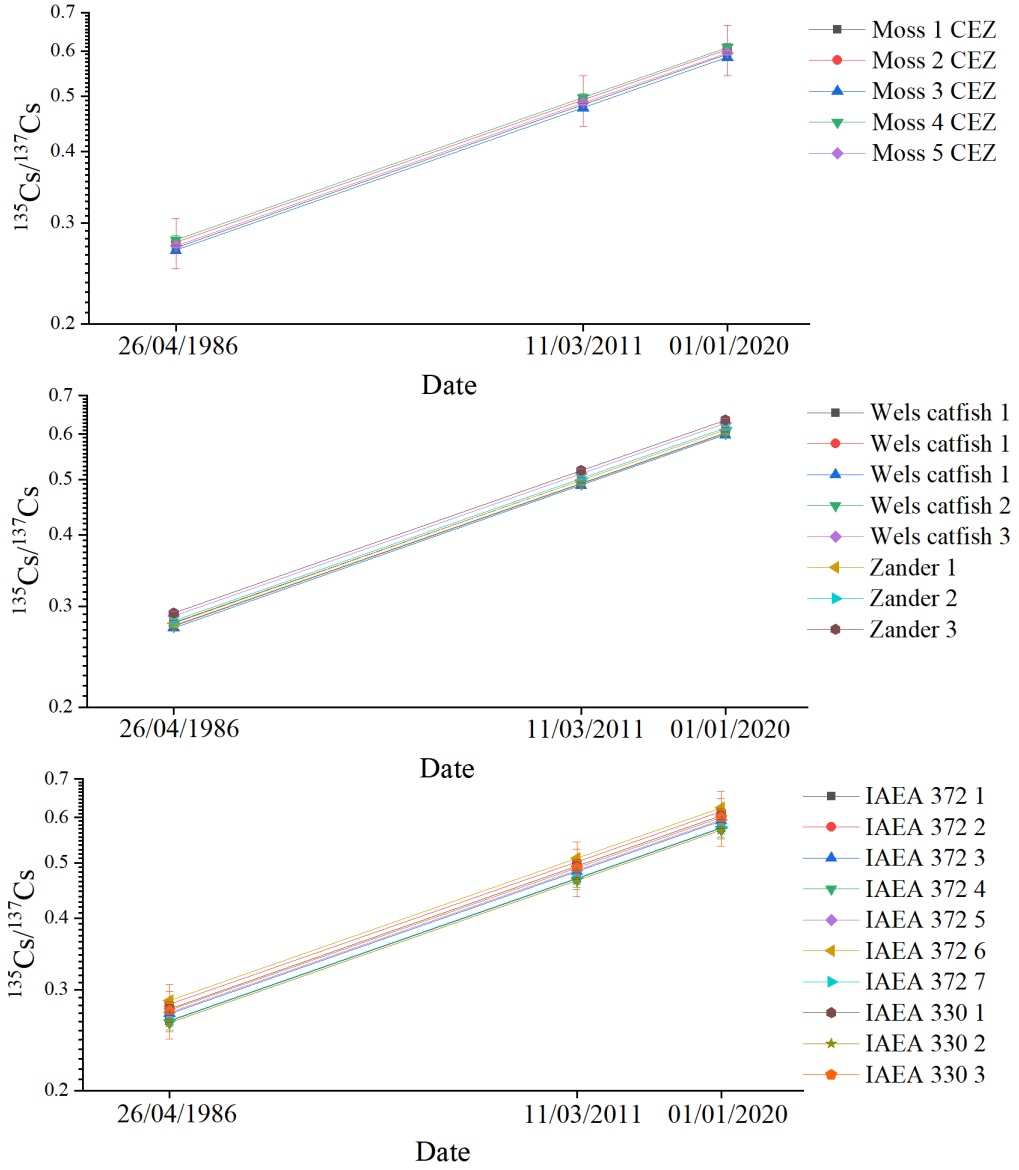

Figure S5a: Graphical illustration of the shift of the $^{135}Cs/^{137}Cs$ isotope ratios for sample clusters from CEZ over time.

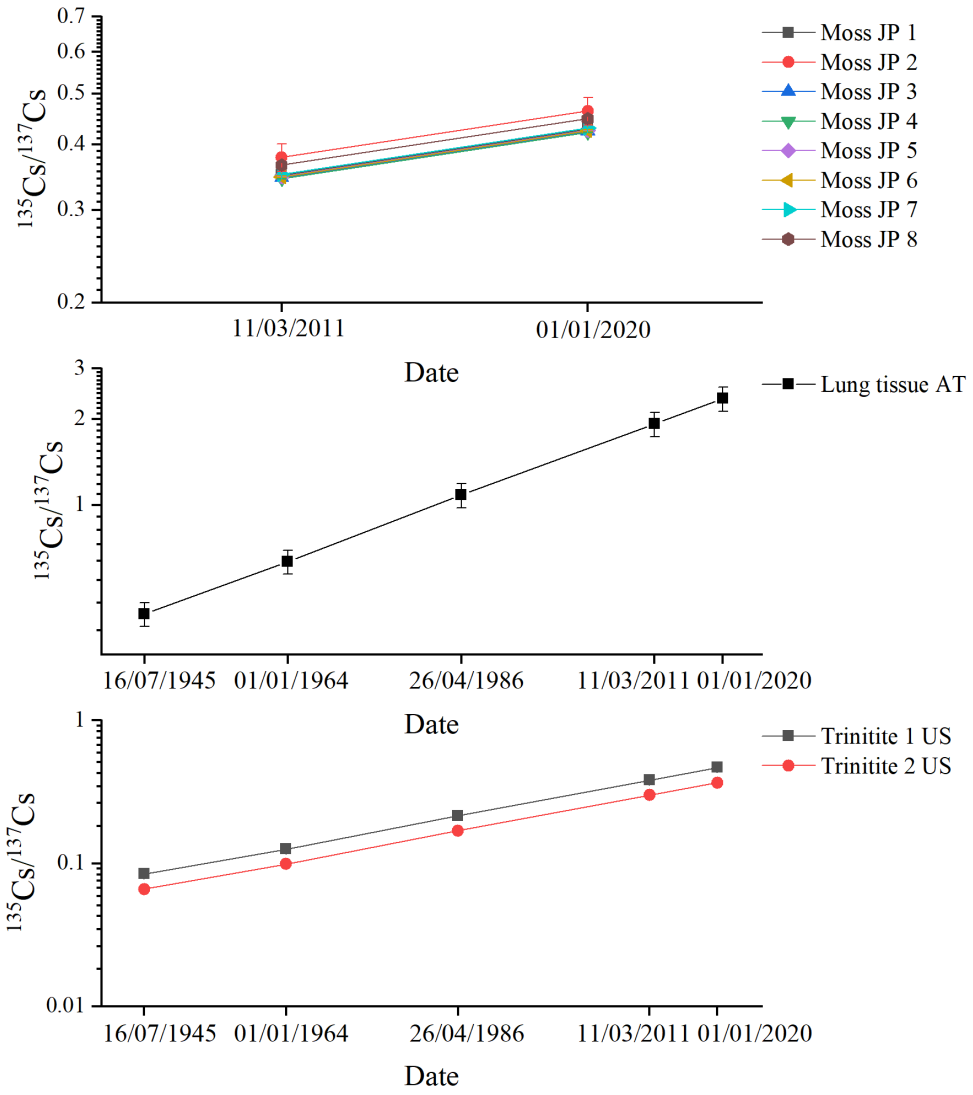

Figure S5b: Graphical illustration of the shift of the $^{135}Cs/^{137}Cs$ isotope ratios for sample clusters from Japan, Austria, and USA over time.

Acknowledgment

My heartfelt thanks go to my supervisor Georg Steinhauser, who enabled this project and thesis to me. Thank you for all the opportunities you gave for me during this time and the freedom to develop solutions creatively. They will be unforgettable for me.
A huge thanks to Clemens Walther for the leading of this institute and his great teaching in chemistry and physics, which brings me to the institute. Thank you as well for being co-referent of my thesis.
Also a huge thanks to Timo Hopp and Thorsten Kleine from University of Münster for the joint research about Ru isotope ratio measurement and related discussions, as well as being a co-referent to my thesis.

I am grateful to my colleague Anica Weller. Together we spent many hours in the laboratory solving problems of any kind. As an additional benefit we also spent wonderful times on business trips to present our works to an international audience.
Stefan Bister, Tobias Blenke, Julia Stadler, Felix Stäger, and Rebecca Querfeld a special thanks to you all for always having a good advice and your help in any area. The discussions with you were always very insightful to my work and increased my motivation.

Many thanks also to Johannes Sterba and Michaela Foster for the help with sample preparation and measurements of INAA in Vienna.
This thesis would have not been possible without the enormous work of the whole "Ring of Five" members for monitoring and measuring. Thank you all for this work you had with the ^{106}Ru. Thanks to Olivier Masson from IRSN for coordinating this case.
A warm thanks to the team of the Radiation Protection Bureau of Health Canada, especially Michael Cooke, Kurt Unger, and Ian Hoffman for invitation, time and possibility for the joint research on modern Ru complex chemistry.

Thanks to Sandra Reinhard, Sascha Sprott, Felix Kegler, and Luisa Syrbe for preparation and evaluation of some samples during their thesis as well as to Tobias Blenke, Darcy van Eerten, Julia Stadler and Anica Weller for helping me with the correction of this work.
Many issues were not possible with the great work of the technical and administrative staff. Thank you for your support and help in any case. Generally, a thanks to all members of the Institute of Radioecology and Radiation Protection for the great time here.

Many thanks to all of my family members and friends for help and support during the last years.

And last but not least I want to thank the *Volkswagen Stiftung* and *Deutsche Forschungsgemeinschaft* for financial support to perform research in this international scale of impact.

Curriculum Vitae

Academic Carrier

Since 10/2017	PhD in Physics at Leibniz Universität Hannover PhD thesis at Institute of Radioecology and Radiation Protection under Prof. Dr. Geoprg Steinhauser "*Analytical Investigations of Understudied Nuclides in Modern Environmental Nuclear Forensics*"
10/2015 - 09/2017	Master study of Analytics at Leibniz Universität Hannover Master thesis at Institute of Radioecology and Radiation Protection under Prof. Dr. Georg Steinhauser "*Separation von Radiosilber aus Umweltproben*"
10/2012 - 09/2015	Bachelor study of Chemistry at Leibniz Universität Hannover Bachelor thesis at the Institute of Physical Chemistry and Electrochemistry under Prof. Dr. Nadja Bigall "*Assemblierung von Nanokristallen mit Hilfe des Tintenstrahldruckverfahrens*"

Education

08/2004 - 08/2012	Geschwister-Scholl Gymnasium Berenbostel Abitur (A Level)
08/2000 - 07/2004	Ratsschule Berenbostel

Publication List

2021 D. Zok, T. Blenke, S. Reinhard, S. Sprott, F. Kegler *et al.*, "Determination of Characteristic vs. Anomalous $^{135}Cs/^{137}Cs$ Isotopic Ratios in Radioactively Contaminated Environmental Samples", *Environ. Sci. Technol.* vol. 55, no. 8, pp. 4984-4991, 2021. DOI: 10.1021/acs.est.1c00180

2020 T. Hopp, D. Zok, T. Kleine, G. Steinhauser, "Non-Natural Ruthenium Isotope Ratios of the Undeclared 2017 Atmospheric Release Consistent with Civilian Nuclear Activities", *Nat. Commun.* vol. 11, no. 1, pp. 1-7, 2020. DOI: 10.1038/s41467-020-16316-3

2020 M.W. Cooke, A. Botti, D. Zok, G. Steinhauser, K.R. Ungar, "Identification of a Chemical Fingerprint Linking the Undeclared 2017 Release of ^{106}Ru to Advanced Nuclear Fuel Reprocessing", *Proc. Natl. Acad. Sci. U. S. A.*, vol. 117, no. 26, pp. 14703-14711, 2020 DOI: 10.1073/pnas.2001914117

2020 A. Weller, D. Zok, S. Reinhard, S.K. Woche, G. Guggenberger, G. Steinhauser, "Separation of Ultratraces of Radiosilver from Radiocesium for Environmental Nuclear Forensics", *Anal. Chem.*, vol. 92, no. 7, pp. 5249-5257, 2020. DOI: 10.1021/acs.analchem.9b05776

2020 I. Spykman, T. Blenke, S. Büchner, D. Degering, K. Eleftheriadis, H.W. Fischer, G. Lasche, O. Masson, J.W. Mietelski, D. Ransby, F. Renz, M.E. Souti, D. Zok, G. Steinhauser, "Searching for the "smoking gun" of the miscarried 2019 Nenoksa nuclear cruise missile test: a null result", *Z. Anorg. Allg. Chem.*, vol. 318, no. 1, pp. 415-421, 2020. DOI: 10.1002/zaac.202000291

2019 O. Masson, G. Steinhauser, D. Zok, O. Saunier *et al.*, "Airborne Concentrations and Chemical Considerations of Radioactive Ruthenium from an Undeclared Major Nuclear Release in 2017", *Proc. Natl. Acad. Sci. U. S. A.*, vol. 116, no. 34, pp. 16750-16759, 2019. DOI: 10.1073/pnas.1907571116

2019 A. Weller, D. Zok, G. Steinhauser, "Uptake and Elemental Distribution of Radiosilver ^{108m}Ag and Radiocesium ^{137}Cs in Shiitake Mushrooms (*Lentinula edode*)", *J. Radioanal. Nucl. Chem.*, vol. 322, no. 3, pp. 1761-1769, 2019. DOI: 10.1021/acs.analchem.9b05776

2019 F. Lübkemann, J.F. Miethe, F. Steinbach, P. Rusch, A. Schlosser, D. Zámbó, T. Heinemeyer, D. Natke, D. Zok, D. Dorfs, N.C. Bigall, "Patterning of NanoparticleBased Aerogels and Xerogels by Inkjet Printing", *Small*, vol. 15, no. 39, pp. 1-8, 2019. DOI: 10.1002/smll.201902186

2018 D. Zok, J. H. Sterba, G. Steinhauser, "Chemical and Radioanalytical Investigations of ^{106}Ru-containing Air Filters from Vienna in Fall 2017: Searching for Stable Element Anomalies", *J. Radioanal. Nucl. Chem.*, vol. 318, no. 1, pp. 415-421, 2018. DOI: 10.1007%2Fs10967-018-6132-6

Oral Presentations and Posters

2020 53. DGMS Jahrestagung - Deutsche Gesellschaft für Massenspektrometrie
Germany, Münster, 1.-4. March 2020
Poster: *"Mapping of Elements in Various Environmental Matrices with LA-ICP-QQQ-MS"*

2019 5. ENVIRA - Environmental Radioactivity
Czech Republic, Prag, 8.-13. September 2019
Oral: *"Nuclear Forensics around the Ruthenium-106 Release in Fall 2017 above Europe"*
Poster: *"Establishing Environmental Nuclear Forensics with Radiocesium Isotopes ^{135}Cs and ^{137}Cs using Triple Quadrupole ICP-MS"*

2019 2. RANC - Radioanalytical and Nuclear Chemistry
Hungary, Budapest, 5.-10. May 2019
Oral: *"Nuclear Forensics on the $^{135}Cs/^{137}Cs$ Ratio by ICP-QQQ-MS"*

2019 83. DPG Frühjahrstagung - Deutsche Physikalische Gesellschaft
Germany, Rostock, 10.-15. March 2019
Oral: *"Nukleare Forensik am Isotopenverhältnis $^{135}Cs/^{137}Cs$ mittels ICP-QQQ-MS"*

2019 27. SAAGAS - Seminar on Activation Analysis and Gamma Spectrometry
Germany, Munich, 24.-27. February 2019
Oral: *"Chemische und Radiochemische Untersuchungen von ^{106}Ru in Umweltproben"*

2018 8. RCA Workshop - Radiochemische Analytik Workshop
Germany, Dresden, 12.-14. June 2018
Oral: *"Chemische und Radioanalytische Untersuchungen von ^{106}Ru in Umweltproben"*

2018 MARC XI - Methods and Applications of Radioanalytical Chemistry
USA, Hawaii, 8.-13. April 2018
Oral: *"Isolation of Radiosilver Nuclides for Forensic Evaluation of Possibly Damaged Reactor Cores"*
Oral: *"Chemical and Radioanalytical Investigations of Ruthenium-106 in Environmental Samples"*

Statutory Declaration

Hiermit bestätige ich, dass die vorliegende Arbeit selbstständig verfasst und keine anderen als die angegebenen Quellen und Hilfsmittel verwendet wurden. Alle Stellen der Arbeit, die wörtlich oder sinngemäß aus anderen Quellen übernommen wurden, sind als solche kenntlich gemacht. Tabellen und Abbildungen sind, soweit nicht mit einer Quelle gekennzeichnet, selbst erstellt worden.